

USE OF THE 1,1'-FERROCENEDICARBOXYLATE AS LIGAND IN CLUSTER  
CHEMISTRY AND NEW IMPROVEMENT APPROACH OF THE BOND VALENCE  
SUM PARAMETERS THROUGH STATISTICAL METHODS

By

ANTONIO MASELLO

A DISSERTATION PRESENTED TO THE GRADUATE SCHOOL  
OF THE UNIVERSITY OF FLORIDA IN PARTIAL FULFILLMENT  
OF THE REQUIREMENTS FOR THE DEGREE OF  
DOCTOR OF PHILOSOPHY

UNIVERSITY OF FLORIDA

2010

© 2010 Antonio Masello

To my family, for their wholehearted love.

## ACKNOWLEDGMENTS

The first acknowledgement is for my advisor, Prof. George Christou. He guided me through a complex research field with expertise, patience and professionalism. He has promoted my critical thinking, led me in developing communication skills and expanded my view of what chemical research is through personal advice or by sponsoring my participation in several conferences. I also would like to equally thank my committee members Dr. Adam Veige, Dr. Daniel Talham, Dr. Mark Meisel, Dr. Nicolò Omenetto and Dr. Stephen Hill for their availability to advise me and follow my research progress.

I would like to thank my research collaborators Dr. Stephen Hill and his students for the HFEPR studies, Dr Wolfgang Wernsdorfer for the micro-Squid measurements, Dr. Yiannis Sanakis and Dr. Athanassios K. Boudalis for the Mössbauer analysis, Dr. Nicolò Omenetto and Jonathan Merten for photochemistry experiments, and Dr. Alexander Angerhofer for preliminary EPR investigations. Special thanks go to Dr. Khalil A. Abboud for the X-ray structure determinations, introduction to basics of X-ray crystallography and his kind and professional guidance while working as an assistant at the X-ray lab. I also warmly thank Dr. Spyros Perlepes, Dr. Anastasios Tasiopoulos and Eleni Moushi for interesting scientific exchanges and occasions of collaboration.

I would like to acknowledge the two teaching advisors Dr. James Horvath and Dr. Adam Veige for their guidance and for developing my teaching skills. The Department of Chemistry at the University of Florida has also been fundamental in its various components with particular regard to the graduate coordinator Dr. Benjamin Smith and the secretary Lori Clark. I greatly thank all the Christou group members beginning with the secretaries Sondra, Melinda and Alice, all the postdoctoral students who positively contributed to my research, especially Muralee, Dinos and Ninetta as well as all the

graduate and undergraduate students. I will particularly remember my former colleagues Nicole, Abhu, Alina and Dolos as well as all the current ones. I thank my friends here in Florida and in Italy for the constant support and the evenings spent at the "Salty Dog" restaurant followed by a last minute "spaghetti alla carbonara" at 4 a.m. Throughout my studies at UF I have had the constant support of my family for whom I keep my deepest feelings of gratitude. They have always been ready to listen and share my joy on shiny days, and provide comfort on the rainy ones.

## TABLE OF CONTENTS

	<u>page</u>
ACKNOWLEDGMENTS.....	4
LIST OF TABLES.....	9
LIST OF FIGURES.....	11
ABSTRACT .....	15
CHAPTER	
1 GENERAL INTRODUCTION .....	17
Transition Metal Clusters .....	17
Bond Valence Sum .....	39
2 Mn <sub>13</sub> - AND Mn <sub>8</sub> -CLUSTERS FROM THE USE OF 1,1'- FERROCENEDICARBOXYLIC ACID .....	45
Introduction .....	45
Properties of FdcH <sub>2</sub> , and Previous Applications .....	47
Synthesis of FdcH <sub>2</sub> .....	55
Synthesis of [Mn <sub>13</sub> O <sub>8</sub> (OR) <sub>6</sub> (fdc) <sub>6</sub> ], (R = Me, Et), [Mn <sub>8</sub> O <sub>4</sub> (fdc) <sub>6</sub> (DMF) <sub>2</sub> (H <sub>2</sub> O) <sub>2</sub> ] and [Mn <sub>8</sub> O <sub>4</sub> (fdc) <sub>6</sub> (DMF) <sub>4</sub> ] .....	60
Description of the Molecular Structures .....	66
[Mn <sub>13</sub> O <sub>8</sub> (OMe) <sub>6</sub> (fdc) <sub>6</sub> ]·8CH <sub>2</sub> Cl <sub>2</sub> ; (2) ·8CH <sub>2</sub> Cl <sub>2</sub> .....	66
[Mn <sub>8</sub> O <sub>4</sub> (fdc) <sub>6</sub> (DMF) <sub>2</sub> (H <sub>2</sub> O) <sub>2</sub> ]·4DMF·4H <sub>2</sub> O; (4)·4DMF·4H <sub>2</sub> O.....	70
[Mn <sub>8</sub> O <sub>4</sub> (fdc) <sub>6</sub> (DMF) <sub>4</sub> ]·4DMF; (5)·4DMF .....	73
Magnetochemistry .....	77
[Mn <sub>13</sub> O <sub>8</sub> (OMe) <sub>6</sub> (fdc) <sub>6</sub> ]·4H <sub>2</sub> O·3MeOH; (2)· 4H <sub>2</sub> O·3MeOH and [Mn <sub>13</sub> O <sub>8</sub> (OEt) <sub>6</sub> (fdc) <sub>6</sub> ]·7EtOH; (3)·7EtOH .....	77
[Mn <sub>8</sub> O <sub>4</sub> (fdc) <sub>6</sub> (DMF) <sub>2</sub> (H <sub>2</sub> O) <sub>2</sub> ]·4DMF·4H <sub>2</sub> O; (4)·4DMF·4H <sub>2</sub> O .....	82
[Mn <sub>8</sub> O <sub>4</sub> (fdc) <sub>6</sub> (DMF) <sub>4</sub> ]·1.5DMF·3H <sub>2</sub> O; (5)·1.5DMF·3H <sub>2</sub> O.....	88
Electrochemistry .....	91
Summary and Conclusions .....	94
Experimental.....	95
[Mn <sub>13</sub> O <sub>8</sub> (OMe) <sub>6</sub> (fdc) <sub>6</sub> ]·4H <sub>2</sub> O·3MeOH; (2)· 4H <sub>2</sub> O·3MeOH.....	95
[Mn <sub>13</sub> O <sub>8</sub> (OEt) <sub>6</sub> (fdc) <sub>6</sub> ]·7EtOH; (3)·7EtOH.....	96
[Mn <sub>8</sub> O <sub>4</sub> (fdc) <sub>6</sub> (DMF) <sub>2</sub> (H <sub>2</sub> O) <sub>2</sub> ]·4DMF·4H <sub>2</sub> O; (4)·4DMF·4H <sub>2</sub> O, Method (a) .....	96
[Mn <sub>8</sub> O <sub>4</sub> (fdc) <sub>6</sub> (DMF) <sub>2</sub> (H <sub>2</sub> O) <sub>2</sub> ]·3DMF·2H <sub>2</sub> O; (4)·3DMF·2H <sub>2</sub> O, Method (b) .....	97
[Mn <sub>8</sub> O <sub>4</sub> (fdc) <sub>6</sub> (DMF) <sub>4</sub> ]·1.5DMF·3H <sub>2</sub> O; (5)·1.5DMF·3H <sub>2</sub> O.....	97
X-Ray Crystallography.....	98
Magnetic Measurements .....	99
Other Measurements.....	100

3	NEW Fe <sub>7</sub> -CLUSTER FROM NON-INNOCENT REACTIONS OF 1,1'-FERROCENEDICARBOXYLIC ACID IN POLAR MEDIA .....	101
	Introduction .....	101
	Synthetic Strategies for Coordination Compounds with Fdc <sup>2-</sup> .....	103
	Synthesis .....	107
	Initial Reactions of FdcH <sub>2</sub> with Fe Sources .....	107
	Photosensitivity of FdcH <sub>2</sub> .....	110
	Further Study with Other Metal Sources.....	113
	Description of the Molecular Structures .....	115
	Magnetochemistry of the Heptanuclear Clusters [M <sub>7</sub> O <sub>3</sub> (OMe)(fdc) <sub>6</sub> (MeOH) <sub>3</sub> ] <sup>n+</sup> ....	122
	Mössbauer Spectroscopy of the [M <sub>7</sub> O <sub>3</sub> (OMe)(fdc) <sub>6</sub> (MeOH) <sub>3</sub> ] <sup>n+</sup> Clusters.....	127
	Electrochemistry of the [M <sub>7</sub> O <sub>3</sub> (OMe)(fdc) <sub>6</sub> (MeOH) <sub>3</sub> ] <sup>n+</sup> Clusters.....	131
	Conclusions .....	134
	Experimental.....	135
	[Fe <sub>7</sub> O <sub>3</sub> (OMe)(fdc) <sub>6</sub> (MeOH) <sub>3</sub> ] <sup>3+</sup> ·[FeCl <sub>4</sub> ] <sup>-</sup> ·2Cl <sup>-</sup> ·8H <sub>2</sub> O·6MeOH; (6)·8H <sub>2</sub> O·6MeOH .....	135
	[Fe <sub>6.2</sub> Mn <sub>0.8</sub> O <sub>3</sub> (OMe)(fdc) <sub>6</sub> (H <sub>2</sub> O) <sub>3</sub> ] <sup>+</sup> ·Cl <sup>-</sup> ·5H <sub>2</sub> O·4MeOH; (7)·5H <sub>2</sub> O·4MeOH .....	136
	[Fe <sub>x</sub> Co <sub>7-x</sub> O <sub>3</sub> (OMe)(fdc) <sub>6</sub> (MeOH) <sub>3</sub> ] <sup>2+</sup> ·2Cl <sup>-</sup> ·solv.; (8)·solv. ....	136
	[Fe <sub>x</sub> Ni <sub>7-x</sub> O <sub>3</sub> (OMe)(fdc) <sub>6</sub> (MeOH) <sub>3</sub> ] <sup>+</sup> ·Cl <sup>-</sup> ·solv.; (9)·solv.....	136
	[Fe <sub>x</sub> Zn <sub>7-x</sub> O <sub>3</sub> (OMe)(fdc) <sub>6</sub> (MeOH) <sub>3</sub> ] <sup>+</sup> ·½[ZnCl <sub>4</sub> ] <sup>2-</sup> ·solv.; (10)·solv. ....	136
	X-Ray Crystallography.....	137
	Magnetic Measurements .....	139
	Other Measurements.....	139
4	NEW APPROACH FOR THE IMPROVEMENT OF THE BOND VALENCE SUM PARAMETERS USING STATISTICAL METHODS .....	141
	Introduction .....	141
	Known Examples of BVS Optimization .....	146
	Approach to a New Optimization Method.....	150
	Definitions.....	150
	Exact Methods.....	152
	Meta-Heuristics .....	153
	Description of the Problem and Choice of the Meta-Heuristics Method .....	153
	The Variable Neighborhood Search .....	155
	Initial Experimental Setup .....	155
	Selection of the Structural Data.....	155
	Proposal for a New BVS Formula.....	161
	Application to the CCDC Database.....	163
	Data Retrieval from the CCDC Database .....	163
	Data and Software Preparation for the Optimization .....	164
	Analysis of the Results .....	167
	Titanium .....	167
	Vanadium.....	168
	Chromium .....	168
	Manganese .....	168

Iron.....	169
Cobalt .....	169
Nickel .....	169
Copper .....	170
Conclusions .....	170

## APPENDIX

A CODES FOR THE COMPOUNDS LISTED .....	172
B FULL CRYSTALLOGRAPHIC TABLES.....	173
C BOND LENGTHS AND ANGLES .....	181
D BVS OPTIMIZATION DATA.....	198
LIST OF REFERENCES .....	202
BIOGRAPHICAL SKETCH.....	215

## LIST OF TABLES

<u>Table</u>	<u>page</u>
2-1 Selected crystal data for complex <b>2</b> ·8CH <sub>2</sub> Cl <sub>2</sub> .....	66
2-2 Bond Valence Sum values for complex <b>2</b> .....	68
2-3 Selected crystal data for complex <b>4</b> ·4DMF·4H <sub>2</sub> O.....	71
2-4 Bond Valence Sum calculations for complex <b>4</b> .....	72
2-5 Selected crystal data for complex <b>5</b> ·4DMF.....	74
2-6 Bond Valence Sum calculations for complex <b>5</b> .....	75
3-1 Selected crystal data for complex <b>6</b> ·2MeOH·2H <sub>2</sub> O.....	116
3-2 Bond Valence Sum calculations for complex <b>6</b> .....	118
3-3 Fe-centroid and centroid-centroid distances (Å) in complex <b>6</b> .....	119
3-4 Bond Valence Sum calculations for complex <b>7</b> according to the Mn and Fe parameters.....	121
3-5 Counterion composition for <b>7-10</b> obtained by Cl microanalysis.....	122
4-1 Expected and calculated Co valences in [Co <sub>8</sub> O <sub>4</sub> (O <sub>2</sub> CPh) <sub>12</sub> (H <sub>2</sub> O)(MeCN) <sub>3</sub> ] based on published data.....	144
4-2 Comparison of BVS values obtained for a series of model compounds by the newly optimized and published <i>r</i> <sub>0</sub> parameters.....	147
4-3 BVS parameters for Fe and Mn obtained from the literature and by a preliminary VNS optimization (with <i>b</i> variable) over a selected database (Å)...	157
4-4 BVS values for [Mn <sub>12</sub> O <sub>12</sub> (O <sub>2</sub> CMe) <sub>16</sub> (H <sub>2</sub> O) <sub>4</sub> ] calculated with published literature data and by preliminary VNS optimization of <i>r</i> <sub>0</sub> and <i>b</i> .....	158
4-5 BVS values for [Fe <sub>3</sub> O(O <sub>2</sub> CMe) <sub>6</sub> (H <sub>2</sub> O) <sub>3</sub> ] <sup>+</sup> calculated with published literature data and by preliminary VNS optimization of <i>r</i> <sub>0</sub> and <i>b</i> .....	159
4-6 <i>R</i> <sub>0</sub> values obtained by computations on the subset data of known valence for iron ( <i>b</i> = 0.37 Å).....	165
B-1 Crystal data and structure refinement for <b>2</b> ·8CH <sub>2</sub> Cl <sub>2</sub> .....	173
B-2 Crystal data and structure refinement for <b>4</b> ·4DMF·4H <sub>2</sub> O.....	174

B-3	Crystal data and structure refinement for <b>5</b> ·3DMF·H <sub>2</sub> O.....	175
B-4	Crystal data and structure refinement for <b>6</b> ·2MeOH·2H <sub>2</sub> O. ....	176
B-5	Crystal data and structure refinement for <b>7</b> ·3DMF·3H <sub>2</sub> O.....	177
B-6	Crystal data and structure refinement for <b>8</b> ·4MeOH·2H <sub>2</sub> O. ....	178
B-7	Crystal data and structure refinement for <b>9</b> ·4MeOH. ....	179
B-8	Crystal data and structure refinement for <b>10</b> ·6MeOH·2H <sub>2</sub> O. ....	180
C-1	Selected bond lengths [Å] and angles [°] for [Mn <sub>13</sub> O <sub>8</sub> (OMe) <sub>6</sub> (fdc) <sub>6</sub> ], <b>2</b> . ....	181
C-2	Selected bond lengths [Å] and angles [°] for [Mn <sub>8</sub> O <sub>4</sub> (fdc) <sub>6</sub> (DMF) <sub>2</sub> (H <sub>2</sub> O) <sub>2</sub> ], <b>4</b> . ....	187
C-3	Selected bond lengths [Å] and angles [°] for [Mn <sub>8</sub> O <sub>4</sub> (fdc) <sub>6</sub> (DMF) <sub>4</sub> ], <b>5</b> . ....	189
C-4	Selected bond lengths [Å] and angles [°] for [Fe <sub>7</sub> O <sub>3</sub> (OMe)(fdc) <sub>6</sub> (MeOH) <sub>3</sub> ] <sup>3+</sup> [FeCl <sub>4</sub> ] <sup>-</sup> ·2Cl <sup>-</sup> , <b>6</b> . ....	194
D-1	<i>R</i> <sub>0 opt</sub> values (Å) obtained for titanium with <i>b</i> <sub>opt</sub> = 0.447. ....	200
D-2	<i>R</i> <sub>0 opt</sub> values (Å) obtained for vanadium with <i>b</i> <sub>opt</sub> = 0.414. ....	200
D-3	<i>R</i> <sub>0 opt</sub> values (Å) obtained for chromium with <i>b</i> <sub>opt</sub> = 0.426. ....	200
D-4	<i>R</i> <sub>0 opt</sub> values (Å) obtained for manganese with <i>b</i> <sub>opt</sub> = 0.617. ....	200
D-5	<i>R</i> <sub>0 opt</sub> values (Å) obtained for iron with <i>b</i> <sub>opt</sub> = 0.630. ....	201
D-6	<i>R</i> <sub>0 opt</sub> values (Å) obtained for cobalt with <i>b</i> <sub>opt</sub> = 0.449. ....	201
D-7	<i>R</i> <sub>0 opt</sub> values (Å) obtained for cobalt with <i>b</i> <sub>opt</sub> = 0.376. ....	201
D-8	<i>R</i> <sub>0 opt</sub> values (Å) obtained for copper with <i>b</i> <sub>opt</sub> = 0.433. ....	201

## LIST OF FIGURES

<u>Figure</u>	<u>page</u>
1-1	Relationship between the energy level diagram of an $M_6$ system and band diagram of a bulk metal. .... 18
1-2	Common bridging modes for the hydroxide and oxide anions ..... 19
1-3	Most common structural types adopted by trinuclear and tetranuclear carboxylate clusters..... 21
1-4	Diagram of the $Mn_4Ca$ cluster supporting water oxidation in the OEC of green plants and cyanobacteria..... 23
1-5	Hypothetical mechanism for the incipient O-O bond formation during the final intermediate state "[S <sub>4</sub> ]" of the OEC. .... 25
1-6	Frontier electronic diagram for a pentacoordinated $Cu^{II}$ ion in a sp geometry and structural sketch of the $Cu^{II}$ acetate. .... 27
1-7	Two possible mechanisms for the Cu-Cu magnetic interaction in Cu(II) acetate..... 29
1-8	Sketch of trinuclear triangular species displaying some of the possible exchange interactions leading to frustration/satisfaction pathways. .... 30
1-9	Double-well energy diagram for a $S = 10$ molecule with negative magnetic anisotropy parameter $D$ . .... 32
1-10	Pov-Ray projection of the $Mn_{12}$ -acetate cluster ..... 34
1-11	MO diagram scheme for the ferrocene molecule in the eclipsed configuration. . 36
1-12	Potential coordination modes for a generic carboxylate. .... 38
1-13	Schematic diagram of the 1,1'-ferrocenedicarboxylic acid ( $fdcH_2$ )..... 38
1-14	Scheme explaining the extension of the delocalization of a conjugated substituent to a ferrocene system..... 39
1-15	Plot of bond strength expressed as valence units (v.u.) vs. the corresponding average bond length in Å for a series of metal oxides. .... 41
2-1	Known coordination modes of $fdc^{2-}$ . .... 48
2-2	Pov-Ray projection of $[{Os}_3H(CO)_{10}]_2fdc$ ..... 49

2-3	Square array of $\text{Mo}_2^{4+}$ units bridged by $\text{fdc}^{2-}$ and analogous arrangement in a square of four $\text{Ga}_2^0$ units. ....	49
2-4	Pov-Ray projection of the $[\text{Sn}_8\text{O}_4(\text{fdc})_6]$ cluster and its cyclic voltammogram in DMF vs. sat. Ag/AgCl. ....	52
2-5	Modified synthesis of the ligand precursor 1,1'-ferrocenedicarboxylic acid. ....	56
2-6	$^1\text{H-NMR}$ spectrum of raw 1,1'-ferrocenedicarboxylic acid saturated in $d^6$ -DMSO.....	57
2-7	400 MHz $^1\text{H-NMR}$ spectrum of 1,1'-ferrocenedicarboxylic acid 0.040 g. in 0.5 mL $d^6$ -DMSO. ....	58
2-8	HREIMS spectrum of the synthesized 1,1'-ferrocenedicarboxylic acid. ....	58
2-9	Comparison of IR spectra for commercial 1,1'-ferrocenedicarboxylic acid and the synthesized product.....	59
2-10	Pov-Ray projection of <b>2</b> . ....	67
2-11	Pov-Ray projection of the $[\text{Mn}^{\text{IV}}\text{Mn}^{\text{III}}_6\text{Mn}^{\text{II}}_6(\mu_5\text{-O})_6(\mu_3\text{-O})_2]^{18+}$ core in $[\text{Mn}_{13}\text{O}_8(\text{OMe})_6(\text{fdc})_6]$ .....	67
2-12	Packing diagram for complex <b>2</b> in Mercury.....	70
2-13	Pov-Ray projection of $[\text{Mn}_8\text{O}_4(\text{fdc})_6(\text{DMF})_2(\text{H}_2\text{O})_2]$ .....	71
2-14	Pov-Ray projection of the core $[\text{Mn}^{\text{III}}_4\text{Mn}_4^{\text{II}}(\mu_4\text{-O})_4]^{12+}$ in <b>4</b> .....	72
2-15	Packing diagram for complex <b>4</b> in Mercury.....	73
2-16	Pov-Ray projection of complex <b>5</b> core. ....	75
2-17	Packing diagram of complex <b>5</b> in Mercury.....	76
2-18	Plot of $\chi_M T$ vs. T for complex <b>2</b> ·4H <sub>2</sub> O·3MeOH and complex <b>3</b> ·7EtOH.....	77
2-19	Plot of reduced magnetization (M/N $\mu_B$ ) vs. H/T for a sample of <b>3</b> ·7EtOH.....	78
2-20	g vs. D error surface for the m/N $\mu_B$ vs. H/T fit for <b>3</b> ·7EtOH.....	80
2-21	Plot of $\chi_M T$ vs. T for complex <b>3</b> ·7EtOH. ....	81
2-22	Plot of $\chi_M''$ vs. T for complex <b>3</b> ·7EtOH in the 1.8-15 K.....	81
2-23	Hysteresis measures for complex <b>2</b> ·8CH <sub>2</sub> Cl <sub>2</sub> in the 0.04-1 K range.....	82
2-24	Plot of $\chi_M T$ vs.T for complex <b>4</b> ·4DMF·4H <sub>2</sub> O. ....	83

2-25	Plot of reduced magnetization ( $M/N\mu_B$ ) vs. $H/T$ for <b>4</b> ·4DMF·4H <sub>2</sub> O. ....	84
2-26	Error plot for the estimation of $g$ and $D$ in <b>4</b> ·4DMF·4H <sub>2</sub> O. ....	85
2-27	Plot of $\chi_M T$ vs. $T$ for complex <b>4</b> ·4DMF·4H <sub>2</sub> O in the 1.8-15 K. ....	85
2-28	Plot of $\chi_M''$ vs. $T$ for complex <b>4</b> ·4DMF·4H <sub>2</sub> O in the 1.8-15 K. ....	87
2-29	Hysteresis measures for complex <b>4</b> ·4DMF·4H <sub>2</sub> O in the 0.04-1 K. ....	87
2-30	Plot of $\chi_M T$ vs. $T$ for complex <b>5</b> ·1.5DMF·3H <sub>2</sub> O. ....	88
2-31	Plot of $\chi_M T$ vs. $T$ for complex <b>5</b> ·1.5DMF·3H <sub>2</sub> O in the 1.8-15 K. ....	89
2-32	Plot of $\chi_M''$ vs. $T$ for complex <b>5</b> ·1.5DMF·3H <sub>2</sub> O. The inset shows tails of peaks in the 1.8 to 4 K region. ....	90
2-33	Superposition of the $\chi_M T$ vs. $T$ plots for <b>4</b> ·4DMF·4H <sub>2</sub> O and <b>5</b> ·3H <sub>2</sub> O·1.5DMF. ....	91
2-34	Solid-state voltammogram of fdch <sub>2</sub> , and complex <b>2</b> . ....	92
3-1	Structure of the pebbm ligand, 1,1'-(1,5-pentanediy)bis-1H-benzimidazole, and its coordination in a chain with cadmium ions. ....	105
3-2	Overlay of IR spectra for fmch in pyridine solution with increasing irradiation times. ....	111
3-3	UV-Visible spectra of ferrocene (Fc), benzoylferrocene (BFc) and 1,1'-dibenzoylferrocene (DFc) ....	112
3-4	Representation of the initial irradiation effect on 1,1'-benzoylferrocene. ....	113
3-5	Pov-Ray projection of $[\text{Fe}_7\text{O}_3(\text{OMe})(\text{fdc})_6(\text{MeOH})_3]^{3+}$ ....	115
3-6	Pov-Ray projection of the core $[\text{Fe}^{\text{III}}_7(\mu_4\text{-O})_3(\mu_3\text{-OMe})]^{14+}$ in <b>6</b> ....	116
3-7	Different chelation modes and respective torsion angles adopted by $\text{fdc}^{\text{n-}}$ in complex <b>6</b> . ....	117
3-8	Pov-Ray projection of two neighboring molecules of complex <b>6</b> in the lattice. ....	118
3-9	Packing diagram of complex <b>6</b> in Mercury. ....	120
3-10	Pov-Ray projection of the cluster cation <b>7</b> and its labeled core ....	121
3-11	Direct current measurement of $\chi_M T$ vs. $T$ for <b>6</b> ·8H <sub>2</sub> O·6MeOH. ....	123
3-12	Magnetic susceptibility plot for <b>6</b> with AC fields ....	125

3-13	Direct current measurement of $\chi_M T$ vs. T for <b>7</b> ·5H <sub>2</sub> O·4MeOH, <b>8</b> ·solv., <b>9</b> ·solv. and <b>10</b> ·solv. ....	126
3-14	AC (in-phase) $\chi_M T$ vs. T and (out-of-phase) $\chi_M''$ vs. T plots for <b>7-10</b> at 250Hz. ....	127
3-15	Overlay of the Mössbauer spectra collected at 250 and 140 K for sample <b>6</b> . ....	129
3-16	Superposition of Mössbauer spectra for <b>7-10</b> at 78 K. ....	131
3-17	Cyclic voltammogram (CV) and differential pulse voltammogram (DPV) of <b>6</b> in acetonitrile .....	132
4-1	Pov-Ray projection of [Co <sub>8</sub> O <sub>4</sub> (O <sub>2</sub> CPh) <sub>12</sub> (H <sub>2</sub> O)(MeCN) <sub>3</sub> ] and its core .....	143
4-2	Plot of the variation in <i>B</i> vs. Mn oxidation state in Mn-O compounds .....	148
4-3	Labeled core of [Mn <sub>12</sub> O <sub>12</sub> (O <sub>2</sub> CMe) <sub>16</sub> (H <sub>2</sub> O) <sub>4</sub> ] .....	157
4-4	Pov-Ray projection of the partially labeled structure of the cation [Fe <sub>3</sub> O(O <sub>2</sub> CMe) <sub>6</sub> (H <sub>2</sub> O) <sub>3</sub> ] <sup>+</sup> .....	159
4-5	Histogram of the errors (absolute values) on the valence estimation by the currently available BVS parameters. ....	160
4-6	Comparison of error distribution for the optimized BVS parameter <i>r</i> <sub>0</sub> and <i>b</i> with the currently published formula .....	162
4-7	Correlation between published or derived <i>r</i> <sub>0</sub> values .....	166
D-1	Exemplified flow chart of <i>chopt</i> algorithm .....	198
D-2	Histograms for the valence errors ( $\Delta$ ) before and after VNS optimization. ....	199

Abstract of Dissertation Presented to the Graduate School  
of the University of Florida in Partial Fulfillment of the  
Requirements for the Degree of Doctor of Philosophy

USE OF THE 1,1'-FERROCENEDICARBOXYLATE AS LIGAND IN CLUSTER  
CHEMISTRY AND NEW IMPROVEMENT APPROACH OF THE BOND VALENCE  
SUM PARAMETERS THROUGH STATISTICAL METHODS

By

ANTONIO MASELLO

December 2010

Chair: George Christou  
Major: Chemistry

This work focused on the synthesis and study of new transition metal clusters capable of multielectron exchange. Reactions of the ligand precursor 1,1'-ferrocenedicarboxylic acid (fdch<sub>2</sub>) in the presence of preformed clusters, such as [Mn<sub>12</sub>O<sub>12</sub>(O<sub>2</sub>CMe)<sub>16</sub>(H<sub>2</sub>O)<sub>4</sub>], led to the isolation of two [Mn<sub>13</sub>O<sub>6</sub>(OR)<sub>6</sub>(fdc)<sub>6</sub>] clusters, where R = Me or Et, and two [Mn<sub>8</sub>O<sub>4</sub>(fdc)<sub>6</sub>(DMF)<sub>4-n</sub>(H<sub>2</sub>O)<sub>n</sub>] clusters where n = 2 or 0 (DMF = N,N-dimethylformamide). The Mn<sub>13</sub> clusters have been magnetically studied and both were confirmed to possess a  $S = 9/2$  ground state with negative magnetic anisotropy,  $D$ . Neither of the two species showed single-molecule magnet behavior or could be further investigated electrochemically due to their low solubility in common solvents. The Mn<sub>8</sub> clusters have been obtained by different synthetic procedures reflecting minor differences in the peripheral composition. Such differences induce distortions that lower the symmetry of the structure containing four DMF molecules, which confer different magnetic properties from the homologous Mn<sub>8</sub> cluster with two DMF and two water molecules. [Mn<sub>8</sub>O<sub>4</sub>(fdc)<sub>6</sub>(DMF)<sub>2</sub>(H<sub>2</sub>O)<sub>2</sub>] has a spin ground-state  $S = 5$  with negative  $D$  and displays out-of-phase magnetic susceptibility signals and

hysteresis below 2 K, whereas  $[\text{Mn}_8\text{O}_4(\text{fdc})_6(\text{DMF})_4]$  has  $S = 2$  with almost negligible out-of-phase signals. Electrochemical investigations were impossible due to insolubility in common solvents.

Reactions of  $\text{fdCH}_2$  in polar media and several metal chlorides allowed for the isolation of the novel family of cationic clusters  $[\text{Fe}_x\text{M}_{7-x}\text{O}_3(\text{OMe})(\text{fdc})_6(\text{MeOH})_3]^{n+}$  ( $M = \text{Mn, Fe, Co, Ni, Zn}$ ). These products result from the photolysis of  $\text{fdCH}_2$  and only the iron-based complex could be fully characterized. The  $\text{Fe}_7$ -cluster possesses  $S = 2$  and is the first true example of a cluster containing an oxidized  $\text{fdc}^{-1}$  unit. All  $\text{Fe}_7\text{M}_{7-x}$  clusters display remarkable electrochemical behavior with simultaneous oxidation of the ferrocenyl units and progressive reductions on the clusters' core.

Along with the synthesis and study of new clusters, a novel work on the optimization of the parameters for the Bond Valence Sum (BVS) method was performed. The work applied meta-heuristic Variable Neighborhood Search (VNS) methods to a large database of inorganic compounds belonging to the first transition row implying a variable value of the parameter  $b$ . The study significantly improved the BVS accuracy on each metal and derived parameters for metal-donor combinations not yet reported in the literature.

## CHAPTER 1 GENERAL INTRODUCTION

### Transition Metal Clusters

In inorganic and organometallic chemistry the term "cluster" is used to indicate molecular compounds containing two or more associated and mutually interacting metal ions.<sup>1</sup> F. A. Cotton was the first to use this term in the early '60s for indicating polynuclear species with metal-metal bonding. Later, other authors defined clusters slightly differently, by referring to any polynuclear compound where a net or substantial degree of metal-metal bonding was present.<sup>2</sup> Nowadays, organometallic chemists adopt the term cluster when referring to a polynuclear species where the metals are held together by metal-metal bonds. In bioinorganic and general coordination chemistry, however, a cluster is a polynuclear species where the structure is mainly held together by bridging ligands, with negligible metal-metal bonds but perhaps with weak exchange interactions.<sup>3</sup>

Along the transition series, metals in groups 3-8 are recognized to produce stable and relatively inert bonds with oxygen or oxygenated ligands, whereas over the "oxo-wall" (groups 9-12) this tendency fades, giving no stable M=O compounds.<sup>4</sup> Analogously, early transition metals have stable interactions with  $\pi$ -donor ligands and the opposite is seen in groups 8-10, where the  $\pi$ -acceptor ligands (especially C $\equiv$ O) greatly promote low oxidation states and metal-metal bonding.<sup>5</sup> The effect of the  $\pi$ -acceptor ligands optimizes the M-M overlap of orbitals, which improves moving down the groups, in other words with the increase in the radial size of metal orbitals.<sup>5</sup> One of the major differences between the clusters that have metal-metal bonds and those that do not is revealed upon increase of the cluster size. In the former type, the properties tend to resemble

those of the bulk metal. For large clusters with M-M bonding there exists a clear correlation between the d-d bandwidth of a metal particle and the highest occupied and lowest unoccupied skeletal molecular orbital (HOMO-LUMO gap) (See Fig. 1-1).<sup>5</sup> Although an actual conduction band cannot be achieved in a cluster, a large number of energetically close electronic levels arise as the size increases, allowing the large systems to achieve numerous redox states.<sup>5</sup>

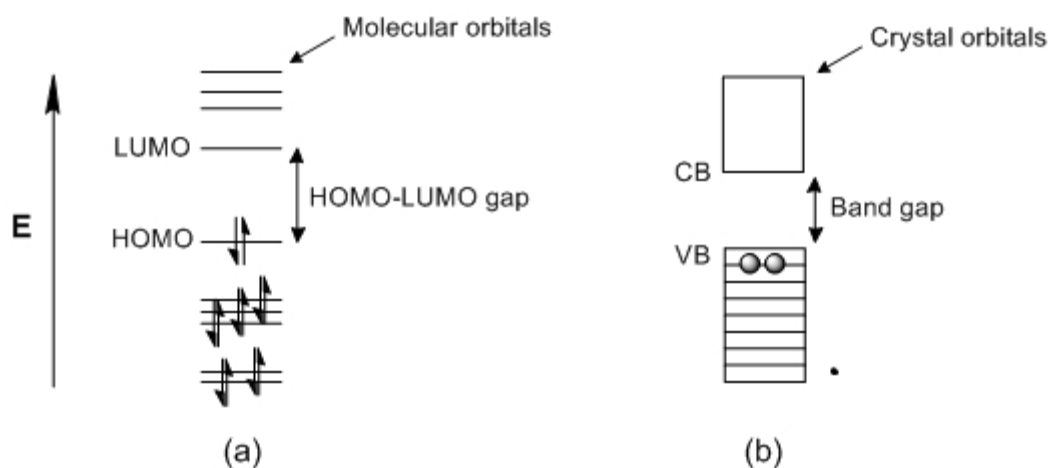
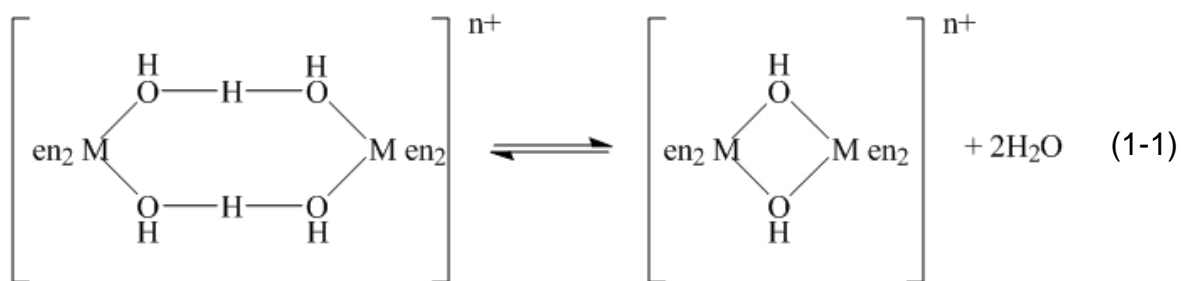


Figure 1-1. Relationship between (a) the energy level diagram of an  $M_6$  system and (b) band diagram of a bulk metal (adapted from ref. <sup>5</sup>).

In a cluster where M-M bonds are not present, each metal carries important properties that it would also carry as a mononuclear compound, particularly the spin. In clusters with M-M bonds the spin of two directly bonded atoms is quenched and the overall number of unpaired electrons is lowered, hence modifying the intrinsic properties of the metal ions.<sup>6</sup> In the other type of clusters, the initial spin of each metal ion is still available and this characteristic gives rise to all the consequent magnetic properties that distinguish clusters with ligand-bridged metals only. The oxide ion is often found to bridge and complete the skeleton structure of most clusters.

When a metal cation binds water it makes the latter more acidic, hence favoring an acid-base dissociation that leaves an hydroxide anion as ligand.<sup>7</sup> High concentrations of hydrated metal cations can promote metal aggregation through "oligation reactions". In this process, a coordinated hydroxide interacts with the proton of a coordinated water molecule on a neighboring hydrated metal. Consequent expulsion of a water molecule leaves the two metals bridged by an hydroxide, as illustrated in Eq. 1-1 (en is ethylenediamine), (adapted from ref. <sup>5</sup>).<sup>7</sup>



Such a process may be accompanied by further hydroxide dissociation to an oxo ligand, which in turn may promote additional metal aggregation. Some of the most common ligation modes for the hydroxo and oxo ligand are displayed in Fig. 1-2.<sup>7</sup>

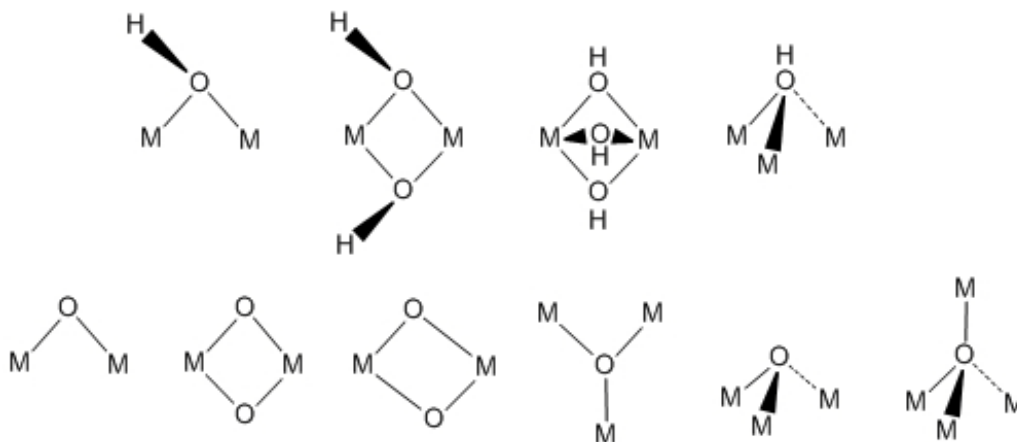


Figure 1-2. Common bridging modes for the hydroxide (top row) and oxide (bottom row) anions (adapted from ref. <sup>5</sup>).

Doubly bridged dinuclear structures are the most common.<sup>7</sup> A survey of the structurally-characterized compounds on the Cambridge Crystallographic Data Centre (CCDC)<sup>8</sup>,

restricted to the first transition row (with the exclusion of Sc and Zn), shows many dinuclear complexes belonging to one of the following three types:  $\{M(OH)_2M\}$ ,  $\{M(O,OH)M\}$  or  $\{M(O)_2M\}$ . In most cases, the peripheral ligation of the metal center is occupied either by bulky monodentate ligands like imidazole<sup>9</sup> or cyclohexylamine<sup>10</sup>, or more often by chelating or even macrocyclic donors like TACN (1,4,7-triazacyclononane)<sup>11</sup>. These systems may be stabilized by large peripheral ligands which hinder other species from attacking the dinuclear center. In the case of  $\{M(OH)_2M\}$ , the absence of Mn examples is noteworthy, whereas Cu and Cr are the two most common metals, covering together over 70% of the structures. The mixed bridged  $\{M(O,OH)M\}$  form is present in only four examples, three with Fe<sup>12-14</sup> and one with Cr<sup>15</sup>. Finally, in the  $\{M(O)_2M\}$  case Mn is the dominant metal with about 40% of the total structures, followed by Ti and V where each represents 25% of the structures. Another very common group of metal assemblies are the oxo centered trinuclear clusters (see Fig. 1-3a), often referred to as "triangles" or "basic carboxylate triangles".<sup>7,16</sup> Cotton and Wang describe in their work the triangles as trinuclear assemblies with virtual  $D_{3h}$  symmetry with a  $\mu_3$ -oxo ligand coplanar with the three metal centers.<sup>17</sup> These authors remark how these units cannot be called clusters because of the long metal-metal separation ( $M-M$  distance  $\geq 3.3\text{\AA}$ ) and thus absence of  $M-M$  bonding. However, the term is nowadays accepted to include ligand bridged metals clusters with weak  $M-M$  exchange interactions. Such compounds are called trinuclear or triangular metal clusters. In addition to bridging carboxylates, they also contain monodentate terminal ligands like water or pyridine, while the metal centers generally are at the oxidation state  $M_3^{III}$  or the mixed  $M_2^{III}M^I$ .<sup>17</sup> A structural survey for trinuclear systems on the CCDC (1<sup>st</sup>

transition row with the exclusion of Sc and Zn) shows that early metals up to Fe have a great tendency to form these oxo-centered structures where the central oxide is coplanar or nearly coplanar with the  $M_3$  plane. While most examples are based on Fe, the later metals (Co, Ni and Cu) rarely assume such a configuration. However, it was found that these elements display oxo-centered trinuclear system with the oxide ion displaced from the trinuclear plane. Beattie et al. discuss in their work how the inclusion of monodentate ligands on positions formerly occupied by a bridging carboxylate may lead to distortions causing the central oxide to move away from the plane.<sup>18</sup> The authors also find a correlation between the strength of the ligands and the consequent effect on the distortion, resulting in a change of the oxide's hybridization with increased  $sp^3$  character (from a pure  $sp^2$  in the coplanar form).<sup>18</sup> From the CCDC results, it is clear that the distortion can reach an M-O-M angle of nearly  $90^\circ$ , like in an "incomplete cubane" type of structure.<sup>8,18</sup>

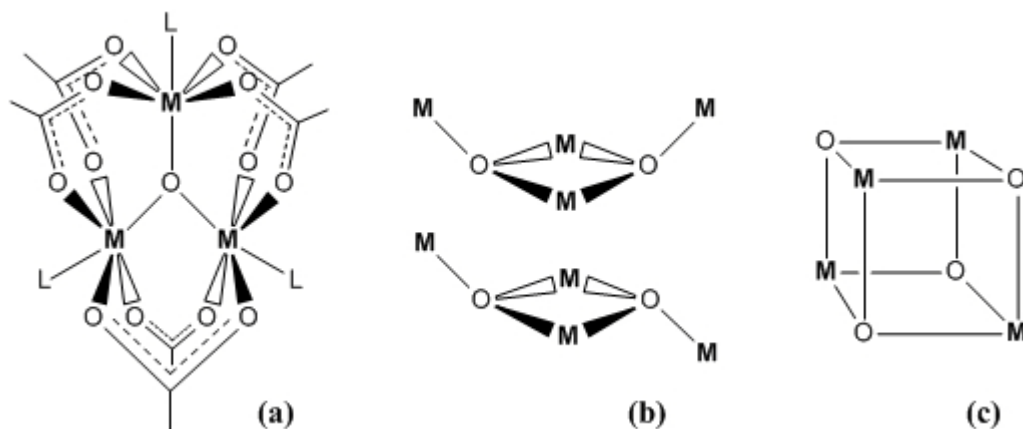


Figure 1-3. Most common structural types adopted by trinuclear (a) and tetranuclear (b) and (c) carboxylate clusters. (a) the full complex  $[M_3O(O_2CMe)_6L_3]^+$ ; (b) the core  $\{Mn_4O_2\}^{n+}$  of the butterfly arrangement, and (c) the core  $\{M_4O_4\}^{n+}$  for the cubane architecture (adapted from ref. <sup>16</sup>).

As the number of metal ions increases, so does the complexity and the number of possible structures. The nuclearity four is generally characterized by the "butterfly" (Fig.

1-3b) and the "cubane" structures (Fig. 1-3c). The butterfly name tries to describe the topology as an approximation of a butterfly's body, where the two middle metals constitute the body and the remaining two symbolize the wingtips. Both types of tetranuclear assembly (i.e., butterfly and cubane) are largely found all along the first transition row without exceptions. While one can find other unique topologies for ligand bridged clusters, most of the higher nuclearity structures can be described as built from combinations of dinuclear, trinuclear (triangular) and tetranuclear (butterfly and cubane) units. For this reason, a detailed analysis of higher nuclearity structures would be redundant.

The complexity of the structures and the ability of transition metals to reach determined oxidation states are the main characteristics for the interesting properties of clusters. For example, Nature has adopted transition metal clusters to carry out particular reactions within cavities protected by large proteins that often have the double function of supporting/distorting the metal structure, and controlling access of substrates to highly reactive intermediate species during enzyme turnover.<sup>19</sup> Such properties depend on two important characteristics: firstly, there is a large variety of possible donor groups to bind metals by virtue of the large choice of amino acid residues. Secondly, the relative rigidity of some protein structural moieties ( $\alpha$ -helix,  $\beta$ -sheet) can cause geometrical distortions (hypothesis of the entatic state) to modify the frontier energy levels, hence tweaking the redox properties.<sup>19</sup>

Among the many examples that show Nature's use of metal clusters, there is the core of the oxygen-evolving center (OEC). This metalloprotein is responsible for the oxidation of water to molecular oxygen and four protons in biological systems capable of

photosynthesis.<sup>20</sup> It has been studied for a long time due to its importance, but the large multi-protein assembly engulfing the OEC has hindered accurate direct structural characterization through X-ray crystallography.<sup>21</sup> Hence, its structural design and definite composition could only be achieved with some degree of approximation.<sup>20-22</sup> According to the last X-ray data, a pentanuclear heterometallic  $Mn_4Ca$  cluster is the heart of the OEC, with a structure similar to the one in Fig. 1-4.<sup>22</sup>

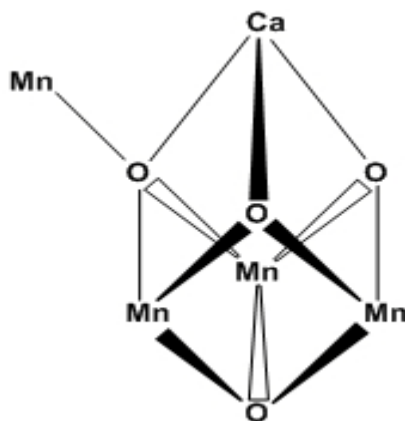


Figure 1-4. Diagram of the  $Mn_4Ca$  cluster supporting water oxidation in the OEC of green plants and cyanobacteria. The cubane structure is distorted by the presence of a Ca ion instead of Mn at one vertex position (adapted from ref. <sup>22</sup>).

The new structural information on the  $Mn_4Ca$  cluster allowed for new hypotheses on the catalysis mechanism. One of the major changes to the earlier models is the preservation of the cluster structure throughout the complete cycle, attributing great stability to the cubane structure while highly reactive species are generated. Theoretical studies have demonstrated that the  $Mn_3Ca$  unit is stable enough to be unaltered during the catalysis.<sup>23</sup> Important co-factors such as one chloride anion bound to the Ca ion and a probable carbonate/bicarbonate anion on the Ca ion have contributed to the description of a new mechanism. Recent <sup>18</sup>O exchange experiments have demonstrated that one of the substrate water molecules is bound to the Ca ion, suggesting that this

water may be coupled with another one located in close proximity and possibly bound to the external Mn ion.<sup>24</sup> The current assumption on the mechanism proposes four deprotonation and four single-oxidation steps, at the end of which the three Mn ions in the cubane unit are Mn<sup>IV</sup> while the Mn outside the cubane is a Mn<sup>V</sup>, containing a doubly bonded oxo ion.<sup>23</sup> The formation of the Mn=O moiety is justified by the deprotonation of a water molecule bound to the outside Mn ion at the beginning of the catalytic cycle. Another substrate water is bound to the adjacent Ca ion and it is thought to perform a nucleophilic attack on the oxo (or oxyl radical) located on the Mn<sup>V</sup> cation, establishing the formation of an O-O bond (see Fig. 1-5).<sup>23</sup> The chloride co-factor is believed to support the orientation of the water molecule that performs the attack, while the carbonate/bicarbonate anion is considered helpful to the stability of the cluster assembly, though its function on the catalysis other than for deprotonation purposes has not yet been explained.<sup>23</sup>

The considerable employment of Mn in biological systems is probably a direct consequence of its high chemical flexibility in conjunction with the availability of many oxidation states in aqueous media. On one side, the states +2, +3 and +4 are quite common and the higher oxidation states can exist under unexceptional conditions.<sup>25</sup> On the other side, general considerations of cationic stability within a metal cluster suggest that very high oxidation states can be supported only if a sufficient number of basic ligands are present. Consequently, while Mn<sup>II</sup> compounds do not require oxide ligands to be stable, the higher oxidation states of Mn<sup>III</sup> and Mn<sup>IV</sup> need one or more oxides to stabilize and balance the high cationic charge. This trend can be extended to the

permanganate anion, where the highest oxidation state  $\text{Mn}^{\text{VII}}$  is ordinarily stable due to four coordinated oxide ligands.

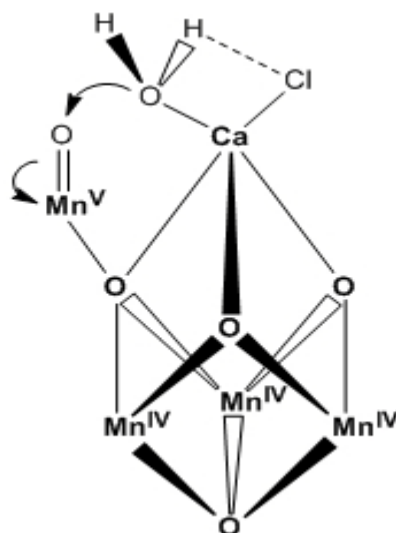


Figure 1-5. Hypothetical mechanism for the incipient O-O bond formation during the final intermediate state "[S<sub>4</sub>]" of the OEC. The chloride anion hydrogen-bonds the water substrate to direct its lone pairs toward the oxo (or oxyl radical) on the  $\text{Mn}^{\text{V}}$ . Upon O-O formation, the new species is deprotonated until molecular oxygen is released (adapted from ref. <sup>23</sup>).

According to this logic, the reactive  $\text{Mn}^{\text{V}}$  in the highest oxidation state of OEC (known as [S<sub>4</sub>]) may not receive enough stabilization by a single oxide to be feasible as a participant of the catalytic cycle. On the contrary, it is plausible that one of the Mn ions within the cubane can directly participate in the catalytic process achieving the high  $\text{Mn}^{\text{V}}$  oxidation state through the support of three bound oxides. Support for this hypothesis comes from the XANES analysis of the PSII, which reveals the absence of the typical signal for a manganyl species in the OEC.<sup>26</sup> The cubic feature,  $\text{Mn}_3\text{Ca}$ , in the  $\text{Mn}_4\text{Ca}$  cluster demonstrates a high degree of stability with an outstanding redox capability and structural adaptation to catalysis. The coexistence of these properties in a metal cluster is the basis for the fundamental characteristics of clusters. While the field of

bioinorganic chemistry has several examples of this type, other fields have been developed around the uniqueness offered by metal clusters.

Physical chemistry is one of the disciplines within which transition metal clusters have been largely studied for their magnetic properties. Transition metal complexes have a demonstrated general propensity to have unpaired electrons (u.e.'s) as result of degenerate d orbitals. Each u.e. contributes to building up an overall magnetic moment vector, referred to as "spin" and is represented commonly by a full arrow ( $\uparrow$ ) to reflect its vector properties. The Pauli exclusion principle tends to maximize the number of u.e. by single occupancy of degenerate orbitals. Because each resulting singly-occupied orbital contributes to the spin it is often referred to as a "magnetic orbital".<sup>6</sup> If in a metal ion the orbital angular momentum is neglected or absent, the algebraic sum of each u.e.'s magnetic moment ( $s = \frac{1}{2}$ ) constitutes approximately the ions total magnetic moment (i.e., the total spin). In transition metal clusters where bridging units do not exist, the metal-metal bonds have a significant contribution from magnetic orbitals, whose overlap produces lower energy molecular orbitals, hence pairing two u.e.'s and thereby quenching their resultant magnetic moment. Clusters of ligand-bridged 3d metals, on the contrary, allow each metal cation to overlap its magnetic orbitals with those of the bridging ligands which, in most cases, are already doubly occupied. This type of metal-ligand interaction preserves the individual number of u.e.'s, allowing for the spin of one metal to interact magnetically with the spin of the neighboring metals in the cluster.<sup>6</sup> Such an interaction via bridging ligands is known as superexchange (see later).

Structure, metal type, metal oxidation state, and ligand type are the main factors in governing the magnetic interaction, or exchange interaction, between metal ions in a

cluster. This interaction is measured by the exchange parameter ( $J$ ) also known as the exchange coupling constant. The realization of magnetic coupling between metal centers in a compound was noted for the first time in copper(II) acetate, a dinuclear molecule of formula  $[\text{Cu}_2(\text{O}_2\text{CMe})_4(\text{H}_2\text{O})_2]$  where the two Cu ions interact magnetically (Fig. 1-6).<sup>27</sup>

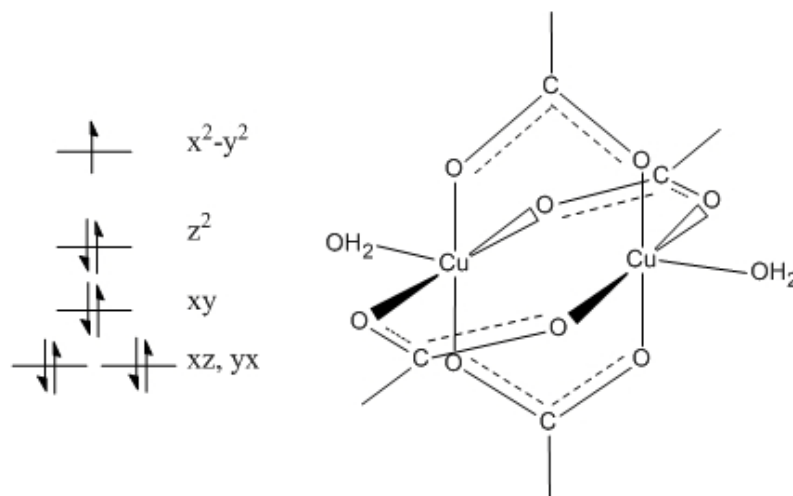


Figure 1-6. Frontier electronic diagram for a pentacoordinated  $\text{Cu}^{\text{II}}$  ion in a  $sp$  geometry (the  $x^2-y^2$  is the magnetic orbital), and structural sketch of the  $\text{Cu}^{\text{II}}$  acetate (adapted from ref. <sup>6</sup>).

Each  $\text{Cu}^{\text{II}}$  has  $s = 1/2$  and copper acetate is paramagnetic at room temperature (i.e., contains u.e.'s), whereas it becomes diamagnetic (i.e., does not contain any u.e.) when the temperature is lowered.<sup>27</sup> Bleaney and Bowers established the basis for magnetochemistry upon discovering that there is an interaction between the two Cu ions.<sup>28</sup> The molecule populated a total spin  $S = 1$  state (corresponding to the sum of two individual  $\text{Cu}^{\text{II}}$  spins  $1/2$ ) at room temperature, but the total spin  $S$  was found to quickly decrease to  $\sim 0$  below  $\sim 200$  K. Bleaney and Bowers explained these observations through the parallel alignment of the vectors relative to each  $\text{Cu}^{\text{II}}$  spin magnetic moment (i.e.:  $\uparrow\uparrow$ ) at room temperature and the antiparallel alignment at lower temperatures (i.e.:

$\uparrow\downarrow$ ) respectively. Initial postulates tried to explain the canceling of the  $S = 1/2$  spins by a so called "direct interaction mechanism" where the two Cu  $d(x^2-y^2)$  magnetic orbitals overlap sideways forming a  $\delta$  bond. The resulting molecular bonding orbital would have accommodated both electrons with the antiparallel alignment and quenched the total  $S$ . Further studies on other dinuclear  $\text{Cu}^{\text{II}}$  systems analogous to the Cu acetate demonstrated how the Cu-Cu distance has negligible influence on the strength of the exchange constant ( $J$ ), and that the coupling is mostly (95%) governed by the four bridging ligands. This other type of interaction is known as the "superexchange mechanism" and in the case of Cu acetate, promotes the antiparallel alignment through a negative  $J$  value. In a dinuclear compound, if  $J$  is negative, the antiparallel alignment is energetically preferred and we refer to an "antiferromagnetic coupling"; on the contrary, the parallel alignment is promoted by a positive  $J$  value and the behavior is called "ferromagnetic". Although the antiparallel alignment is the ground state in the case in which  $J$  is negative, if its magnitude is lower than  $\sim 500 \text{ cm}^{-1}$ , the higher energy parallel alignment is accessible through thermal population, resulting in a behavior similar to the one typical of the Cu acetate (see Fig. 1-7).<sup>6,29</sup>

In addition to the two mechanisms of direct interaction and superexchange, there is a third one known as "spin polarization" which acts especially in ionic systems and for this reason is not often very relevant to clusters. The three mechanisms are always present in every molecular structure or polynuclear assembly, although one of them will generally prevail and direct the magnetic interactions, depending on the nature of the system.<sup>6</sup> Trinuclear systems represent the next level of complexity for the study of the magnetic properties of clusters. Generally, these units display a more complex magnetic

behavior, a result of the increased number of interactions that complicate the number and the distribution of the magnetic levels. Further complications are also due to the effects of possible spin frustration/satisfaction pathways.

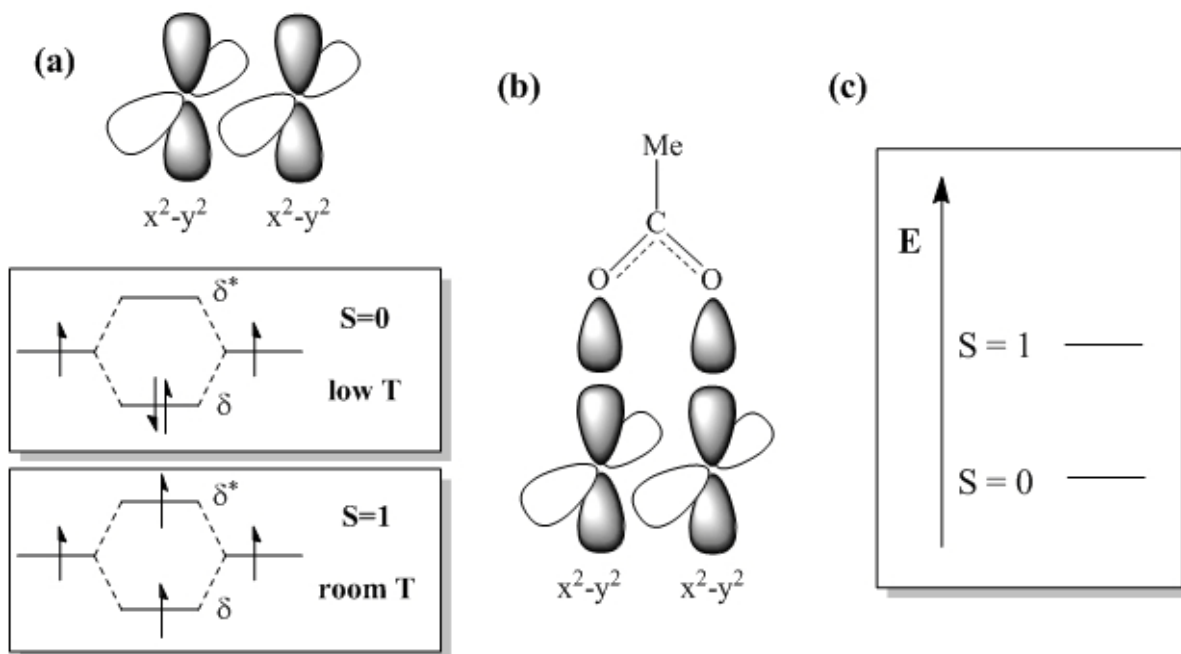


Figure 1-7. Two possible mechanisms for the Cu-Cu magnetic interaction in Cu(II) acetate: (a) scheme of the sideways d-d direct overlap forming the  $\delta$  and  $\delta^*$  MOs. The top inset shows the possible quenching of the spin at low T, while the bottom one displays how through thermal excitation the  $S = 1$  is reached. (b) representation of the incipient  $\sigma$  overlap of one acetate ligand responsible for superexchange interaction through the O-C-O bonds. (c) Relative energy diagram for the two possible states  $S = 0$  and  $S = 1$ .  $S = 0$  is the ground state while  $S = 1$  is the thermally accessible excited state (adapted from ref. 6).

For instance, in a trinuclear triangular system having  $M_1$ ,  $M_2$  and  $M_3$  metals there will be, save for a few exceptions<sup>30</sup>, a minimum of two different J. This is due to the tendency of trinuclear clusters to distort from generalized equilateral symmetry down to isosceles (2J system) or scalene (3J system). The spin of a metal ion in a triangle experiences two J simultaneously, each associated with an exchange pathway. The two J can have opposite sign, hence promoting each a different orientation of the spin.

When one of the J is much larger in magnitude than the other it governs the spin orientation, otherwise J of comparable strengths will compete leading to cases of doubtful prediction of the spin orientation (spin-frustration) (see Fig. 1-8).

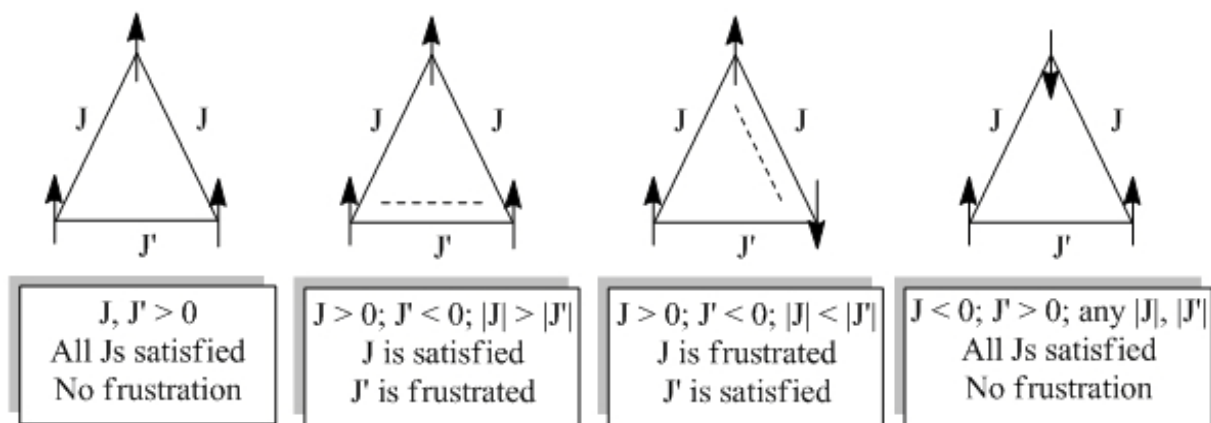


Figure 1-8. Sketch of trinuclear triangular species displaying some of the possible exchange interactions leading to frustration/satisfaction pathways due to comparable J values.

The magnitude and sign of the exchange interaction in these and more complex systems cannot be known "a priori", but they are instead calculated by applying the Heisenberg-Dirac-Van Vleck spin-coupling Hamiltonian.<sup>31</sup> For a simple ion pair, like in copper(II) acetate, the Hamiltonian operator would be:

$$\hat{H}_{ij} = -2\mathbf{J}_{ij} \hat{S}_i \hat{S}_j. \quad (1-2)$$

The Hamiltonian solutions in Eq. 1-2 express the energy levels of a dinuclear system as a function of the coupling J and the spin angular momentum operator  $\hat{S}$ . The Van Vleck equation (see Eq. 1-3) establishes the relationship between the molar magnetic susceptibility ( $\chi_M$ ) and the temperature, considering the various possible energy levels of the system. The expression of such energy levels in terms of couplings and spin operators according to the Hamiltonian will ultimately allow for the estimation of the J values through fitting of the experimental  $\chi_M$  vs. T plots. The Van Vleck equation is

reported in Eq. 1-3, where the  $\chi_M$  is expressed as the sum of the magnetic contribution from each energetic level weighted according to its population based on the Boltzmann distribution.<sup>6</sup>

$$\chi_M = N \frac{\sum_n (E_n^{(1)2} / kT - 2E_n^{(2)}) \cdot e^{(-E_n^{(0)} / kT)}}{\sum_n e^{(-E_n^{(0)} / kT)}} \quad (1-3)$$

The Hamiltonian description for systems of three or more metal ions soon becomes complicated and its analytical solution often requires the handling of large secular matrices, which hinder the rigorous approach, beginning with pentanuclear systems. A shortcut to the rigorous analysis of small systems takes advantage of the molecular symmetry and the mathematical formulation of the Hamiltonian eigenvalues. This way of proceeding is known as the "equivalent operator method". It involves the use of the Kambe's vector coupling and allows for finding the J values without solving the secular matrix.<sup>6,32</sup> For larger systems, where the J values can only be obtained through alternative computational methods, some important parameters such as the ground-state spin, S, can be determined through low-temperature magnetometry or high-field EPR analysis. The description of the total spin in terms of the individual metal ion components is known as "giant spin approximation" and, except for some cases, this represents a good approximation for the description of the global spin in a polynuclear system.<sup>33</sup> Another very important parameter to consider in polynuclear system is the behavior of the magnetic anisotropy, through the axial zero-field splitting parameter *D*. The individual anisotropies of each metal ion combine, giving the system an overall expression of *D*, which applies to the total spin of the molecule. According to

the meaning of the magnetic anisotropy, the molecular system will have a preferential orientation for the total spin  $S$  along one axis (axial anisotropy). The sign of  $D$  is responsible for the disposition of the  $m_s$  levels on a relative scale of energy, where  $m_s$  is the projection of  $S$  along the preferential magnetization direction. When  $D$  is positive the perpendicular projection of  $S$  is the most stable (i.e.;  $m_s = 0$  for  $S$  integer, or  $m_s = \pm \frac{1}{2}$  for  $S$  half-integer). When  $D$  is negative the "almost parallel" projections are stabilized the most (i.e.:  $m_s = \pm S$ ).<sup>34</sup> A useful way of depicting this system is through the so-called "double-well" potential diagram (Fig. 1-9). The presence of a negative  $D$  allows the system to be in a bi-stable state in the absence of external perturbations, hence the molecular spin vector  $S$  can either assume (by convention) the orientation up or down. If such a system is subjected to an external magnetic field, the spin orientation aligned parallel with the external field will be energetically more favorable than the orientation antiparallel, which changes the population of the two states through removal of their degeneration.

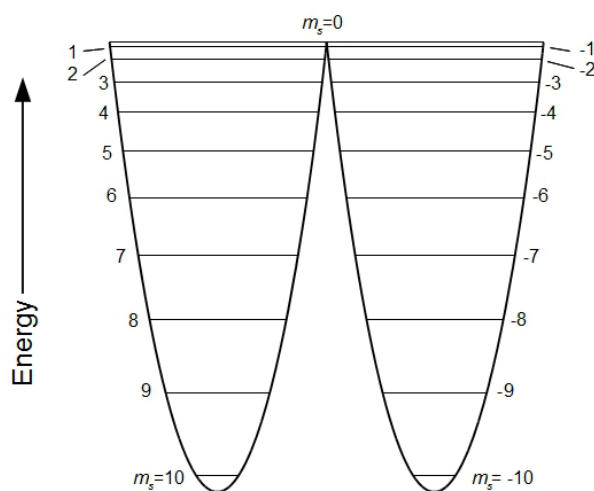


Figure 1-9. Double-well energy diagram for a  $S = 10$  molecule with negative magnetic anisotropy parameter  $D$ . In the absence of an external field the two most stable levels are the  $m_s = \pm 10$  (adapted from ref. <sup>34</sup>).

Once the external field is quenched, the two states again become degenerate and the spin orientation will be randomized with equal population. The combination of both a large  $S$  and large and negative  $D$  value creates the conditions for an energy barrier to the reversal of the magnetization. When the temperature is below a critical value, known as "blocking temperature", the thermal energy is significantly lower than the energy barrier and these molecules can retain their magnetic vector alignment for a long time.<sup>34</sup> The commonly known materials capable of retaining their magnetization below a critical temperature are known as magnets and their property arises from long-range interactions along an almost infinite lattice of metal ions. On the contrary, in molecular clusters that behave like a magnet, the ability of retaining the magnetization is a property intrinsic to each molecule. Such a cluster can show hysteresis of the magnetization, like conventional magnets, and for this reason they have been called single-molecule magnets (or SMM).<sup>35</sup> A very well known example of SMM is referred to as "Mn<sub>12</sub>", a molecular cluster that contains 4Mn<sup>IV</sup> and 8Mn<sup>III</sup> ions bridged by oxo and acetate groups. The core is described as {Mn<sub>4</sub><sup>IV</sup>Mn<sub>8</sub><sup>III</sup>(μ<sub>3</sub>-O)<sub>12</sub>}<sup>16+</sup> in the overall structure of [Mn<sub>12</sub>O<sub>12</sub>(O<sub>2</sub>CMe)<sub>16</sub>(H<sub>2</sub>O)<sub>4</sub>]. The compound initially synthesized in 1980<sup>36</sup> did not receive much attention until 1991<sup>37</sup>, when its magnetic properties were investigated. The Mn<sub>12</sub> structure and composition are at the basis of its magnetic characteristics: the four Mn<sup>IV</sup> ions are arranged at the center in a cubane-like fashion and surrounded by an almost planar ring of eight Mn<sup>III</sup> (see Fig. 1-10). In the ground state of the molecule the four Mn<sup>IV</sup> ions ( $s = 3/2$  each) are ferromagnetically coupled with each other and antiferromagnetically coupled with the surrounding Mn<sup>III</sup> ions ( $s = 2$  each) accounting for the total spin ground-state  $S = 10$ .

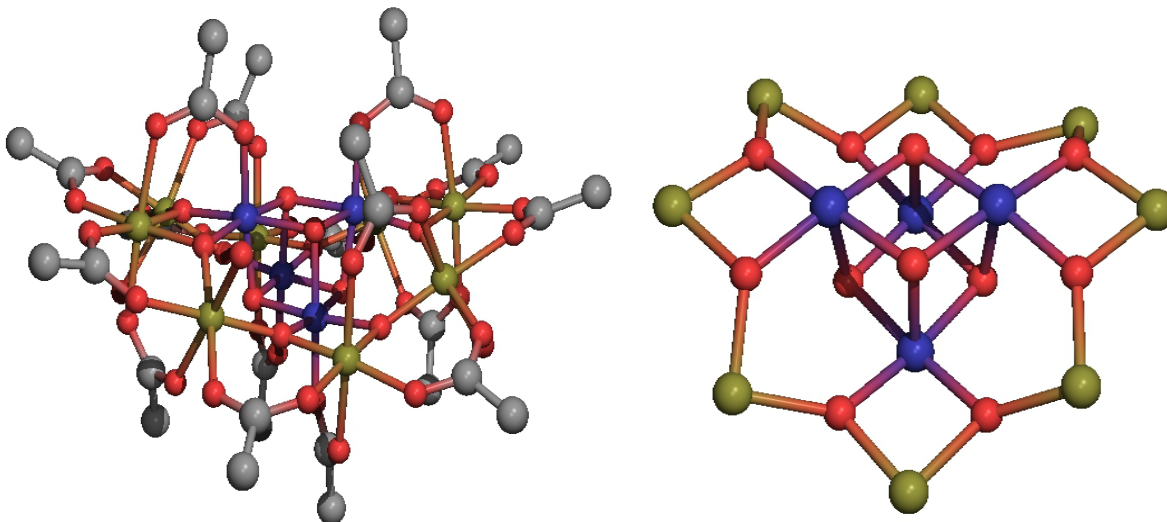


Figure 1-10. Left: Pov-Ray projection of the  $\text{Mn}_{12}$ -acetate cluster. Right: core of the  $\text{Mn}_{12}$ -acetate displaying the central cubane surrounded by an almost planar arrangement of eight Mn ions. Color code: blue ( $\text{Mn}^{\text{IV}}$ ), yellow ( $\text{Mn}^{\text{III}}$ ), red (O), grey (C).

The presence of the Jahn-Teller distorted  $\text{Mn}^{\text{III}}$  ions is the main source of the axial magnetic anisotropy<sup>34,38</sup>, which results in an overall  $D = -0.50 \text{ cm}^{-1}$  (or  $-0.7 \text{ K}$ ).<sup>39</sup> The barrier to the reorientation of the  $m_s$  vector from 10 to  $-10$  or vice versa, passing through the perpendicular disposition  $m_s = 0$ , is theoretically expected to be  $100D$  or  $70 \text{ K}$ . Relaxation experiments have revealed that there is an effective barrier of about  $65 \text{ K}$  to the reversal of the magnetization in  $\text{Mn}_{12}$ , hence indicating a limited ability to retain the magnetization direction for  $\text{Mn}_{12}$ .<sup>40</sup> However, it was demonstrated that at  $1.5 \text{ K}$  the relaxation time is long enough to be hardly measurable, creating the basis for the use of information storage devices.<sup>34</sup> There are many other examples in the literature of SMMs, such as  $[\text{Fe}_8\text{O}_2(\text{OH})_{12}(\text{tacn})_{12}]\text{Br}_8$ <sup>41-42</sup>,  $[\text{Mn}_4\text{O}_3\text{Cl}(\text{O}_2\text{CMe})_3(\text{dbm})_3]$ <sup>35,43-44</sup>,  $[\text{Ni}(\text{hmp})(\text{MeOH})\text{Cl}]_4$ <sup>45</sup>, and they all contributed to the development of studies on quantum tunneling of the magnetization<sup>46</sup> and SMM application for quantum computing and information storage<sup>47-48</sup>.

The two main research fields of interest in polynuclear clusters are based on the electronic properties that an assembly of 3d metals can display. The relatively low interaction among metal ions allows for the stable retention of a particular oxidation state. In the case of a catalyst, this is useful in performing and stabilizing reactions with highly reactive intermediates, whereas in an SMM it preserves the total spin of the molecule. According to the Robin-Day classification<sup>49</sup> most of the oxo-bridged 3d molecular clusters fall into either class I or II, which represent a localized or partially delocalized charge on the metal ions, respectively. The presence of peripheral ligands with a very stable electronic asset represents another factor in conjunction with the poor delocalization that limits the electronic exchange over clusters. Although this combination is advantageous for the applications so far described, the area of clusters carrying electroactive ligands is still relatively unexplored. One of the main points of interest would be the study of the effects of an increased capability for the exchange of electrons on the properties of a cluster. In order to probe this field a very well known electroactive platform was used: ferrocene. Since its first synthesis by Kealy and Pauson in 1951<sup>50</sup>, ferrocene showed, on contrary to other iron-organometallic compounds, a large degree of stability. The molecule was stable in air and could be heated to a relatively high temperature without significant decomposition.<sup>50</sup> The first proposal for the correct structure of ferrocene was made in 1952 by Wilkinson et al.<sup>51</sup>: a "sandwich" arrangement of one Fe<sup>II</sup> in between two cyclopentadienyl units. In 1952 Woodward et al. proposed the current common name for the molecule (ferrocene or fc) and showed the similarity with benzene toward reactivity. On this basis, they also justified the stability of the compound.<sup>52</sup> The electronic structure of the ferrocene

conforms with the 18 electron rule and foresees 16 electrons in bonding type MOs and two frontier electrons paired up in a non-degenerate non-bonding MO (Fig. 1-11).<sup>53-54</sup>

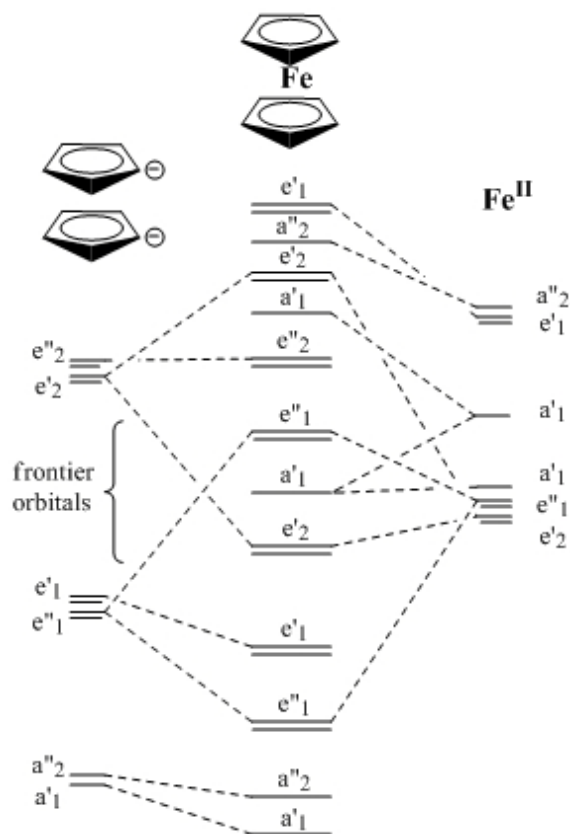


Figure 1-11. MO diagram scheme for the ferrocene molecule in the eclipsed configuration. The frontier orbital  $a'_1$  is the HOMO completing the 18 electrons count. Upon oxidation ferrocene becomes ferricenium, a paramagnetic species (adapted from ref. <sup>54</sup>).

Electrochemical investigations soon showed the fast and reversible characteristic oxidation of ferrocene (fc) to the ferricenium ( $fc^+$ ) cation by loss of one electron.<sup>55-56</sup> The oxidation results in one electron being removed from a non-bonding orbital, leaving the newly formed species ( $fc^+$ ) with an almost unchanged stability with respect to fc.<sup>54</sup> The properties of fc make of it an extraordinarily important molecule adopted in many studies and widely used in research without solution of continuity. Ferrocene is also considered to be the ideal platform in the present study for another important property

resulting from its oxidation. In fact, while fc is diamagnetic (all electrons are paired together),  $fc^+$  has one unpaired electron that makes the species paramagnetic with a spin of  $\frac{1}{2}$ .

The fast and reversible electrochemistry of ferrocene is also observed in its derivatives as well as the switching between the two magnetic states (i.e.: diamagnetic and paramagnetic). This behavior is of great interest in magnetochemistry because it offers the possibility to analyze directly the effect of a "spin-active" ligand on the magnetic core of a cluster. Theoretically, the magnetic interaction can be turned "on" by oxidation and turned "off" by reduction. Despite the small spin value associated with the  $fc^+$  unit, its influence on the coupling may modulate the spin coupling pattern of larger spins in the cluster and contribute to the magnetic anisotropy of the system. The typical high rate of the process  $fc = fc^+ + e^-$  could enhance a faster electron exchange in clusters containing fc. Such clusters may be oxidized initially at the fc units and later replenish those electrons with others belonging to the metal core. More generally, the presence of fc units over a cluster could sustain a faster movement of electrons toward an acceptor. In order to anchor the ferrocene on a cluster, the ligand should contain a ferrocenyl moiety as well as groups capable of promoting aggregation through bridging. A very well known group capable of assisting cluster formation and stabilization is the carboxylate, which by virtue of the two oxygen atoms can bridge with remarkable flexibility.<sup>57</sup> The potential binding modes for a carboxylate are shown in Fig. 1-12.<sup>58</sup> The ligand precursor selected to fulfill the above-mentioned requirements is the 1,1'-ferrocenedicarboxylic acid, for short fdch<sub>2</sub> (see Fig. 1-13). The contemporary presence of two chelating groups on the ferrocenyl unit can offer better coordination and promote

metal aggregation. Such an assembly also offers the opportunity to isolate new cluster topologies resulting from the use of dicarboxylate ligands with restricted flexibility.

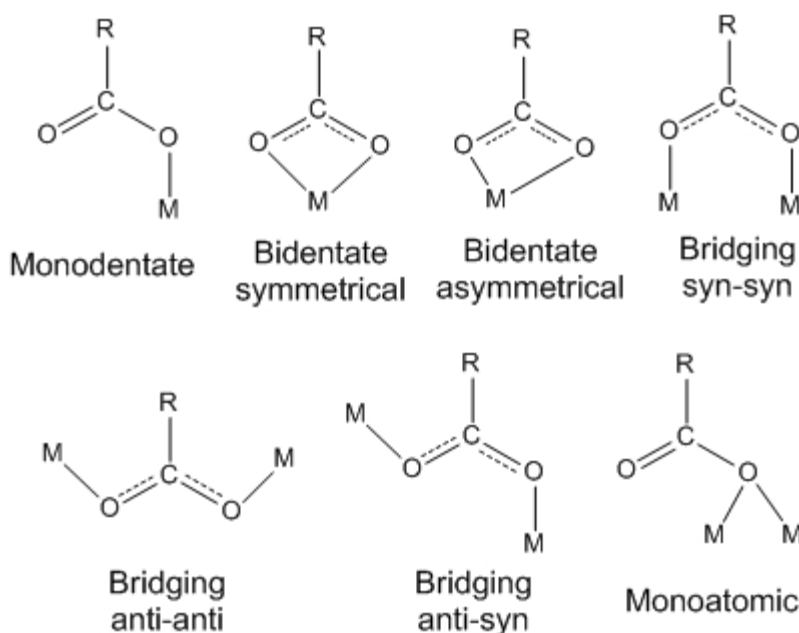


Figure 1-12. Potential coordination modes for a generic carboxylate (adapted from ref. <sup>58</sup>).

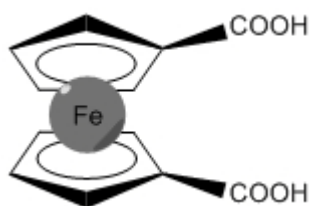


Figure 1-13. Schematic diagram of the 1,1'-ferrocenedicarboxylic acid (fdch<sub>2</sub>). Ligand precursor of the corresponding dianionic ligand 1,1'-ferrocenedicarboxylate.

The two cyclopentadienyl moieties stand on parallel, or nearly parallel, planes and each substituent must lay on one of these planes. The rotation about the ferrocene molecular axis is the only degree of freedom, and its energy barrier is very low compared to thermal energy at room temperature.<sup>59-60</sup> For a conjugated system such as the carboxylate, direct attachment to a cyclopentadienyl ring extends the  $\pi$  conjugation to the aromatic ring. In the case of ferrocenecarboxamides this is demonstrated through

a decreased rotational barrier for the C-N bond as a result of a partial delocalization after an intramolecular charge transfer, according to the scheme shown in Fig. 1-14.<sup>61</sup> The extended delocalization of the ferrocenyl units entails significant magnetic exchange interactions between the metal ions in the cluster core and ligand.<sup>62</sup> The final purpose of this study is to obtain new oxo-bridged 3d transition metal clusters which display a large affinity for multielectron exchange while retaining other important properties such as SMM behavior. Chapters 2 and 3 report the synthesis and full characterization of new clusters of this type.

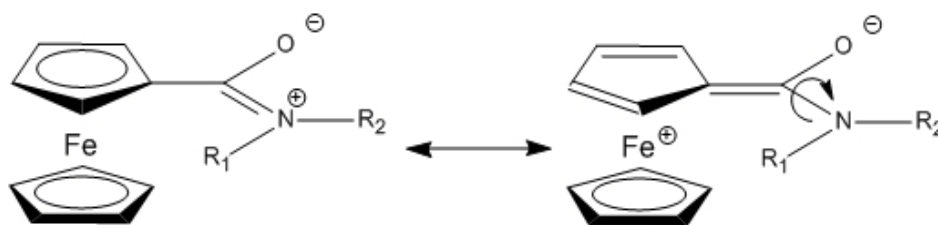


Figure 1-14. Scheme explaining the extension of the delocalization of a conjugated substituent to a ferrocene system. The increased freedom of rotation along the C-N bond is proof of the extension of the delocalization of the  $\pi$  system on the ferrocenyl unit (adapted from ref. <sup>61</sup>).

### Bond Valence Sum

The Bond Valence Sum method (or BVS) represents a useful approach to estimate the oxidation state of an ion (generally a metal) in a coordination compound.<sup>63</sup> In an attempt to develop and expand the solid state theory, Linus Pauling approached in 1929 various chemical structures in terms of purely electrostatic effects and relative size of the ions.<sup>64</sup> Pauling's observations resulted in a series of rules and principles describing the ionic arrangement and energy of a crystal lattice. Conforming to the first rule, each cation must be surrounded by a number of anions located at the vertex of a polyhedron, whose shape is determined by the mutual cation/anion radius ratio and the overall coordination number (C.N.). The second rule defines a stable structure as one

where the charge of a particular anion is counterbalanced by the sum of the partial positive charges, each belonging to a surrounding cation. The third and fourth rules empirically correlate lattice stability with the number of anions shared at the vertices or faces of polyhedra, especially in the case of high valence cations and low coordination numbers. The final rule states that the number of different types of polyhedra found in a lattice naturally tends to be very small, as the same typology of atoms will prefer the same and most stable arrangement.<sup>64</sup> The important intuition that Pauling expressed in the second rule was confirmed by Bragg in 1930 when he experimentally demonstrated the validity of the principle applied to a silicate structure.<sup>65</sup> Later, Pauling realized that a cation and its neighboring anion shorten their relative ionic radii as a consequence of an increasingly higher electronic density in between the two species.<sup>66</sup> This latter work represents the first attempt to identify a relation between the length of a bond and its strength. In 1947 Donnay and Allmann deduced the direct correlation standing between valence and bond length through an exponential function.<sup>67-68</sup> Brown and Shannon confirmed the existence of such a correlation in 1973, with the publication of the common exponential function found across a large pool of inorganic compounds based mainly on metal oxides (see Fig. 1-15).<sup>69</sup>

The plot in Fig. 1-15 clearly shows how the sum of the bond strength in terms of valences correlates with the average bond length in several metal oxides. The data is clustered near integer values of valence displaying an exponential behavior. Such profile is a clear proof of the existence of a correlation between the length of a bond and its strength. Although this general behavior is here evident for metal oxide is also reflected in most metal-to-ligand bonds.

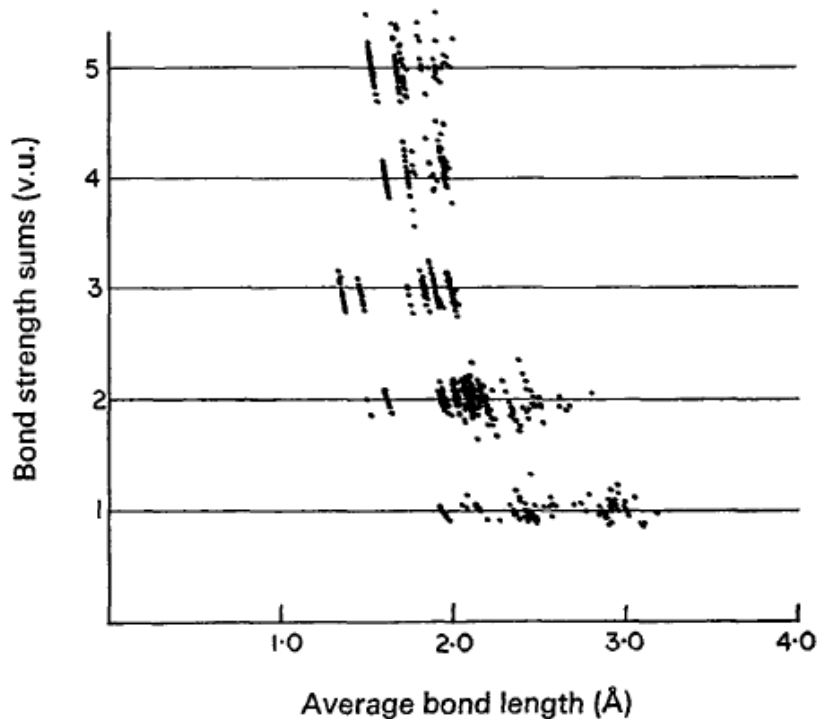


Figure 1-15. Plot of bond strength expressed as valence units (v.u.) vs. the corresponding average bond length in Å for a series of metal oxides selected and published by Brown and Shannon (reported from ref.<sup>69</sup>, [Reproduced with permission of the International Union of Crystallography](#)).

Attempts to establish a semi empirical function for the prediction of the valence through the sum of all the bond lengths were made by different authors and resulted in two main expressions reported in Eqs. 1-4 and 1-5.

$$s = s_0 \cdot (R/R_0)^{-N}. \quad (1-4)$$

$$R = R_1 - 2k \cdot \log(s). \quad (1-5)$$

In these expressions  $s_0$ ,  $R_0$ ,  $N$ ,  $R_1$  and  $k$  are all empirical parameters.<sup>70</sup> Both expressions were leading to very comparable results and while Eq. 1-4 is still used for achieving the valence sum of bridging or terminal ligand anions (especially oxygen) a more general expression was coined by Brown and Altermatt<sup>71</sup>, which replaced Eq. 1-5:

$$s = e^{\frac{r_0 - r}{B}} \quad (1-6)$$

Equation 1-6 introduces with respect to Eqs. 1-4 and 1-5 the new empirical parameter B (note that in the literature we often see "R<sub>0</sub>" instead of r<sub>0</sub> and "b" instead of B). Both B (in Eq. 1-6) and N (in Eq. 1-4) are determined through the fit of experimental data, and their value reflects the concavity of the exponential function. Between the two parameters, B shows a lower degree of oscillation with the nature of the metal ion and for this reason Eq. 1-6 is generally preferred.<sup>71</sup> Since Eqs. 1-4 to 1-6 estimate the valence along a bond, it is necessary to sum all the contributions from each bond in order to calculate the valence of a cation, as is inherently suggested by the name of the method: Bond Valence Sum.

In Eq. 1-6, r<sub>0</sub> represents the length in Å of a bond having unitary valence for a given value of B and its magnitude depends on the metal type and the oxidation state under investigation. On the contrary, B is known as the "universal parameter"<sup>72</sup> and its value is set to 0.37 Å following Brown and Altermatt findings that most of the inorganic compounds could be analyzed satisfactorily adopting that number.<sup>73</sup> One of the major strengths of this model is its flexibility of application, which makes it adaptable to any coordination environment regardless of the coordination number. According to the BVS model, a metal ion with the same oxidation state will generally displays longer bonds with an increase in C.N.

The BVS model is largely adopted in inorganic chemistry to determine the oxidation state of metal ions in their coordination environment. In fact, transition metals typically form a large variety of coordination compounds while adopting different

oxidation states. The BVS model represents a powerful method for achieving details on the oxidation states based solely on structural information. The outcome of a BVS analysis is a valence number that approaches an integer, which is suggestive of the actual oxidation state of the metal.

Technological advances in X-ray diffraction have led to a quicker and more accurate determination of crystal structures, hence promoting the wide use of this analytical technique. The consequence is an increase of the number of structural determinations available. While initial published collections of  $r_0$  and B values were sufficient to suggest the correct oxidation state of a metal ion in most cases, the increased volume of structural data requires a more representative set of parameters. For this reason, researchers have conducted several studies aimed at the minimization of the error in the estimating the oxidation states through BVS. This task has been most commonly approached by improvements in the fitting procedure of the exponential distributions through mathematical analysis, which also appears to be the only type of analysis reported by the literature. In cluster chemistry, the application of the BVS model and relative parameters to metal ions in a cluster can be subjected to significant discrepancies from the actual oxidation states. Among the various factors to consider, physical constraints in rigid structures may be responsible for bond elongation or compression, which can mislead the BVS results. Another basic cause of BVS discrepancy could reside in the adoption of non-representative  $r_0$  and B parameters for metal ions in a cluster environment. Many BVS optimizations utilize very selective criteria that reject a large portion of structures from crystallographic databases and

focus on mononuclear species or inorganic polymers. These last ones are at the basis of structures describing minerals and do not well-represent metal clusters.

The purpose of the present study is to approach the BVS parameter optimization under a new perspective that moves away from the precision of rigorous mathematical analysis over a relatively limited number of structures and toward modern statistical methods applied to the largest up-to-date collection of crystallographic data. The study includes all the metal structures of the first transition row (with the exclusion of organometallic ones) belonging to the Cambridge Crystallographic Data Centre (CCDC)<sup>8</sup> which recently reached over 500000 structures. The work and relative results are discussed in detail in Chapter 4.

## CHAPTER 2

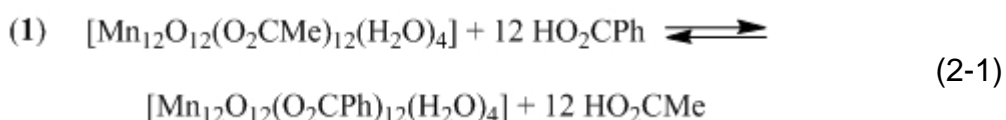
### Mn<sub>13</sub>- AND Mn<sub>8</sub>-CLUSTERS FROM THE USE OF 1,1'-FERROCENEDICARBOXYLIC ACID

#### Introduction

The synthesis of transition metal clusters has been largely fueled in the last two decades by the discovery of the Single-Molecule Magnet (SMM) phenomenon<sup>35,37</sup> and its potential application towards molecular storage of information.<sup>74</sup> The great advantage offered by SMMs to preserve the direction for the magnetization vector below a particular blocking temperature ( $T_b$ ) makes these molecules ideal candidates as ultra-small nanoscale magnets.<sup>34</sup> Prerequisites for a metal cluster to function as a SMM are the presence of a large and well isolated spin ground-state  $S$  and a large negative axial magnetic anisotropy  $D$ .<sup>75</sup> A simple approach to achieve a cluster possibly possessing a large  $S$  is to assemble a large number of 3d transition metal ions. This task is performed with bridging ligands where metal aggregation through oxide formation is favored. The downside of this approach is the poor control on the final molecular assembly, which governs the various intramolecular exchange interactions among spins. The nature of the metal ions and their disposition in the cluster are responsible for the magnitude of the magnetic anisotropy, and not necessarily the number of metal ions. This concept is well explained in the literature by the sentence : "Unfortunately, bigger is not necessarily better as far as SMMs are concerned".<sup>34</sup> For example, the largest Mn cluster known to date is a Mn<sub>84</sub> torus<sup>76</sup> possessing a total spin of only  $S = 6$ . In contrast, much smaller molecular systems are capable of SMM behavior, primarily due to large anisotropies. For example, the Mn<sub>4</sub> cubane cluster<sup>77</sup> with  $S = 9/2$  is a SMM with a well-isolated ground state and has been extensively used for numerous studies on SMM properties. Several strategies for the formation of M-M bonded clusters<sup>78</sup> have been suggested,

however the same does not apply in the case of ligand-bridged 3d metal clusters. The complexity of the reaction system leading to cluster formation makes its full description challenging, and for this reason the targeted synthesis of a coordination cluster is usually very difficult.<sup>79</sup>

New clusters of chosen nuclearity and ligation may be synthesized via substitution reactions on preformed materials. This approach is successful especially in clusters containing carboxylates. It has been demonstrated that the conjugate acid of a ligand precursor can replace a bound carboxylate through its transformation to the corresponding acid. The main factors in the substitution are the relative acidity of the attacking and leaving groups, the presence of preferential substitution sites, and the ligand size. The neutral complex  $[\text{Mn}_{12}\text{O}_{12}(\text{O}_2\text{CPh})_{12}(\text{H}_2\text{O})_4]$  can be prepared either by a direct comproportionation reaction of  $\text{Mn}^{\text{II}}$  and  $\text{Mn}^{\text{III}}$  ions in the presence of benzoic acid<sup>80</sup> or in a higher yield by two cycles of ligand substitution with benzoic acid on the preformed  $[\text{Mn}_{12}\text{O}_{12}(\text{O}_2\text{CMe})_{12}(\text{H}_2\text{O})_4]$ <sup>81</sup>. The stronger acidity of the benzoic acid ( $\text{pK}_a = 4.19$ )<sup>82</sup> with respect to the acetic acid ( $\text{pK}_a = 4.75$ )<sup>82</sup> promotes the protonation and removal of the acetate ligands as shown in Eq. 2-1.



Weaker acids can also be employed for such substitutions, but the equilibrium has to be driven in the forward direction through constant removal of acetic acid as a toluene azeotrope.<sup>83</sup> In  $[\text{Mn}_{12}\text{O}_{12}(\text{O}_2\text{CR})_{12}(\text{H}_2\text{O})_4]$ , eight carboxylate groups are attached only at the Jahn-Teller elongated  $\text{Mn}^{\text{III}}$  bonds. This subgroup of ligands can thus undergo easier substitution allowing for the isolation of partially substituted products

such as:  $[\text{Mn}_{12}\text{O}_{12}(\text{O}_2\text{CR})_8(\text{O}_2\text{CR}')_8(\text{H}_2\text{O})_4]$ <sup>84</sup> or  $[\text{Mn}_{12}\text{O}_{12}(\text{NO}_3)_4(\text{O}_2\text{CCH}_2\text{Bu}^t)_{12}(\text{H}_2\text{O})_4]$ <sup>85</sup>. Finally, the large size of an incoming ligand may prevent a complete substitution or make it rather difficult because of steric hindrance.<sup>86</sup> In the present work, the ligand precursor 1,1-ferrocenedicarboxylic acid has been used as a potential route to new Mn clusters. The acidity of  $\text{fdcH}_2$  ( $\text{pK}_a < 5.7$  in 50% EtOH)<sup>87</sup> is comparable to the one for benzoic acid ( $\text{pK}_a = 5.68$  in 50 % EtOH)<sup>87</sup> hence making the ligand precursor capable of ligand substitutions reactions on carboxylate (especially acetate) clusters such as  $[\text{Mn}_{12}\text{O}_{12}(\text{O}_2\text{CMe})_{12}(\text{H}_2\text{O})_4]$ .

### **Properties of $\text{FdcH}_2$ , and Previous Applications**

As already summarized in Chapter 1, the  $\text{fdcH}_2$  ligand precursor is a good candidate because it contains the electroactive ferrocenyl unit along with two carboxylic acid units. It has been shown that  $\text{fdc}^{2-}$  can bind transition metal ions in a variety of ways (see Fig. 2-1).<sup>88</sup> Having a large number of possible chelation modes, the  $\text{fdc}^{2-}$  opens up the possibility for the isolation of different structural topologies. The restricted flexibility of  $\text{fdc}^{2-}$  limits the degrees of freedom of the two coordinating groups, in contrast to a monocarboxylate ligand where the only limitation may come from steric constraints. Furthermore,  $\text{fdc}^{2-}$  is structurally more adaptable than a rigid dicarboxylate, and may allow for the formation of clusters with unprecedented conformations.

The presence of the ferrocene group provides a redox capability and allows the possibility of exploring the magnetic influence of a ligand  $S = 1/2$  spin on the magnetic properties of the cluster. Due to its interesting redox properties, ferrocene has been applied extensively in the past to produce multifunctional materials. Its combination with other molecular systems has expanded their properties and consequently, their potential applications.<sup>89-92</sup> The stability of this organometallic assembly allows for ease

of substitution at the cyclopentadienyl positions resulting in a large variety of derivatives that promoted its use.<sup>93</sup>

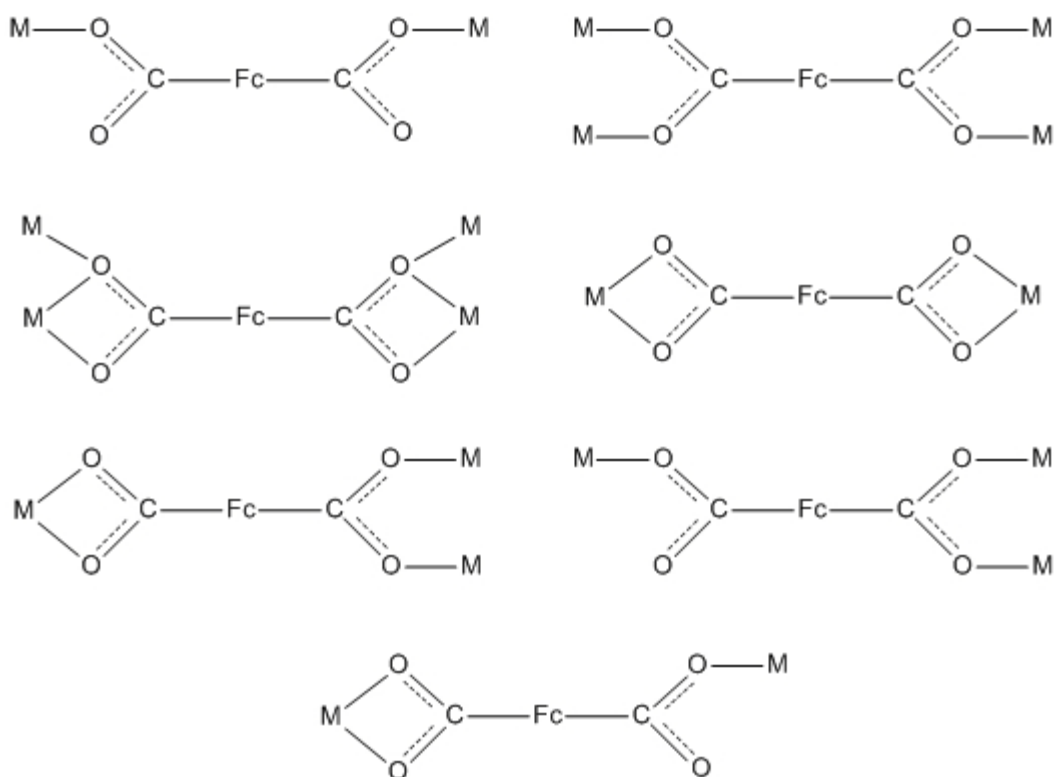


Figure 2-1. Known coordination modes of  $\text{fdc}^{2-}$  (adapted from ref. <sup>88</sup>).

The first  $\text{fdCH}_2$  synthesis was published in 1959 used lithiation of ferrocene to give the product in 24% yield<sup>93</sup> whereas the first metallic adduct reporting  $\text{fdc}^{2-}$  as ligand was with U and was characterized in 1973.<sup>94</sup> The use of  $\text{fdCH}_2$  as ligand precursor in coordination chemistry aiming towards the formation of polynuclear species was published much later by Lee et al. in 1996.<sup>95</sup> They were able to bridge two trinuclear Os units of the type  $[\text{Os}_3(\text{CO})_{10}(\text{MeCN})_2]$  with one  $\text{fdc}^{2-}$  unit giving the new heptanuclear  $\text{Os}_6\text{Fe}$  species:  $[\{\text{Os}_3\text{H}(\text{CO})_{10}\}_2\text{fdc}]$ , see Fig. 2-2. Another example of a polynuclear system obtained from the assembly of smaller units was reported by Cotton et al. in 1999 involving a square array of  $\text{Mo}_2^{4+}$  and  $\text{Rh}_2^{4+}$  units (see Fig. 2-3a).<sup>96-97</sup> Almost

concurrently, Uhl et al. produced a very similar macrocyclic square assembly of  $\text{Ga}_2^0$  units supported by four bridging  $\text{fdc}^{2-}$  ligands (see Fig. 2-3b).<sup>98</sup>

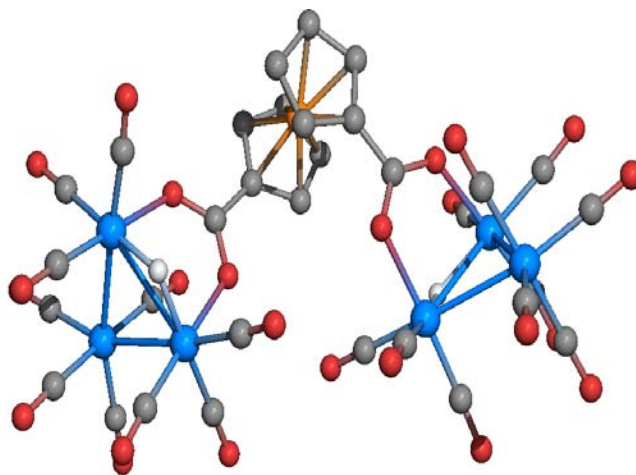


Figure 2-2. Pov-Ray projection of  $[\{\text{Os}_3\text{H}(\text{CO})_{10}\}_2\text{fdc}]$ , the first example of the use of  $\text{fdcH}_2$  to give a polynuclear system.<sup>95</sup>

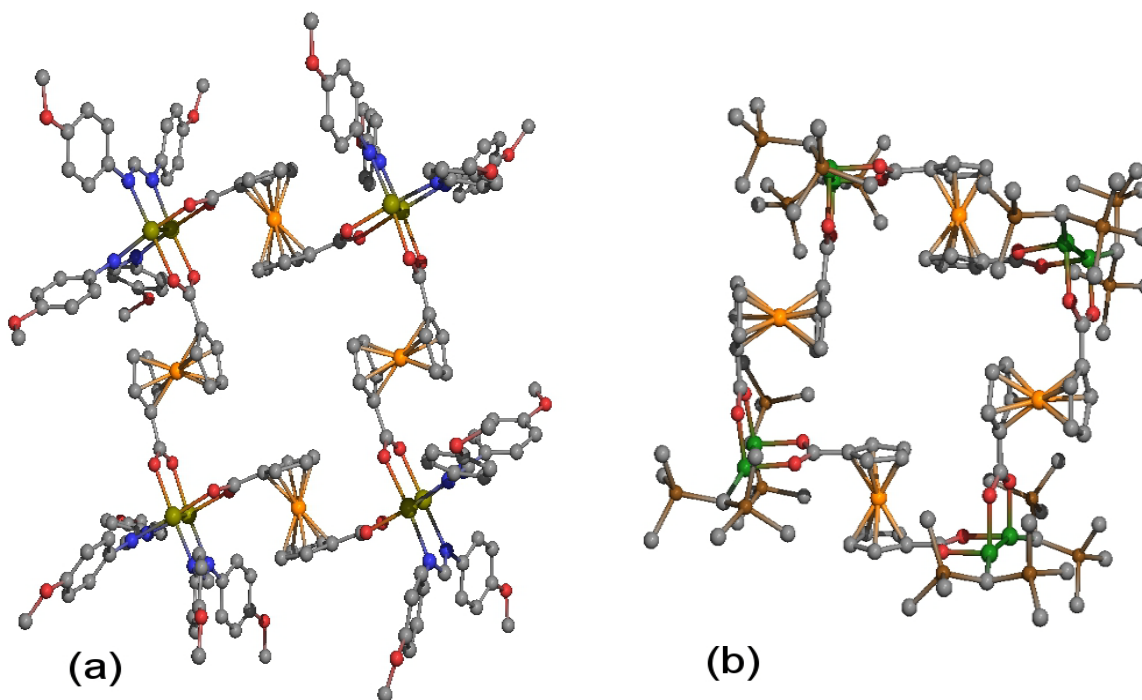


Figure 2-3. (a) Square array of  $\text{Mo}_2^{4+}$  units (olive green) bridged by  $\text{fdc}^{2-}$  and (b) analogous arrangement in a square of four  $\text{Ga}_2^0$  (green) units.<sup>96-98</sup>

The main interest in using the  $\text{fdc}^{2-}$  ligand in these coordination compounds resides in the large flexibility offered by the ligand in forming unusual structures while

achieving multifunctional systems. In this regard, many research groups are pursuing properties such as electrochemical activity<sup>88,95-106</sup>, magnetism<sup>88,102,107-110</sup> and luminescence,<sup>88,108,111</sup> within broader programs studying stabilization of M-M bonds<sup>95-98,112</sup>, catalysis<sup>95,113-114</sup> and exploration of new topologies in discrete units<sup>95,100-103,105-107,109-110,112,114-117</sup> or polymeric systems.<sup>99,104,108,111,115,118</sup>

In cases where the electrochemical activity in polynuclear systems was pursued, the ligand  $\text{fdc}^{2-}$  showed a variety of behaviors. As a general guideline, the electrochemical profile of a multiferrocenyl species should display one redox process associated with each ferrocenyl unit. On the basis of statistical considerations, the separation between the first and second peak is expected to be  $\sim 36.6$  mV, the separation between the second and the third  $\sim 56.5$  mV and so on.<sup>96</sup> The position of the half-wave potentials ( $E_{1/2}$ ) and the separation between two consecutive redox processes ( $\Delta E_{1/2}$ ) are complex to predict, however the three main factors that govern the processes are as follows. Firstly, substantial structural changes such as bond formation or dissociation, variation in the coordination number and geometry upon charge transfer may shift the comproportionation equilibrium. Secondly, a direct Coulomb-type interaction may affect the situation significantly, if two or more redox centers are in close proximity. A  $(n-1)^+$  center will be more readily oxidized than the corresponding  $n^+$  center just on the basis of electrostatic considerations, hence the interaction with a positively charged center will increase the  $\Delta E_{1/2}$  separation for oxidation. Finally, delocalization promotes the stabilization of intermediate oxidation states, which again increases the  $\Delta E_{1/2}$ .<sup>99</sup>

In the specific case of  $\text{fdc}^{2-}$  units as redox centers, crystallographic data have shown that ferrocene<sup>119</sup> and its ferricenium<sup>120</sup> salts remain almost unchanged with respect to the interatomic distances upon redox processes, implying a negligible energy change in the conversion of  $\text{fdc}^{2-}$  to  $\text{fdc}^-$  and vice versa.<sup>54</sup> The interatomic distance between the two irons of  $\text{fdc}^{2-}$  units should be comparable to or smaller than  $\sim 7.6 \text{ \AA}$  in order for the iron ions to have a significant electrostatic interaction.<sup>99</sup> The only other possible interaction is along the bonds, which may be governed by the number and type of bonds separating the two ferrocenyl units.

At one extreme, there are cases where the  $\text{fdc}^{2-}$  units do not interact and the  $E_{1/2}$  separation follows the thermodynamical statistical distribution previously mentioned. Examples of such systems are the macrocyclic assemblies made by Cotton et al.<sup>97</sup> and Uhl et al.<sup>98</sup> depicted in Fig. 2-3. Other systems of different nuclearity and shape also exemplify non communicating ferrocenyl systems, such as  $[\text{Pb}_4\text{Na}_4(\text{fdc})_6(\text{H}_2\text{O})_6]$ <sup>100</sup>,  $[\text{Mn}_{13}\text{O}_8(\text{fdc})_6(\text{OMe})_6]$ <sup>101</sup>, bis- $[\text{Pt}_2(\text{fdc})(\text{Pet}_3)_2(\text{C}_{14}\text{H}_8)]$ <sup>103</sup> and  $[\text{Sn}_8\text{O}_4(\text{fdc})_6]$ <sup>105</sup>. In dimeric structures of the type  $[\text{M}_2(\text{fdc})_2(2,2'\text{-bpy})_2(\text{H}_2\text{O})_2]$  ( $\text{M} = \text{Cd}, \text{Zn}, \text{Ni}, \text{Co}$ )<sup>88</sup>,  $[\text{Cu}_2(\text{fdc})_2(\text{Py})_2(\text{DMF})_2(\text{H}_2\text{O})_2]$ <sup>99</sup>,  $[\text{Ni}_2(\text{fdc})_2(\text{py})_4(\text{H}_2\text{O})_2]$ <sup>99</sup>,  $[\text{Sn}_2(\text{fdc})_2\text{R}_4]$  ( $\text{R} = \text{n-Bu}$  or  $\text{Bz}$ )<sup>106</sup> or  $[\text{Te}_2(\text{fdc})_2(\text{C}_6\text{H}_4\text{OMe})_4]$ <sup>106</sup> the degree of interaction amongst the two ferrocenyl units varies, as suggested by the different  $\Delta E_{1/2}$  values.

Another important factor is the  $E_{1/2}$  value for the oxidation of a coordinated  $\text{fdc}^{2-}$  unit. It is generally found that the electron withdrawing effect exerted by the coordinated metal ions moves the oxidation of the ferrocenyl units towards more anodic potentials (more positive potentials), which translates as expenditure of more energy for removal of an electron. Although this may be intuitive, there are two examples where such a

trend is not observed. The polymeric  $[\text{Ba}(\text{fdc})(\text{H}_2\text{O})]_\infty$  by Guo et al.<sup>104</sup> showed (in the solid state) that  $E_{1/2}$  for the oxidation of the  $\text{fdc}^{2-}$  is almost the same as that for uncoordinated  $\text{fdcH}_2$ . In order to understand this behavior, the authors synthesized another polymeric compound containing Sm:  $[\text{Sm}_6(\text{fdc})_4(\text{H}_2\text{O})_n]_\infty$ . The conclusion of the study was that both alkaline-earth and lanthanide metal ions leave the redox potentials of ferrocenyl-based bridging ligands relatively unaffected, contrary to what was generally observed for transition metals. Unfortunately, there is no other published data of this type to confirm or contest the conclusion.

An important study on the stability of a coordinated  $\text{fdc}^-$  species comes from the Sn cluster  $[\text{Sn}_8\text{O}_4(\text{fdc})_6]$  isolated through solvothermal synthesis by Zheng et al.<sup>105</sup> (see Fig. 2-4). In this compound, the six  $\text{fdc}^{2-}$  units display some degree of lability in DMF solution (solvent of choice for electrochemical investigation).

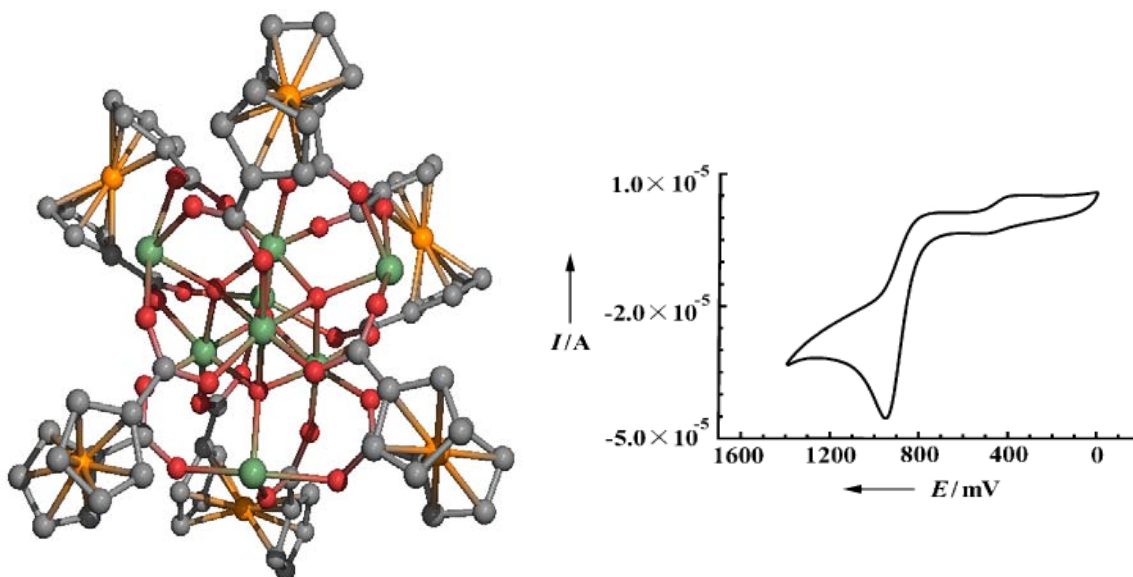


Figure 2-4. Pov-Ray projection of the  $[\text{Sn}_8\text{O}_4(\text{fdc})_6]$  cluster and its cyclic voltammogram in DMF vs. sat. Ag/AgCl (the latter reported from ref. <sup>105</sup>, Copyright Wiley-VCH Verlag GmbH & Co. KGaA. Reproduced with permission).

When the potential is scanned in the anodic region a reversible feature is observed which is assigned to the free ligand. At higher potentials appears the irreversible oxidation of the coordinated  $\text{fdc}^{2-}$  units in the cluster. The authors explain the irreversibility of this process with the decrease in basicity of the ligand upon oxidation. Such an effect would probably cause the oxidized  $\text{fdc}^-$  units to dissociate partially or totally from the Sn core and promote an irreversible rearrangement soon after. Quite opposite behavior is found in the large  $\text{Ga}_8(\text{fdc})_4$ -macrocycle where the system shows an initial irreversible oxidation of the Ga-Ga bond, then a combined four-electron reversible wave followed by another irreversible oxidation.<sup>98</sup> The multi-electron wave is associated with the simultaneous oxidation of the ferrocenyl units.

With respect to magnetic properties, the literature reports only two polynuclear clusters possessing  $\text{fdc}^-$  units which have been investigated;  $[\text{Zn}_6\text{O}_2(\text{fdc})_5(\text{H}_2\text{O})(\text{DMF})]$  and  $[\text{Zn}_8\text{O}_4(\text{fdc})_6(\text{H}_2\text{O})_3]$  by Kim et al. in 2007<sup>107</sup>. The authors invoke the presence of a mixed-valence state of the iron ions due to charge balance considerations and to explain the net paramagnetic behavior of the clusters. The first Zn cluster is expected to have two  $\text{Fe}^{\text{III}}$  and three  $\text{Fe}^{\text{II}}$  ions in the ferrocenyl units, whereas the second cluster four  $\text{Fe}^{\text{III}}$  and two  $\text{Fe}^{\text{II}}$  ions. Based on magnetic measurements, the authors suggest the presence of antiferromagnetic interactions amongst the  $\text{fdc}^-$  units in both molecules and no further description of the ground state or coupling pathways was reported. The magnetic data, however, reveal some mismatch with the assumed composition of the clusters and the orange color of these compounds does not match with the expected intense blue color of ferricenyl units. The synthesis of these Zn-clusters was performed by diffusion of the reagents for  $[\text{Zn}_6\text{O}_2(\text{fdc})_5(\text{H}_2\text{O})(\text{DMF})]$  and by solvothermal methods

for  $[\text{Zn}_8\text{O}_4(\text{fdc})_6(\text{H}_2\text{O})_3]$ . Experimental details do not specify the ambient light conditions and in case of light exposure there may be photodecomposition of the ligand<sup>121</sup> and scrambling of Fe into the cluster core. The photo-instability of ferrocenyl units is well known in chemistry and it will be discussed in detail in Chapter 3. Another published study, reporting  $\text{fdc}^{2-}$  units in a Co dimer introduced the possibility of contamination by Fe into the final product to explain some deviations in the expected magnetic behavior.<sup>88</sup> No description was found in the literature about the magnetic coupling promoted by the  $\text{fdc}^{2-}$  unit. This could be the consequence of the relatively low number of reports on  $\text{fdc}^{2-}$  as a ligand in metal clusters. The magnetism of other compounds containing  $\text{fdc}^{2-}$  is considered to be solely due to the cluster core. Furthermore, Mössbauer investigations displayed no charge exchange between  $\text{fdc}^{2-}$  and the core ions in two Fe-core clusters.<sup>109</sup>

The other often investigated property of ferrocenyl-rich systems is fluorescence. This phenomenon is typical of ferrocene and most of its derivatives, like the sodium salt of the ligand ( $\text{Na}_2\text{fdc}$ ) or its acidic precursor ( $\text{fdcH}_2$ ). The absorption peak at  $\sim 245$  nm results in fluorescence emission at  $\sim 393$  nm in solid  $\text{Na}_2\text{fdc}$ .<sup>88,111</sup> This property is exhibited in clusters containing  $\text{fdc}$  groups as a consequence of the intraligand nature of the fluorescence process. Such observation derives from the relatively unchanged position of the fluorophore emission as free ligand or as coordinating group. The ligand-to-ligand charge transfer (LLCT) is not remarkably affected by the nature of the polynuclear assembly of which it is part of. However, presence of relaxing groups nearby, such as hydroxide, may be responsible for enhancing the dispersion of energy, which accounts for the decreased intensity of the emission band.<sup>108</sup>

## Synthesis of FdCH<sub>2</sub>

The ligand precursor fdCH<sub>2</sub> is a commercially available compound used in various fields. However, in order to perform an exhaustive study as a ligand in cluster chemistry, relatively large quantities are necessary. Hence, its synthesis was initially attempted in the laboratory. 1,1'-ferrocenedicarboxylic acid was isolated as the main reaction product and later purified by fractional precipitation and crystallization techniques.

Chromatographic methods were not employed due to the bulk amounts of the material to be treated and due to the photo-instability of the components. Extensive analysis proved fdCH<sub>2</sub> purification ineffective for the complete removal of the by-products. The effect of such impurities in the system forming clusters is unknown although the possibility for undesirable side reactions exists.

One of the most recent publications to achieve the ferrocene based diacid reports the use of a lithiation reaction followed by electrophilic attack of carbon dioxide on the cyclopentadienyl rings.<sup>122</sup> The synthesis has been slightly modified and performed as follow. *n*-Butyllithium in hexane was added dropwise to a solution of TMEDA (tetramethylethylenediamine) and ferrocene in anhydrous ethyl ether with continuous stirring under argon atmosphere at 0° C. After the reagents were completely mixed the system was slowly warmed up to room temperature and allowed to stir overnight. The reaction formed an orange precipitate of the dilithium salt of ferrocene which was then reacted with an excess of CO<sub>2</sub> by bubbling the gas through the solution, yielding the dilithium 1,1'-ferrocenedicarboxylate. Deionized water was added until complete dissolution of the precipitate occurred. After filtration, the product was extracted with dichloromethane/water and the aqueous phase acidified with diluted hydrochloric acid. The orange precipitate of 1,1'-ferrocenedicarboxylic acid resulting from acidification was

filtered and washed with deionized water. After complete drying the isolated product accounted for a 85 % yield, against the 68 % reported in the literature. The increased yield might be due to a longer reaction time between the complex *n*-BuLi-TMEDA and ferrocene with respect to the published procedure. The adopted reaction scheme is reported in Fig. 2-5.

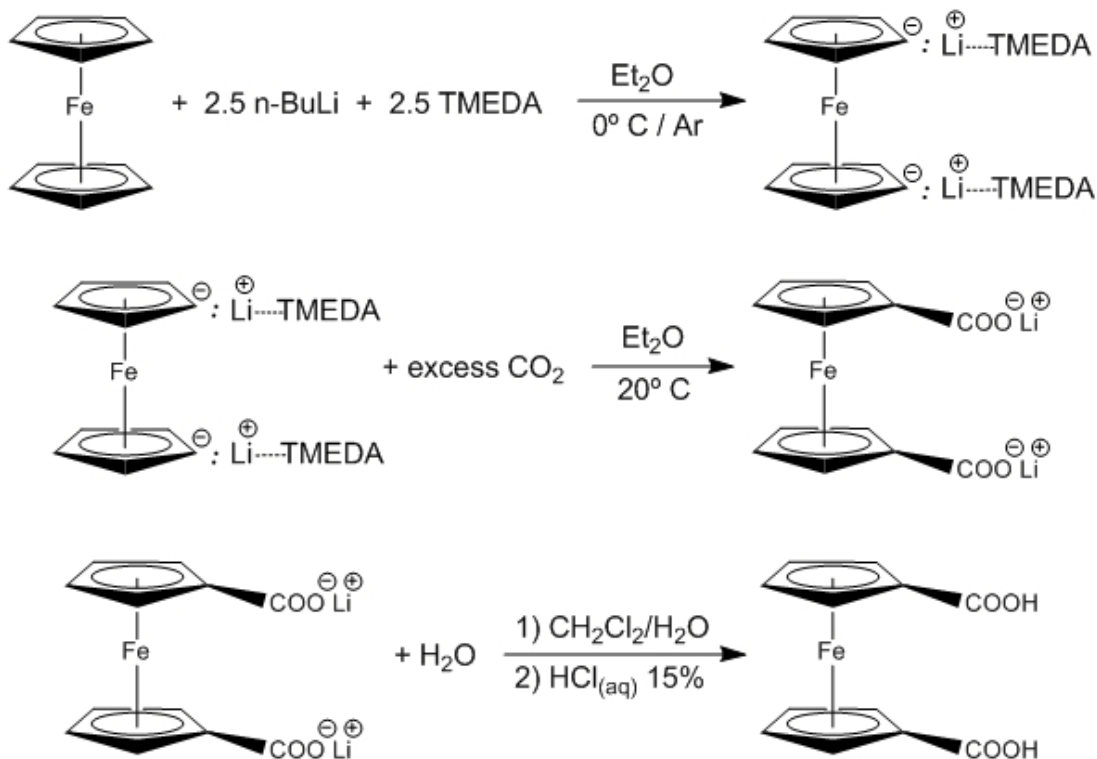


Figure 2-5. Modified synthesis of the ligand precursor 1,1'-ferrocenedicarboxylic acid. The yield of isolated product is ~85%.

The isolated fdCH<sub>2</sub> was analyzed using the following techniques: <sup>1</sup>H-NMR, HR/EI-MS, IR and elemental analysis. The <sup>1</sup>H-NMR data were collected at room temperature in a DMSO-*d*<sup>6</sup> solution (Fig. 2-6) and compared with the spectrum obtained from published databases.<sup>123</sup> DMSO is dimethylsulfoxide and is the solvent of choice for the NMR measurement for both enhancing the solubility of fdCH<sub>2</sub> and to reproduce the same experimental conditions of the spectral database.

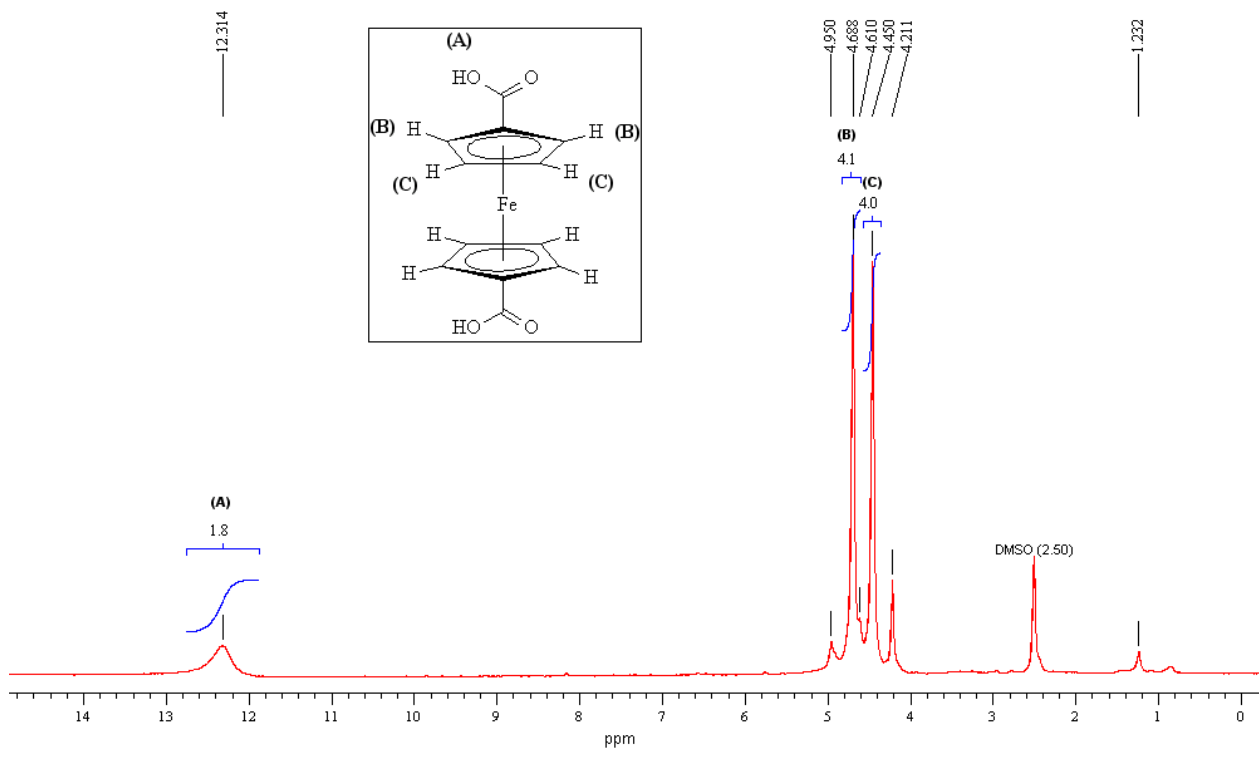


Figure 2-6. <sup>1</sup>H-NMR spectrum of raw 1,1'-ferrocenedicarboxylic acid saturated in *d*<sup>6</sup>-DMSO.

The <sup>1</sup>H-NMR spectrum shows the expected peaks for the hydrogen nuclei belonging to the cyclopentadiene rings at 4.450 and 4.688 ppm with integrated relative areas of 4.0 and 4.1, respectively (reference for the integration is the peak at 4.450 ppm). A low-field signal at 12.314 is indicative of the two acidic protons. The intensity of this last signal is not generally reliable due to a fast kinetic exchange. Additional peaks found at 1.232, 4.211 ppm are probably due to solvent impurities and unreacted ferrocene respectively, hence their presence will not affect the reactions forming clusters. Peaks at 4.610 and 4.950 ppm may belong to products of mono-substitution of ferrocene, such as ferrocenecarboxylic acid. For comparison, the 400 MHz <sup>1</sup>H-NMR spectrum from a public database is reported (Fig. 2-7).<sup>123</sup> The spectrum of high purity fdCH<sub>2</sub> confirms its presence as the major component in the reaction product.

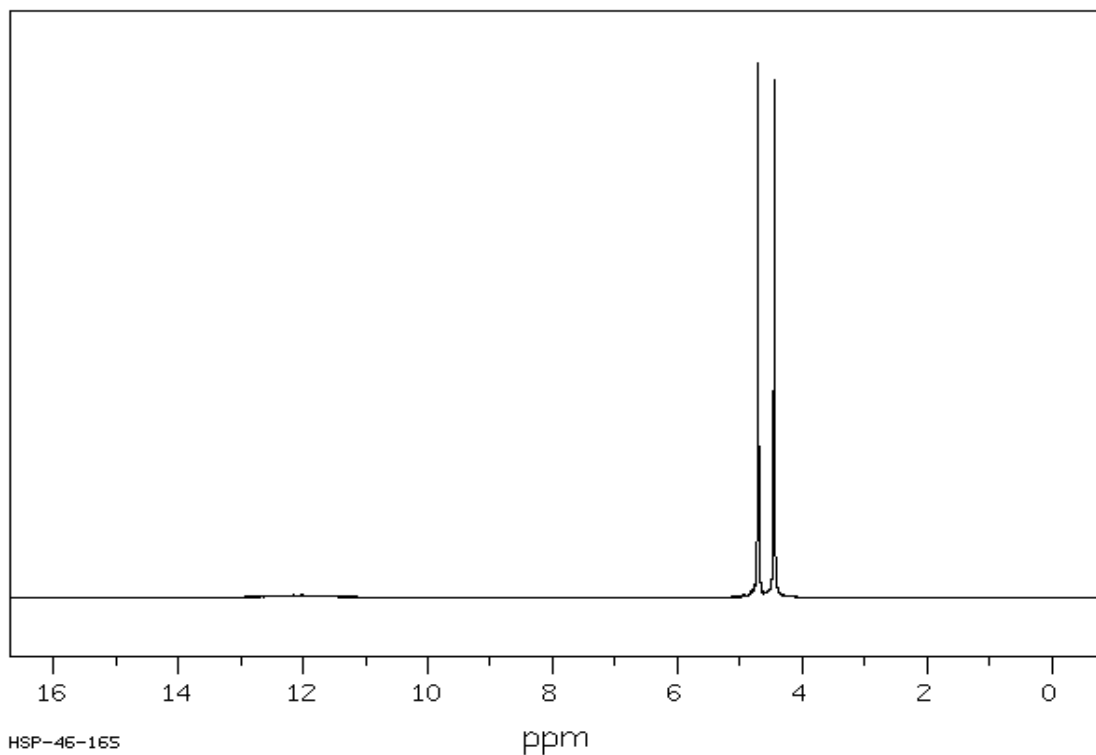


Figure 2-7. 400 MHz  $^1\text{H}$ -NMR spectrum of 1,1'-ferrocenedicarboxylic acid 0.040 g. in 0.5 mL  $d^6$ -DMSO (reported from ref. <sup>123</sup> with authors permission from SDBSWeb: <http://riodb01.ibase.aist.go.jp/sdbs/> (National Institute of Advanced Industrial Science and Technology, June 5<sup>th</sup> 2010).

Further investigations were performed with High Resolution Electron Ionization Mass Spectroscopy (HREIMS) showing only a low intensity molecular peak at  $m/z = 272.9808$  due to the low volatility (Fig. 2-8). The theoretical  $m/z$  is 272.9844 and these results are supported by published investigations.<sup>124</sup>

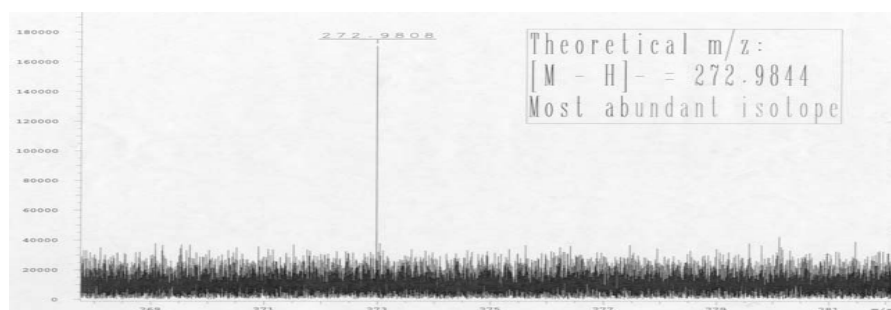


Figure 2-8. HREIMS spectrum of the synthesized 1,1'-ferrocenedicarboxylic acid. The low volatility allowed only for the detection of the molecular peak.

The characterization by IR spectroscopy of the synthesized  $\text{fdCH}_2$  against a commercially available source revealed almost superimposable spectra (Fig. 2-9). Some of the characteristic vibrational modes could also be identified by comparison with literature data.<sup>125</sup>

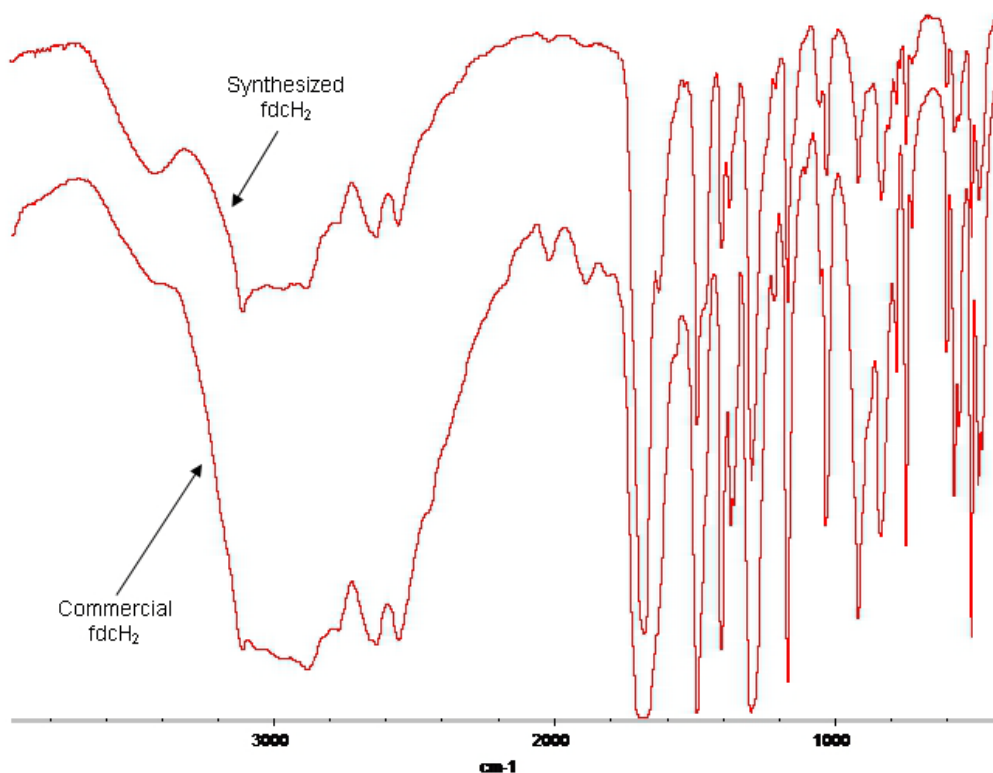


Figure 2-9. Comparison of IR spectra for commercial 1,1'-ferrocenedicarboxylic acid and the synthesized product.

Typical bands for the carboxylic acid were observed at 2636, 2552 and 917  $\text{cm}^{-1}$  in the spectrum of the synthesized  $\text{fdCH}_2$ , which could be assigned to the OH stretching and out-of-plane OH deformation vibrations. The very strong band found at 1683  $\text{cm}^{-1}$  was due to the C=O stretching vibrations. The bands at 1491 and 1297  $\text{cm}^{-1}$  were assigned to on-plane bending modes of the C–O–H group.<sup>125</sup> Finally, the results from microanalysis were in close agreement with the expected theoretical composition.

### Synthesis of $[\text{Mn}_{13}\text{O}_8(\text{OR})_6(\text{fdc})_6]$ , (R = Me, Et), $[\text{Mn}_8\text{O}_4(\text{fdc})_6(\text{DMF})_2(\text{H}_2\text{O})_2]$ and $[\text{Mn}_8\text{O}_4(\text{fdc})_6(\text{DMF})_4]$

The use of  $\text{fdCH}_2$  as a ligand precursor with preformed Mn clusters has led to changes in the nuclearity and eventual isolation of two new homonuclear  $\text{Mn}_{13}$  and  $\text{Mn}_8$  cluster complexes. The approach used was the substitution reaction on the  $[\text{Mn}_{12}\text{O}_{12}(\text{O}_2\text{CMe})_{16}(\text{H}_2\text{O})_4] \cdot 4\text{H}_2\text{O} \cdot 4\text{MeCO}_2\text{H}$ , (**1**)  $\cdot 4\text{H}_2\text{O} \cdot 4\text{MeCO}_2\text{H}$ , complex according to published procedures.<sup>126-128</sup> To a solution of **1** in MeCN, a solution of  $\text{fdCH}_2$  in  $\text{CH}_2\text{Cl}_2$  was added in stoichiometric excess. Complete removal of the acetate ligands is ensured by removal of acetic acid as a toluene azeotrope (28:72 %; b.p. 101° C / 1 atm)<sup>83</sup>. The solution was treated repeatedly with small portions of toluene, evaporated at reduced pressure and the product was successively redissolved in MeCN and used for crystallization according to different techniques. The procedure did not lead to crystalline product for structural characterization, although the IR spectrum of the isolated solid showed the  $\text{Mn}_{12}$  starting material to be absent.

A variety of other reaction conditions were therefore explored. Complex **1** was suspended in a mixture of MeCN and MeOH in various ratios and heated with  $\text{fdCH}_2$  (also in variable stoichiometries). Experimental results showed that a 1:1 ratio MeCN/MeOH is optimal with a stoichiometric ratio 1:4 (**1** :  $\text{fdCH}_2$ ) for the isolation of reddish-brown needles after filtration and crystallization with diethyl ether (~ 5% yield). The product was characterized by X-ray crystallography as  $[\text{Mn}_{13}\text{O}_8(\text{OMe})_6(\text{fdc})_6] \cdot 8\text{CH}_2\text{Cl}_2$  [**(2)**  $\cdot 8\text{CH}_2\text{Cl}_2$ ]. Further synthetic efforts based on different solvent mixtures demonstrated the possibility to produce complex **2** using  $\text{CH}_2\text{Cl}_2/\text{MeOH}$  (1:1) as the solvent but in with a low 5% yield.

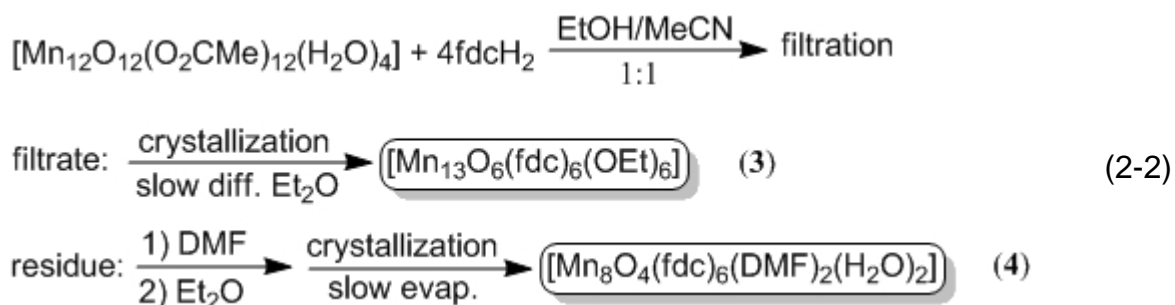
Complex **2** was reported in the literature in 2003, when M. Kondo *et al.* synthesized it in 33% yield by diffusion of an acetone solution of  $\text{fdCH}_2$  into a methanolic solution of  $\text{Mn}(\text{O}_2\text{CMe})_2$  under aerobic conditions.<sup>101</sup> Although the present work led to this known compound, it could not have been predicted, and it also provided the opportunity for a further study of its properties. The Kondo paper was limited to the electrochemical characterization of the  $\text{Mn}_{13}$  cluster in the solid state. This study has now carried out the characterization of its magnetic properties.

A detailed description of the mechanism governing such reactions represents a challenge, but it is reasonable to assume the initial binding of one of the carboxylate groups of  $\text{fdCH}_2$  on **1** with displacement of an acetate group in the form of acetic acid.<sup>127-</sup><sup>128</sup> At this point, in analogy with a chelating ligand, the proximal vicinity of the two carboxylates in  $\text{fdc}^{2-}$  increase the probability of the second carboxylate moiety to bind, once the first carboxylate group enters the coordination of the Mn core. The progressive substitution of two acetate groups by an  $\text{fdc}^{2-}$  likely causes the rearrangement of the cluster core. In this particular case, two or more molecular fragments contribute to increase the nuclearity, as all the acetate groups are displaced by  $\text{fdc}^{2-}$  groups.

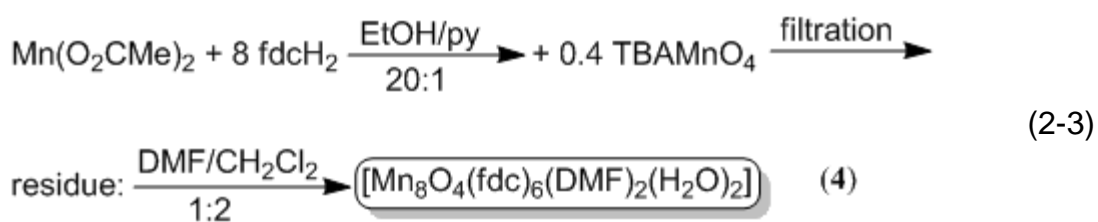
Besides complex **2**, another cluster with the same core but slightly different ligation was obtained. The use of a mixture of EtOH and MeCN (1:1) led to an almost identical core where the external methoxide ligation was replaced by ethoxides. The identification of the new cluster  $[\text{Mn}_{13}\text{O}_8(\text{OEt})_6(\text{fdc})_6]$  (**3**) was based on IR spectra, microanalysis and magnetic behavior. The reaction process for complex **3** is actually superior to that for **2** in that it gives a cleaner reaction and slightly higher yield of product

(7%). The reactions to both **2** and **3** give large amounts of insoluble brown precipitates that justify the low yield for the isolation of these clusters. One unfortunate property of **2** and **3** is their very low solubility. With the purpose of increasing the solubility, other reactions were attempted to further change the peripheral ligation. A mixture of **1**/fdCH<sub>2</sub> (1:4) was stirred in the presence of benzyl alcohol. This reaction allowed for the isolation of a microcrystalline product not suitable for X-ray analysis. Its IR comparison with the previously characterized complex **2** showed that it had a different structure. However, this new product was not pursued, as it did not show sufficient solubility in any common solvent.

Detailed synthetic studies of the initial reaction system for **2** was completed with the isolation of another Mn cluster incorporating the ligand fdc<sup>2-</sup>. This new compound has the molecular formula [Mn<sub>8</sub>O<sub>4</sub>(fdc)<sub>6</sub>(DMF)<sub>2</sub>(H<sub>2</sub>O)<sub>2</sub>].4DMF.4H<sub>2</sub>O [**(4)**.4DMF.4H<sub>2</sub>O]. The brown precipitate resulting from the reaction of **1** with fdCH<sub>2</sub> was resuspended in a mixture (1:1) of DMF/CH<sub>2</sub>Cl<sub>2</sub> where it would dissolve only slightly and be filtered. Dark needle shaped crystals were obtained by slow diffusion of ether into the filtrate. The new compound was characterized by single-crystal X-ray diffraction and supported by IR and elemental analysis. Eq. 2-2 summarizes the synthesis of **3** and **4**. Unfortunately, the yield of **4** is very low ( $\leq 2\%$ ), as otherwise expected for a minor reaction product and for the large amount of undissolved precipitate. Careful inspection of the crystalline product under an optical microscope showed the presence of an amorphous substance in addition to the crystals of **4**. Manual separation and IR analysis suggested the amorphous product to be structurally very close to the cluster **4** although a complete identification was never achieved.

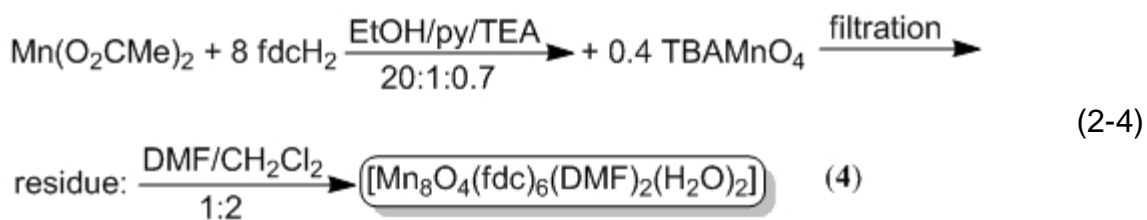


Due to the low yield and cocrystallization of unidentified material, complex **4** could not be obtained in high purity via this synthetic route. Hence, efforts were made to find another route to the  $\text{Mn}_8$  cluster. An alternative method was found when different Mn sources were explored and the ligand precursor  $\text{fdch}_2$  was used in a comproportionation reaction between  $\text{Mn}^{\text{II}}$  and  $\text{Mn}^{\text{VII}}$  to generate  $\text{Mn}^{\text{III}}$ . A mixture of  $\text{Mn}(\text{O}_2\text{CMe})_2$  and  $\text{fdch}_2$  in  $\text{EtOH/py}$  was oxidized with tetrabutylammonium permanganate ( $\text{TBAMnO}_4$ ) to give a brown suspension. Recrystallization of the collected solid from  $\text{DMF/CH}_2\text{Cl}_2$  (1:1) led to complex **4**, but with an unidentified byproduct. The scheme for the alternative synthesis of **4** is shown in Eq. 2-3.



Although the new procedure to **4** is still contaminated with some impurity, it is overall superior to the earlier one, and suggested that further modification might allow pure **4** to be obtained. Through other experiments, it had been found that addition of small amounts of triethylamine (TEA) to the reaction systems can completely prevent the co-crystallization of byproducts. This modification in the present reaction successfully allowed for the sole isolation of the  $\text{Mn}_8$  complex in higher yields (~ 40%)

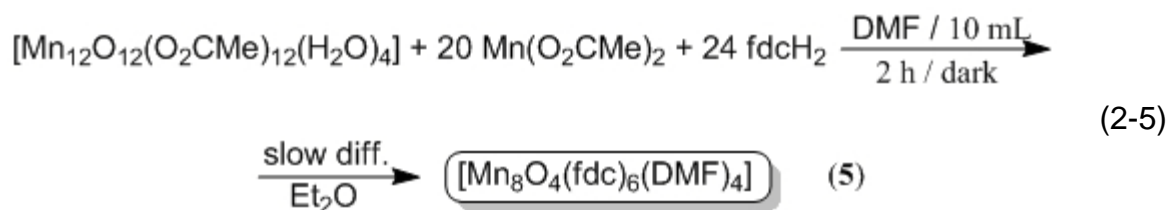
(see Eq. 2-4). The product was obtained as a powder, but IR spectra, elemental analysis and magnetic measurements all indicated the product to be pure.



The role of the TEA in preventing the accumulation of impurities is unclear. The reaction mechanism may be influenced by TEA in several ways. The TEA can change the pH, and also may act as a mild reducing agent. With comproportionation proving a superior approach, further improvements were sought to the yield. A new reaction scheme was subsequently developed by considering factors such as the average oxidation state of the core, the ratio of the Mn ions to the oxide ions, the number and protonation state of the ligands as well as the number and type of the peripheral ligation.

The formula  $[\text{Mn}_4^{\text{III}}\text{Mn}_4^{\text{II}}\text{O}_4(\text{fdc})_6(\text{DMF})_2(\text{H}_2\text{O})_2]$  indicated an average oxidation state of +2.5 for Mn. There are on average two  $\text{Mn}^{2.5+}$  ions per oxide, six fully deprotonated  $\text{fdc}^{2-}$  units, two DMF molecules and two water molecules. To reach the intermediate state of  $\text{Mn}^{2.5+}$  a comproportionation reaction between  $\text{Mn}^{\text{II}}$  and  $\text{Mn}^{\text{VII}}$  could be employed. An improved procedure was devised using  $[\text{Mn}_{12}\text{O}_{12}(\text{O}_2\text{CMe})_{16}(\text{H}_2\text{O})_4]$  was used as the source of the higher oxidation state ( $\text{Mn}^{3.33+}$ ), and  $\text{Mn}^{2+}(\text{O}_2\text{CMe})_2$  for the lower oxidation state. It was thought that there may be a possible advantage in a combination where one of the metal sources is a preformed cluster and the other is mononuclear rather than both being mononuclear. It is conceivable that during the reaction some fragmentation and rearrangement of the  $\text{Mn}_{12}$  core occur to form the final

product of different nuclearity. In this process, the immediate availability of a mononuclear species might assist in completing fragments leading to the Mn<sub>8</sub> product. The Mn<sub>12</sub> cluster is also a good source of oxide ions with a Mn/O ratio of 1:1. It was suspected that this might also assist formation of Mn<sub>8</sub> upon addition of the mononuclear Mn<sup>II</sup>, by approaching the expected ratio of 2:1 for the Mn<sub>8</sub> cluster. Finally, the presence of DMF as solvent can provide terminal ligands and keep intermediates soluble allowing for clean formation of Mn<sub>8</sub>. This approach worked spectacularly well. The reaction scheme is shown in Eq. 2-5. The product is the new cluster [Mn<sub>4</sub><sup>III</sup>Mn<sub>4</sub><sup>II</sup>O<sub>4</sub>(fdc)<sub>6</sub>(DMF)<sub>4</sub>], (**5**), which except for two DMF molecules replacing water, is identical in composition and structural topology to **4**. The compound forms X-ray quality crystals with an overall yield of isolated product of ~ 85% with respect to Mn. Cluster **5** was characterized by X-ray crystallography, IR spectroscopy and elemental analysis.



Attempted application of this synthetic strategy to Mn<sub>13</sub> clusters raised immediate challenges due to the solvent. While the Mn<sub>13</sub> clusters have alkoxides as peripheral ligands, complex **1** is not soluble in alcohols. The solubility of the reactants is crucial for reaching at the initial stages of the reaction; the targeted Mn oxidation state through comproportionation. While a solvent like acetonitrile could be suitable for complex **1**, the same is not true for fdcH<sub>2</sub>. To avoid these problems, [Mn<sub>12</sub>O<sub>12</sub>(O<sub>2</sub>CMe)<sub>16</sub>(H<sub>2</sub>O)<sub>4</sub>] was treated in a acetonitrile/toluene mixture with eight equivalents of trimethylacetic acid and evaporated once to drive an acetate substitution reaction. The partially substituted

product,  $[\text{Mn}_{12}\text{O}_{12}(\text{O}_2\text{CMe})_{16-n}(\text{O}_2\text{C}^t\text{Bu})_n(\text{H}_2\text{O})_4]$  is readily soluble in ethanol and it was employed in a comproportionation reaction with  $\text{Mn}(\text{O}_2\text{CMe})_2$  in the presence of  $\text{fdCH}_2$ . The system gives an immediate formation of a glossy brown precipitate that the IR analysis suggested was composed mainly of the  $\text{Mn}_8$  cluster. This suggests preferential formation of a  $\text{Mn}_8$  structure over  $\text{Mn}_{13}$  and it was not further pursued.

### Description of the Molecular Structures

#### $[\text{Mn}_{13}\text{O}_8(\text{OMe})_6(\text{fdc})_6] \cdot 8\text{CH}_2\text{Cl}_2; (\mathbf{2}) \cdot 8\text{CH}_2\text{Cl}_2$

A Pov-Ray projection of complex **2** and its labeled core are shown in Fig. 2-10 and Fig. 2-11. The crystallographic data and structure refinement details are listed in Table 2-1. The complex crystallized in the triclinic space group P-1 and consists of a  $[\text{Mn}^{\text{IV}}\text{Mn}^{\text{III}}_6\text{Mn}^{\text{II}}_6(\mu_5\text{-O})_6(\mu_3\text{-O})_2(\mu_3\text{-OMe})_6]^{12+}$  core with the peripheral ligation provided by six bridging  $\mu_4\text{-fdc}^{2-}$  ligands. The core can be described as consisting of three layers; a central one where six coplanar  $\text{Mn}^{\text{II}}$  surround the central and unique  $\text{Mn}^{\text{IV}}$ . Other two layers are present one above and one below and contain each three  $\text{Mn}^{\text{III}}$  ions. Six of the eight oxo ligands are unusual in the sense that they are pentacoordinated, whereas the remaining two possess the more common coordination three.

Table 2-1. Selected crystal data for complex  $\mathbf{2} \cdot 8\text{CH}_2\text{Cl}_2$  (full data in Tab. B-1).

Parameter	Value
Empirical formula	$\text{C}_{92}\text{H}_{94}\text{Cl}_{16}\text{Fe}_6\text{Mn}_{13}\text{O}_{38}$
Formula weight, $\text{g mol}^{-1}$	3424.26
Temperature, K	173(2)
Wavelength, $\text{\AA}^a$	0.71073
Crystal system	Triclinic
Space group	P-1
Unit cell dimensions, $\text{\AA}$	$a = 14.1308(12), b = 15.1738(12), c = 15.3656(13)$
Unit cell angles, deg	$\alpha = 119.4700(10)^\circ, \beta = 91.4320(10)^\circ, \gamma = 100.339(2)^\circ$
Volume, $\text{\AA}^3$	2797.0(4)
Z	1
$\rho_{\text{calc}}, \text{g cm}^{-3}$	1.969

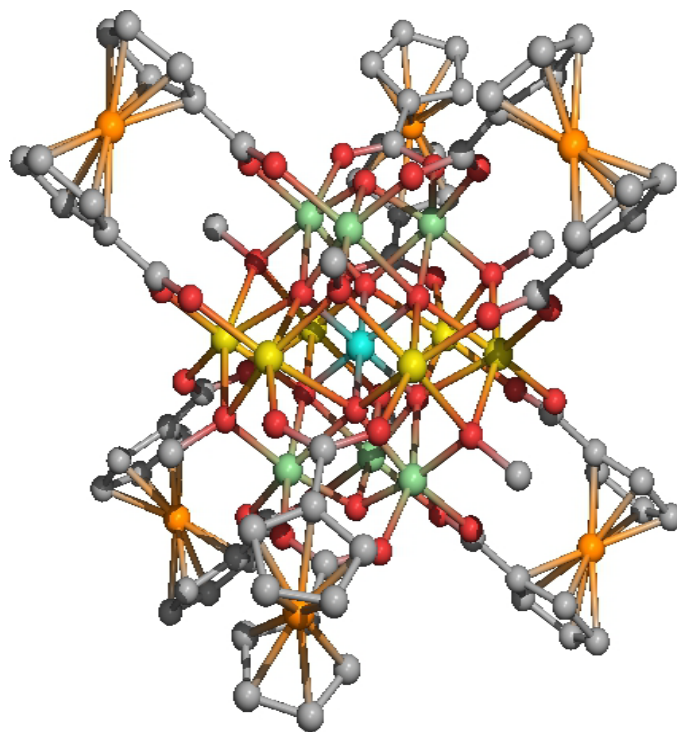


Figure 2-10. Pov-Ray projection of **2**: Mn<sup>IV</sup> cyan, Mn<sup>III</sup> light green, Mn<sup>II</sup> yellow, O red, Fe orange. Hydrogen atoms have been omitted for clarity.

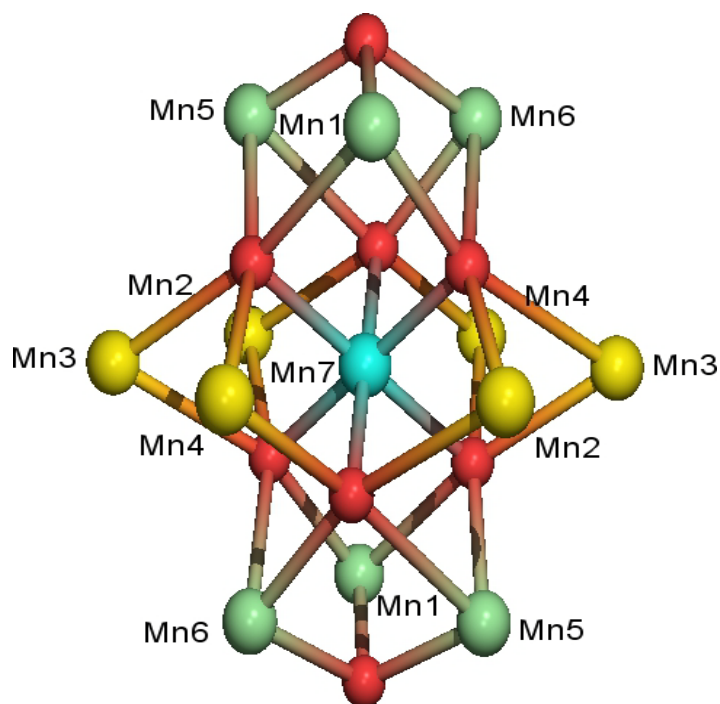


Figure 2-11. Pov-Ray projection of the  $[\text{Mn}^{\text{IV}}\text{Mn}^{\text{III}}_6\text{Mn}^{\text{II}}_6(\mu_5\text{-O})_6(\mu_3\text{-O})_2]^{18+}$  core in  $[\text{Mn}_{13}\text{O}_8(\text{OMe})_6(\text{fdc})_6]$ : Mn<sup>IV</sup> cyan, Mn<sup>III</sup> light green, Mn<sup>II</sup> yellow, O red.

The assignment of the oxidation states was based on charge balance considerations and quantitative evaluation of the bond lengths through Bond Valence Sum (BVS) calculations. The classical BVS value for an atom is an estimated value of its valence based on a collection of bond lengths measured through X-ray crystallography. The ion's oxidation state ( $z_i$ ) is estimated through the sum of individual valences assigned to each of its bonds ( $s_{ij}$ ). Every ( $s_{ij}$ ) value derives from the existing correlation between bond length and bond strength through two experimentally determined parameters,  $R_0$  and  $b$  (this last one usually taken as 0.37 Å).<sup>64,70-71,129-131</sup> The BVS method has been explained in detail in Chapter 1 (see Eq. 1-6), and used for these determinations without application of the newly optimized parameters  $R_0$  and  $b$  discussed in Chapter 4. Table 2-2 summarizes the BVS calculations for complex **2** showing in bold the number closer to the actual valence value.

Table 2-2. Bond Valence Sum values for complex **2**.

Atom	Mn <sup>II</sup>	Mn <sup>III</sup>	Mn <sup>IV</sup>
Mn1	3.407	<b>3.142</b> *	3.083
Mn2	<b>2.082</b> *	1.920	1.884
Mn3	<b>2.025</b> *	1.867	1.832
Mn4	<b>1.988</b> *	1.833	1.799
Mn5	3.366	<b>3.104</b> *	3.046
Mn6	<b>3.377</b>	<b>3.114</b> *	3.056
Mn7	<b>4.457</b>	4.110	<b>4.033</b> *

The number with an asterisk is the one closest to the actual charge for which it was calculated. The oxidation state of a particular atom can be taken as the nearest whole number to the value in bold.

The BVS method fails if applied to the estimation of the oxidation state of an iron in a ferrocenyl unit. As already mentioned in the Introduction, the two common oxidation states for the iron within cyclopentadienyl ligands display only a small difference in the Fe-C bond lengths. Furthermore, ferrocenyl units display an opposite trend to the BVS, where the Fe-C bonds are elongated with the higher metal oxidation state (Fe<sup>III</sup>) and

slightly shorter with the lower oxidation state ( $\text{Fe}^{\text{II}}$ ).<sup>132-133</sup> In this case, the difficult assessment of the iron oxidation state in the fdc units through statistical methods can be avoided. From charge balance considerations, it is clear that all the iron atoms must be in the  $\text{Fe}^{\text{II}}$  state, i.e. as ferrocenyl units. The previous description of the core of **2** consisting of three layers (Fig. 2.11): one comprising a  $\text{Mn}^{\text{II}}_6$  hexagon with a central  $\text{Mn}^{\text{IV}}$  atom and  $\text{Mn}^{\text{III}}_3$  triangular layers above and below, implies for this molecule the coexistence of three different Mn oxidation states, as well besides oxygen ions with unusual  $\mu_5$  coordination: the core is held together by six  $\mu_5\text{-O}^{2-}$ , two  $\mu_3\text{-O}^{2-}$  and six  $\mu_3\text{-OMe}^-$  groups. Finally, the peripheral ligation is provided by six  $\mu_4\text{-fdc}^{2-}$  groups with *syn, syn, syn*  $\eta^1: \eta^1: \eta^1: \eta^1: \mu_4$  ligation mode. The torsion angle between the two carboxylate groups of the  $\text{fdc}^{2-}$  is less than  $30^\circ$ , accounting for a synperiplanar configuration<sup>134</sup>.

The six  $\text{Mn}^{\text{III}}$  ions have nearly octahedral coordination geometry with Jahn-Teller (JT) distortions, as expected for high-spin  $d^4$  ions. The distortion is typical in the fact that two *trans*-bonds are elongated and are the weaker among the six. The elongation is in fact observed along the axis containing the carboxylate ( $\mu_5\text{-O}^{2-}$ )–Mn–( $\mu_4\text{-fdc}^{2-}$ ) rather than two oxides ( $\mu_3\text{-O}^{2-}$ )–Mn–( $\mu_3\text{-O}^{2-}$ ) with an averaged difference of 0.262 Å. Such an arrangement is often seen in cluster chemistry, where the peripheral ligation can easily rearrange, while the core has a tendency of being more rigid, hence being less prone to distortions. The same arrangement of Mn ions in a cluster was first reported in 1996.<sup>135</sup> The packing diagram of the complex revealed a large presence of H- $\pi$  interactions involving the H atoms of the cyclopentadienyl rings with the  $\pi$  electron cloud of

cyclopentadienyl rings on adjacent molecules (Fig. 2-12). These interactions very likely contribute to the complete insolubility of the crystals in common solvents.

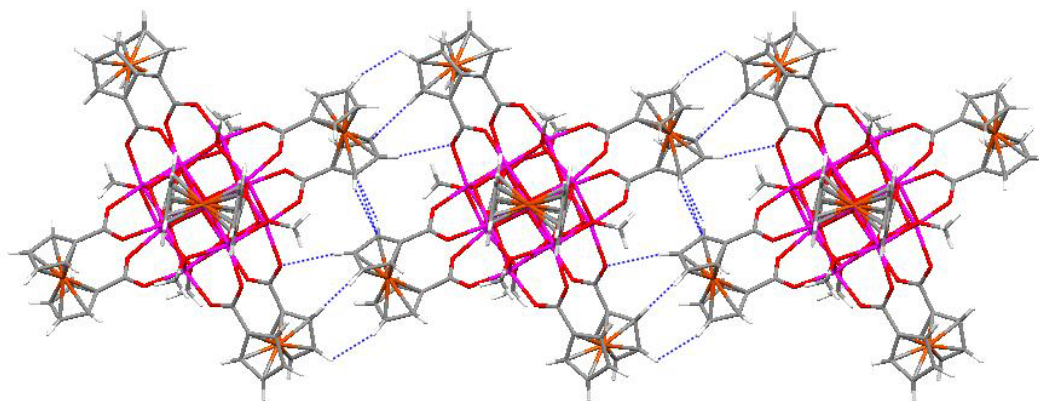


Figure 2-12. Packing diagram for complex **2** in Mercury<sup>136</sup>. The H- $\pi$  interactions between the molecules in the lattice are shown with dotted lines.

**[Mn<sub>8</sub>O<sub>4</sub>(fdc)<sub>6</sub>(DMF)<sub>2</sub>(H<sub>2</sub>O)<sub>2</sub>] $\cdot$ 4DMF $\cdot$ 4H<sub>2</sub>O; (**4**) $\cdot$ 4DMF $\cdot$ 4H<sub>2</sub>O**

Fig. 2-13 and 2-14 show Pov-Ray projections of complex **4** and its core respectively. Table 2-3 presents the main crystallographic data and structure refinement details. The complex crystallizes in the monoclinic space group C2/c. The cluster contains a core comprising a central [Mn<sup>III</sup><sub>4</sub>( $\mu_4$ -O)<sub>4</sub>]<sup>4+</sup> cubane where each O<sup>2-</sup> ion is attached to a Mn<sup>II</sup> ion. The overall topology results from two concentric Mn<sub>4</sub> tetrahedra. The peripheral ligation is completed by six fdc units and four terminal positions are occupied by two DMF and two water molecules. BVS calculations were applied as in the case of the Mn<sub>13</sub> and allowed for the clear identification of the oxidation states of the various Mn ions. The inner Mn ions in the core were confirmed as Mn<sup>III</sup>, whereas all the external pentacoordinated ions were identified as Mn<sup>II</sup>. Overall the core is made of an inner Mn<sup>III</sup> tetrahedron and outer Mn<sup>II</sup> tetrahedron conferring to the core pleasant aesthetic properties for a virtual T<sub>d</sub> symmetry.

Table 2-3. Selected crystal data for complex 4·4DMF·4H<sub>2</sub>O (full data in Tab. B-2).

Parameter	Value
Empirical formula	C <sub>90</sub> H <sub>102</sub> N <sub>6</sub> Fe <sub>6</sub> Mn <sub>8</sub> O <sub>40</sub>
Formula weight, g mol <sup>-1</sup>	2682.40
Temperature, K	173(2)
Wavelength, Å <sup>a</sup>	0.71073
Crystal system	Monoclinic
Space group	C2/c
Unit cell dimensions, Å	a = 23.282(3), b = 19.331(3), c = 22.198(3)
Unit cell angles, deg	α = 90°, β = 97.885(3)°, γ = 90°
Volume, Å <sup>3</sup>	9896(3)
Z	4
ρ <sub>calc</sub> , g cm <sup>-3</sup>	1.660

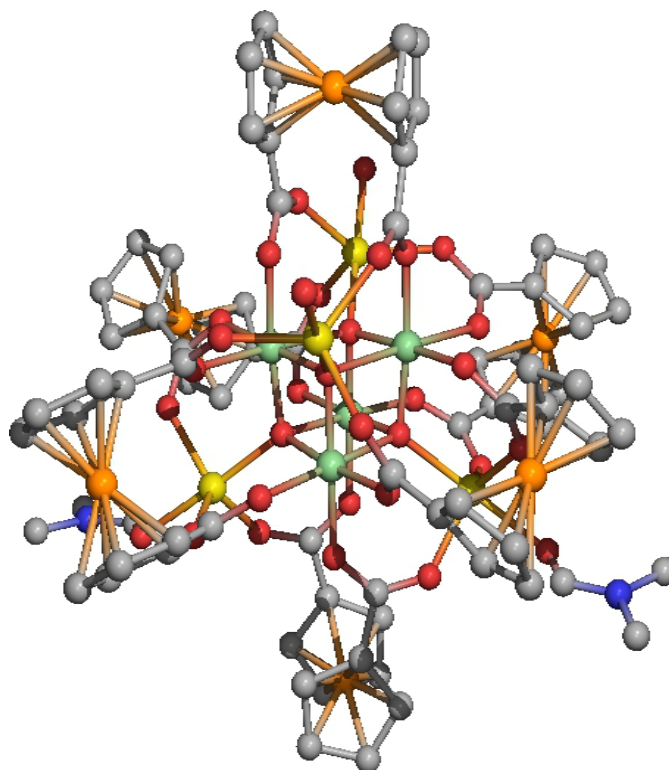


Figure 2-13. Pov-Ray projection of [Mn<sub>8</sub>O<sub>4</sub>(fdc)<sub>6</sub>(DMF)<sub>2</sub>(H<sub>2</sub>O)<sub>2</sub>]: Mn<sup>III</sup> light green, Mn<sup>II</sup> yellow, O red, Fe orange, N blue. Hydrogen atoms have been omitted for clarity.

The four Mn<sup>II</sup> ions are very close to a trigonal bipyramidal geometry with  $\tau$  values of 0.78 and 0.81 for Mn1 and Mn4 respectively.  $\tau$  is a parameter that quantitates the extent of distortion from a square pyramidal to trigonal bipyramidal geometry for a general ML<sub>5</sub> complex. If the two sets of trans ligands at the base of a square pyramidal

complex are called  $L_x$ ,  $L_x'$  and  $L_y$ ,  $L_y'$ , while the apical ligand is  $L_z$ , the largest basal angle is called  $\beta$  (for instance  $L_x$ -M- $L_x'$ ). After rearrangement<sup>137</sup>,  $\beta$  will become the axis of the trigonal bipyramid. The other basal angle in the square pyramidal configuration ( $L_y$ -M- $L_y'$ ) is called  $\alpha$ . The degree of structural distortion is obtained through the formula:  $\tau = (\beta - \alpha) / 60$ , where  $\tau$  is 0 for an ideal square pyramidal complex and increases to a maximum of  $\tau = 1$  for an ideal trigonal bipyramid geometry.<sup>138-139</sup>

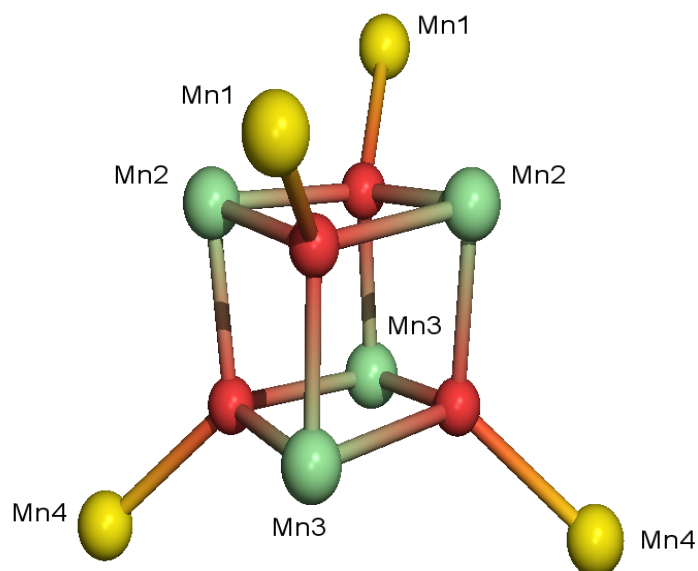


Figure 2-14. Pov-Ray projection of the core  $[\text{Mn}^{\text{III}}_4\text{Mn}^{\text{IV}}(\mu_4\text{-O})_4]^{12+}$  in **4**:  $\text{Mn}^{\text{III}}$  light green,  $\text{Mn}^{\text{II}}$  yellow, O red. The  $\text{Mn}^{\text{II}}$  ions (Mn1, Mn4) are fixed at the corners of a tetrahedron that includes a smaller tetrahedron of  $\text{Mn}^{\text{III}}$  ions (Mn2, Mn3).

Results of the BVS calculations are shown in Table 2-4.

Table 2-4. Bond Valence Sum calculations for complex **4**.

Atom	$\text{Mn}^{\text{II}}$	$\text{Mn}^{\text{III}}$	$\text{Mn}^{\text{IV}}$
Mn1	2.113 *	1.949	1.912
Mn2	3.284	3.028 *	2.972
Mn3	3.240	2.990 *	2.937
Mn4	2.162 *	1.994	1.956

The number with an asterisk is the one closest to the actual charge for which it was calculated, and the nearest whole number to it is the oxidation state of that atom.

The four  $\text{Mn}^{\text{III}}$  ions show Jahn-Teller distortion, as expected, with axial elongations of 0.265Å and 0.451Å for Mn3 and Mn2, respectively, compared with the compressed

axes. The four Jahn-Teller axes on the cluster are arranged nearly parallel with respect to each other. The coordination around the core consists of six  $\text{fdc}^{2-}$  groups. As in the case of complexes **2** and **3**, it is possible to infer the charge of the ferrocenyl units by charge balance. Each carboxylate group of an  $\text{fdc}^{2-}$  bridges a  $\text{Mn}^{\text{II}}/\text{Mn}^{\text{III}}$  pair adopting the same syn, syn,  $\eta^1: \eta^1: \mu_4$ -coordination mode seen in complex **2**. The peripheral ligation is completed by O-bound DMF molecules for two of the four  $\text{Mn}^{\text{II}}$  ions and water for the remaining two  $\text{Mn}^{\text{II}}$ . The torsion angles between the two carboxylate groups of the  $\text{fdc}^{2-}$  units vary: four  $\text{fdc}^{2-}$  groups have torsion angles of  $<30^\circ$  (synperiplanar configuration) and the other two have angles between  $30^\circ$  and  $90^\circ$  (synclinal configuration).<sup>134</sup> The packing diagram of **4** also shows the presence of H- $\pi$  interactions among the ferrocenyl units belonging to adjacent clusters (Fig. 2-15). As for  $[\text{Mn}_{13}\text{O}_8(\text{OMe})_6(\text{fdc})_6]$ , complex **4** is very insoluble, and the H- $\pi$  interactions likely contribute significantly to the lattice stabilization.

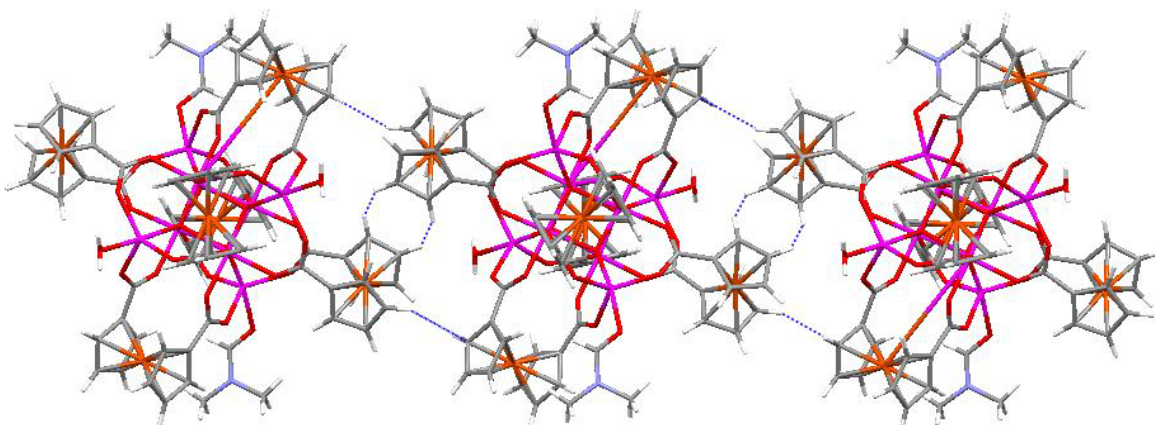


Figure 2-15. Packing diagram for complex **4** in Mercury<sup>136</sup>. Three molecules are shown along with dotted lines indicating some of the H- $\pi$  intermolecular interactions.

#### **$[\text{Mn}_8\text{O}_4(\text{fdc})_6(\text{DMF})_4]\cdot 4\text{DMF}$ ; (**5**)-4DMF**

The crystallographic structure of complex **5** is analogous to that of **4** with respect to the core description and main ligation. The only major difference is in the peripheral

presence of four O-bound DMF molecules, instead of two DMF and two water molecules. The terminal DMF molecule directly bound to the Mn6 ion is disordered with one water molecule, and the latter appears 30% of time. Crystallographic data is listed in Tab. 2-5. The structure underwent full refinement, but without the creation of complete crystallographic tables. The cluster also shows a lowered symmetry in that it crystallizes in the P2<sub>1</sub>/c space group and all the Mn ions are thus crystallographically inequivalent. Fig. 2-16 shows the core of **5** and its superposition with the core of **4**. The central cubanes are essentially superimposable, but there are some small differences in the angles to the external Mn<sup>II</sup>.

Table 2-5. Selected crystal data for complex **5**-4DMF (full data in Tab. B-3).

Parameter	Value
Empirical formula	C <sub>96</sub> H <sub>104</sub> N <sub>8</sub> Fe <sub>6</sub> Mn <sub>8</sub> O <sub>36</sub>
Formula weight, g mol <sup>-1</sup>	2720.49
Temperature, K	173(2)
Wavelength, Å <sup>a</sup>	0.71073
Crystal system	Monoclinic
Space group	P2 <sub>1</sub> /c
Unit cell dimensions, Å	a = 24.015(2), b = 14.865(14), c = 29.558(3)
Unit cell angles, deg	α = 90°, β = 101.088(5)°, γ = 90°
Volume, Å <sup>3</sup>	10354.5(3)
Z	4
ρ <sub>calc</sub> , g cm <sup>-3</sup>	1.745

BVS calculations confirmed the oxidation state of the various Mn ions and the values are reported in Table 2-6. The Mn<sup>III</sup> ions in clusters **4** and **5** display the common Jahn-Teller distortion with axial elongation, where the axes are nearly parallel to each other. These distortions cause the two faces of the inner cubanes perpendicular to the elongation axis to be nearly rhombic (sides of equal length), whereas the remaining four faces on each of the two cubanes are deformed close to a rhomboidal shape (opposite sides of equal length).

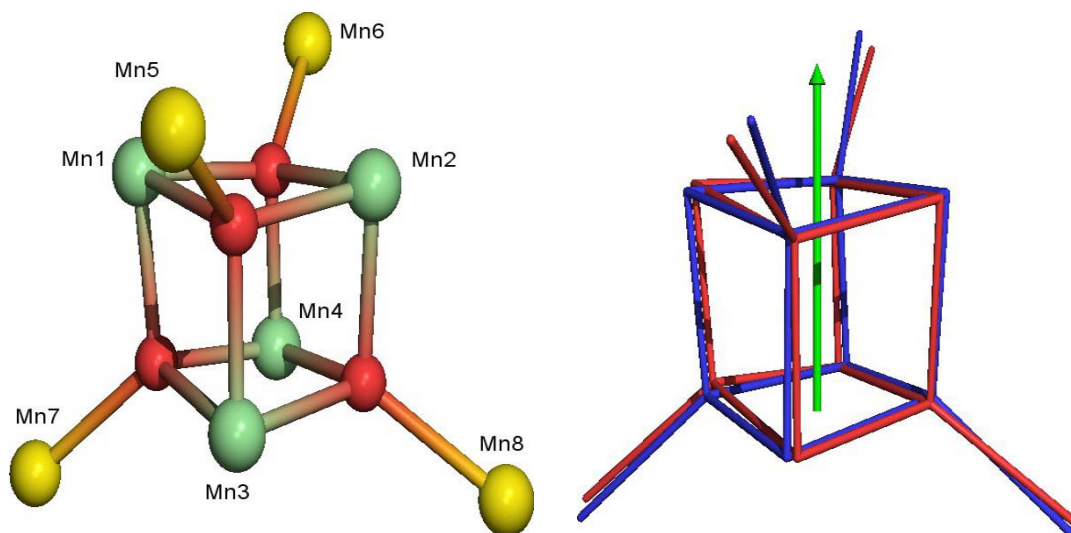


Figure. 2-16. Left: Pov-Ray projection of complex **5** core: Mn<sup>III</sup> light green, Mn<sup>II</sup> yellow, O red. Right: structural overlap of the two cluster cores **4** and **5**. The green arrow indicate the direction for the Jahn-Teller elongation.

Table 2-6. Bond Valence Sum calculations for complex **5**.

Atom	Mn <sup>II</sup>	Mn <sup>III</sup>	Mn <sup>IV</sup>
Mn1	3.344	3.083 *	3.026
Mn2	3.341	3.081 *	3.023
Mn3	3.434	3.167 *	3.107
Mn4	3.407	3.142 *	3.083
Mn5	2.086 *	1.923	1.887
Mn6	2.097 *	1.934	1.897
Mn7	2.077 *	1.915	1.879
Mn8	2.087 *	1.924	1.888

The number with an asterisk is the one closest to the actual charge for which it was calculated and the nearest whole number to it is the oxidation state of that atom.

The JT elongations for the Mn<sup>III</sup> ions are 0.589, 0.620, 0.602 and 0.540 Å for Mn1, Mn2, Mn3, and Mn4, respectively, compared to the compression axes. These values are significantly higher if compared than those observed for the Mn3 values in **4**. Another peculiarity of cluster **5** is with respect to the geometry of its Mn<sup>II</sup> ions. In fact, only the Mn6 and Mn7 compare to the ones found in complex **4**, with  $\tau$  values of 0.84 and 0.74 (hence close to a trigonal bipyramid). Mn5 and Mn8 on the contrary, show much smaller  $\tau$  values of 0.22 and 0.54 respectively (hence closer to a square pyramid). The coordination and disposition of the  $\text{fcd}^{2-}$  units is almost unchanged as compared to

**4**, although differences in the ferrocenyl torsion angles reflect the distortion of the cluster core. There is one  $\text{fdc}^{2-}$  ligand above each face of the inner  $\text{Mn}^{\text{III}}$  cubane and the  $\text{fdc}^{2-}$  keeps both carboxylate units nearly parallel while binding two metal ions on that cubane face. The torsion angle of the ligand units is a consequence of the coordination  $\text{M1-O-(O'C-fc-CO)-O'-M2}$  while satisfying the M1-M2 distance on the same cubane face. According to this analysis, the smaller torsion angle ( $\sim 29^\circ$ ) is found for both **4** and **5** on the  $\text{fdc}^{2-}$  units above the nearly rhombic faces of the cubane. The remaining faces are more distorted from an idealized square or rhombic geometry, requiring slightly larger  $\text{fdc}^{2-}$  torsion angles ( $\sim 30^\circ$  and  $\sim 36^\circ$ ). A comparison of the torsion angles on the two molecular systems reveals differences of only a few degrees, nonetheless these differences are significant. The molecular lattice shows H- $\pi$  interactions analogous to **4**, but to a lesser extent. In this case, the terminal DMF molecules have a larger contribution in establishing contacts with neighboring molecules. Some of the intermolecular interactions in **5** are shown in Fig. 2-17 where as for the  $\text{Mn}_{13}$  cluster hydrogen atoms from a ferrocenyl unit interact with the electronic cloud of another ferrocenyl group.

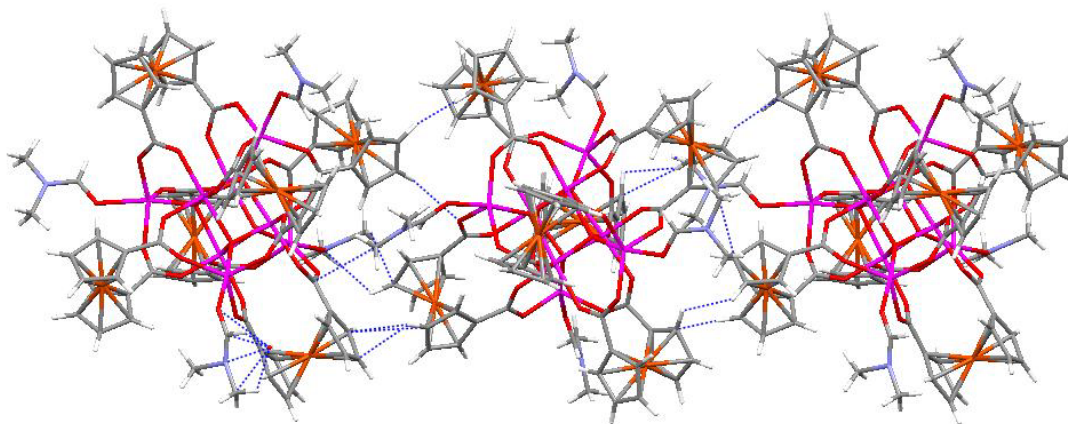


Figure 2-17. Packing diagram of complex **5** in Mercury<sup>136</sup>. Dotted lines indicate some of the H- $\pi$  interactions in the lattice.

## Magnetochemistry

**[Mn<sub>13</sub>O<sub>8</sub>(OMe)<sub>6</sub>(fdc)<sub>6</sub>]·4H<sub>2</sub>O·3MeOH; (2)·4H<sub>2</sub>O·3MeOH and  
[Mn<sub>13</sub>O<sub>8</sub>(OEt)<sub>6</sub>(fdc)<sub>6</sub>]·7EtOH; (3)·7EtOH**

Variable-temperature DC susceptibility measurements were performed in the 5.0 to 300 K range on powdered microcrystalline samples of complexes **2** and **3**. The microcrystals were embedded in eicosane to prevent torquing after the application of magnetic field. This experiment requires the use of a constant field which was set at 1.0 kG (0.1 T); (Fig. 2-18). The data for complexes **2** and **3** are nearly superimposable with an initial value of  $\sim 47 \text{ cm}^3\text{Kmol}^{-1}$  at 300 K that steadily decreases to  $\sim 11.5 \text{ cm}^3\text{Kmol}^{-1}$  at 5 K. This profile indicates predominant antiferromagnetic interactions among the Mn ions within the cluster. It should be noted that the diamagnetic ferrocenyl units do not have any contribution to the magnetic properties these clusters, as indicated in the crystal structures. The high nuclearity of these clusters prevent fitting of the data by matrix diagonalization to obtain the individual exchange parameters.

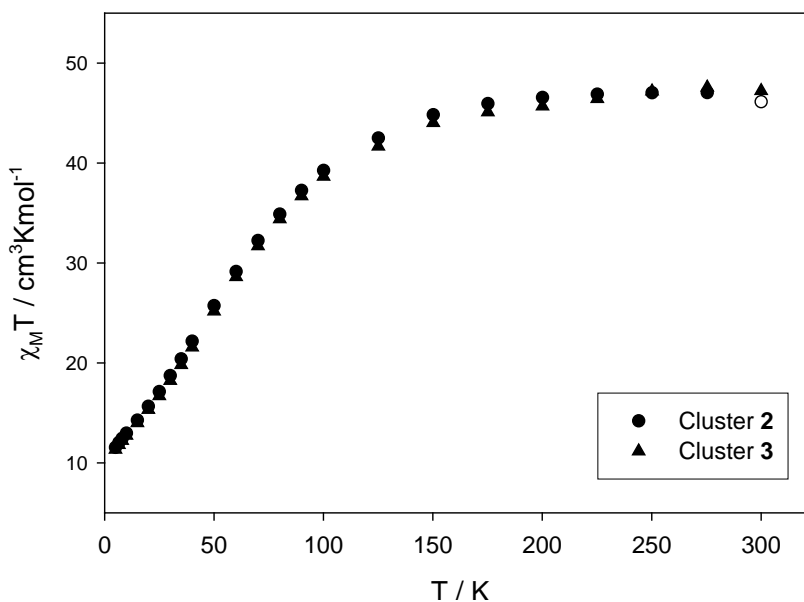


Figure 2-18. Plot of  $\chi_M T$  vs. T for complex **2**·4H<sub>2</sub>O·3MeOH (●) and complex **3**·7EtOH (▲).

Also the Kambe equivalent operator method<sup>32</sup> can not be applied for this case. However, the ground-state spin ( $S$ ) of the complexes was determined by two independent methods: fitting of the variable-temperature ( $T$ ) and variable-field ( $H$ ) DC magnetization data, and extrapolation to low temperature of the AC susceptibility measurements (Fig. 2-19). DC magnetization data were collected in the 1.8-10.0 K range in fields varying between 0.1 and 7 T and fit using the program MAGNET<sup>140</sup> to a model that assumes exclusive population of the ground state.

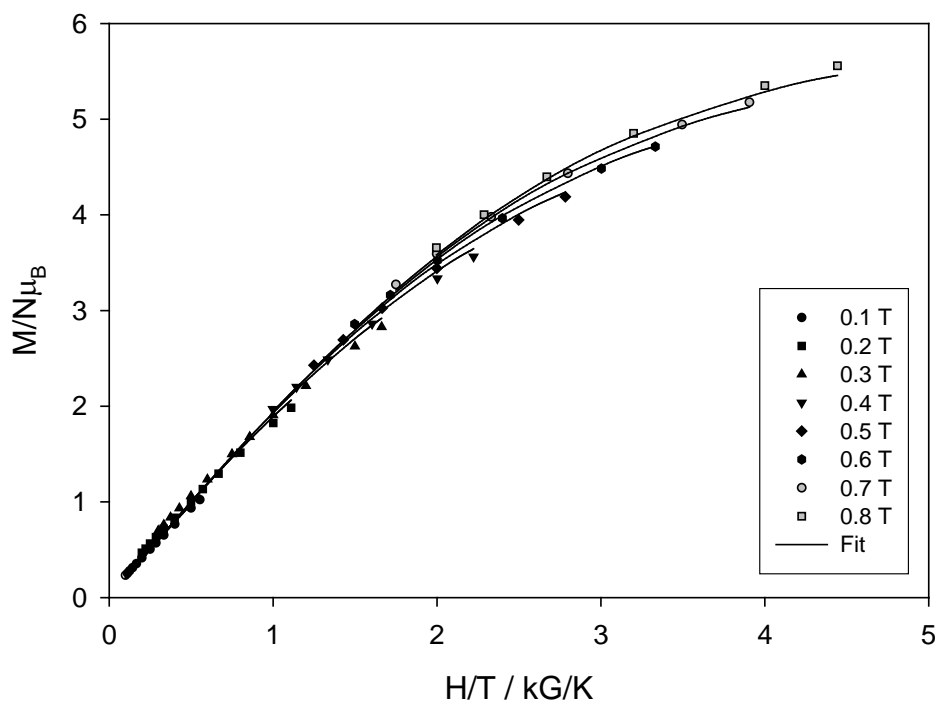


Figure 2-19. Plot of reduced magnetization ( $M/N\mu_B$ ) vs.  $H/T$  for a sample of  $3 \cdot 7\text{EtOH}$ .

The analysis includes axial zero-field splitting ( $\hat{S}_z^2 D$ ) and the Zeeman effect ( $g\mu_B\mu_0\hat{S}\cdot H$ ), and incorporates a full powder average. A good fit could not be obtained using all data up to 7 T. This is typically the observed when there are low-lying excited states. One way to avoid this problem is to use only data collected in small fields. In this case, a satisfactory fit was obtained using only data up to 0.8 T (solid lines in Fig. 2-19).

The ground-state spin  $S$  for complex **3** was found to be  $9/2$ , with a  $g$  and  $D$  value of  $1.91 (\pm 0.10)$  and  $-0.23 (\pm 0.05) \text{ cm}^{-1}$ , respectively.

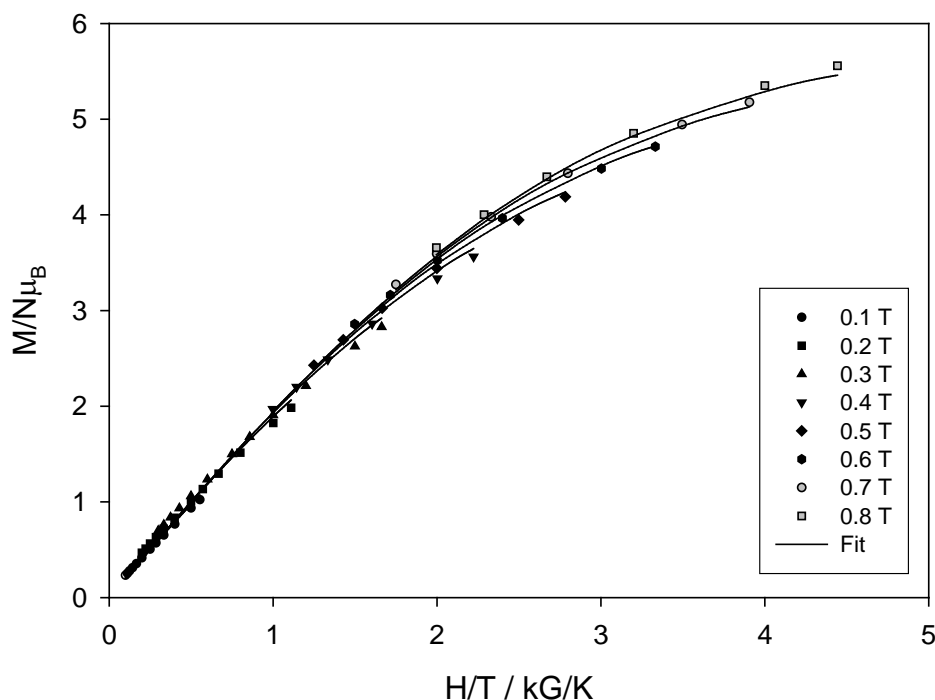


Figure 2-19. Plot of reduced magnetization ( $M/N\mu_B$ ) vs.  $H/T$  for a sample of **3**·7EtOH.

To assess the precision of the fit parameters, the root-mean square error surface for the fit was generated as a function of  $g$  and  $D$  using the program GRID.<sup>141</sup> The obtained error surface is depicted in Fig. 2-20 as a convenient 2-D contour plot, and the absolute minimum is the best-fit estimation of  $g$  and  $D$ . The nature of the minimum in the error surface reflects the precision of the fit parameters. Hence, a poorly defined and "soft" minimum will be correlated with large errors in the estimated  $g$  and  $D$  fit values. Estimation of  $\pm 0.10$  and  $\pm 0.05$  for the absolute error in  $g$  and  $D$ , respectively, is a safe assumption. Another method to estimate the ground state  $S$  value for **3** is to measure the AC response of a sample in a particular temperature range, in this case 1.8 to 15.0 K using a 3.5 G AC field oscillating at 50, 250 and 997 Hz. AC

measurements are performed in the absence of a DC field, and can thus avoid complication from low-lying excited states as expected for **3**.

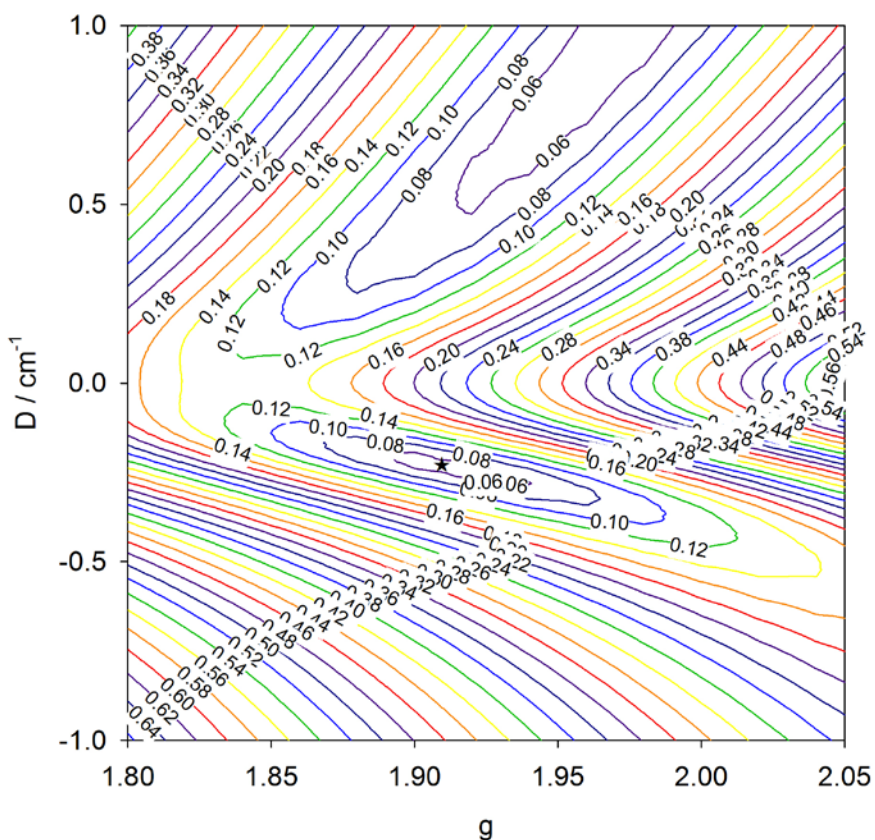


Figure 2-20.  $g$  vs.  $D$  error surface for the  $m/N\mu_B$  vs.  $H/T$  fit for **3**·7EtOH. The numbers indicate the magnitude of the error and slowly decrease on moving towards the absolute minimum, marked with a star.

The real, or in-phase, AC susceptibility ( $\chi_M'$ ) of the complex is plotted as  $\chi_M'T$  vs.  $T$  in Fig. 2-21. Extrapolation of the  $\chi_M'T$  to 0 K, from temperatures above  $\sim 4$  K (to avoid the effects of weak intermolecular interactions) gives a value of  $\sim 10.5 \text{ cm}^3\text{Kmol}^{-1}$ . This value indicates a ground state of  $9/2$  for this cluster, and  $g \leq 2$ , as expected for Mn, in agreement with the DC magnetization fits. Data for complex **2** are similar to those for complex **3**. The alternating current out-of-phase data down to 1.8 K for complexes **2** and **3** show no out-of-phase  $\chi_M''$  AC signals that would indicate the slow relaxation of the magnetization vector (Fig. 2-22). To explore whether slow relaxation might be seen at

even lower temperatures, single crystals were measured using a micro-SQUID apparatus down to 0.04 K with the precaution of leaving the crystals in the mother liquor up to the measure to prevent solvent loss.<sup>142</sup> Magnetization vs. DC field measurements were performed at different temperatures and at various field scan rates (Fig. 2-23).

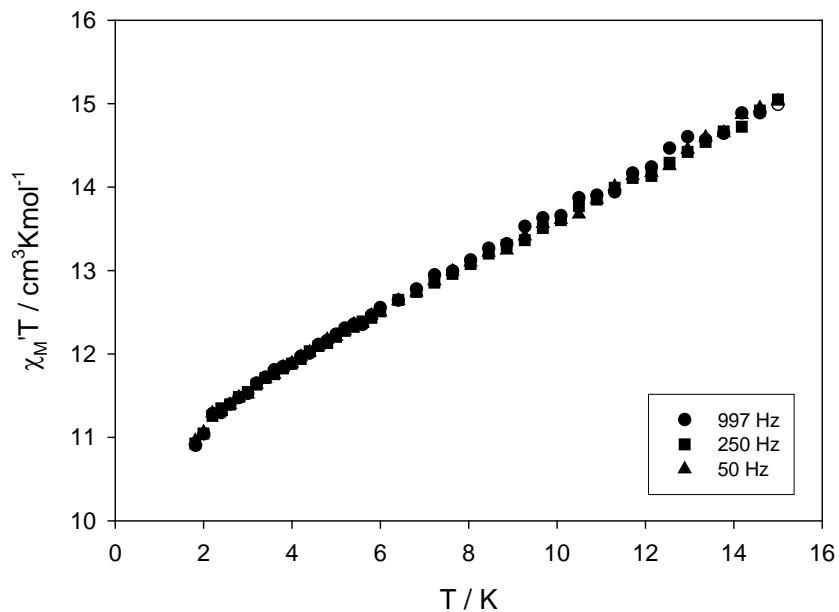


Figure 2-21. Plot of  $\chi_M' T$  vs. T for complex **3**·7EtOH.

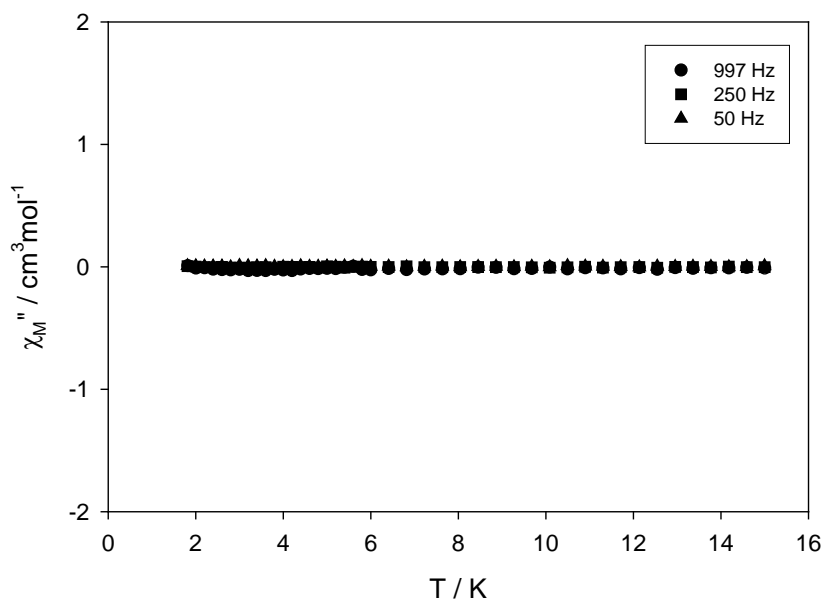


Figure 2-22. Plot of  $\chi_M''$  vs. T for complex **3**·7EtOH in the 1.8-15 K.

The absence of hysteresis indicates the absence of a significant barrier to the relaxation even at 0.04 K. The similar behavior for the two species **2** and **3**, isomeric with respect to the core, but with a different set of peripheral alkoxides suggests very poor influence of the alkoxides in the coupling patterns. This argument may be extended to the hysteresis measurement in expecting the same type of behavior for both **2** and **3**.

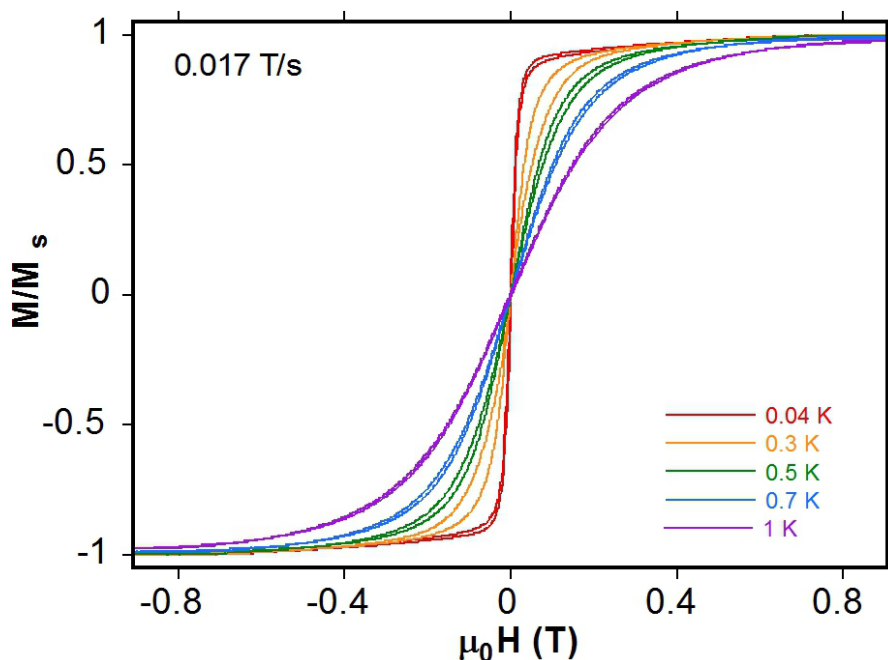


Figure 2-23. Hysteresis measures for complex **2**·8CH<sub>2</sub>Cl<sub>2</sub> in the 0.04-1 K range.

**[Mn<sub>8</sub>O<sub>4</sub>(fdc)<sub>6</sub>(DMF)<sub>2</sub>(H<sub>2</sub>O)<sub>2</sub>]·4DMF·4H<sub>2</sub>O; (**4**)·4DMF·4H<sub>2</sub>O**

A microcrystalline sample of **4**·4DMF·4H<sub>2</sub>O was embedded in eicosane and its magnetic behavior was investigated as previously discussed for complexes **2** and **3** (*vide supra*). Variable-temperature DC susceptibility measurements were performed leading to the plot shown in Fig. 2-24. The  $\chi_M T$  profile for complex **4**·4DMF·4H<sub>2</sub>O remains almost unchanged with decreasing temperature after starting at about 15 cm<sup>3</sup>Kmol<sup>-1</sup>. The data fluctuate slightly before reaching a final value of 13.64 cm<sup>3</sup>Kmol<sup>-1</sup>

at 5.00 K. The overall decrease of susceptibility is indicative of predominant antiferromagnetic interactions among the Mn ions within the cluster consistent with depopulation of excited states of higher spin (i.e.: with larger ferromagnetic presence). The contribution of the Fe<sup>II</sup> ions to the magnetism has been disregarded, since the electron exchange rate between the Fe<sup>II</sup> ions and the core is expected to be negligible.<sup>110</sup>

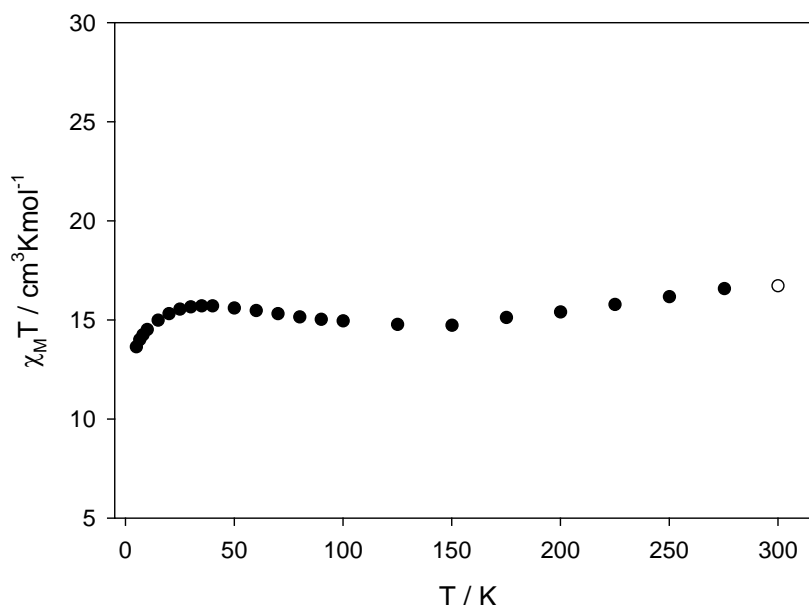


Figure 2-24. Plot of  $\chi_M T$  vs.  $T$  for complex **4**·4DMF·4H<sub>2</sub>O.

The complexity of the structure despite the relatively high symmetry also compared to the previous Mn<sub>13</sub> clusters, again prevents application of the Kambe vector type of approach to determine the various coupling patterns. Fitting of the variable-temperature ( $T$ ) and variable-field ( $H$ ) DC magnetization data, and AC susceptibility measurements were therefore employed to determine the ground-state spin. The reduced magnetization data was acquired using the methods previously described for **2** and **3** by fitting of the data with Magnet<sup>136</sup> (Fig 2-25).

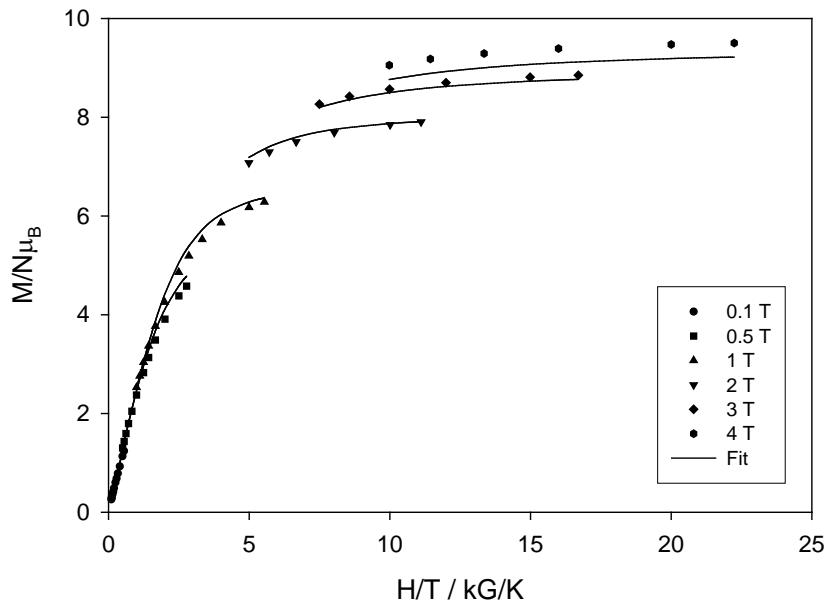


Figure 2-25. Plot of reduced magnetization ( $M/N\mu_B$ ) vs.  $H/T$  for **4**·4DMF·4H<sub>2</sub>O.

In the fit of reduced magnetization (RM) data vs.  $H/T$ , data collected in fields up to 4 T were used for the fit, suggesting a ground state better isolated from excited states than for **2** and **3**. The fit suggests a spin ground-state  $S = 5$  with  $g$  and  $D$  parameters of  $1.97 (\pm 0.10)$  and  $-0.32 (\pm 0.05) \text{ cm}^{-1}$ , respectively. The precision of the fit has been estimated by the error on the magnetization as a surface function of  $g$  and  $D$ . Fig. 2.26 shows the 2-D contour plot of this surface where a well-isolated absolute minimum appears in the region about the  $g$  and  $D$  values obtained with the program MAGNET. As for complexes **2** and **3**, it is safe to estimate the error on  $g$  and  $D$  as  $\pm 0.10$  and  $\pm 0.05 \text{ cm}^{-1}$ , respectively. Alternate current measurements on a sample of **4** were taken following the same procedure described previously for **2** and **3**. The in-phase component of the susceptibility,  $\chi_M T$ , shows a monotonic decrease with lowering of the temperature suggesting depopulation of excited states of higher spin with respect to the ground state (Fig. 2-27). A non-linear decrease with lowering the temperature may also be due to weak intermolecular interactions.

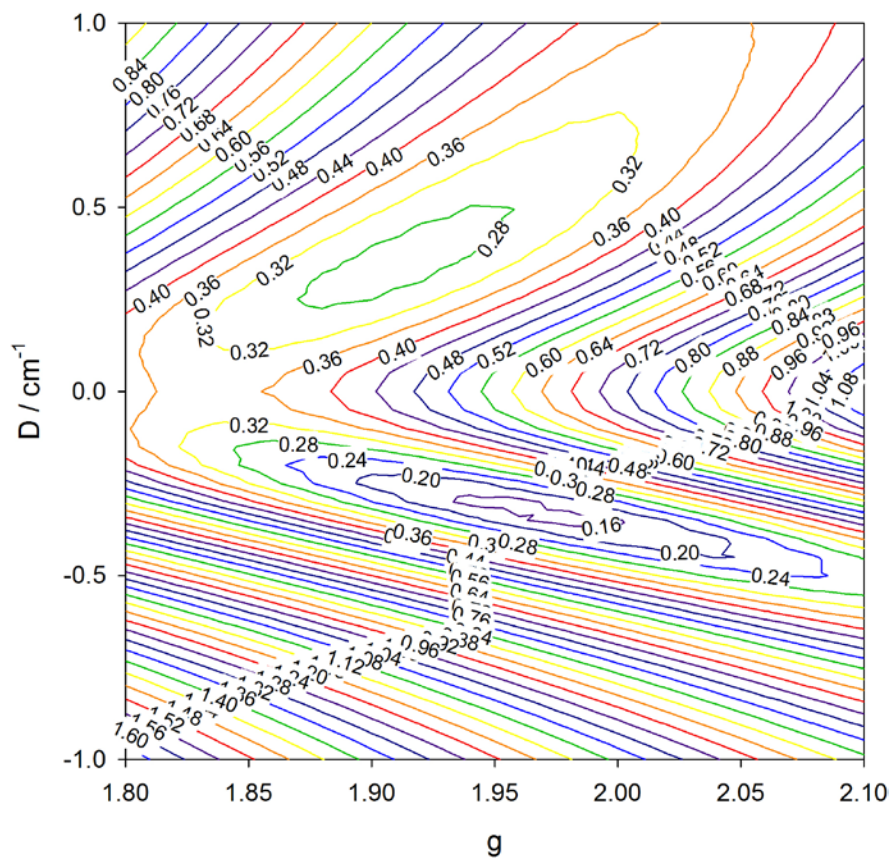


Figure 2-26. Error plot for the estimation of  $g$  and  $D$  in  $4 \cdot 4\text{DMF} \cdot 4\text{H}_2\text{O}$ . The numbers indicate the magnitude of the error, which slowly decreases moving towards the absolute minimum, marked with an asterisk.

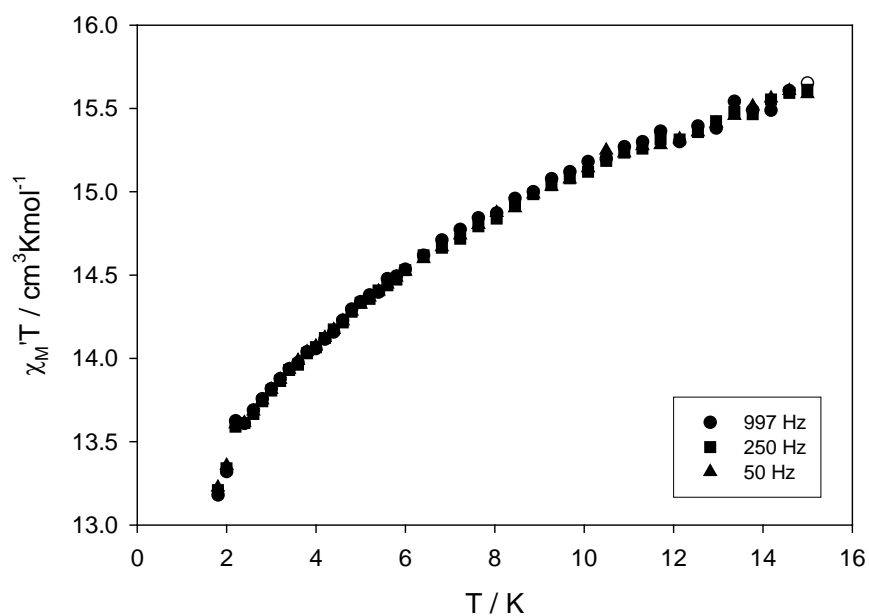


Figure 2-27. Plot of  $\chi_M T$  vs.  $T$  for complex  $4 \cdot 4\text{DMF} \cdot 4\text{H}_2\text{O}$  in the 1.8-15 K.

The initial  $\chi_M T$  value of  $\sim 15.6 \text{ cm}^3 \text{Kmol}^{-1}$  at 15 K reaches  $\sim 13.7 \text{ cm}^3 \text{Kmol}^{-1}$  at 2.2 K with a nearly linear progression. At lower temperatures, the  $\chi_M T$  value has a sudden drop reaching  $\sim 13.2 \text{ cm}^3 \text{Kmol}^{-1}$  at 1.8 K. The sharp decrease is due to slow relaxation of the magnetization vector by partial transfer of the in-phase susceptibility component to the out-of-phase. In extrapolating the  $\chi_M T$  value to 0 K for the estimation of the ground state, the region where slow relaxation occurs should be avoided as well as data generally at higher temperature up to  $\sim 6$  K because potentially it is affected by intermolecular interactions. The plot suggests a  $\chi_M T$  of  $\sim 13.8 \text{ cm}^3 \text{Kmol}^{-1}$  at 0 K for which it corresponds a spin ground-state  $S = 5$  with  $g = 1.92$ . This is a reliable estimation considering that the immediately neighboring integer values of  $S$  (i.e., 4 and 6) would lead to unacceptable values of  $g$  for a Mn-oxide compound. The AC in-phase data are hence confirming the  $S = 5$  ground state for **4** as suggested by the reduced magnetization data. As expected from the profile of the in-phase magnetic susceptibility vs.  $T$  plot, the out-of-phase data display an increase in magnitude from zero at the lower end of the selected temperature range (Fig. 2-28). The  $\chi_M''$  vs.  $T$  plot shows tails of out-of-phase peaks consistent with the sudden drop in the  $\chi_M T$  between 2.2 and 1.8 K. A process of slow relaxation of the magnetization is also consistent with the appearance at higher temperatures for the out-of-phase components  $\chi_M''$  detected at a higher frequency of the oscillating field. Further investigation of this phenomenon requires lower temperatures and a micro-SQUID. Magnetization versus DC fields were measured on a single crystal to verify if the slow relaxation of the magnetization detected below  $\sim 2.5$  K may lead to hysteresis that displays temperature and scan rate dependence (Fig. 2-29), i.e. if **4** is a single-molecule magnet. The scanning of the

magnetization vs. applied field at different temperatures with a fixed scan rate produced the plot in Fig. 2.29 where it is evident some hysteresis occurs below 2 K. Most importantly there is an increase of the coercivity with the decreasing temperature; one of the diagnostic features of a single-molecule magnet.

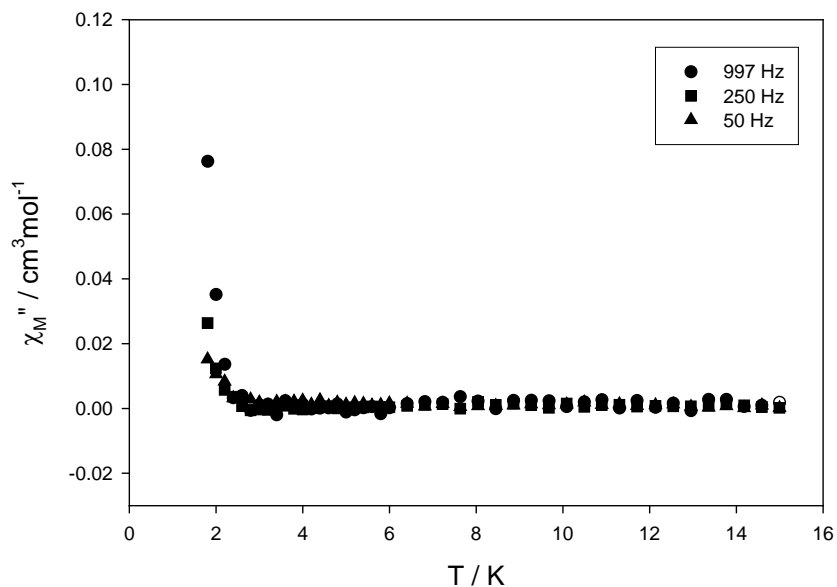


Figure 2-28. Plot of  $\chi_M''$  vs.  $T$  for complex  $4 \cdot 4\text{DMF} \cdot 4\text{H}_2\text{O}$  in the 1.8-15 K.

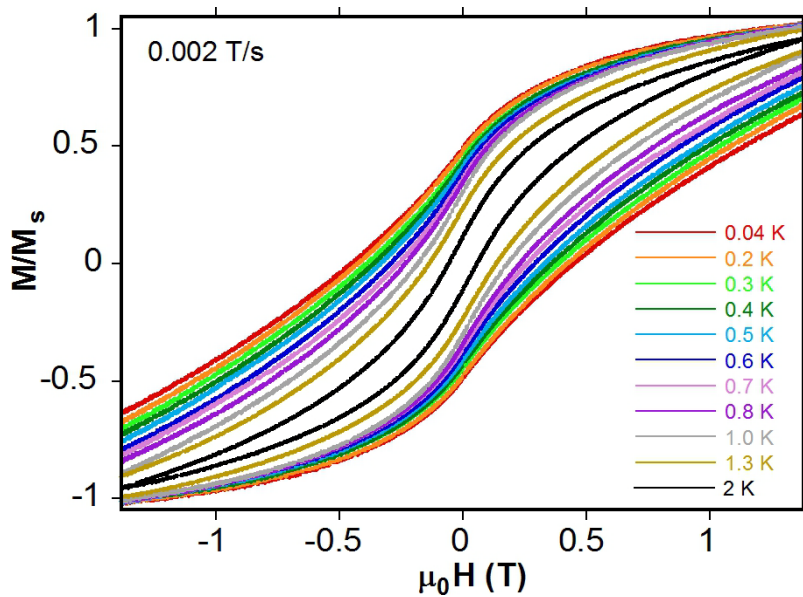


Figure 2-29. Hysteresis measures for complex  $4 \cdot 4\text{DMF} \cdot 4\text{H}_2\text{O}$  in the 0.04-1 K.

**[Mn<sub>8</sub>O<sub>4</sub>(fdc)<sub>6</sub>(DMF)<sub>4</sub>·1.5DMF·3H<sub>2</sub>O; (5)·1.5DMF·3H<sub>2</sub>O**

Complex **5** was studied under the same conditions as compound **4**. DC measurements for a microcrystalline sample of **5** show a monotonically decreasing value of  $\chi_M T$  with decreasing temperature (Fig. 2-30).

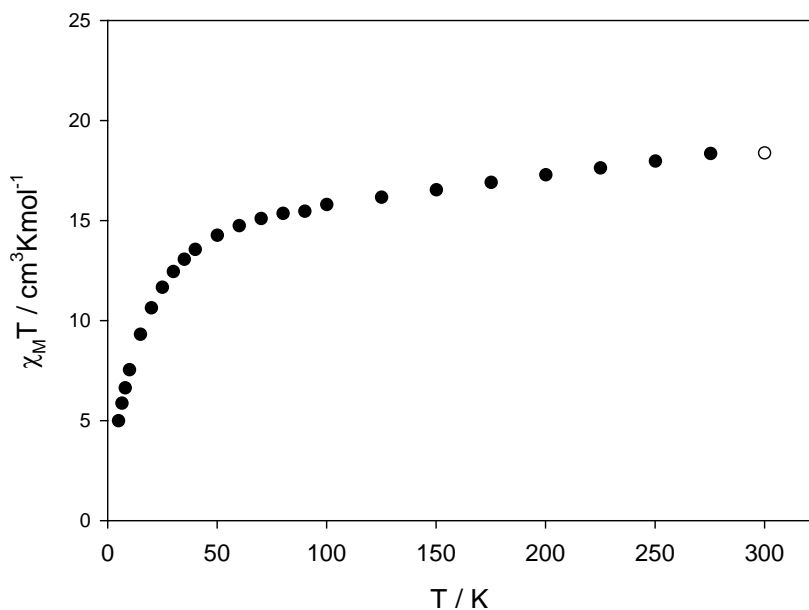


Figure 2-30. Plot of  $\chi_M T$  vs. T for complex **5**·1.5DMF·3H<sub>2</sub>O

From the initial  $18.64 \text{ cm}^3 \text{Kmol}^{-1}$  at room temperature,  $\chi_M T$  has a slow and steady decrease up to ~80 K, from where it displays a more pronounced decline to the final point of  $4.99 \text{ cm}^3 \text{Kmol}^{-1}$  at 5 K. A reliable estimation of the ground state from the  $\chi_M T$  vs. T plot was not possible due to the steep decrease of the data in the low-temperature region. It is likely that the weak magnetic exchange interactions associated with the Mn<sup>II</sup> ions produce excited states close to the ground state. With the aim of assessing the ground state *S* of **5**, the program MAGNET<sup>140</sup> was used to attempt the fitting of reduced magnetization vs. H/T data. Unfortunately, the application failed at producing meaningful data for *g* and *D* with any combination of the measured fields in the 0.1 to 7

T. At this point, the estimation of  $S$  was based only on the AC in-phase data, measured in the same conditions as for complex **4** (Fig. 2-31).

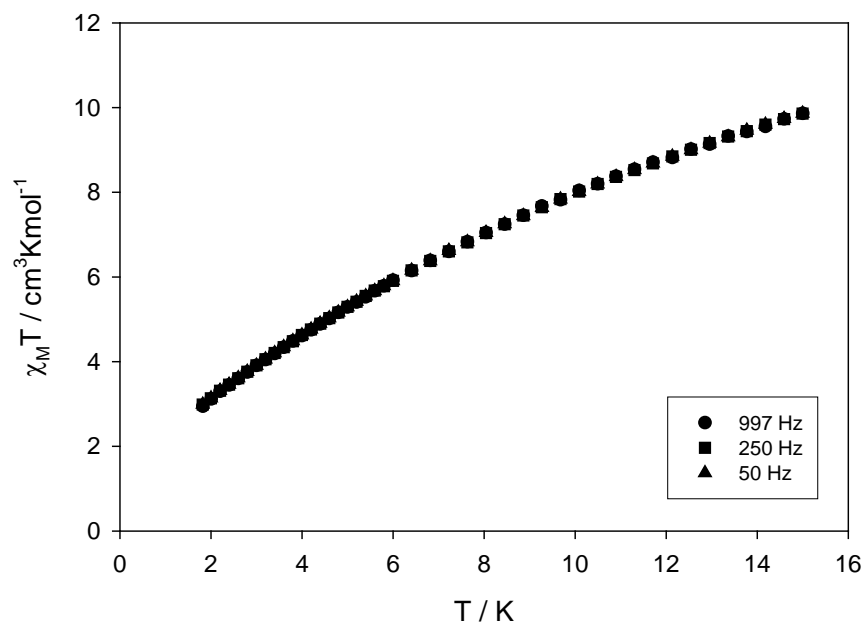


Figure 2-31. Plot of  $\chi_M T$  vs.  $T$  for complex **5**·1.5DMF·3H<sub>2</sub>O in the 1.8-15 K.

The plot of  $\chi_M T$  vs.  $T$  shows a decrease in susceptibility with almost constant progression up to the final point of  $2.98 \text{ cm}^3\text{Kmol}^{-1}$  at 1.8 K from the initial  $9.86 \text{ cm}^3\text{Kmol}^{-1}$  at 15 K. Extrapolation to 0 K from the data at higher temperature led to  $\sim 3 \text{ cm}^3\text{Kmol}^{-1}$ , suggesting of the spin ground-state  $S = 2$  ( $g = 2$ ) for complex **5**. The adjacent integer spins  $S = 3$  or  $1$  with respect to the ground state, respectively, are excluded due to the unacceptable  $g$  values implied being either too low or too high, respectively. The AC out-of-phase measurements do not indicate slow relaxation of the magnetization with decreasing temperature. However, the data points near 1.8 K suggest the beginning of a peak. It is possible that the molecule has a substantial magnetic anisotropy, but its spin ground-state is much lower than **4** and not large enough to create a sufficiently high barrier to the reorientation of the magnetic vector (See Fig. 2-32 and inset).

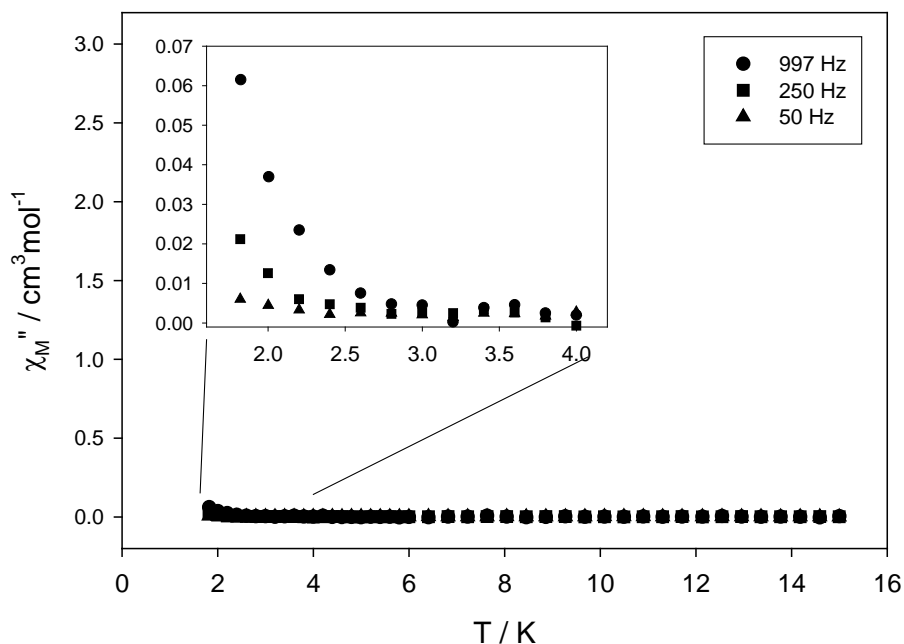


Figure 2-32. Plot of  $\chi_M''$  vs. T for complex **5**·1.5DMF·3H<sub>2</sub>O. The inset shows tails of peaks in the 1.8 to 4 K region.

Compounds **4** and **5** clearly exemplify how small differences in molecular structure can result in a large difference in magnetic behavior. As described in detail in the structure elucidation, **4** is slightly more symmetric than **5**, which contains two nearly square pyramidal Mn<sup>II</sup> ions, and a more asymmetrically distorted central cubane due to a stronger Jahn-Teller elongation. As previously mentioned, the unambiguous assessment of the magnetic exchange parameters for cluster **4** is prohibitive due to its high nuclearity and relatively low symmetry. The same applies to an even greater extent for complex **5** due to its lower symmetry with respect to **4**. For these reasons, only general conclusions about the different magnetic behavior of **4** and **5** can be made. Compounds **4** and **5** manifest magnetic differences beginning with the room temperature data of the  $\chi_M T$  vs. T (Fig. 2-33). According to the spin-only formula, both compounds should display a  $\chi_M T$  of  $\sim 29.5 \text{ cm}^3 \text{ K mol}^{-1}$  at 300 K accounting for the independent magnetic behavior of each metal ion.

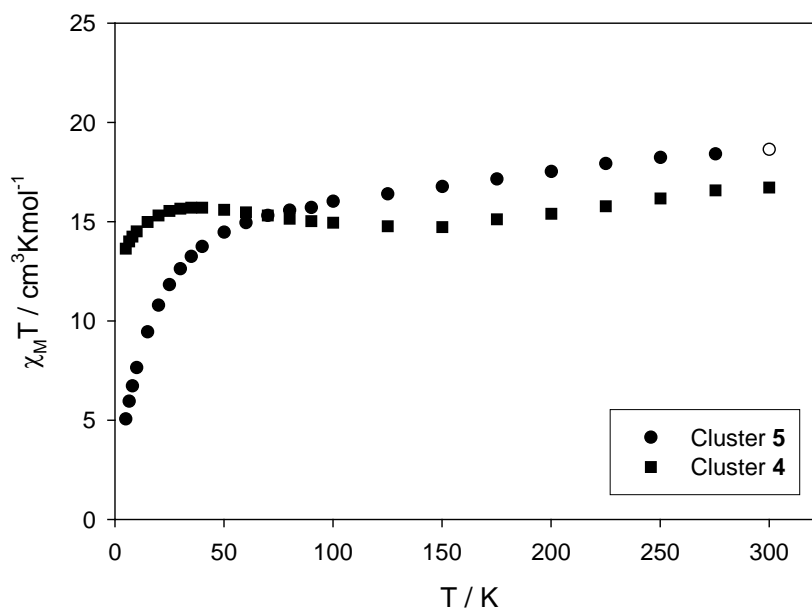


Figure 2-33. Superposition of the  $\chi_M T$  vs.  $T$  plots for **4**·4DMF·4H<sub>2</sub>O and **5**·3H<sub>2</sub>O·1.5DMF.

However, both possess significantly lower susceptibility values that imply strong antiferromagnetic couplings even at room temperature. As the temperature is lowered, both **4** and **5** behave similarly with a steady decrease in  $\chi_M T$  up to ~150 K. Below this point the two molecules diverge showing different  $\chi_M T$  vs.  $T$  profiles and ground state values. Magnetic studies on clusters have largely demonstrated how small variations of angles along magnetic exchange pathway or bond lengths can affect the magnitude of the magnetic interaction.<sup>143-145</sup> Hence, different  $J$  values are ultimately responsible for the different magnetic behavior of **4** and **5**.

### Electrochemistry

Compounds **2**, **3**, **4** and **5**, each have six ferrocenyl units bound to the core. This could result in the observation of multielectron transfer through cyclic voltammetry. The literature presents such a process for complex **2**.<sup>101</sup> The investigation was conducted in the solid state and the results were compared with the free ligand precursor  $\text{fdCH}_2$  (Fig.

2-34). The CV shows the oxidation of all the ferrocenyl units on the cluster occurring at the same potential. The authors explained this behavior by describing the cluster as an assembly of ferrocenyl units, which lack mutual electronic influence, so that the redox processes on each of them can be considered as an independent event. The authors also explain how a shift to a higher potential for the ferrocenyl units in the cluster is due to the electron-withdrawing effect exerted by the cluster's core with respect to the free ligand precursor. Solution-phase CV analysis for complexes **2**, **3**, **4** and **5** failed due to their low solubility in common non-aqueous media. No significant signals could be observed. This represents the main obstacle for CV investigation of these clusters.

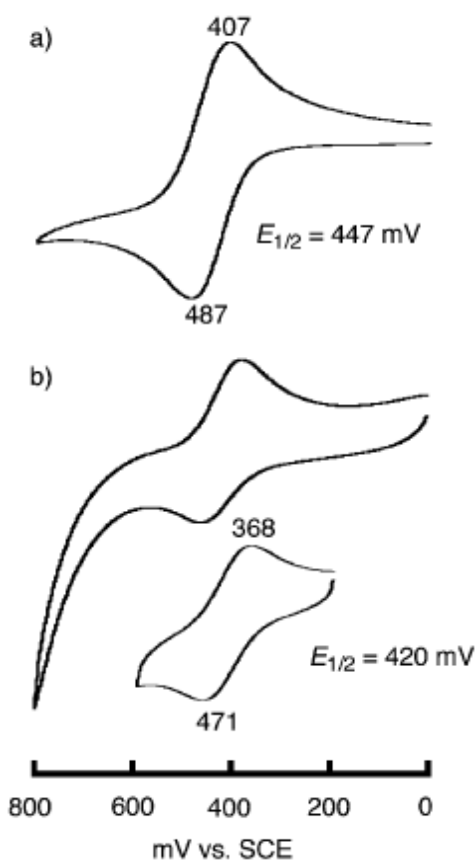


Figure 2-34. Solid-state voltammogram of (a) fdCH<sub>2</sub>, and (b) complex 2. The measurements are referenced against the standard calomel electrode (SCE) (reported from ref. 101, Reproduced by permission of The Royal Society of Chemistry, <http://dx.doi.org/10.1039/b210475j>).

Chemical oxidation of **2**, **3** and **4** was attempted in order to try to isolate the corresponding cationic species that may be more soluble. The presence of  $\text{fdc}^{2-}$  in the compounds discussed so far allows the possibility for the oxidation of one or more of these ferrocenyl units, leading to a net positive charge on the molecule. This is often an advantage for the dissolution of compounds in polar solvents. Common oxidizing agents like  $\text{Ce}^{\text{IV}}$  salts,  $(\text{NH}_4)_2\text{Ce}(\text{NO}_3)_6$  or  $\text{Ce}(\text{OH})_4$ , were added to a slurry of the compounds **2**, **3** or **4** in acetonitrile, benzonitrile, dimethylformamide or dimethylsulfoxide. In no case, did clean oxidation to a soluble species occur. Despite the discoloration of the solution with time (for  $\text{Ce}^{\text{IV}}$  to  $\text{Ce}^{\text{III}}$ ), there was no build up of a blue color from charged clusters in solution (ferricenyl units have intense blue color). To ensure a sufficient oxidizing strength, attempts were made with the use of a stronger oxidizing agent than for  $\text{Ce}^{\text{IV}}$  in MeCN (i.e.: lower reduction potential). The reagent of choice was as a triarylaminium radical cation,  $[\text{N}(\text{aryl})_3]^{\text{+}}$ . This type of oxidizing agent is widely used in organic chemistry and to a less extent for inorganic molecules. Substitution of the aryl positions with proper electron-withdrawing groups allows these cations to span a wide range of potentials.<sup>146</sup> The  $[\text{N}(\text{C}_6\text{H}_4\text{Br-2,4})_3]^{\text{+}}[\text{SbCl}_6]^{-}$  has a redox potential in MeCN of 1.14 V vs.  $\text{Fc}$ <sup>146-148</sup> and can be easily synthesized.<sup>149</sup> Unfortunately, even this oxidizing agent did not allow the isolation of the desired products. On the other hand, attempts to reduce one of the Mn ions on the core were also made using ferrocene as a mild reducing agent in acetonitrile. It has been demonstrated that  $\text{Fc}$  can reduce  $\text{Mn}^{\text{III}}$  ions in a metal cluster and act as a counter ion in the isolated product.<sup>150</sup> Several attempts with different solvents and counterions did not lead to the expected results. In all cases the substrate remained unreacted.

## Summary and Conclusions

It was hoped that 1,1'-ferrocenedicarboxylic acid would lead to many new  $Mn_x$  products when employed in cluster chemistry, but with few exceptions the results have been disappointing. The reaction with preformed  $[Mn_{12}O_{12}(O_2CMe)_{16}(H_2O)_4] \cdot 4H_2O \cdot 4MeCO_2H$  has led to the isolation of new polynuclear  $Mn_{13}$  clusters. Although complexes **2** and **3** are based on a core already known in the literature,  $[Mn^{IV}Mn^{III}_6Mn^{II}_6(\mu_5-O)_6(\mu_3-O)_2(\mu_3-OMe)_6]^{12+}$ , the two clusters have been synthesized differently from the published work<sup>101</sup>, and a more detailed study of its synthesis and physicochemical properties has been reported. Furthermore the isolation of **3** demonstrates the possibility of minor changes in the peripheral ligation. Such a characteristic might be useful for studying the electrochemical behavior of the cluster and as a means to improve solubility.

The other Mn polynuclear complexes, **4** and **5**, exhibit a new core topology with the central  $[Mn^{III}_4(\mu_4-O)_4]^{4+}$  inside a tetrahedron of four  $Mn^{II}$  ions. A similar core structure is present in the literature only for a  $Co_8$  complex with benzoate peripheral ligation published by the Christou group in 1995<sup>151</sup>, and an  $Fe_8$  complex by Raptis et al. in 1999.<sup>152</sup> The use of dicarboxylate ligands with restricted flexibility has led to the isolation of clusters possessing different structure and nuclearity. The ferrocenyl units are also located in a highly symmetric fashion and can potentially display interesting electrochemical behavior. The high symmetry of complexes **2** and **3** affects the position of the elongated Jahn-Teller axes and this might be the cause of a low magnetic anisotropy. A low  $D$  value, although negative, in conjunction with the predominant antiferromagnetic coupling may hinder SMM properties in these molecules. On the other

hand, complexes **4** and **5** possess nearly parallel Jahn-Teller axes, which may be the cause of the slow relaxation of the magnetization for **4**. Complex **5**, however, has a much smaller ground state *S*. Unfortunately, the lack of solubility of these clusters prevents their study in solution particularly with respect to the electrochemical behavior, one of the original objectives of this work. Important questions on the effect of modifications of the redox states of the ferrocenyl units and the resulting magnetic behavior remain unanswered.

### Experimental

All manipulations were performed under aerobic conditions, using materials as received, except where otherwise stated. The preformed cluster  $[\text{Mn}_{12}\text{O}_{12}(\text{O}_2\text{CMe})_{16}(\text{H}_2\text{O})_4] \cdot 4\text{H}_2\text{O} \cdot 4\text{MeCO}_2\text{H}$  (**1**) was obtained by a published method<sup>36</sup> as well as for  $[\text{N}(\text{C}_6\text{H}_4\text{Br-2,4})_3]^+[\text{SbCl}_6]^-$  which was also prepared according to literature.<sup>149</sup> The ligand precursor  $\text{fdCH}_2$  was initially synthesized as previously indicated in this chapter and then obtained from commercial sources. The experiments were initially all carried in the presence of light and then repeated later in the dark during both the reaction and crystallization of products. This was done to rule out the possibility of interfering photochemical reactions of the ferrocenyl ligand.

#### **$[\text{Mn}_{13}\text{O}_8(\text{OMe})_6(\text{fdc})_6] \cdot 4\text{H}_2\text{O} \cdot 3\text{MeOH}$ ; (**2**) $\cdot 4\text{H}_2\text{O} \cdot 3\text{MeOH}$**

To a stirred suspension of  $\text{fdCH}_2$  (0.5 mmol, 0.137 g) in a mixture  $\text{CH}_2\text{Cl}_2/\text{MeOH}$  (1:1; 25 mL), was added complex **1** as a solid (0.125 mmol, 0.257g). The mixture was stirred for one hour and then filtered on a P2 filter paper. A dark brown solution was obtained and carefully layered with diethyl ether. Dark brown needle shaped crystals begin to appear after one week. Longer crystallization times leads to the appearance of a precipitate, which has not been characterized. The crystals collected after one week

were dried under vacuum yielding ~5% of product. The crystals analyze for **(2)**·4H<sub>2</sub>O·3MeOH. Anal. Calcd. (found) for C<sub>81</sub>H<sub>86</sub>Mn<sub>13</sub>Fe<sub>6</sub>O<sub>45</sub>: C, 34.39 (34.42) %; H 3.06 (2.95) %. Selected IR data (KBr pellet, cm<sup>-1</sup>): 1660 (vs), 1581 (vs), 1479 (vs), 1391 (vs), 1357 (vs), 1254 (w), 1193 (m), 1099 (w), 1026 (m), 924 (w), 821 (w), 798 (m), 780 (s), 605 (m), 582 (m), 506 (s), 456 (m). The same compound was obtained using a mixture of MeCN/MeOH (1:1, 25 mL).

#### **[Mn<sub>13</sub>O<sub>8</sub>(OEt)<sub>6</sub>(fdc)<sub>6</sub>]·7EtOH; (3)·7EtOH**

To a stirred suspension of fdCH<sub>2</sub> (0.5 mmol, 0.137 g) in a mixture CH<sub>2</sub>Cl<sub>2</sub>/EtOH (1:1; 25 mL), was added complex **1** as a solid (0.125 mmol, 0.257g). The mixture was stirred for one hour and then filtered on a P2 filter paper. A dark brown solution was obtained and carefully layered with diethyl ether. Dark brown needle shaped crystals begin to appear after one week. In this case, a longer crystallization time did not lead to the appearance of a powder. The crystals were isolated by filtration, and vacuum dried. The yield is ~7%. The crystals analyze for **(3)**·7EtOH. Anal. Calcd. (found) for C<sub>98</sub>H<sub>102</sub>Mn<sub>13</sub>Fe<sub>6</sub>O<sub>45</sub>: C, 38.60 (38.60) %; H 3.37 (3.51) %. Selected IR data (KBr pellet, cm<sup>-1</sup>): 1710 (w), 1562 (vs), 1487 (vs), 1394 (vs), 1361 (vs), 1193 (m), 1096 (vw), 1025 (s), 926 (w), 871 (w), 826 (w), 788 (m), 641 (s), 583 (s), 527 (vs), 477 (m).

#### **[Mn<sub>8</sub>O<sub>4</sub>(fdc)<sub>6</sub>(DMF)<sub>2</sub>(H<sub>2</sub>O)<sub>2</sub>]·4DMF·4H<sub>2</sub>O; (4)·4DMF·4H<sub>2</sub>O, Method (a)**

Resuspending the solid residue from the preparation of **(2)** or **(3)** in DMF (10 mL) and filtering again on P2 filter paper gave a dark brown solution is obtained. The liquid formed by slow evaporation dark brown needles after 2 weeks. The yield of the vacuum dried product after the first crystal collection is ~2%. Longer crystallization time promotes the formation of a non-identified precipitate. The crystals analyze for **(4)**·4DMF·4H<sub>2</sub>O. Anal. Calcd. (found) for C<sub>90</sub>H<sub>102</sub>N<sub>6</sub>Mn<sub>8</sub>Fe<sub>6</sub>O<sub>40</sub>: C, 40.30 (41.60) %, H

3.83 (3.59) %, N, 3.13 (2.44) %. Selected IR data (KBr pellet,  $\text{cm}^{-1}$ ): 1685 (s), 1577 (vs), 1475 (vs), 1392 (vs), 1537 (vs), 1197 (m), 1029 (m), 923 (w), 829 (w), 798 (w), 780 (m), 635 (m), 517 (s).

**$[\text{Mn}_8\text{O}_4(\text{fdc})_6(\text{DMF})_2(\text{H}_2\text{O})_2]\cdot 3\text{DMF}\cdot 2\text{H}_2\text{O}$ ; (4) $\cdot 3\text{DMF}\cdot 2\text{H}_2\text{O}$ , Method (b)**

To a slurry of  $\text{Mn}(\text{O}_2\text{CMe})_2$  (0.066 mmol, 0.0163 g.) and  $\text{fcdH}_2$  (0.55 mmol, 0.150 g.) in a 25 mL of EtOH/py/TEA (20:1:0.7) was added solid  $[\text{t-Bu}_4\text{N}]^+[\text{MnO}_4]^-$  (0.06 mmol, 0.009 g.). A fine dark powder forms within an hour. The powder was collected and washed with EtOH, then partially redissolved in a mixture DMF/ $\text{CH}_2\text{Cl}_2$  to yield block crystals of (4) $\cdot 3\text{DMF}\cdot 2\text{H}_2\text{O}$  by slow diffusion of ether. The yield for the powder product is 40%. (4) $\cdot 3\text{DMF}\cdot 2\text{H}_2\text{O}$ . Anal. Calcd. (found) for  $\text{C}_{87}\text{H}_{91}\text{N}_5\text{Mn}_8\text{Fe}_6\text{O}_{37}$ : C, 40.61 (40.70) %, H 3.56 (3.84) %, N, 2.72 (2.53) %. Selected IR data (KBr pellet,  $\text{cm}^{-1}$ ): 1683 (s), 1578 (vs), 1475 (vs), 1389 (vs), 1534 (vs), 1198 (m), 1025 (m), 920 (w), 827 (w), 800 (w), 782 (m), 634 (m), 518 (s).

**$[\text{Mn}_8\text{O}_4(\text{fdc})_6(\text{DMF})_4]\cdot 1.5\text{DMF}\cdot 3\text{H}_2\text{O}$ ; (5) $\cdot 1.5\text{DMF}\cdot 3\text{H}_2\text{O}$**

To an orange solution of  $\text{fcdH}_2$  (0.5 mmol, 0.137 g.) in 10 mL of DMF was added solid  $\text{Mn}(\text{O}_2\text{CMe})_2$  (0.4 mmol, 0.102 g.). The solution was stirred until all the solid was dissolved. Meanwhile, freshly made crystals of  $[\text{Mn}_{12}\text{O}_{12}(\text{O}_2\text{CMe})_{16}(\text{H}_2\text{O})_4]$  were crushed in a mortar and one equivalent (0.021 mmol, 0.043 g.) were slowly added as a solid to the stirring solution. The reaction vessel was completely screened from light with aluminium foil, and the solution left stirring for two hours at room temperature. The resulting thick brown suspension was centrifuged and the supernatant was isolated and put to crystallize in the dark by slow diffusion of diethyl ether. The product forms overnight X-ray quality crystals of 5 which after few days result in a yield of ~85% for the

isolated product. The crystals analyze for **(5)**·1.5DMF·3H<sub>2</sub>O. Anal. Calcd. (found) for C<sub>90</sub>H<sub>102</sub>N<sub>6</sub>Mn<sub>8</sub>Fe<sub>6</sub>O<sub>40</sub>: C, 41.01 (40.97) %, H 3.60 (3.45) %, N, 2.97 (3.06) %. Selected IR data (KBr pellet, cm<sup>-1</sup>): 1682 (s), 1576 (vs), 1480 (vs), 1389 (vs), 1536 (vs), 1201 (m), 1035 (m), 920 (w), 834 (w), 796 (w), 762 (m), 628 (m), 520 (s).

### X-Ray Crystallography

Data were collected at 173 K on a Siemens SMART PLATFORM equipped with A CCD area detector and a graphite monochromator utilizing MoK<sub>α</sub> radiation ( $\lambda = 0.71073$  Å). Suitable single crystals of **2**·8CH<sub>2</sub>Cl<sub>2</sub>, **4**·4DMF·4H<sub>2</sub>O and **5**·4DMF were attached to a glass fiber using silicone grease and transferred to the goniostat where they were cooled for characterization and data collection. Cell parameters were refined using up to 8192 reflections. A full sphere of data (1850 frames) was collected using the  $\omega$ -scan method (0.3° frame width). The first 50 frames were re-measured at the end of data collection to monitor instrument and crystal stability (maximum correction on I was < 1 %). Absorption corrections by integration were applied based on measured indexed crystal faces. The structure was solved by the Direct Methods in *SHELXTL6*<sup>153</sup>, and refined using full-matrix least squares. The non-H atoms were treated anisotropically, whereas the hydrogen atoms were calculated in ideal positions and riding on their respective carbon atoms. The asymmetric unit of **2**·8CH<sub>2</sub>Cl<sub>2</sub> consists of a half Fe<sub>6</sub>Mn<sub>13</sub> cluster and four dichloromethane molecules. The latter were disordered and could not be modeled properly, thus program SQUEEZE<sup>154</sup>, a part of the PLATON<sup>155</sup> package of crystallographic software, was used to calculate the solvent disorder area and remove its contribution to the overall intensity data. A total of 615 parameters were refined in the final cycle of refinement using 12232 reflections with  $I > 2\sigma(I)$  to yield R<sub>1</sub> and wR<sub>2</sub> of

4.79% and 11.9%, respectively. Refinement was done using  $F^2$ . The asymmetric unit of **4**-4DMF-4H<sub>2</sub>O consists of a half cluster and two DMF molecules, one of which is disordered and refined in two positions and two water molecules. The protons on the coordinated water, O14, were found and refined freely whereas the protons on the uncoordinated, O17 and O18, were found but were constrained to their respective parent atoms. A total of 670 parameters were refined in the final cycle of refinement using 32126 reflections with  $I > 2\sigma(I)$  to yield  $R_1$  and  $wR_2$  of 4.56% and 9.27%, respectively. Refinement was done using  $F^2$ . The asymmetric unit of **5**-4DMF consists of the Mn<sub>8</sub>Fe<sub>6</sub> cluster and four DMF solvent molecules. The latter molecules were disordered and could not be modeled properly, thus program SQUEEZE<sup>154</sup>, a part of the PLATON<sup>155</sup> package of crystallographic software, was used to calculate the solvent disorder area and remove its contribution to the overall intensity data. The cluster has one of its coordinated DMF ligand disordered where the O atoms if common to both parts while the rest were refined in two parts. Their site occupation factors were dependently refined. In the final cycle of refinement, 23801 reflections (of which 15611 are observed with  $I > 2\sigma(I)$ ) were used to refine 1210 parameters and the resulting  $R_1$ ,  $wR_2$  and S (goodness of fit) were 4.29%, 9.47% and 0.928, respectively. The refinement was carried out by minimizing the  $wR_2$  function using  $F^2$  rather than F values.  $R_1$  is calculated to provide a reference to the conventional R value but its function is not minimized.

### **Magnetic Measurements**

The magnetic measurements were performed with a Quantum Design MPMS-XL SQUID. The samples were collected in the crystalline form, briefly dried under vacuum

and grinded to microcrystals. The microcrystalline products were transferred in a gelatin capsule and embedded in eicosane to prevent torquing. The assessment of the solvation composition was done through microanalysis of the freshly prepared microcrystalline product. Unless otherwise stated all the measurements were carried as described later. DC susceptibility was obtained in the 5 to 300 K range with an applied field of 0.1 T. AC in-phase and out-of-phase were performed in the 1.8 to 15 K range of temperature with an oscillating field at 50, 250 and 997 Hz and 3.5 G of magnitude. Reduced magnetization data were acquired using two modalities: low field or high field. In the low field configuration, the magnetization was measured in a set of DC field ranging from 0.1 to 1.0 T, whereas in the high field the magnitude of the applied magnetic vector ranged from 1.0 to 7.0 T. The reduced magnetization procedure and the relative data were appropriately selected to obtain the best fitting profile through the software GRID<sup>141</sup> and MAGNET<sup>140</sup>. The magnetic data for all measurements were corrected for the diamagnetic response of the sample and the eicosane.

### **Other Measurements**

IR spectra were recorded on a Nicolet Nexus 670 FT-IR spectrometer. The samples were prepared as KBr pellet and analyzed in the range 400-4000  $\text{cm}^{-1}$ .

CHAPTER 3  
NEW Fe<sub>7</sub>-CLUSTER FROM NON-INNOCENT REACTIONS OF 1,1'-  
FERROCENEDICARBOXYLIC ACID IN POLAR MEDIA

**Introduction**

The recurring presence of 3d metals in many biological entities as well as new molecular systems capable of carrying out different functions based on their properties has promoted efforts by many research groups worldwide towards the synthesis and study of 3d metal assemblies. Quite prominent are the polynuclear 3d metal complexes that are enzyme active sites, and many efforts have been made to achieve metal clusters that can model the M<sub>x</sub> sites of such biomolecules. For example, the synthesis and study of clusters can help in understanding how molecules like ferritin start with simple mononuclear iron sources and build large Fe/O cores of up to 4500 metal ions.<sup>156</sup> The overall process that begins with metal uptake from the environment (homeostasis) to the final core constitution is generally known as "biomineralization" and is important in the perspective of large metal storage systems as well as smaller cubane-like cores capable of remarkable electrochemical properties.<sup>19</sup> Iron is one of the most abundant and dominant metals in biological systems, but many other metal ions have been also incorporated within biomolecules and play a catalytic or electron transport role.<sup>19</sup>

Another well explored area of interest for transition metal clusters is the synthesis of materials capable of retaining their magnetization in the absence of an externally applied magnetic field. Such behavior is commonly found in the many metal, metal oxide and other magnets, but reducing their size to the nanoscale for small-scale application results in the loss of their properties unless the temperature is reduced.<sup>6</sup> Some metal clusters can, also, preserve the magnetization if kept below a blocking

temperature, and they constitute an example of a molecular approach to magnetic nanoscale materials. The existence of such a magnetic property at the molecular level is termed as single-molecule magnetism.<sup>35</sup> Due to the necessity for a single-molecule magnet (SMM) to possess a large and well isolated spin ground-state  $S$  and a large and negative magnetic anisotropy  $D$ , the metal ion of choice to fulfill both these requirements has been Mn at higher ( $\text{Mn}^{\text{III}}$ ,  $\text{Mn}^{\text{IV}}$ ) oxidation states. In particular the  $\text{Mn}^{\text{III}}$  ion, with an individual spin of  $s = 2$  and significant  $D$  from the presence of Jahn-Teller distortion, represents an ideal starting point for achieving clusters with SMM properties. With the use of Mn ions, clusters with very large spin states up to ( $S = 83/2$ ) have been isolated.<sup>157</sup> In addition to Mn, other metals have also been used for obtaining clusters with a significant net spin. For example, polynuclear iron clusters containing  $\text{Fe}^{\text{III}}$  ions can display interesting magnetic properties.  $\text{Fe}^{\text{III}}$  ions, as mononuclear species in octahedral geometry, display the large spin  $S = 5/2$  but at the same time their relative electronic isotropy ( $t_{2g}^3 e_g^2$ ) is the cause of a small magnetic anisotropy ( $D$ ). The importance of the topological arrangement in polynuclear iron clusters is such that, despite their tendency for predominant antiferromagnetic couplings, it is still possible to find examples of SMM behavior: examples include  $[(\text{Fe}_8\text{O}_2(\text{OH})_{12}(\text{tacn})_6)\text{Br}_7(\text{H}_2\text{O})]\text{Br}$  ( $S = 10$ )<sup>158</sup> and  $[\text{Fe}_4(\text{OMe})_6(\text{dpm})_6]$  ( $S = 5$ )<sup>159</sup> (where tacn = 1,4,7-triazacyclononane and Hdpm = dipivaloylmethane).<sup>160</sup>

Numerous iron clusters contain alkoxides and they are synthesized following one of two general strategies: by the use of a chelating agent carrying a short alcoholic chain or by direct attack of carboxylates in alcoholic media.<sup>160</sup> In the first case, the chelating group may establish an initial bond to the metal center and then the close

vicinity of one or more alcohol groups cause their coordination with often deprotonation. In the second method, the carboxylate groups exhibit a great affinity for iron ions promoting chelation assisted by an alcoholic solvent for completing the peripheral ligation or acting as bridges.<sup>42,161-163</sup> Iron clusters are also often synthesized by reacting salts of the metal with carboxylates or by treatment of preformed clusters (for example iron triangles) with chelates.<sup>164-166</sup>

In the attempt to isolate iron clusters of a new structural type, several conditions and stoichiometries have been explored with 1,1'-ferrocenedicarboxylic acid. As explained in the previous chapter, the purpose of this research was to achieve clusters with expanded redox properties. The following chapter will discuss synthetic strategies that involve different starting materials, as well as the conditions found to lead to an unexpected behavior of the ligand precursor in the presence of light. As a result of these efforts, a new cluster of iron possessing six ferrocenyl units has been isolated and fully characterized. This iron compound was the first of a series of new isomorphous clusters isolated in this work.

### **Synthetic Strategies for Coordination Compounds with $\text{Fdc}^{2-}$**

In cluster chemistry, targeted reactions to achieve specific final products may be delusive due to the complexity of the reaction system involved.<sup>79</sup> Reactions with  $\text{fdch}_2$  are not an exception to the above and there are only few cases in the literature where this ligand precursor has formed targeted products. A classic example of control over the final product is given by the reaction of the osmium complex  $[\text{Os}_3(\text{CO})_{10}(\text{MeCN})_2]$  with  $\text{fdch}_2$  in chloroform. The stronger  $\text{fdc}^{2-}$  replaces the weaker MeCN ligands on two trinuclear units, hence acting as a bridge in the final product:  $[(\text{Os}_3\text{H}(\text{CO})_{10})_2(\text{fdc})]$ .<sup>95</sup> Analogously, dinuclear M-M bonded complexes can be subject to bridging by  $\text{fdc}$  by

displacement of some ligands. Examples come from the formation of  $\{\text{Mo}_2\text{fdc}\}_4$  and  $\{\text{Ga}_2\text{fdc}\}_4$  macrocyclic units starting with the  $\{\text{Mo}_2\}$  and  $\{\text{Ga}_2\}$  dinuclear blocks, respectively.<sup>96,98</sup> Another example of successful planning of a reaction product comes from the pairing of two molecular units by means of a  $\text{fdc}^{2-}$ . When  $[(\text{O}_2\text{NO})(\text{Et}_3\text{P})_2\text{Pt}-\text{L}-\text{Pt}(\text{Et}_3\text{P})_2(\text{ONO}_2)]$ , (where L=2,9-phenanthrenediyl or 1,8-anthracenediyl) is reacted with  $\text{fdcNa}_2$  in a 1:1 ratio, it forms a macrocycle by displacing the nitrate with a carboxylate group and releasing sodium nitrate as byproduct.<sup>103</sup> Despite the elegance and the control of the systems listed, other authors report similar targeted syntheses resulting in unexpected products. An example is found for the M-M dimer  $\{\text{Re}_2\}$ , where the reaction with  $\text{fdcH}_2$  did not lead to the expected dimer-of-dimers  $\{\text{Re}_2\}\text{fdc}\{\text{Re}_2\}$ , but rather to chelation by the  $\text{fdc}^{2-}$  on a single unit to form  $\{\text{Re}_2\}\text{fdc}$ .<sup>112</sup>

The use of  $\text{fdcH}_2$  or  $\text{fdc}^{2-}$  as a bridging unit establishes the feasibility of a controlled oligomerization reaction where the final product contains only a few repeating units instead of an infinite chain. However, this type of reaction has proven successful only in the few cases just mentioned, its application towards the preparation of smaller nuclearity metal complexes has been relatively unsuccessful. In general, polymerization seems to result from simple reaction systems with mononuclear species, leading to the formation of insoluble precipitates and only minor quantities of molecular compounds. The problem of polymerization has been mainly dealt with in three ways in the literature of  $\text{fdcH}_2$ : the use of chelating agents to limit and direct the reactivity to specific metal sites; reactions performed by slow diffusion of the reagents, and the use of solvothermal conditions. In reactions with 3<sup>rd</sup> and 4<sup>th</sup> row transition metals, chelating agents like bpy (2,2'-bipyridine), phen (1,10-phenanthroline) and tmeda (*N,N,N',N'*-tetramethyl-ethane-

1,2-diamine) produced molecular species of the type  $\{M_2(fdc)_2\}$  where  $M = Co, Ni, Cu, Zn$  or  $Cd$ .<sup>88,111,115</sup> The use of bidentate non-chelating ligands with particular geometries like pebbm ((1,1'-(1,5-pentanediy)bis-1H-benzimidazole) or prbbm (1,1'-(1,3-propanediy)bis-1H-benzimidazole) (Fig. 3-1) led to the formation of infinite chains (1D polymerization) or sheets (2D polymerization) with simple cadmium salts. In these cases, the coordination mode of the  $fdc^{2-}$  and the nature of the product could be controlled by ligands capable of blocking some coordination positions while guiding the build up of the polymer.<sup>111</sup>

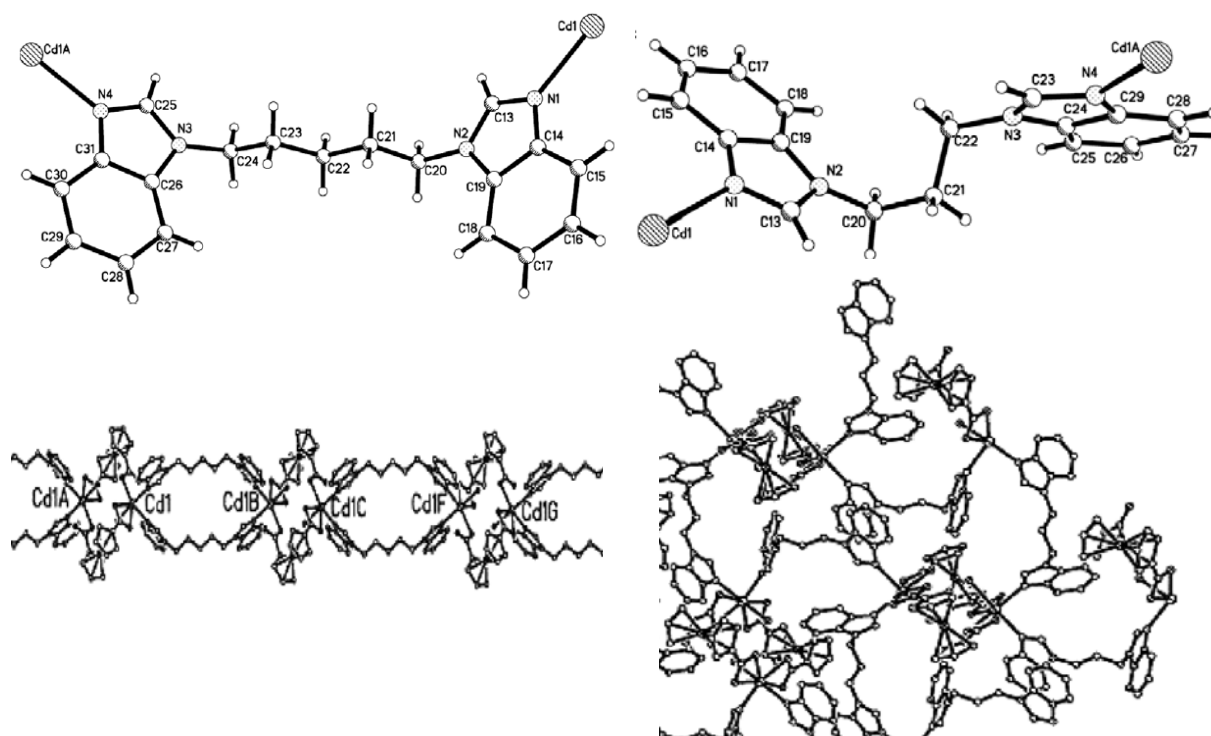


Figure 3-1. Structure of the pebbm ligand, 1,1'-(1,5-pentanediy)bis-1H-benzimidazole, (top left) and its coordination in a chain with cadmium ions (bottom left). Structure of the prbbm ligand, 1,1'-(1,3-propanediy)bis-1H-benzimidazole, (top right) and its coordination to form sheets with cadmium ions (bottom right). Adapted from ref. <sup>111</sup>, with permission of Elsevier.

A similar scheme where the ligand exerts lesser control employs pyridine in a solvent with weak coordinating capabilities, such as DMF. As a monodentate ligand,

pyridine blocks some metal positions but cannot bridge to other metal centers. A literature example demonstrates how the added coordinating effect of the solvent is sufficient in reactions with Ni<sup>II</sup> or Cu<sup>II</sup> salts to prevent polymerization, while in other reactions with lanthanide ions, the absence of pyridine or DMF results in the formation of 2D-networks.<sup>104</sup> The latter literature example represents an intermediate situation where the use of both co-ligands and slow diffusion of the reagent led to the isolation of well defined molecular and polymeric products.

Reactions with co-ligands are generally performed with direct mixing of the reagents, while those where there are no co-ligands, and the solvent is a mild coordinating agent, are generally performed using diffusion. There are two main advantages of diffusion reactions leading to polymers: firstly, the reactants will interact as if in a highly diluted solution and secondly the extended reaction time allows the products to crystallize as they form. The main disadvantage of this reaction is the long period of completion; it may be avoided in ordinary reaction types, but they result in insoluble precipitates difficult to characterize. The literature reports different examples of diffusion reactions where the  $\text{fdc}^{2-}$  ligand is added to the metal ions using different approaches. A mixture of  $\text{fdcH}_2$  and  $\text{Zn}^{\text{II}}$  ions in DMF forms the  $\{\text{Zn}_6\text{O}_2(\text{fdc})_5\}$  assembly by slow diffusion of triethylamine (TEA).<sup>107</sup> In another case, a solution of the ligand is slowly added of the metal source and TEA solution yielding a chain of  $\{\text{Eu}_2(\text{fdc})_3(\text{H}_2\text{O})_4\}_n$ .<sup>118</sup> A third example uses the weakly basic anion of the metal source,  $\text{Mn}(\text{O}_2\text{CMe})_2$ , to deprotonate the ligand precursor by slow diffusion and form a  $\text{Mn}_{13}(\text{fdc})_6$  cluster.<sup>101</sup> Finally, other methods have employed the already deprotonated  $\text{fdc}^{2-}$  sodium salt to successfully produce sheet-shaped coordination polymers of  $\text{Ba}^{\text{II}}$

and Sm<sup>III</sup>.<sup>104</sup> Analogous reagents (i.e.:  $\text{fdc}^{2-}$  and the metal ion) in the case of Pb<sup>II</sup> slowly produced a crystalline product instead of a precipitate, probably due to the slow kinetics of the process.<sup>100</sup> Reactions under solvothermal conditions represent another pathway to the isolation of well-defined compounds of  $\text{fdc}^{2-}$ . The high temperatures and generally long reaction times allow for structural rearrangement of polymeric products into smaller monomeric units or discrete molecular systems. A controlled cooling time is also crucial for favoring crystallization. This method yields molecular clusters like  $[\text{Zn}_8\text{O}_4(\text{fdc})_6(\text{H}_2\text{O})_3]$ ,  $[\text{Cu}_4(\text{fdc})_2]$ ,  $[\text{Sn}_8\text{O}_4(\text{fdc})_6]$ ,  $[\text{R}_2\text{Sn}(\text{fdc})_2]$  and  $[\text{R}_2\text{Te}(\text{fdc})_2]$  (R = aliphatic or aromatic chain).<sup>105-107</sup>

The synthetic methods to M-fdc compounds so far discussed are not exclusive nor exhaustive. The synthesis of  $[\text{Mn}_{13}\text{O}_8(\text{fdc})_6(\text{OMe})_6]$ , **2**, was achieved through slow diffusion by Kondo et al.<sup>101</sup> while as described in Chapter 2, the same compound was isolated by mixing a preformed Mn-cluster in methanol with  $\text{fdCH}_2$ . Besides **2**, other clusters were successfully isolated by simple reaction of preformed clusters and  $\text{fdCH}_2$  leading to assemblies of different topology.

## Synthesis

### Initial Reactions of $\text{FdcH}_2$ with Fe Sources

The reaction of  $\text{fdCH}_2$  with iron sources was found to be an extremely complicated one, and a large number of different reaction conditions were explored in developing the procedure to pure and crystalline products. These involved different iron sources, solvent compositions, and reagent ratios. The use of Fe<sup>II</sup> chloride in MeOH was finally found to give the reproducible product  $[\text{Fe}_7\text{O}_3(\text{OMe})(\text{fdc})_6(\text{MeOH})_3]^{3+}[\text{FeCl}_4]\text{Cl}_2$ , (**6**) in pure form. The solvent, MeOH, played a crucial role because ensured sufficient solubility of both the  $\text{FeCl}_2$  and sparingly soluble  $\text{fdCH}_2$  reagents and, importantly, to

some extent the product. In addition, the MeOH was of course necessary to provide the MeO<sup>-</sup> ligation found in **6** (vide infra). After overnight stirring with the room lights on, the reaction was filtered to give a green/blue filtrate and much light grey-blue residue. Layering of the filtrate with Et<sub>2</sub>O/hexanes gave well-formed crystals of **6**·(solv) not contaminated with any grey-blue powder. A number of other crystallization methods were also explored but these gave a mixture of crystals and powder, and the two components were determined not to be the same compound, as the color and also IR spectra indicated. The grey-blue powder was essentially insoluble in common solvents and could not be characterized further. The large amount of solvent molecules in **6**·(solv) concluded from the crystal structure is consistent with the presence of Cl<sup>-</sup> anions and their hydrogen-bonding to solvent molecules. To get an estimate of the content, the crystals were dried very briefly under vacuum, and the elemental analysis (including Cl) was consistent with the formula **6**·8H<sub>2</sub>O·6MeOH. This formulation was used for the magnetism studies (vide infra).

Many different reaction conditions have been explored in an attempt to increase the very low yield of **6**. The formula of **6** has a ratio of fdc<sup>2-</sup> to other Fe of 8:6, but reactions with different fdc<sup>2-</sup>:FeCl<sub>2</sub> reagent ratios showed the optimum reaction ratio to be 2:1; higher or lower fdc<sup>2-</sup>:FeCl<sub>2</sub> ratios were found to give mixtures of products, often containing both microcrystalline solid and fine powders, including unreacted fdcH<sub>2</sub> starting material, for the higher ratio reactions. Much of the powder was completely insoluble in all tested solvents, suggesting polymer formation from fdc<sup>2-</sup> adopting a bridging mode between different Fe<sub>7</sub> or other Fe<sub>x</sub> units. The addition of base to deprotonate and solubilize fdcH<sub>2</sub> and hopefully increase the yield of **6** also led to

mixtures of products as judged from IR spectra and a variety of colored materials. The other products might be completely different compounds from **6**, or other oxidation states of **6**, or both; however, the complexity of the reaction and the obtained mixtures of solids has prevented from obtaining other compounds in pure form for identification. Mixed solvent systems were also explored, but with no success. For example, a mixed MeOH/MeCN solvent medium did not have a significant effect on the amount or purity of the product **6** unless the MeCN was present at >20% (v/v), at which values there was a decreased and even no amount of crystals of **6** obtained. Fe<sup>III</sup> salts were also explored as starting materials, but this approach proved unsuccessful as a route to **6**; the main product was again an insoluble powder precipitate and no noticeable amount of complex **6**. It was then accepted the use of FeCl<sub>2</sub> as the starting material in reproducible reactions to pure **6** although in very low yields.

It was during the above experiments with FeCl<sub>2</sub> under different conditions that it was noticed the effect of ambient light on the FeCl<sub>2</sub> reactions. It was already realized that long reaction times were necessary for the reaction to give the dark green/blue solution color indicative of **6** from the initial orange suspension of fdCH<sub>2</sub>. Significant darkening of the solution is apparent only after a few hours stirring and thus long reaction times (~24 hours) were routinely used. One reaction mixture was divided into two portions, one of which was kept in room light overnight and the other in the dark. The one exposed to light gave the dark colored solution characteristic of **6**, whereas the other kept its original orange color, and did so for many weeks. This can be attributed to the known photo-lability of ferrocenyl units substituted with electron-withdrawing groups, discussed in detail in the next section.

## Photosensitivity of FdCH<sub>2</sub>

Although ferrocene is known for its thermal stability and inertness under several reaction conditions, this organometallic group, once bound to a photoactive compound, is also responsible for remarkable changes in the photoreactivity.<sup>167</sup> Bozak et al. have demonstrated how the presence of ferrocene in carbonylated aromatic systems stops their photoreduction.<sup>168</sup> Also, it has been shown that the ferrocenyl moiety is susceptible to photodissociation upon exposure to radiation especially in the ultraviolet and visible region. According to L. H. Ali et al.<sup>169</sup>, Nesmeyanov<sup>170</sup> had first described the photodissociation of fdCH<sub>2</sub> in aqueous media by prolonged exposure to light. In their work, Ali et al.<sup>170</sup>, described the effect of photoirradiation on various ferrocenyl ketones. In the case of ferrocenyl aryl ketones (fc-CO-Ar), the presence of water as an impurity proved to be necessary for the photodecomposition. There was no decomposition in rigorously dried solvents until some water was added, and it was also observed that the reaction rate increased as a ratio of 1:1 with the substrate was achieved. On the contrary, carboxylated substrates like ferrocenecarboxylic (fmCH) and 1,1'-ferrocenedicarboxylic acids were susceptible to decomposition even in dry solvents. The decomposition was monitored by IR of the dried reaction products. A common pathway was found for ketones and carboxylate derivatives showing that, besides other changes, there is a decrease in the intensity for the carbonyl vibration while a new band appeared at lower frequencies about 1540-1600 cm<sup>-1</sup> ( 100 cm<sup>-1</sup> in range). This band increases as the substrate is depleted and concurrently a sharp and weak CO<sub>2</sub> vibrational band starts appearing (2323 cm<sup>-1</sup>). The CO<sub>2</sub> released with prolonged irradiation is at the expense of the newly formed peaks between 1540 and 1600 cm<sup>-1</sup> (see Fig. 3-2). Along with the IR studies, Ali et al.<sup>169</sup> followed the formation of the

decomposed product by NMR. In case of both fmCH and fdCH<sub>2</sub>, the signals of the cyclopentadienyl protons were broadened even after a short exposure.

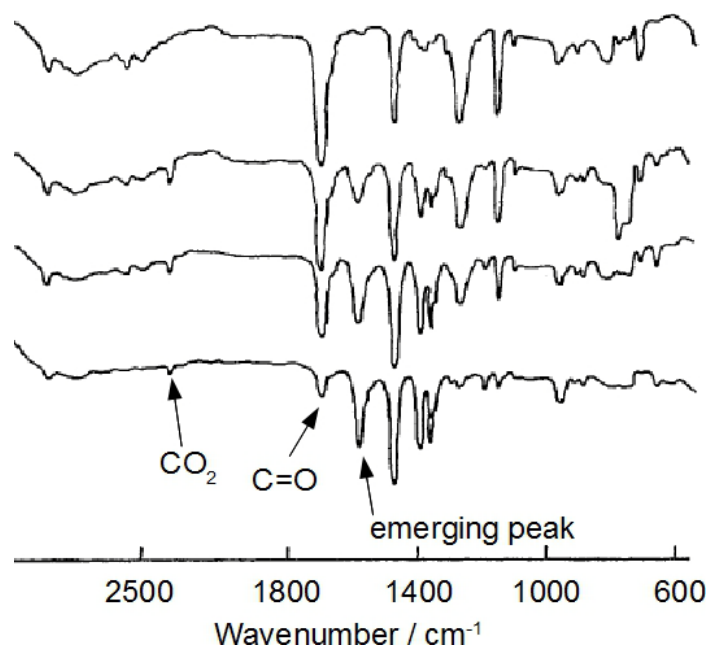


Figure 3-2. Overlay of IR spectra for fmCH in pyridine solution with increasing irradiation times, top to bottom. As observed for ferrocenyl ketones, the C=O stretching decreases in intensity while a neighboring band grows and a peak for CO<sub>2</sub> appears (adapted from ref. <sup>169</sup>).

The effect became more evident on increasing the irradiation time. As the authors have suggested, the line-broadening is due to a paramagnetically induced relaxation and demonstrates the intramolecular character of the process in the signals for traces of acetone. The final products of the decomposition reactions for fmCH and fdCH<sub>2</sub> showed cyclopentadiene, CO<sub>2</sub> and some uncharacterized carboxylates of Fe<sup>III</sup>. More recently, Ding <sup>171</sup> and then Yamaguchi <sup>172</sup>, studied in detail the electronic behavior of substituted-ferrocene compounds with particular regard to highly conjugated electron-withdrawing groups. The authors refer to previous work where the effect of benzoyl substitution was studied. Ferrocene shows two doubly-degenerate ligand field electronic transitions in the visible region at 442 and 325 nm, while higher intensity bands are found in the UV

region corresponding to metal-to-ligand and ligand-to-metal transitions (MLCT and LMCT) (Fig. 3-3). Upon benzoyl substitution, the transitions in the visible are greatly enhanced in intensity and slightly shifted to lower energies. The authors assign this behavior as a result of the extended conjugation of the substituent with the cyclopentadienyl ring, increased delocalization of d electrons, and consequent relaxation of the Laporte-forbidden nature of d-d transitions.

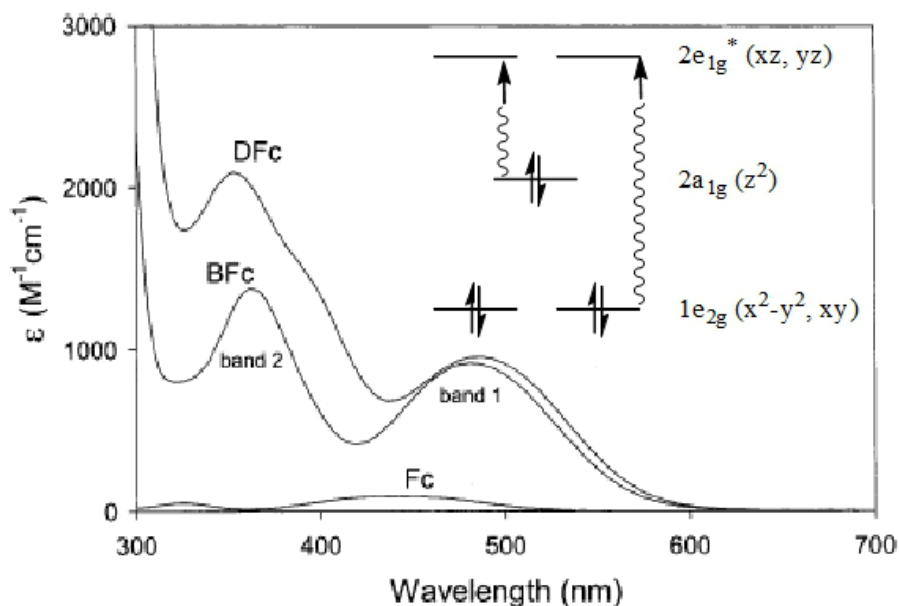


Figure 3-3. UV-Visible spectra of ferrocene (Fc), benzoylferrocene (BFc) and 1,1'-dibenzoylferrocene (DFc) (reported from ref. <sup>171</sup>, Copyright 2003 American Chemical Society). The inset shows the frontier electronic states for ferrocene. The transition  $2a_{1g} \rightarrow 2e_{1g}^*$  corresponds to the "band 1" in the spectra, whereas the transition  $1e_{2g} \rightarrow 2e_{1g}^*$  corresponds to the "band 2" (adapted from ref. <sup>172</sup>).

The bathochromic effect of the absorption bands of benzoylferrocene and 1,1'-dibenzoylferrocene with respect to ferrocene is due to increased stabilization of the LUMO (essentially based on ligands orbitals). Such an interpretation is supported by the negligible fluorescence of the ferrocene as compared to its highly delocalized derivatives. These considerations led Ding and Yamaguchi to consider the

photodecomposition of the substituted ferrocene due to a MLCT-produced long-lived charge separation, which is particularly stable in polar solvents. Ding hypothesized that the intermediate resulting from the irradiation of 1,1'-dibenzoylferrocene is a zwitterionic species, where one electron is removed from a metal orbital (mainly d in character) and delocalized over the ligand  $\pi$ -system (Fig. 3-4).<sup>171</sup>

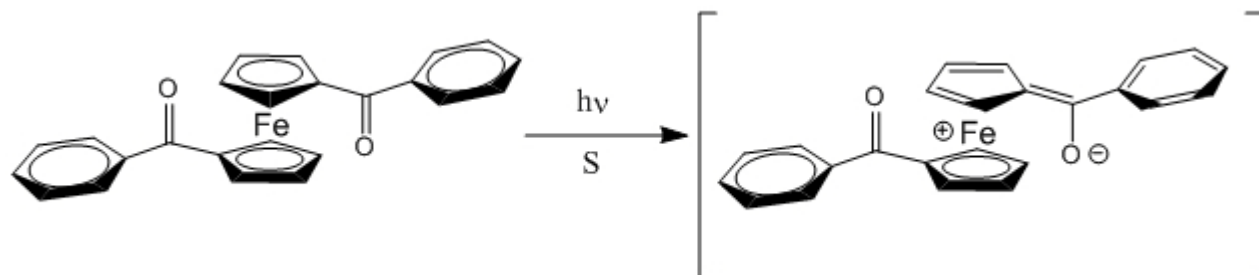


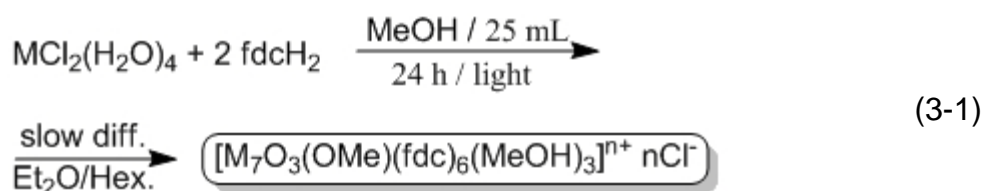
Figure 3-4. Representation of the initial irradiation effect on 1,1'-benzoylferrocene as a general example for other electron withdrawing conjugated systems substituted on the ferrocene assembly (adapted from ref. <sup>171</sup>).

The evolution of this species may then lead to attack by polar solvent molecules resulting in the expulsion of one cyclopentadienyl ligand, or there may be an initial dissociation of the cyclopentadienyl unit followed by coordination of the solvent. Although a complete characterization of all decomposition products has not been possible, especially due to the high sensitivity of the species initially produced, the effect of UV and visible radiation in the decomposition process of ferrocene and many conjugated derivatives is obvious. Hence, in presence of light partial decomposition with concurrent attack of solvent molecules should be expected.

### Further Study with Other Metal Sources

Something similar to what has been afore described is likely occurring in the reactions to **6**, accelerating and directing the reactivity towards the formation of the cluster, but the heterogeneous nature and complexity of the present reaction systems

make it difficult to study this in more detail. However, support for the involvement of photo-released Fe from fdCH<sub>2</sub> under the previously described reaction conditions was obtained by alternative means. When the analogous reaction that gives **6** was explored using MCl<sub>2</sub> (M = Mn, Co, Ni, Zn), dark colored crystals were obtained again and in low yield. These were found to be isomorphous with **6**, as determined by IR spectral comparisons and X-ray diffraction studies; in the case of M = Mn, a full crystal structure coupled with the results of a complete elemental analysis (C, H, N, Cl, Mn, Fe) revealed the formulation [Fe<sub>6.2</sub>Mn<sub>0.8</sub>O<sub>3</sub>(OMe)(fdc)<sub>6</sub>(H<sub>2</sub>O)<sub>3</sub>]Cl, (**7**), for the isolated product; the product is thus a mixture of species with different Fe:Mn ratios. In addition, the high Fe:Mn ratio is consistent with the structure of **6** being highly favored for Fe. The isomorphous products from the reactions with M = Co, Ni, or Zn, were not analyzed in the same detail, but it seems clear that a similar situation is occurring as for the Mn product, following the reaction scheme in eq. 3-1 to give the general species [Fe<sub>x</sub>M<sub>7-x</sub>O<sub>3</sub>(OMe)(fdc)<sub>6</sub>(MeOH)<sub>3</sub>]<sup>n+</sup>·nCl, where M = Co (**8**), Ni (**9**) or Zn (**10**).



The reaction was also extended to larger Ca<sup>II</sup>, Cd<sup>II</sup>, and Ce<sup>IV</sup> reagents, hoping to crystallographically identify any site preferences for different metals in a mixed-metal product, structurally analogous to **6** or otherwise, but these reactions gave crystalline products that were confirmed by crystallography to be isostructural with **6** and to contain only Fe, i.e. they were complex **6**.

### Description of the Molecular Structures

The structure and labeled  $[\text{Fe}_7\text{O}_3(\text{OMe})]^{14+}$  core of **6** are shown in Fig. 3-5 and 3-6, respectively; while Tab. 3-1 resumes some crystallographic data. The cation consists of an  $[\text{Fe}_7(\mu_4\text{-O})_3(\mu_3\text{-OMe})]^{14+}$  core comprising a central cubane whose  $\text{O}^{2-}$  ions are each also attached to one additional Fe atom. The core is very similar to the other previously reported octanuclear Fe cluster possessing a central  $\text{Fe}_4(\mu_4\text{-O})_4$  cubane and four other Fe ions bound to the oxides.<sup>152,173-175</sup> The structure of **6** differs from the mentioned octanuclear clusters in that one  $\mu_4\text{-O}$  in the central cubane is a  $\mu_3\text{-OMe}$ , accounting for the missing iron ion in the structure.

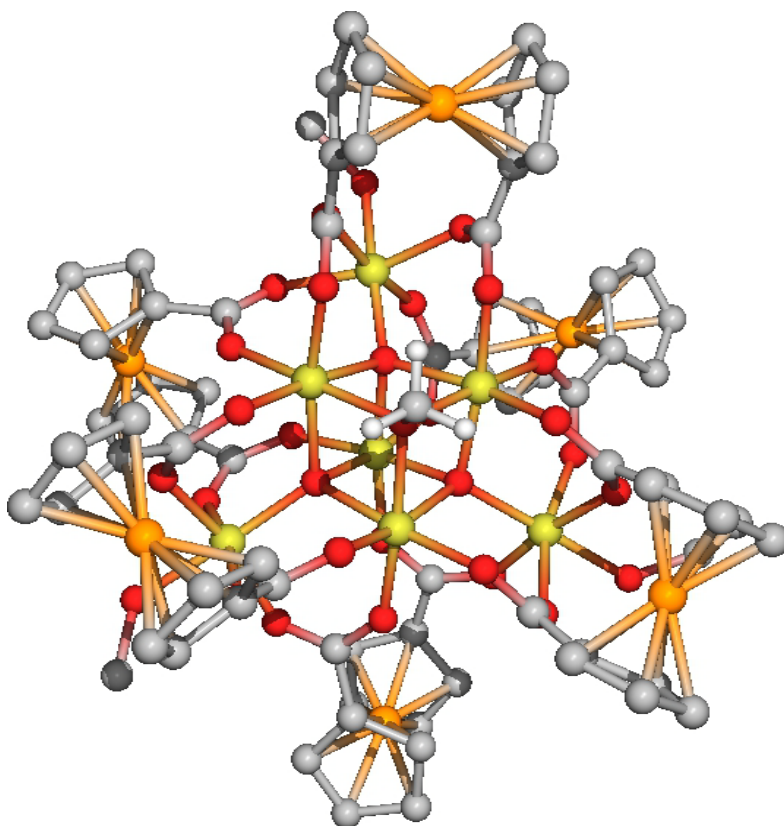


Figure 3-5. Pov-Ray projection of  $[\text{Fe}_7\text{O}_3(\text{OMe})(\text{fdc})_6(\text{MeOH})_3]^{3+}$ : core  $\text{Fe}^{\text{III}}$  yellow, fdc Fe ions orange, O red. Hydrogen atoms have been omitted for clarity.

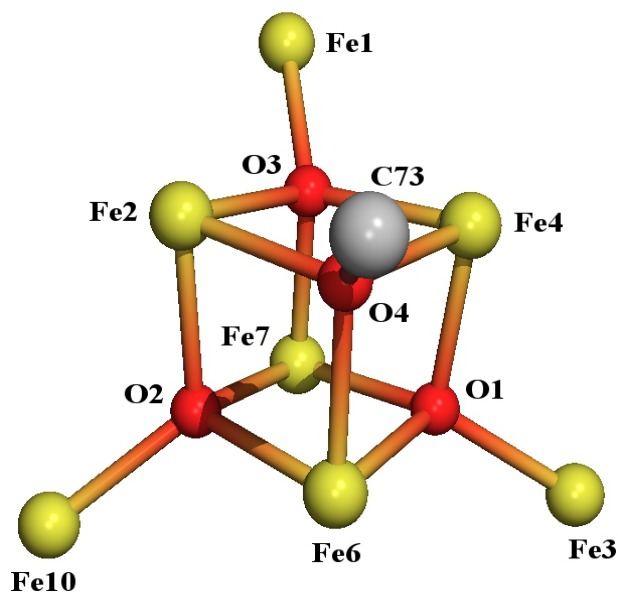


Figure. 3-6. Pov-Ray projection of the core  $[\text{Fe}^{\text{III}}_7(\mu_4\text{-O})_3(\mu_3\text{-OMe})]^{14+}$  in **6**: Fe<sup>III</sup> yellow, O red. The axis through the atoms C73, O4 and Fe7 describes the ideal  $C_3$  rotational axis.

Table 3-1. Selected crystal data for complex **6**·2MeOH·2H<sub>2</sub>O (full data in Tab. B-4).

Parameter	Value
Empirical formula	C <sub>76</sub> H <sub>63</sub> Cl <sub>6</sub> Fe <sub>14</sub> O <sub>31</sub>
Formula weight, g mol <sup>-1</sup>	2466.86
Temperature, K	173(2)
Wavelength, Å <sup>a</sup>	0.71073
Crystal system	Monoclinic
Space group	<i>P2</i> <sub>1</sub> / <i>c</i>
Unit cell dimensions, Å	<i>a</i> = 18.4240(12), <i>b</i> = 24.6645(15), <i>c</i> = 24.1746(15)
Unit cell angles, deg	$\alpha$ = 90°, $\beta$ = 109.349(1)°, $\gamma$ = 90°
Volume, Å <sup>3</sup>	10364.9(11)
Z	4
$\rho_{\text{calc}}$ , g cm <sup>-3</sup>	1.671

These seven Fe atoms all have distorted octahedral geometry. Peripheral ligation is provided by six fdc<sup>n-</sup> groups (*n* = 1, 2; see below), whose six Fe atoms form a slightly distorted octahedron about the central core, and three MeOH molecules. This gives a complete cation of crystallographic  $C_1$  but virtual  $C_3$  symmetry, with the virtual rotation axis passing through Fe7 and methoxide atoms O4 and C73. As a result, the fdc<sup>n-</sup> groups separate into two sets of three by virtual symmetry: One set (Fe9, Fe11, Fe13),

those furthest from the methoxide group, bridge four Fe atoms in an  $\eta^1:\eta^1:\eta^1:\eta^1:\mu_4$  mode with each carboxylate bridging a separate  $\text{Fe}_2$  pair, whereas the other set bridges three Fe atoms in a  $\eta^1:\eta^1:\eta^1:\eta^1:\mu_3$  mode (Fig. 3-7).

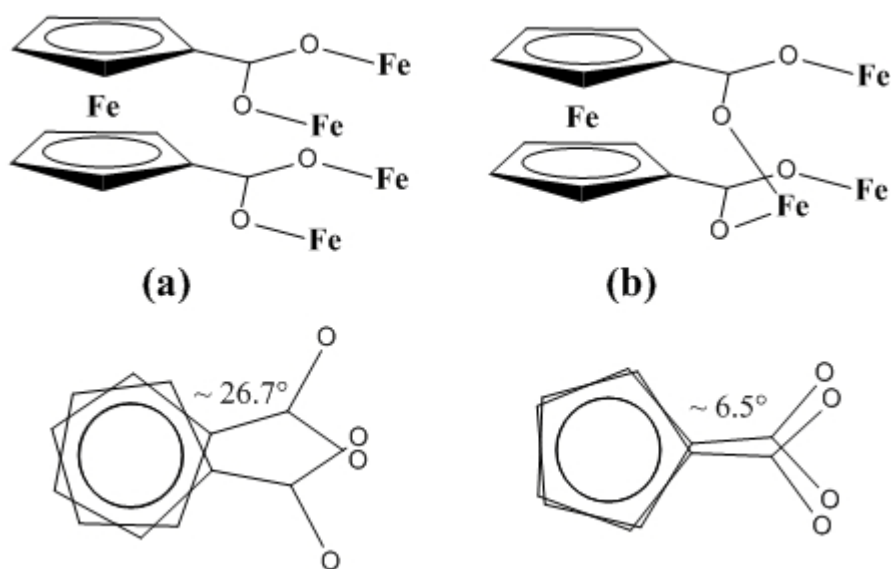


Figure 3-7. Different chelation modes and respective torsion angles adopted by  $\text{fdc}^{n-}$  in complex **6**. In (a)  $\eta^1:\eta^1:\eta^1:\eta^1:\mu_4$  mode, in (b)  $\eta^1:\eta^1:\eta^1:\eta^1:\mu_3$  mode.

The ability of the two Cp rings to twist relative to each other clearly assists in this binding flexibility of  $\text{fdc}^{n-}$ : the  $\mu_4$  mode has a torsion angle of  $\sim 26.7^\circ$  and thus an almost staggered  $\text{FeCp}_2$  conformation (ideal value  $36^\circ$ ), whereas the  $\mu_3$  mode has a torsion angle of  $\sim 6.5^\circ$  and thus an essentially eclipsed conformation (Fig. 3-7).<sup>134</sup> Ligation at each external Fe atom is completed by a terminal MeOH group. The orientation of the  $\text{fdc}^{n-}$  groups, and the resulting  $C_3$  rather than  $C_{3V}$  virtual symmetry, leads to the cation being chiral, and the crystal comprises a racemic mixture of the two enantiomers related by mirror planes (Fig. 3-8). The seven non- $\text{fdc}^{n-}$  Fe atoms are in the  $\text{Fe}^{\text{III}}$  oxidation state, as suggested by the metric parameters and confirmed by bond valence sum (BVS) calculations,<sup>176</sup> which gave values in the 2.94–3.09 range (Tab. 3-2).

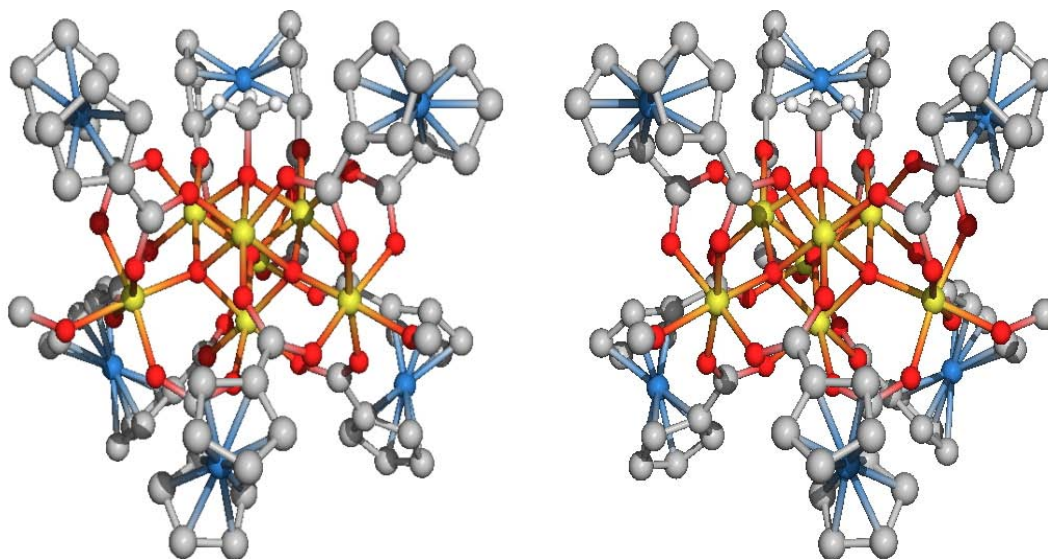


Figure 3-8. Pov-Ray projection of two neighboring molecules of complex **6** in the lattice. The objects are related by an ideal mirror plane.

Table 3-2. Bond Valence Sum calculations for complex **6**.<sup>176</sup>

Atom	Fe <sup>II</sup>	Fe <sup>III</sup>
Fe(1)	2.88	3.08 *
Fe(2)	2.77	2.96 *
Fe(3)	2.79	2.99 *
Fe(4)	2.80	2.99 *
Fe(6)	2.89	3.09 *
Fe(7)	2.75	2.94 *
Fe(10)	2.79	2.99 *
Fe(14)**	2.87	3.11 *

The number with an asterisk is the one closest to the actual charge for which it was calculated and the nearest whole number to it represent the oxidation state. \*\*Relative to the counter ion  $[\text{FeCl}_4]^-$ .

Given the  $[\text{Fe}_7\text{O}_3(\text{OMe})(\text{fdc})_6(\text{MeOH})_3]^{3+}$  formula of the cation, this indicates that one of the ligands is in the oxidized  $\text{fdc}^-$  oxidation level, the remainder being  $\text{fdc}^{2-}$ ; in fact, at least one oxidized ligand was expected from the blue color of the cation, which is not a color expected for Fe/O clusters but which is characteristic of the ferrocenium cation,  $\text{Cp}_2\text{Fe}^+$ .<sup>177</sup> The BVS approach is not reliable for assigning the Fe<sup>II</sup>/Fe<sup>III</sup> oxidation state within such an organometallic unit, and other distances within **6** were considered to probe this point. Oxidation of a free ferrocene unit to ferrocenium leads to a

lengthening of the centroid-centroid distance (centroid = CT = the center of the Cp ring) by  $<0.1 \text{ \AA}$  on average,<sup>132-133</sup> which is a small change. Substituents on the rings and binding to additional metal centers will affect these changes. Shown in Tab. 3-3 are the Fe-CT and CT-CT distances in **6**, and it can be seen that neither parameter shows any major difference that could be assigned to clearly being in the oxidized state.

Table 3-3. Fe-centroid and centroid-centroid distances ( $\text{\AA}$ ) in complex **6**.

Atom	Fe-CT <sup>a,b</sup>	CT-CT <sup>a,c</sup>
Fe(5) <sup>d</sup>	1.636, 1.652	3.288
Fe(8) <sup>d</sup>	1.645, 1.652	3.297
Fe(12) <sup>d</sup>	1.656, 1.659	3.314
Fe(9) <sup>e</sup>	1.646, 1.640	3.287
Fe(11) <sup>e</sup>	1.649, 1.650	3.299
Fe(13) <sup>e</sup>	1.647, 1.653	3.299
Average	1.649	3.297

<sup>a</sup> CT = centroid. <sup>b</sup>  $\pm 0.001 \text{ \AA}$ . <sup>c</sup>  $\pm 0.002 \text{ \AA}$ . <sup>d</sup> related by virtual symmetry. <sup>e</sup> related by virtual symmetry.

The distances at Fe12 do show slightly longer values, but these differences are statistically borderline. It can be concluded that although (i) the blue color of the crystal clearly indicates that **6** contains an oxidized (ferricenium-containing)  $\text{fdc}^-$  ligand, and (ii) distances at Fe12 are slightly longer than those at other ferrocenyl Fe atoms, there is nevertheless no unequivocal statistical evidence from the structural parameters for one of the ligands being in the oxidized ( $\text{fdc}^-$ ) level. This is, of course, consistent with the only small changes expected on oxidation and the possibility in **6** of static disorder of the oxidized ligand amongst the three groups related by virtual symmetry, and even amongst all six of them. As in the case of the Mn clusters discussed in Chapter 2, also the lattice of compound **6** displays numerous H- $\pi$  interactions and some  $\pi$ - $\pi$  interactions amongst the  $\text{fdc}$  units, and in some cases between  $\text{fdc}$  and the  $[\text{FeCl}_4]^-$  counter ion (Fig. 3-9). The distance of the ferrocenyl units supports from adjacent molecules promoted the formation of these interactions.

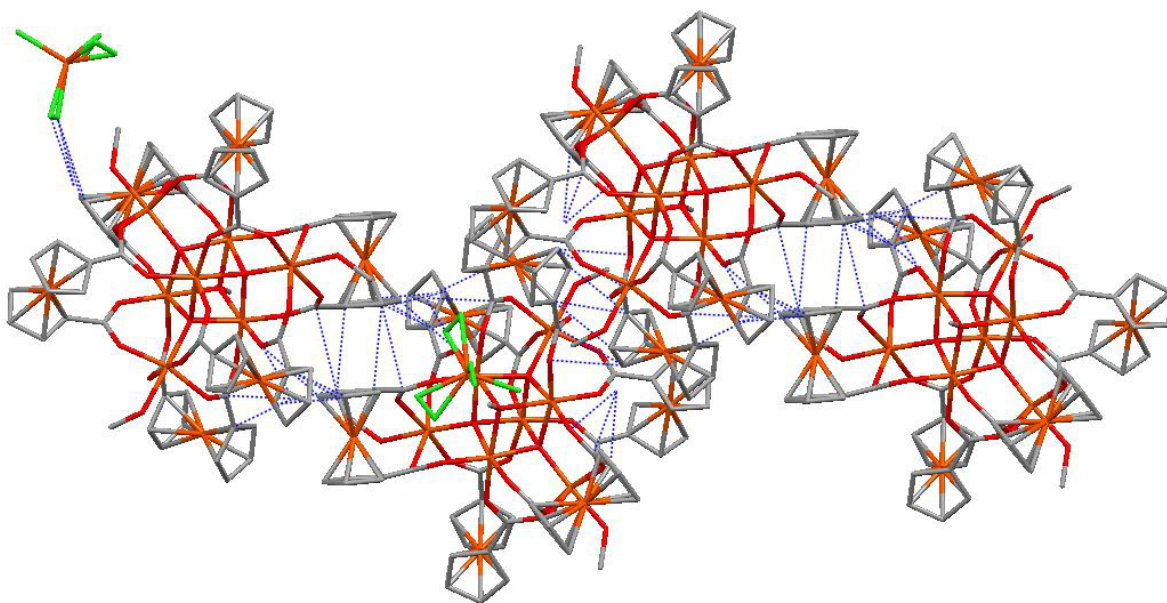


Figure 3-9. Packing diagram of complex **6** in Mercury<sup>136</sup>. Blue dotted lines indicate some of the H- $\pi$  and  $\pi$ - $\pi$  interactions in the lattice.

All clusters **7-10** were characterized by X-ray crystallography. Despite minimal differences in the peripheral composition and counterions the isolated cationic clusters can be described through the general formula  $[\text{Fe}_x\text{M}_{7-x}\text{O}_3(\text{OMe})(\text{fdc})_6(\text{MeOH})_3]^{n+} \cdot n\text{Cl}^- \cdot (\text{solv})$ . These species are virtually isostructural (with the exclusion of the peripheral ligation) and result in complexes isomorphous to **6**. The most well studied of the series is complex **7**, and it will be used as the structurally representative for the family of clusters **7-10** (Fig. 3-10). The main structural difference between cluster **6** and the series **7-10** is the higher symmetry of the latter for a  $C_3$  rotational axis (along C25, O11 and Mn3) that causes many structural elements to be related by symmetry.

The crystallographic equivalence of many metal ions represented a problem for the conclusive identification of the oxidation states by BVS. In fact, the BVS analysis for these clusters indicated ambiguous oxidation states. In the case of complex **7**, for

example, application of the BVS method for Mn or Fe ions led to oxidation states intermediate between +2 and +3, Tab. 3-4.

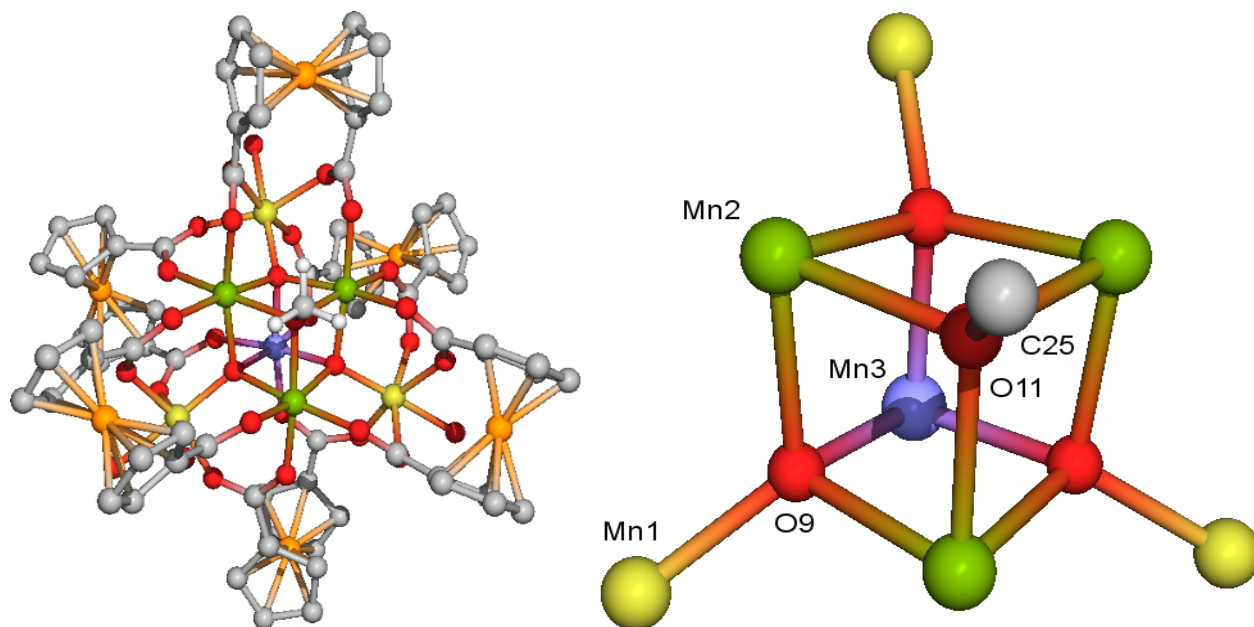


Figure 3-10. Pov-Ray projection of the cluster cation **7** (left) and its labeled core (right). In the core, all the metal ions related by symmetry have the same color.

Table 3-4. Bond Valence Sum calculations for complex **7** according to the Mn and Fe parameters.

Atom	Mn <sup>II</sup>	Mn <sup>III</sup>	Mn <sup>IV</sup>	Fe <sup>II</sup>	Fe <sup>III</sup>
Mn1	3.22	2.97	2.91	2.77	2.96
Mn2	2.66	2.45	2.40	2.28	2.44
Mn3	3.05	2.81	2.76	2.61	2.80

Due to the uncertainty in the determination of **7-10** metal composition by X-ray analysis, a Cl microanalysis was obtained with the purpose of achieving information on the total charge. The data allowed for the complete formulation of the counter ions, but leaving unclear the exact metal composition (Tab. 3-5). As mentioned previously in the chapter, only **7** was fully characterized with the further microanalysis for Mn and Fe.

The crystalline product for the reactions with the larger ions Cd<sup>II</sup>, Hg<sup>II</sup>, Ce<sup>III</sup> and Ca<sup>II</sup> showed the same structural topology as **7**. However, in this case all metal ions could be

clearly identified as iron ions due to the relatively small electronic density compared to Cd, Hg, Ce and Ca. Additional crystallographic data for **6** are listed in appendix C.

Table 3-5. Counterion composition for **7-10** obtained by Cl microanalysis.

Compound	Composition
<b>7</b>	$[\text{Fe}_{6.2}\text{Mn}_{0.8}\text{O}_3(\text{OMe})(\text{fdc})_6(\text{H}_2\text{O})_3]^+ \cdot \text{Cl}^-$
<b>8</b>	$[\text{Fe}_x\text{Co}_{7-x}\text{O}_3(\text{OMe})(\text{fdc})_6(\text{MeOH})_3]^{2+} \cdot 2\text{Cl}^- \cdot \text{solv}$
<b>9</b>	$[\text{Fe}_x\text{Ni}_{7-x}\text{O}_3(\text{OMe})(\text{fdc})_6(\text{MeOH})_3]^+ \cdot \text{Cl}^- \cdot \text{solv}$
<b>10</b>	$[\text{Fe}_x\text{Zn}_{7-x}\text{O}_3(\text{OMe})(\text{fdc})_6(\text{MeOH})_3]^+ \cdot \frac{1}{2}[\text{ZnCl}_4]^{2-} \cdot \text{solv}$

The complete composition for **8-10** has not been established.

### Magnetochemistry of the Heptanuclear Clusters $[\text{M}_7\text{O}_3(\text{OMe})(\text{fdc})_6(\text{MeOH})_3]^{n+}$

Variable temperature magnetic susceptibility ( $\chi_M$ ) data were acquired in the range 5.0 to 300 K with a steady magnetic field of 1kOe (0.1 T) for the clusters **6-10**. The samples were prepared as described in the experimental section and analyzed for their  $\chi_M T$  vs. T profile. Figure 3-11 reports the behavior of cluster **7** which shows a steady decrease of the  $\chi_M T$  value from  $16.39 \text{ cm}^3\text{Kmol}^{-1}$  at 300 K to  $7.56 \text{ cm}^3\text{Kmol}^{-1}$  at 40 K. Past this temperature the  $\chi_M T$  is essentially constant. The magnetic data for **6** include the contribution of the paramagnetic high spin anion  $[\text{FeCl}_4]^-$ , which has  $S = 5/2$  and a  $\chi_M T$  of  $\sim 4.38 \text{ cm}^3\text{Kmol}^{-1}$  (for  $g = 2$ ). In an attempt to remove the contribution of this paramagnetic entity, a sample of  $[\text{NEt}_4][\text{FeCl}_4]$  was prepared according to a literature procedure<sup>178</sup> and measured in the same conditions. With the assumption of an independent magnetic behavior of the cationic cluster and its counterion, the  $\chi_M T$  for  $[\text{FeCl}_4]^-$  was subtracted from the  $\chi_M T$  of **6**.

The assumption of minimal exchange interactions between the cluster and its ferric cation is supported by observation of only weak Cl...H-C contacts to cyclopentadienyl units in the lattice. The net susceptibility for the cluster decreases steadily from  $11.62 \text{ cm}^3\text{Kmol}^{-1}$  at 300 K to  $3.17 \text{ cm}^3\text{Kmol}^{-1}$  at 40 K and raises again

after this point to  $4.37 \text{ cm}^3\text{Kmol}^{-1}$  at 1.8K. The latter behavior is most probably an artifact originated from the  $\chi_{\text{M}}T$  subtraction. It is evident from the  $\chi_{\text{M}}T$  plot that the  $[\text{FeCl}_4]^-$  units have some intermolecular interactions below 40 K that cause an apparent decrease in the measured  $\chi_{\text{M}}T$ .

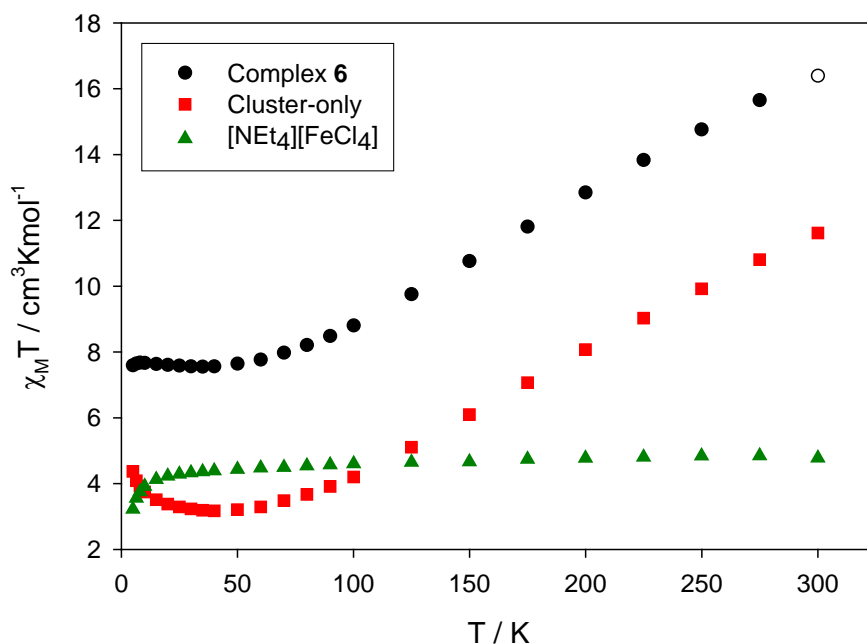


Figure 3-11. Direct current measurement of  $\chi_{\text{M}}T$  vs.  $T$  for  $6 \cdot 8\text{H}_2\text{O} \cdot 6\text{MeOH}$ . The plot also displays the behavior of only the cationic cluster by subtraction of the  $[\text{FeCl}_4]^-$   $\chi_{\text{M}}T$ .

It is then appropriate to consider the  $\chi_{\text{M}}T$  value at 40K as the low-temperature plateau for the cation of  $6 \cdot 8\text{H}_2\text{O} \cdot 6\text{MeOH}$  (which differs by  $4.39 \text{ cm}^3\text{Kmol}^{-1}$  from that of the anion-cation pair,  $4.3 \text{ cm}^3\text{K mol}^{-1}$  being the expected value for the anion). The data just obtained are indicative of an  $S = 2$  ground state with  $g \approx 2.05$ . The  $\chi_{\text{M}}T$  profile indicates strong antiferromagnetic interactions within the  $\text{Fe}^{\text{III}}$  core ions and the ground state can be explained by the antiferromagnetic coupling of a net  $S = 5/2$  spin on core with a  $S = 1/2$  of one oxidized  $\text{fcd}^-$  ligand. The value of  $g$ , slightly higher than 2, is common for high spin  $\text{Fe}^{\text{III}}$  systems and it is also in agreement with the  $g > 2$  generally

found in ferricenyl groups.<sup>179-181</sup> The low symmetry of the cluster cation and the relatively large number of possible pairwise exchange parameters ( $J_{ij}$ ) hinder the application of the matrix diagonalization for the fitting of the  $\chi_M T$  vs.  $T$  data as well as the Kambe vector coupling method.<sup>32</sup>

The ground state was also evaluated by alternating current measurements in the 1.8-15K range with a 3.5 Oe oscillating field at 50, 250 and 997 Hz. This determination has the advantage of avoiding complications from an applied steady field. In the case of an absent out-of-phase component of the magnetization ( $\chi_M''$ ), the in-phase signal ( $\chi_M'$ ) corresponds to the DC  $\chi_M T$  allowing for its determination in the absence of an external DC field. Figure 3-12 shows the  $\chi_M T$  vs.  $T$  plot of **6** as well as the  $\chi_M''$  which is confirmed to be negligible throughout the observed temperature range. The  $\chi_M T$  vs.  $T$  plot appears almost  $T$  independent with a value of  $\sim 8 \text{ cm}^3 \text{Kmol}^{-1}$  down to  $\sim 5 \text{K}$ , below which it decreases slightly to  $\sim 7.3 \text{ cm}^3 \text{Kmol}^{-1}$ . The effect of decreasing  $\chi_M T$  may result from a combination of weak inter-ionic exchange interactions and zero-field splitting. The net value for  $\chi_M T$  is obtained again by subtraction of the  $\chi_M T$  for  $[\text{FeCl}_4]^-$  ( $4.38 \text{ cm}^3 \text{Kmol}^{-1}$ ) to that for **6** and is  $\sim 3.6 \text{ cm}^3 \text{Kmol}^{-1}$ . This value is slightly higher than the one found for the corresponding measurement in the dc field ( $3.1 \text{ cm}^3 \text{Kmol}^{-1}$ ). This could be due to experimental errors and some degree of magnetic interaction between the cationic cluster and its counterion. Such discrepancy, although significant, does not affect the correct identification of the spin ground-state, because of the substantial difference from other possible values of  $S = 1$  and  $S = 3$  with expected  $\chi_M T$  value of  $1.0 \text{ cm}^3 \text{Kmol}^{-1}$  and  $6.0 \text{ cm}^3 \text{Kmol}^{-1}$ , respectively. Hence the assignment of  $S = 2$  with  $g > 2$  for **6** is confirmed.

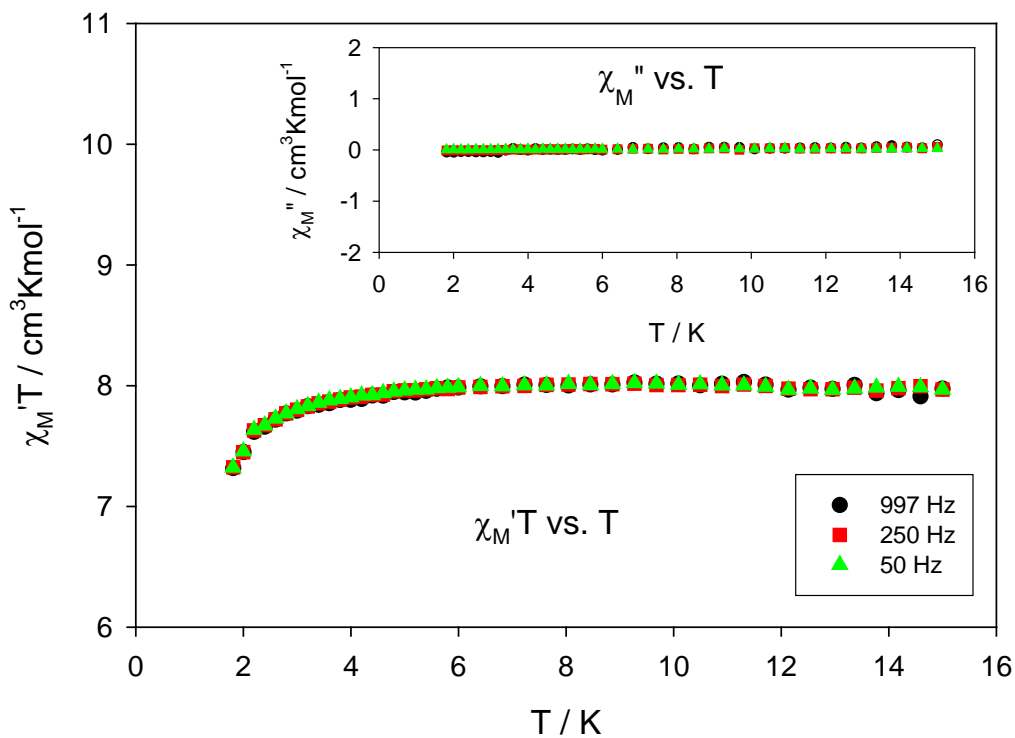


Figure 3-12. Magnetic susceptibility plot for **6** with AC fields. The inset shows the out-of-phase component ( $\chi_M''$ ), while the main plot represents the in-phase component of  $\chi_M' T$  vs.  $T$ .

The software MAGNET<sup>140</sup> failed in producing a good fit for the reduced magnetization data collected for complex **6**. Possible reasons are low-temperature inter-ionic interactions, low spin values, and presence of a ferricenyl unit for its  $g$  substantially higher than 2. The magnetic studies on the remaining isomorphous clusters were performed following the same type of approach for **6**. Figure 3-13 shows the behavior of the heptanuclear family of clusters in a variable temperature DC field measurement where a strong component of the antiferromagnetic interactions throughout the series can be observed the steady and steep decrease of the in-phase magnetic susceptibility. The data follow approximately the same profile for the decreasing of  $\chi_M T$  vs.  $T$ , from an initial  $\chi_M T$  value at of  $\sim 12 \text{ cm}^3 \text{K mol}^{-1}$  300 K down to  $\sim 2.4 \text{ cm}^3 \text{K mol}^{-1}$  at 5 K. The only exception is for compound **10**, for which the  $\chi_M T$  appears shifted to a lower value

throughout the temperature range by  $\sim 1.4 \text{ cm}^3\text{Kmol}^{-1}$ , hence beginning at  $\sim 10 \text{ cm}^3\text{Kmol}^{-1}$  at 300 K and ending at  $\sim 1 \text{ cm}^3\text{Kmol}^{-1}$  at 5 K..

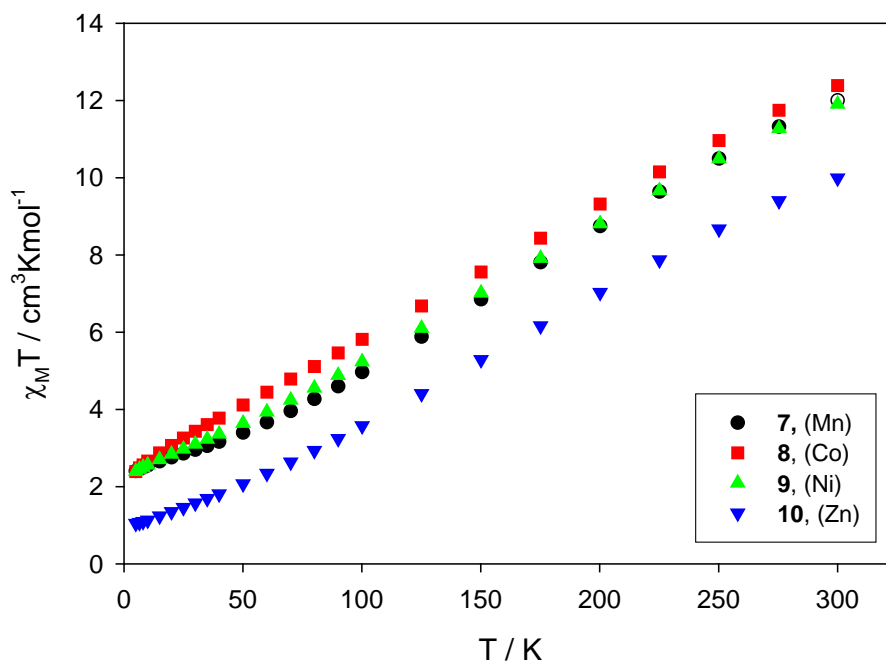


Figure 3-13. Direct current measurement of  $\chi_M T$  vs. T for **7**- $5\text{H}_2\text{O}$ - $4\text{MeOH}$ , **8**-solv., **9**-solv. and **10**-solv.

The uncertainty in the determination of the molecular mass for compounds **8-10** may be cause of a slight vertical shift of the data leaving the overall profile unchanged. However, due to the relatively small variation in mass by passing from an iron for example to a manganese one, the measurement should still allow for qualitative observations. While compounds **7-9** converge to approximately the same low-temperature value for the  $\chi_M T$  of  $\sim 2.2 \text{ cm}^3\text{Kmol}^{-1}$  at 0 K, **10** converge to a  $\chi_M T$  value of  $\sim 1$  at the same temperature, hence suggesting for the latter a spin ground-state  $S = 1$ . Alternating current measurements for the detection of the in-phase and out-of-phase signals confirmed for the clusters **7-10** a similar behavior in the low-temperature region (Fig. 3-14). The plot of  $\chi_M T$  vs. T shows an almost linear decay up to  $\sim 2.4 \text{ cm}^3\text{Kmol}^{-1}$  at 1.8 K for **7-9**, whereas the lowest temperature value for **10** is  $\sim 1.1 \text{ cm}^3\text{Kmol}^{-1}$ .

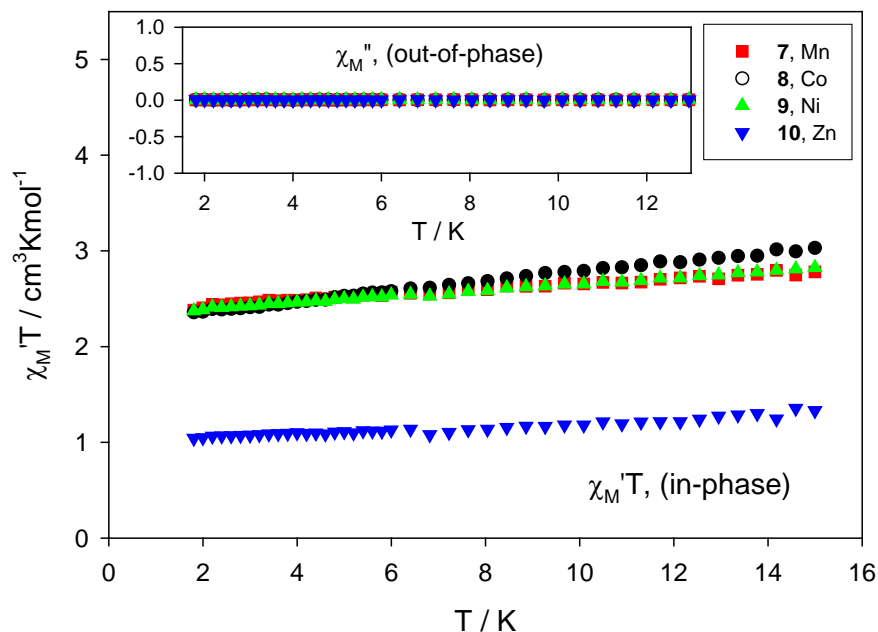


Figure 3-14. AC (in-phase)  $\chi_M'T$  vs. T and (out-of-phase)  $\chi_M''$  vs. T (inset) plots for **7-10** at 250Hz.

The AC in-phase confirms compound **10** to possess a spin ground-state  $S = 1$ , while showing still overlapping data in the low temperature region for **7-9**. The uncertainties in composition and oxidation states of the core do not allow for a unique prediction of the possible spin value. Extrapolation to 0 K of the  $\chi_M'T$  vs. T leads to  $\sim 2.35$   $\text{cm}^3\text{Kmol}^{-1}$  suggesting two close values for the spin ground-state:  $S = 2$  with  $g = 1.8$  ( $\chi_M'T = 2.43$   $\text{cm}^3\text{Kmol}^{-1}$ ) and  $S = 3/2$  with  $g = 2.2$  ( $\chi_M'T = 2.27$   $\text{cm}^3\text{Kmol}^{-1}$ ). In this case, the large presence of iron in the core supports the  $S = 3/2$  because of the  $g > 2$ , typical of high spin  $\text{Fe}^{\text{III}}$ .

### Mössbauer Spectroscopy of the $[\text{M}_7\text{O}_3(\text{OMe})(\text{fdc})_6(\text{MeOH})_3]^{n+}$ Clusters

Mössbauer studies have been employed as a reliable source for oxidation states of iron centers as well as their chemical environment. The  $^{57}\text{Fe}$  Mössbauer spectra is sensitive to the number and different types of iron atoms based on the oxidation state and chemical environment. The spectrum of compound **6** is a complex case to analyze

due to the elaborate structure and variety of iron sites related by virtual symmetry and difference in oxidation state. The main features that are expected for

$[\text{Fe}_7\text{O}_3(\text{OMe})(\text{fdc})_6(\text{MeOH})_3]^{3+} \cdot [\text{FeCl}_4]^- \cdot 2\text{Cl}^-$  are:

- Five  $\text{Fe}^{\text{II}}$  ferrocenyl sites within the  $\text{fdc}^{2-}$  ligands. These give rise to characteristic doublets with quadrupole splitting  $\Delta E_Q > 2.0$  mm/s.<sup>182</sup>
- One  $\text{Fe}^{\text{III}}$  ferricenyl site within the  $\text{fdc}^-$  ligand. For these,  $\Delta E_Q$  is relatively small.<sup>182</sup> In pure ferricenium complexes,  $\Delta E_Q \approx 0.0$  mm/s whereas in mixed-valence complexes in a trapped-valence situation,  $\Delta E_Q \approx 0.4$  mm/s for the ferricenium moiety.<sup>183</sup>
- Seven high-spin  $\text{Fe}^{\text{III}}$  sites of the octahedral  $\text{FeO}_6$  type. The isomer shift is expected to be 0.45 - 0.50 mm/s at 78K with a moderate  $\Delta E_Q$  ( $\approx 0.4 - 0.6$  mm/s).<sup>182</sup>
- One  $\text{Fe}^{\text{III}}$  site within the  $[\text{FeCl}_4]^-$  anion. The isomer shift of this four coordinated ferric site is smaller than that of the octahedral sites and  $\Delta E_Q$  is negligible.<sup>184</sup>

According to this description the Fe sites that would be most readily resolved are the five ferrocenyl groups due to their large  $\Delta E_Q$  as compared to the ferricenyl group. On the other hand, the  $[\text{FeCl}_4]^-$  counter ion as well as the  $\text{fdc}^{-1}$  will be hard to detect due to their overall small contribution ( $\sim 7\%$  each). The Mössbauer spectrum of **6** was collected at 140 and 250 K and consists of two quadrupole doublets (Fig. 3-15). The spectrum at 250 K displays well-resolved peaks of an outer doublet with lines at  $-0.62$  and  $+1.56$  mm/s each having small line-width (FWHM  $\approx 0.25$  mm/s). The high resolution of these peaks allows for their parameters and total contribution to be estimated with high accuracy. The isomer shift ( $\delta = 0.48 \pm 0.02$  mm/s) and quadrupole splitting ( $\Delta E_Q = 2.16 \pm 0.02$  mm/s) are in agreement with the values expected for a ferrocene species, hence the outer doublet signal is assigned to the  $\text{fdc}^{2-}$  units. The small line width of these peaks suggests a site with a narrow distribution of energies, which despite the different orientations is predicted by theoretical calculations.<sup>185</sup> The remaining portion of

the spectrum is occupied by a relatively broad and asymmetric doublet whose peaks are located at +0.20 mm/s and +0.65 m/s with an average  $\Delta E_Q$  of  $\sim 0.40$  mm/s and an average  $\delta$  of  $\sim 0.45$  mm/s. This portion of the spectrum is comprising all the signals from the seven  $\text{FeO}_6$  sites, the  $[\text{FeCl}_4]^-$  anion and the ferricenyl moieties. The data in this case cannot be resolved to individual contributing signals that would allow for an unambiguous characterization of the  $\text{Fe}^{\text{III}}$  species.

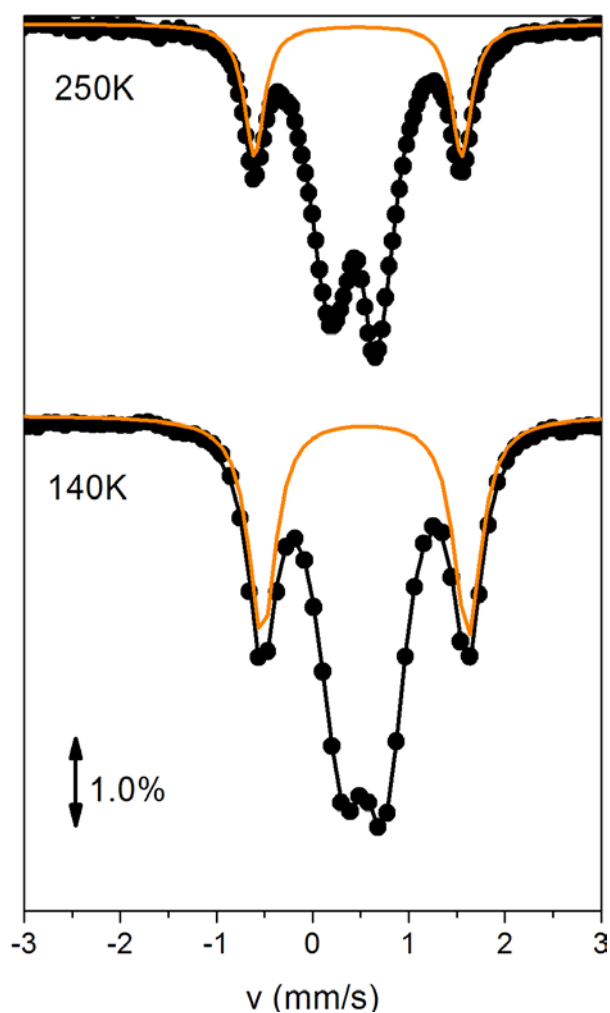


Figure. 3-15. Overlay of the Mössbauer spectra collected at 250 and 140 K for sample 6.

The outer doublet assigned to the  $\text{fdc}^{2-}$  units, accounts for only 22% of the total iron signal at 250 K. This value is much lower than the expected  $\sim 36\%$  for five  $\text{fdc}^{2-}$

ligands on each molecule. In fact, this value is predicted for only three  $\text{fdc}^{2-}$  per molecule (theoretically  $\sim 21\%$  of total iron), and contrasts with other analytical data. It is believed that different Debye-Waller factors are associated with different iron sites. The literature reports examples of molecules featuring a biferrocenium where the latter was reported having a smaller Debye-Waller factor than other iron sites.<sup>186</sup> According to this observation it is believed that in **6**, due to the smaller Debye-Waller factor, the contribution of the  $\text{fdc}^{2-}$  units is underestimated as compared to the other sites. To prove this assumption, a Mössbauer spectrum at lower temperature (i.e., 140 K) was collected and checked for an increased contribution from the ferrocenyl sites (Fig. 3-15). The obtained spectrum is very similar to the one at 250 K, however, as proposed, the contribution of the  $\text{fdc}^{2-}$  sites has increased to 31 %. The different dependence of the Debye-Waller factor with the temperature for  $\text{fdc}^{2-}$  and the other  $\text{Fe}^{\text{III}}$  sites, implies that this parameter increased faster for the  $\text{fdc}^{2-}$  units than it did for other sites in the same temperature range. Further lowering of the temperature up to 4.2 K increased the contribution of the ferrocenyl units to 35 %, consistent with the theoretical value for five  $\text{fdc}^{2-}$  groups.

The Mössbauer spectra of the compounds **7-10** display a singular similitude with each other. For reasons already explained, it is not possible to distinguish the contributions from different sites that result in the central doublet. However, the spectra of **7-10** support a relatively large presence of Fe in the core with a slight diminished contribution from ferric ions to the central doublet when compared to **6**. Furthermore, the similarity of the spectra in Fig. 3-16 suggests a very close  $\text{fdc}^-/\text{fdc}^{2-}$  ratio for the four cluster cations **7-10**.

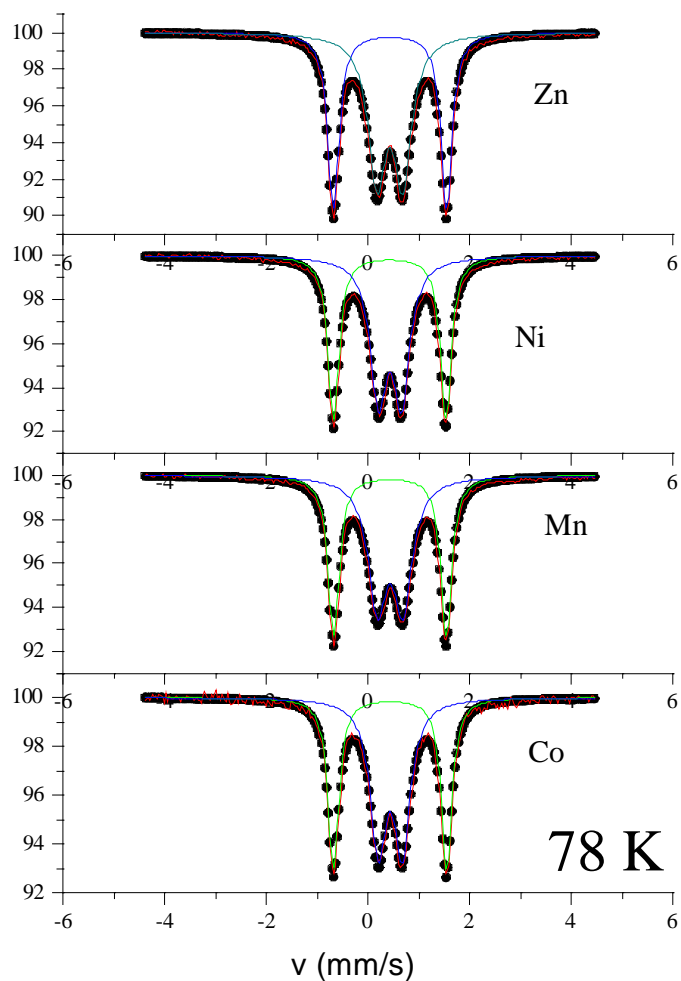


Figure 3-16. Superposition of Mössbauer spectra for **7-10** at 78 K.

### Electrochemistry of the $[M_7O_3(OMe)(fdc)_6(MeOH)_3]^{n+}$ Clusters

The large variety of metal centers and ferrocenyl units is of great interest for electrochemical investigations. For this purpose, a freshly prepared crystalline sample of **6** was dried under vacuum and used to obtain a solution in dry acetonitrile and used in a standard three-electrode electrochemical cell. The concentration of the analyte reached saturation before the intended concentration of 1 mM due to its limited solubility in acetonitrile. Figure 3-17 shows the cyclic voltammogram (CV) at 100 mV/s (top) and the differential pulse voltammogram (DPV) at 20 mV/s (bottom).

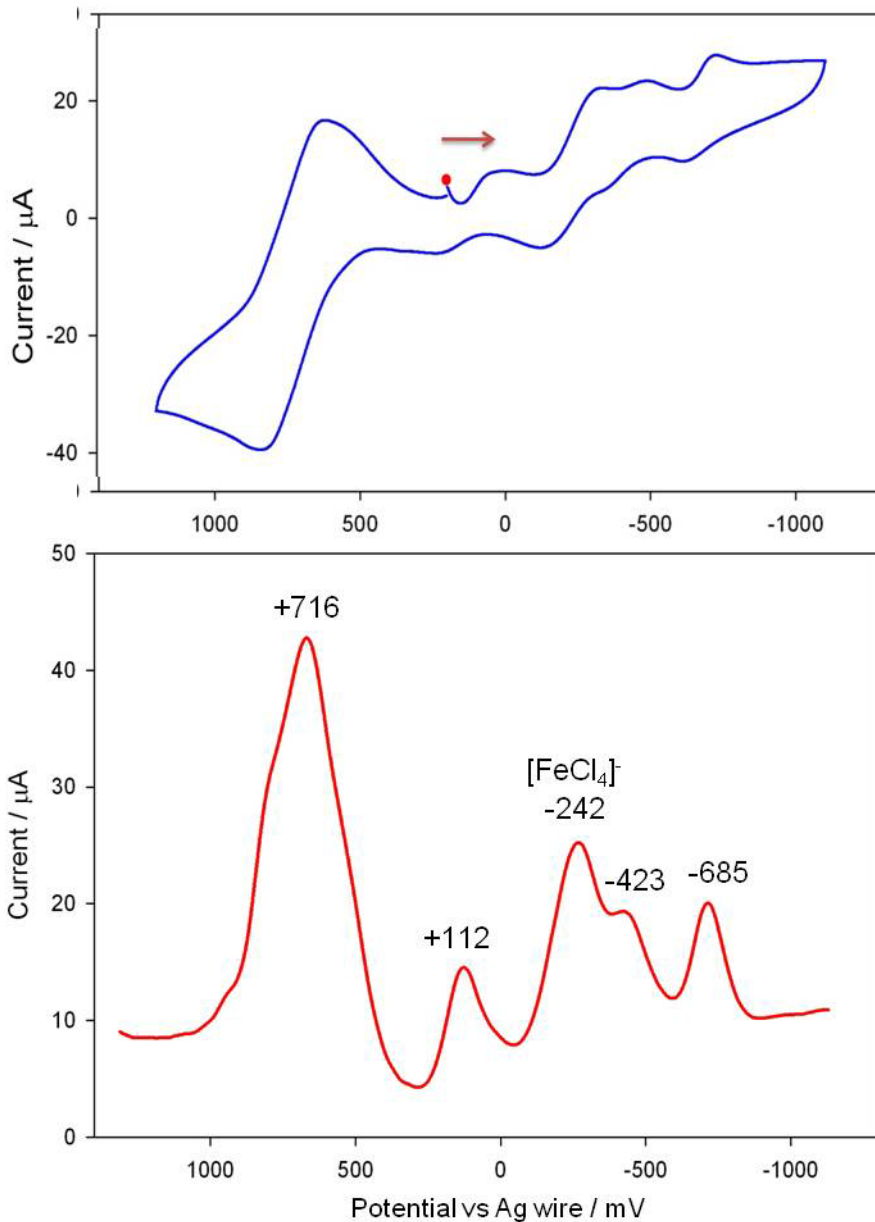


Figure 3-17. Cyclic voltammogram (CV, top) and differential pulse voltammogram (DPV, bottom) of **6** in acetonitrile ( $n\text{-Bu}_4\text{NPF}_6$  0.1 M as supporting electrolyte).

As it is clear from the plots, cluster **6** displays a rich electrochemical behavior corresponding to four reversible reductions and a single envelope for multiple oxidations. The second and third reduction peaks overlap, however, both seem to involve single-electron processes and in particular the one localized at -242 mV takes place on the counterion  $[\text{FeCl}_4]^-$ . The latter was identified by comparison with the redox

behavior of  $[\text{NEt}_4][\text{FeCl}_4]$  in the same conditions of solvent and electrolyte. While the three reduction processes on the cluster cation are considered to happen at the core ions, the large oxidation peak is attributed to the almost simultaneous oxidation of the  $\text{fdc}^{2-}$  groups. Upon starting the measurement at the rest potential (+195 mV vs.  $\text{fc}/\text{fc}^+$ ) there is a spike in the current which can be assigned to the reduction of one oxidized  $\text{fdc}^-$  ligand. Thus the large oxidation should be consistent with the overlapping of six single-electron oxidations of the  $\text{fdc}^{2-}$ . The  $\text{fdc}^{2-}$  groups behave near-independently and hence are being oxidized essentially at the same potential. Confirmation of this assignment is obtained through the measurement of the peak heights showing a ratio of 10:1 (rather than a 6:1) for the oxidation vs. reduction features. This mismatch can be caused by different electron transfer kinetics from the outer  $\text{fdc}^{2-}$  redox sites with respect to the inner ones. A difference can also be appreciated by comparing the reduction of the counterion  $[\text{FeCl}_4]^-$  with a sharper and higher peak than the other reduction peaks.

DPV plots provide better resolution of the redox processes. In this case the measurement is performed against a silver wire reference electrode, with the redox couple  $\text{fc}/\text{fc}^+$  at +180 mV. The large oxidation peak exhibits shoulders which confirm its origin from overlapping separate features, consistent with the two sets of  $\text{fdc}$  groups by symmetry and a minor degree of electronic communication among the groups. Considering all the redox processes localized on the cation of cluster **6**, it is possible to access ten oxidation levels ranging from the fully oxidized form  $[\text{Fe}^{\text{III}}_7(\text{fdc}^-)_6]^{15+}$ , through the isolated  $[\text{Fe}^{\text{III}}_7(\text{fdc}^-)(\text{fdc}^{2-})_5]^{10+}$ , to the  $[\text{Fe}^{\text{III}}_4\text{Fe}^{\text{II}}_3(\text{fdc}^{2-})_6]^{6+}$  reduced level. Application of the same technique to clusters **7-10** produced very similar results with minor changes

in the redox potentials and the absence of reduction peaks due to redox active counterions.

### Conclusions

The reactions of  $\text{fdCH}_2$  with  $\text{Fe}^{\text{II}}$  or  $\text{Fe}^{\text{III}}$  sources have proved to be very challenging due to the formation of amorphous precipitates that are essentially insoluble in all inert solvents. This is probably due to the formation of polymeric products, a situation that is commonly encountered in the chemistry of  $\text{fdc}^{2-}$ . However, it should also be noted that neutral molecular compounds of  $\text{fdc}^{2-}$  are also often very insoluble, such as the  $\text{Mn}_{13}$  and  $\text{Mn}_8$  clusters described in Chapter 2 and that has unfortunately precluded their study in solution. Nevertheless, the slow reaction of  $\text{fdCH}_2$  with  $\text{FeCl}_2$  also gives a more soluble fraction that was crystallized and characterized as  $\mathbf{6} \cdot 8\text{H}_2\text{O} \cdot 6\text{H}_2\text{O}$ . The solubility is undoubtedly assisted by its cationic nature. The photo-release of Fe from  $\text{fdCH}_2$  was shown to occur and give  $\mathbf{6}$  or mixed-metal analogs when other metal reagents were employed (for example **7-10**); in fact, there are literature studies attempting to characterize the photodecomposition products of  $\text{fdCH}_2$ ,<sup>169,187-188</sup> and under the conditions of this study at least they drive the formation of the cation of  $\mathbf{6}$ .

The unusual nature of  $\mathbf{6}$  was immediately evident from its blue color, hence it can be concluded from the various data that it contains one oxidized  $\text{fdc}^-$  ligand. This is the first example of this ligand in inorganic chemistry. There is one other claim of a  $\text{fdc}^-$  ligand, in the compounds  $[\text{Zn}_6\text{O}_2(\text{fdc})_5(\text{H}_2\text{O})(\text{DMF})]$  and  $[\text{Zn}_8\text{O}_4(\text{fdc})_6(\text{H}_2\text{O})_3]$  made by hydrothermal reaction of  $\text{fdCH}_2$  with  $\text{Zn}(\text{NO}_3)_2$ ,<sup>107</sup> however, the reported magnetic data and the dark red color are not consistent with  $\text{fdc}^-$  and it could be possible that some of the Zn sites are occupied by  $\text{Fe}^{\text{III}}$  released from  $\text{fdc}^{2-}$  under the high energy reaction conditions. The electrochemical studies indicate a new class of compound that has rich

redox behavior, and that offers possibility of being isolated and characterized at different oxidation levels. However, considering the low yield of **6**, this requires a route to greater amounts of cluster than are currently available. Nevertheless, the incorporation of multiple  $\text{fdc}^n$  ligands into magnetic metal clusters has the potential for interesting new magnetic and redox behavior.

### Experimental

All manipulations were performed under aerobic conditions, using materials as received, except otherwise stated. All experiments were initially carried in the presence of light and then repeated later in the dark during both reaction and crystallization periods. This procedure was applied to ensure the role of light in reactions with the ferrocenyl ligand.

#### **$[\text{Fe}_7\text{O}_3(\text{OMe})(\text{fdc})_6(\text{MeOH})_3]^{3+} \cdot [\text{FeCl}_4]^- \cdot 2\text{Cl}^- \cdot 8\text{H}_2\text{O} \cdot 6\text{MeOH}$ ; (**6**) $\cdot 8\text{H}_2\text{O} \cdot 6\text{MeOH}$**

A suspension of  $\text{fdcH}_2$  (0.25 mmol, 0.067 g) and  $\text{FeCl}_2 \cdot 4\text{H}_2\text{O}$  (0.5 mmol, 0.099 g) in MeOH (25 mL) was allowed to stir under normal laboratory light conditions for 24 h. The initial orange color changed to dark after a few hours. The mixture was filtered on a P2 filter paper from which a dark brown solution was obtained and set for crystallization by slow diffusion with a ether/hexanes (1:1) mixture. Dark blue hexagonal shaped crystals appeared after one week on the walls of the vials. The crystallization was accompanied by the formation of a blue precipitate, which could not be characterized. The crystals were dried under vacuum. Yield: 2 to 5%. The crystals analyze for (**6**) $\cdot 8\text{H}_2\text{O} \cdot 6\text{MeOH}$ . Anal. Calcd. (found) for  $\text{C}_{82}\text{H}_{103}\text{Cl}_6\text{Fe}_{14}\text{O}_{45}$ : C, 35.13 (35.05) %; H 3.70 (3.49) %; Cl 7.59 (7.65) %. Selected IR data (KBr pellet,  $\text{cm}^{-1}$ ): 1575 (vs), 1481 (vs), 1400 (vs), 1362 (s), 1195 (w), 1115 (w), 1082 (w), 1031 (vw), 928 (vw), 832 (vw), 781 (w), 621 (w), 589 (w), 522 (m), 491(m).

**[Fe<sub>6.2</sub>Mn<sub>0.8</sub>O<sub>3</sub>(OMe)(fdc)<sub>6</sub>(H<sub>2</sub>O)<sub>3</sub>]<sup>+</sup>·Cl<sup>-</sup>·5H<sub>2</sub>O·4MeOH; (7)·5H<sub>2</sub>O·4MeOH**

The procedure is identical to that for **6** with the use of MnCl<sub>2</sub>·4H<sub>2</sub>O as metal source in the same stoichiometric amount. The isolation procedure and yield are comparable to that for **6**. The crystals analyze for (7)·5H<sub>2</sub>O·4MeOH. Anal. Calcd. (found) for C<sub>77</sub>H<sub>83</sub>ClMn<sub>0.8</sub>Fe<sub>12.2</sub>O<sub>40</sub>: C, 38.39 (38.28) %; H, 3.47 (3.61) %; Cl 1.47 (1.65) %; Mn 1.82 (1.58) %; Fe 28.28 (28.70) %. Selected IR data (KBr pellet, cm<sup>-1</sup>): 1577 (vs), 1486 (vs), 1395 (vs), 1361 (s), 1197 (w), 1119 (w), 1088 (w), 1029 (vw), 925 (vw), 831 (vw), 777 (w), 627 (w), 585 (w), 524 (m), 493(m).

**[Fe<sub>x</sub>Co<sub>7-x</sub>O<sub>3</sub>(OMe)(fdc)<sub>6</sub>(MeOH)<sub>3</sub>]<sup>2+</sup>·2Cl<sup>-</sup>·solv.; (8)·solv.**

The procedure is identical to that for **6** with the use of CoCl<sub>2</sub>·4H<sub>2</sub>O as metal source in the same stoichiometric amount. The isolation procedure and estimated yield are comparable to that for **6**. Selected IR data (KBr pellet, cm<sup>-1</sup>): 1578 (vs), 1486 (vs), 1395 (vs), 1361 (vs), 1197 (m), 1029 (w), 925 (vw), 831 (w), 778 (m), 630 (w), 586 (w), 523 (s), 492 (w), 451 (w).

**[Fe<sub>x</sub>Ni<sub>7-x</sub>O<sub>3</sub>(OMe)(fdc)<sub>6</sub>(MeOH)<sub>3</sub>]<sup>+</sup>·Cl<sup>-</sup>·solv.; (9)·solv.**

The procedure is identical to that for **6** with the use of NiCl<sub>2</sub>·4H<sub>2</sub>O as metal source in the same stoichiometric amount. The isolation procedure and estimated yield are comparable to that for **6**. Selected IR data (KBr pellet, cm<sup>-1</sup>): 1577 (vs), 1485 (vs), 1397 (vs), 1359 (s), 1196 (w), 1118 (w), 1085 (w), 1030 (vw), 924 (vw), 833 (vw), 774 (w), 624 (w), 586 (w), 524 (m), 492(m).

**[Fe<sub>x</sub>Zn<sub>7-x</sub>O<sub>3</sub>(OMe)(fdc)<sub>6</sub>(MeOH)<sub>3</sub>]<sup>+</sup>·½[ZnCl<sub>4</sub>]<sup>2-</sup>·solv.; (10)·solv.**

The procedure is identical to that for **6** with the use of ZnCl<sub>2</sub> anhydrous as metal source in the same stoichiometric amount. The isolation procedure and estimated yield are comparable to that for **6**. Selected IR data (KBr pellet, cm<sup>-1</sup>): 1577 (vs), 1484 (vs),

1393 (vs), 1362 (s), 1196 (w), 1121 (w), 1089 (w), 1028 (vw), 925 (vw), 832 (vw), 775 (w), 626 (w), 583 (w), 521 (m), 491(m).

### **X-Ray Crystallography**

Data were collected at 173 K on a Siemens SMART PLATFORM equipped with a CCD area detector and a graphite monochromator utilizing MoK $\alpha$  radiation ( $\lambda = 0.71073$  Å). Suitable single crystals of **6**·2MeOH·2Et<sub>2</sub>O, **7**·3DMF·3MeOH, **8**·3MeOH, **9**·4 MeOH and **10**·2MeOH·Et<sub>2</sub>O were attached to a fiber glass using silicone grease and transferred to the goniostat where they were cooled to the temperature indicated above for characterization and data collection. All cell parameters were refined using up to 8192 reflections. A full sphere of data (1850 frames) was collected using the  $\omega$ -scan method (0.3° frame width). The first 50 frames were re-measured at the end of data collection to monitor instrument and crystal stability (maximum correction on I was < 1 %). Absorption corrections by integration were applied based on measured indexed crystal faces.

The structure was solved by the Direct Methods in *SHELXTL*<sup>153</sup>, and refined using full-matrix least squares. The non-H atoms were treated anisotropically, whereas the hydrogen atoms were calculated in ideal positions and were riding on their respective carbon atoms. The asymmetric unit of **6** consists of a Fe<sub>13</sub> cluster cation, and FeCl<sub>4</sub> anion, two methanol and two ether solvent molecules. All the solvent molecules were disordered and could not be modeled properly, thus program SQUEEZE<sup>154</sup>, a part of the PLATON<sup>155</sup> package of crystallographic software, was used to calculate the solvent disorder area and remove its contribution to the overall intensity data. Three of the four chloro ligand of the FeCl<sub>4</sub> anion in **6** are rotationally disordered

and were refined in two parts with their site occupation factors refining to 0.577(2) and 0.423(2) for the major and minor parts, respectively. A total of 1119 parameters were refined for **6** in the final cycle of refinement using 8375 reflections with  $I > 2\sigma(I)$  to yield  $R_1$  and  $wR_2$  of 4.06% and 8.31%, respectively. Refinement was done using  $F^2$ .

The asymmetric unit of **7** consists of a 1/3 of a  $Mn_7$  cluster (located on a 3-fold rotation axis), a dimethylformamide and an methanol molecule. The protons on the coordinated water molecules could not be located in a Difference Fourier map and were not included in the final cycle of refinement. A total of 352 parameters were refined in the final cycle of refinement using 5265 reflections with  $I > 2\sigma(I)$  to yield  $R_1$  and  $wR_2$  of 3.59% and 9.70%, respectively. The asymmetric unit of **8** consists of a third of  $Fe_6Co_7$  cluster and three methanol molecules of crystallization. A total of 366 parameters were refined in the final cycle of refinement using 14255 reflections with  $I > 2\sigma(I)$  to yield  $R_1$  and  $wR_2$  of 2.53% and 6.27%, respectively. The asymmetric unit of **9** consists of a third of  $Fe_6Ni_7$  cluster and four methanol molecules of crystallization. A total of 366 parameters were refined in the final cycle of refinement using 13661 reflections with  $I > 2\sigma(I)$  to yield  $R_1$  and  $wR_2$  of 2.74% and 6.50%, respectively. The asymmetric unit of **10** consists of a 1/3  $Fe_6Zn_7$  cluster cation (clusters are located on 3-fold rotation axes), a 1/6  $ZnCl_4$  dianion (anions located on -3 rotation axes), thus the ratio is 2  $Fe_6Zn_7$  cation to 1  $ZnCl_4$  anion. In the asymmetric unit there is also an ether molecule and two methanol molecules. A total of 381 parameters were refined in the final cycle of refinement using 4282 reflections with  $I > 2\sigma(I)$  to yield  $R_1$  and  $wR_2$  of 7.56% and 19.85%, respectively.

## **Magnetic Measurements**

The magnetic measurements were performed with a Quantum Design MPMS-XL SQUID. The samples were collected in the crystalline form and briefly dried under vacuum. The microcrystalline products were transferred in a gelatin capsule and embedded in eicosane to prevent torquing. The assessment of the solvation composition was done through microanalysis of the freshly prepared microcrystalline product. Unless otherwise stated all the measurements were carried as described. DC susceptibility was obtained in the 5 to 300 K range with an applied field of 0.1 T. AC in-phase and out-of-phase were performed in the 1.8 to 15 K range of temperature with an oscillating field at 50, 250 and 997 Hz and 3.5 G of magnitude. Reduced magnetization data were acquired using low field or high field. In the low field configuration, the magnetization was measured in a set of DC field ranging from 0.1 to 1.0 T, whereas in the high field the magnitude of the applied magnetic vector ranged from 1.0 to 7.0 T. The reduced magnetization procedure and the relative data were appropriately selected to obtain the best fitting profile through the software GRID<sup>141</sup> and MAGNET<sup>140</sup>. The magnetic data for all measurements were corrected for the diamagnetic response of the sample and the eicosane.

## **Other Measurements**

IR spectra were recorded on a Nicolet Nexus 670 FT-IR spectrometer. The samples were prepared as KBr pellet and analyzed in the range 400-4000  $\text{cm}^{-1}$ . Elemental analyses (C, H and N) were performed by the in-house facilities of the University of Florida, Chemistry Department. Chlorine and metal analyses were obtained from Desert Analytics (Tucson, Arizona). Cyclic voltammetry (CV) and differential pulse voltammetry (DPV) were performed with a BASi CV50W

electrochemistry instrument and a three-electrode cell, using dry MeCN as solvent and  $\text{NBu}_4\text{PF}_6$  (0.1 M) as supporting electrolyte. A glassy carbon working electrode (BASi model MF-2012) and a coiled platinum wire as auxiliary electrode were employed, and the reference electrode was Ag wire; under the same conditions, ferrocene was at 0.18 V. The MeCN was distilled over  $\text{CaH}_2$  and stored over activated molecular sieves.  $\text{NBu}_4\text{PF}_6$  was recrystallized in the dark from a  $\text{H}_2\text{O}/\text{EtOH}$  (1:1 v/v) and dried under vacuum.  $^{57}\text{Fe}$  Mössbauer spectra were obtained at NCSR "Demokritos" and were recorded in the constant acceleration mode at temperatures controlled with a Janis cryostat. Isomer shifts are reported relative to iron metal at room temperature set at 0 mm/s.

## CHAPTER 4 NEW APPROACH FOR THE IMPROVEMENT OF THE BOND VALENCE SUM PARAMETERS USING STATISTICAL METHODS

### **Introduction**

Since the work done by Brown and Altermatt on an alternative and more general formulation for the Bond Valence Sum (BVS) method, its application to chemistry and closely related disciplines has grown rapidly.<sup>71</sup> For example, research on superconductivity has adopted BVS to monitor the valence of Cu ions in metal oxide layers resulting from doping reactions.<sup>189</sup> In these cases, the doping directly affects the temperature at which the material acts as a superconductor, thereby making the BVS method of significant importance in this field. In other more exotic studies, BVS was paired with theoretical models to predict acidic strengths (or pKa),<sup>190</sup> probe the presence and strength of H-bonding,<sup>191</sup> or localize preferential regions for proton solvation in a crystalline lattice.<sup>192</sup> Nevertheless, of the several uses found for the BVS method, two areas have been most dominant in its application: metalloenzymes and solid-state materials. In the first case, biological molecules often host metallic ions at the site of enzymatic activity, and the determination of the metals' oxidation state represents a basic requirement for fully understanding the chemical reactivity displayed by this type of system. In this area, Thorp began to explore the use of BVS to interpret EXAFS data on metalloproteins.<sup>193</sup> His studies confirmed the applicability of the method for biological metal sites, albeit with some approximations. The other major applications of BVS span areas ranging from geology to cluster chemistry. Application to polymeric structures, like in mineral chemistry, seems to have a greater accuracy than the non-polymeric molecular systems. Despite some discrepancies found in this last application, BVS is widely used for the determination of the oxidation states in mononuclear or polynuclear

systems. Examples have been shown in the previous chapters, where the method was used to predict the metal oxidation states in complicated polynuclear systems based on crystallographic data. As mentioned in the introductory chapter, the BVS model uses bond lengths between an ion and its first sphere of coordinated atoms to achieve an estimation of the oxidation state. The method assigns to each bond a contribution to the total valence through the existing correlation between bond length and bond strength as described by the formula (1-5), repeated here for convenience as (4-1), where  $r_0$  and  $B$  are empirical parameters and  $r$  is the bond length in Å.

$$s = e^{\frac{r_0 - r}{B}} \quad (4-1)$$

By summing of all the  $s$  values of a coordination sphere, the valence is obtained and it represents an approximation of the formal oxidation state. The empirical values,  $r_0$  and  $B$ , have been calculated and reported for many metal-ligand combinations and different oxidation states.  $B$  is taken as constant with a value of 0.37 Å.<sup>71</sup> For instance, by applying the BVS to a metal ion in the +2 oxidation state with  $r_0$  values appropriate for that oxidation state, the sum of all its bond valences (each obtained through Eq. 4-1) will lead to a value close to the integer two. The same calculation applied with  $r_0$  parameters for another oxidation state will tend to the integer two, but with a larger discrepancy.

The initial calculations for  $r_0$  and  $B$  made by Brown and Altermatt were based on crystallographic data obtained on inorganic ionic crystalline lattices with homoleptic metal ions. In this context, the term homoleptic would refer only to the first coordination sphere.<sup>71</sup> The relatively limited number of high quality crystal structures and the choice

of metal ions with the same environment has led to a set of parameters that fit accurately for the same type of structures, but they do not work as well when applied to molecular systems. Shortly after the introduction of BVS application to metalloenzymes, Thorp and coworkers realized that the  $r_0$  parameters could be improved for biomolecules.<sup>194</sup> The extensive application of the BVS approach to mononuclear and polynuclear systems has suggested an analogous procedure for improvement by modifying the  $r_0$  parameter. It is now possible to find reports that describe efforts aiming towards more tailored values of  $r_0$  (and B in some instances).<sup>195-197</sup> In most cases, application of the BVS to metallic clusters results in negligible discrepancies from integer values but in some other situations the method fails completely. The cluster  $[\text{Co}_8\text{O}_4(\text{O}_2\text{CPh})_{12}(\text{H}_2\text{O})(\text{MeCN})_3]$ , for example, has a Co-oxo core crystallographically described by eight different cobalt ions. From neutrality considerations the core is described as  $[\text{Co}^{\text{III}}_4\text{Co}^{\text{II}}_4\text{O}_4]^{12+}$  (Fig. 4-1).<sup>151</sup>

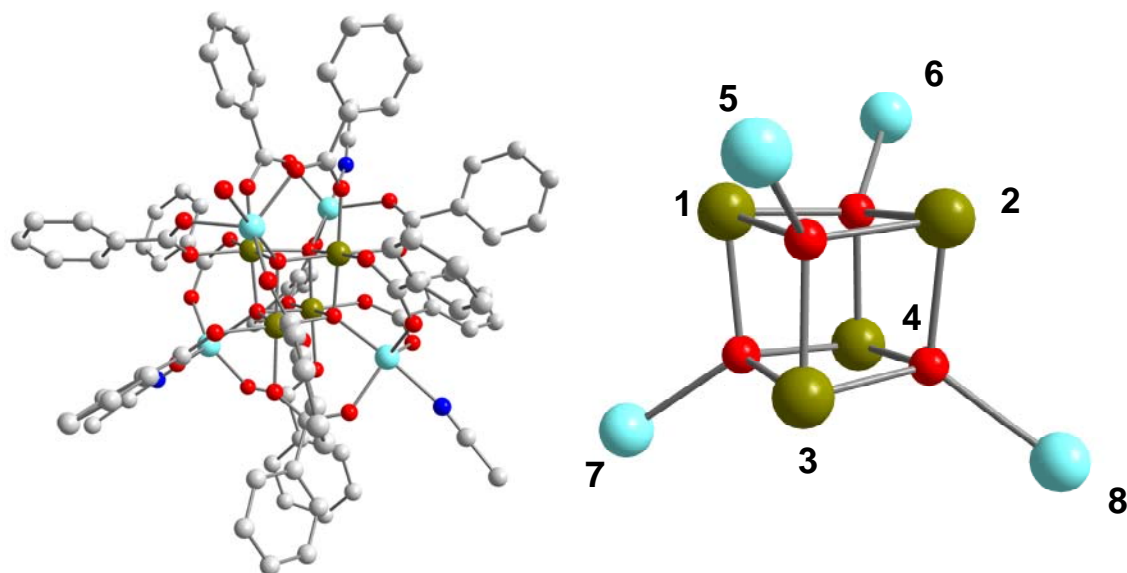


Figure 4-1. Pov-Ray projection of  $[\text{Co}_8\text{O}_4(\text{O}_2\text{CPh})_{12}(\text{H}_2\text{O})(\text{MeCN})_3]$  (left) and its core (right). The numbers identify the crystallographic label of the metal ions.<sup>151</sup>

The literature reports the following data for Co BVS:  $r_0$  (Co<sup>II</sup>-O) = 1.70 Å,  $r_0$  (Co<sup>III</sup>-O) = 1.692 Å and  $r_0$  (Co-N) = 1.84 Å (with the assumption of B = 0.37 Å).<sup>131</sup> Table 4-1 shows the obtained valence values for these metal ions. The atoms Co1-Co4 are Co<sup>III</sup> species, whereas the remaining Co5-Co8 are Co<sup>II</sup>. The BVS indicates a valence close to the expected value only for Co5, Co7 and Co8. All other atoms have significantly higher values than the expected, making the BVS approach of little use for this cluster.

Table 4-1. Expected and calculated Co valences in [Co<sub>8</sub>O<sub>4</sub>(O<sub>2</sub>CPh)<sub>12</sub>(H<sub>2</sub>O)(MeCN)<sub>3</sub>] based on published data.<sup>131,151</sup>

Atom	Actual oxidation state	BVS value as Co <sup>II</sup>	BVS value as Co <sup>III</sup>
1	+3	3.32	3.39
2	+3	3.39	3.47
3	+3	3.39	3.47
4	+3	3.39	3.46
5	+2	1.97 *	2.01
6	+2	2.35	2.39
7	+2	2.18 *	2.21
8	+2	2.15 *	2.19

The numbers with an asterisk represent the only values close to the actual oxidation state.

Although it could be hypothesized that the presence of mixed-valency is leading to intermediate average oxidation states, the authors exclude this possibility and in any case the ligation would not support the total charge for the core ( $\approx +14.4$ ) suggested by BVS. Despite the two different values for the  $r_0$  in the case of Co coordination to oxygen and only one for the coordination to nitrogen, the data show better accuracy for Co ions bonded to nitrogen. It is likely that the proposed  $r_0$  parameters are better suited for a polymeric type of Co environment rather than a molecular system. To test this hypothesis, the calculation was reversed and the corresponding  $r_0$  values were obtained for the expected Co oxidation states of Co<sub>8</sub>. Also, it was believed that this could provide numbers more suitable for applying the BVS method for other similar molecular Co

systems. The reversal of the BVS formula leading to  $r_0$  for a metal ion implies the solution of a system of equations as shown in Eq. 4-2.

$$\begin{cases} R_0 = r_i + b \cdot \ln(v_i) \\ R_0 = r_j + b \cdot \ln(v_j) \\ \dots \\ R_0 = r_z + b \cdot \ln(v_z) \\ V = v_i + v_j + \dots + v_z \end{cases} \quad (4-2)$$

In Eq. 4-2,  $V$  is the final valence of a metal ion,  $r_i$  and  $v_i$  are the bond distance the partial valence for the  $i^{\text{th}}$  ligand atom, respectively, and  $b = B$  (0.37 Å). The new  $r_0$  (or  $R_0$ ) for  $\text{Co}^{\text{III}}$  has been calculated as the average of the four different  $r_0$  values (obtained by use of Eq. 4-2) each belonging to one of the four different  $\text{Co}^{\text{III}}$  ions in the  $\text{Co}_8$  cluster, and is equal to 1.644 Å (compared with the current 1.692 Å). As expected, application of the new  $r_0$  on the same metal ions for which it was obtained leads to values very close to their actual valence (Co1 = 3.132, Co2 = 2.978, Co3 = 2.970 and Co4 = 2.917). Since the same metal ions in a similar coordination environment will produce similar  $r_0$  values, the averaged  $r_0$  found will be a suitable parameter for similar molecular systems. It should be noted that the extraction of an  $r_0$  from a homoleptic ion, as in the case of the  $\text{Co}^{\text{III}}$  ions of  $\text{Co}_8$ , will not account for the influence of one type of ligand over another for the same oxidation state.

It is thus evident that although the current tabulated  $r_0$  and  $B$  are fairly effective in the estimation of the valence, they may require further modification for molecular systems on which they will be applied. Reasons for significant discrepancies of the BVS values from the expected ones cannot easily be explained; however, they might be due to the main differences existing between a polymeric system and a molecular system. In

the first type of arrangement, metal ions show a relatively limited number of coordination numbers, lie in generally high symmetry environments, and experience fewer distortions than in a molecular system. The infinite lattice in a mineral generally represents a stable equilibrium where the energies associated with bond distances and coordination geometries achieve a minimum. On the other hand, a molecular compound has a much larger degree of variation. In the case of a metal-oxo cluster, for example, the inner metal ions constituting the core will adjust according to the strongest bonds, which are generally to metals in the higher oxidation state. In large structures, there will likely be a number of bonds to lower oxidation state metal ions that will be compressed or elongated. Moreover, in a polymer each metal is still surrounded by other metal ions in the same arrangement, in a molecular cluster the core is surrounded by ligands. It may be expected that the outer ligands adjust as per the core; however, they may exert significant electronic effects on the metal ions, impose geometric restrictions, or introduce steric hindrance effects. The quantification of these effects is not straightforward due to the large variety of possible cases, nevertheless optimization of the BVS parameters for molecular systems has proven to be an effective way to circumvent these difficulties.

### **Known Examples of BVS Optimization**

One of the first examples of BVS optimization comes from Liu and Thorp<sup>194</sup> who worked on the estimation of the oxidation states in metalloenzymes by BVS. The authors collected a series of published crystallographic data on bond distances of mononuclear and polynuclear systems in biomolecules with the aim of creating a database of structures to obtain a new set of  $r_0$ . The computation relied on fitting of the data to the possible combinations of the metals with the most common biological

ligands O, N and S. Hence, the problem consisted of a three-parameter fit for the groups M-O, M-N and M-S. The algorithm calculates the BVS value (independently from the donor combination) for each metal center, and by calculating the difference from the expected valence finds a new  $r_0$ . The adjustment of  $r_0$  to a BVS value closer to the actual valence is obtained through a standard Marquardt algorithm. The authors describe the input files as one entry per each metal center, which consists of the list of bond lengths and bond types (i.e. the donor). The starting point for the BVS calculation is chosen using the  $r_0$  values published by Brown.<sup>71</sup> The optimization, performed on 829 entries, displayed a reduction in the error when applied for some examples (Table 4-2).

Table 4-2. Comparison of BVS values obtained for a series of model compounds by the newly optimized and published<sup>71</sup>  $r_0$  parameters (reported from ref. <sup>194</sup>).

Ion	BVS <sup>a</sup>	BVS <sup>b</sup>	Ion	BVS <sup>a</sup>	BVS <sup>b</sup>
Fe <sup>II</sup>	2.15	1.99	V <sup>IV</sup>	4.44	4.00
Fe <sup>III</sup>	3.28	3.00	V <sup>V</sup>	5.47	5.00
Mn <sup>II</sup>	2.07	1.99	Ni <sup>II</sup>	2.88	1.99
Mn <sup>III</sup>	3.29	3.06	Ni <sup>III</sup>	3.44	3.00
Mn <sup>IV</sup>	4.03	4.00	Mo <sup>IV</sup>	4.65	3.99
Cu <sup>II</sup>	1.84	1.98	Mo <sup>V</sup>	5.49	4.98
V <sup>III</sup>	3.35	3.00	Mo <sup>VI</sup>	6.68	5.98

<sup>a</sup> Calculated taking the  $r_0$  values from Brown.<sup>71</sup> <sup>b</sup> Calculated with the optimized  $r_0$ .

Another example of BVS optimization is found in the work of Urusov<sup>198</sup> who introduced a different type of approach for the optimization of the  $r_0$  and  $B$  parameters (in Eq. 4-1). The main idea consists in finding a particular  $B$  value for a given metal where  $r_0$  would represent the length of a bond with unitary contribution to the valence. When this is accomplished, it is possible to demonstrate that the parameter  $B$  becomes a pure function of the softness of the metal ion. Previous work done by Zocchi<sup>199-200</sup> demonstrated the existence of such a correlation in the case of Mo. Urusov focused on Mn and analyzed a limited number of polymeric structures (mainly from minerals) which displayed a bond with a partial valence of one (i.e.:  $s_{ij} = 1$ ). Such an interaction

possessing unitary valence is not easily observed as it needs homoleptic coordination and well-defined structures for which simple considerations about the electronic distribution can be assumed. This method requires the estimation of which bond has unitary contribution to the valence of the metal center. The need for a homoleptic structure has directed efforts on systems carrying O-based ligands, probably due to the large availability of polymeric structures where O is the bridging ligand. By this method, Zocchi has found that for  $\text{Mo}^{\text{III}}$ -,  $\text{Mo}^{\text{IV}}$ -,  $\text{Mo}^{\text{V}}$ - and  $\text{Mo}^{\text{VI}}$ -O compounds, the values  $r_0 = 1.8788 \text{ \AA}$  and  $B = 0.3046$  can be applied with sufficient accuracy to a Mo-O complex in that range of valences. Urusov found that for  $\text{Mn}^{\text{II}}$  to  $\text{Mn}^{\text{VII}}$  while  $r_0$  is fixed (i.e.  $r_0 = 1$ ),  $B$  shows a progressive variation with the valence (Fig. 4-2).

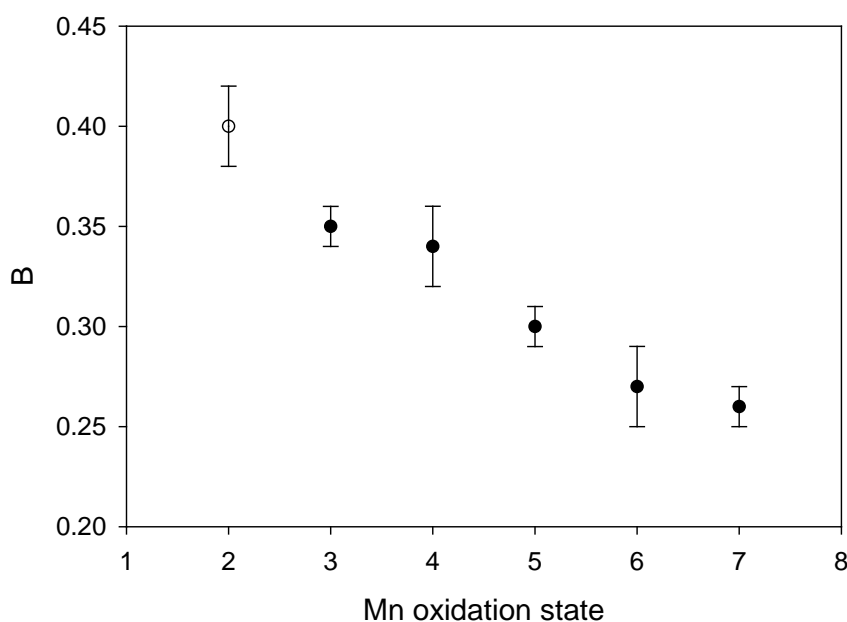


Figure 4-2. Plot of the variation in  $B$  vs. Mn oxidation state in Mn-O compounds obtained by Urusov.<sup>198</sup>

The plot in Fig. 4-2 shows an almost linear dependence of  $B$  with respect to the valence (in homoleptic Mn-O compounds) with some deviation for  $\text{Mn}^{\text{III}}$ , probably due to the Jahn-Teller effect, and for  $\text{Mn}^{\text{VII}}$  due to a non-linear increase of the rigidity in the

coordination polyhedron. The approaches of Zocchi and Urusov constitute a new example for treatment of crystallographic data for improving the BVS method, however they are limited to homoleptic systems, and hence to the relatively small number of structures and the category of metal-O compounds (polymeric). The strategies described so far are for the improvement of the method in its classical formulation.

Research on this topic has also led to a more radical approach where the classic formulation for the BVS (Eq. 4-1) has been modified. Datta and coworkers<sup>201</sup> while analyzing metal ions with zero or negative formal oxidation states modified Eq. 4-1 and established a new relation between  $V_{ij}$  (valence along the  $ij^{\text{th}}$  bond) and  $r_{ij}$  ( $ij^{\text{th}}$  bond length). The authors consider the valence of a bond ( $V_{ij}$ ) and its length  $r_{ij}$  correlated by a linear function rather than an exponential. This concept was explored in the past by other researchers; however, Datta and coworkers introduced new constants and terms, which modify this relation to describe the experimental data more accurately. The linear expression for  $V_{ij}$  as function of  $r_{ij}$  is:  $V_{ij} = r_{ij}^{-N}$  (where  $n$  is an adjustable constant). The new expression is shown in Eq. 4-3, where  $K$ ,  $K'$  and  $N$  are empirical constants,  $n$  is the coordination number and  $V_i$  is the valence for the ion.

$$V_i + K = \left( 1 + \frac{K'}{n} \right) \cdot \sum_j \frac{R_{K,K'}}{r_{ij}^N} \quad (4-3)$$

The adaptation of the parameters for Eq. 4-3 consisted of an initial evaluation of the best constants  $K$  and  $K'$  (i.e.: 4 and 20 respectively) and then minimization of the valence error by variation of  $N$  through a least-squares fitting of data (from homoleptic compounds). The database contained 415 structures of Ni and Cu with common donors like N, O, S, P, and for the first time C. Although this method is of great help for metal

ions in low oxidation states, its application as a general method for different type of metal ions may be difficult due to the large number of parameters in consideration.

All of these examples report least-squares fitting methods on relatively limited databases either for the number of entries or the nature of the compounds. The other major limitation of these methods is in not specifying any contribution from a possible dependence of one donor atom on another one of a different nature. For instance, the choice of homoleptic compounds during the optimization procedures has led to data that fit well for homoleptic systems, but they do not explicitly refer to deviations consequent to adopting these parameters on heteroleptic and molecular compounds. All these problems call for a new approach and different optimization procedures.

### **Approach to a New Optimization Method**

#### **Definitions**

Optimization represents part of everyday activities even without realizing it. Fletcher describes the simple act of reaching the work location as an act of optimization.<sup>202</sup> The *optimal* path will minimize the time needed that is then considered the *objective* (parameter in need of optimization) of the optimization. The objective can be expressed as a mathematical function, the *objective function* that associates time with the possible paths. To perform the optimization it is necessary to know the correspondence between each entry in the *domain* of the objective function (all the paths) with the objective (the time). Essentially, for an objective function  $y=f(x)$  are calculated all the solutions for each  $x'$  belonging to the domain, to find the value  $\underline{x}$  for which  $\underline{y}$  is the minimum possible (the optimal one). It is generally verified that a currently working solution is optimized with attempts that are numerically close in the domain. Translation of these basic concepts to more realistic problems often implies more than

one objective making the optimization more complex in its mathematical formulation (*multiobjective*)(for instance, reaching work while stopping for gas). Another important factor may consist in limiting the domain by applying meaningful *constraints*; for example, selecting only the paths accessible with the type of transportation adopted. In biochemistry, the minimization of stable energy states of proteins is found by optimization of the structure within physical constraints.<sup>203</sup> The branch of mathematics that deals with extracting useful information from large-size databases is called *data mining* and it has been used here to improve by optimization the parameters used in the classical BVS formulation (Eq. 4-1).<sup>204</sup> Once the objective function and the constraints have been established, the actual optimization may be very hard to define especially in the case of a *global optimization*. A global optimization is performed on functions that can present more than one minimum (or *optimum* in general) and described by an objective function like:  $f : x \in A \rightarrow y \in B$ . The solution to this minimization problem will be an  $x' \in A$  that satisfies all the constraints requirements and that produces a value  $y'$  which is the smallest in  $B$  (Eq. 4-4).

$$x' \in A: f(x) \geq f(x') \quad \forall x \in A. \quad (4-4)$$

It is possible to find subgroups of  $A$  where there are values of  $x$  for which the function is the smallest than for all other solutions and constitute *local optima*. A *global* minimum is defined as the best local minimum amongst all the ones that can be found within the whole feasible domain of the objective function. Finally, the most demanding task in an optimization is to create an appropriate function that describes the system behavior. This is called *modeling*, and the quality of the optimization is directly dependent on the coherence of the mathematical expression in describing the real life

application. Although simplifications are often necessary, the model should still represent the problem for the solutions to be acceptable.

### **Exact Methods**

An exact method of optimization consists in defining the domain  $A$  the objective function, then applying to it all the constraints that define a subset  $C$  (where  $C \subseteq A$ ) and solving the function for all the possible values  $x$  of  $C$ . Finally, by comparison of all the possible outcomes, the optimal  $y'$  value is found and so is the corresponding  $x'$  (the solution of the optimization). This method is known as *exhaustive search* and is a method that guarantees the solution (or solutions) for the optimization. The application of this method is generally limited by two factors: the complexity of the mathematical function and the number of elements to evaluate. For application to real problems the function may result too complex for applying constraints or even to describe its general form. On the other hand, even a relatively limited group of elements may be too demanding computationally as evident by any interval  $[a, b]$  of  $\mathbb{R}$ , which containing an infinite number of elements it will require infinite time to analyze.

Linear functions (where the variables can be multiplied by constants and the results summed together) are the simplest to approach; however, they find only limited application. Non-linear functions can be approached by differentiation where a descending path in the objective function can guide the optimization toward the rapid localization of minima (derivative = 0).<sup>205</sup> This approach can be limited by those differentiable functions that result in very complex derivatives or that contain multiple minima. A derivative of zero can be found in any minima and the algorithm cannot make a distinction between any minima and the global minimum (or absolute minimum).

A complex function is often approximated with one of easier interpretation for the optimization with the prerequisite that the solutions found converge to the one that would be found for the original function.<sup>206</sup> All the methods that aim at the analytical solution of an optimization are known as *exact methods* and they can be applied only to some functions and with some hypothesis. In all those case where an exact method fails or cannot be applied the optimization is performed by *meta-heuristic* methods.

### **Meta-Heuristics**

Meta-heuristic methods, differently from exact methods, do not guarantee a solution and in the cases where a solution is found it only entails some probability of being the actual global minimum. The lower degree of accuracy in finding the solution to a problem is compensated by a large flexibility of application and faster execution. The quality of the solution greatly depends on the algorithm built for the optimization. Various optimization methods by meta-heuristics are inspired by observation of natural phenomena where the scientists build algorithms capable of finding solutions for the objective functions by adopting the same strategies found by nature. The most important examples are the physical annealing<sup>207</sup>, the music improvisation<sup>208</sup>, the Darwinian theory of evolution<sup>209</sup> and the behavior of animals (ants, bees or monkeys).<sup>210-212</sup> Amongst the meta-heuristic methods of optimization, there are few categories not inspired by natural behaviors. The *Variable Neighborhood Search* (VNS)<sup>213</sup> is an example of these categories and it has been used for the optimization in the present work.

### **Description of the Problem and Choice of the Meta-Heuristics Method**

The BVS method relies on the sum of the terms arising from Eq. 4-1, which only provides the partial valence attributable to a M-L bond. The system of Eq. 4-2 shows

how it is possible to adapt the  $r_0$  value for a given metallic coordination environment of specified valence so that  $r_0(V, M, L)$  would perfectly fit the known valence ( $V$ ). This approach is appropriate for systems of similar characteristics, but it may not be suitable for many other complexes due to the large number of possible environments. There is thus a necessity to formulate the optimization problem with the purpose of establishing a set of  $r_0$  parameters capable of representing the largest possible group of metal environments having same metal type, valence and bound to the same subset of ligands. The error in the estimation of the valence is described by the difference in absolute value ( $\Delta$ ) between the estimated valence ( $V$ ) and the actual oxidation state, approximated with the valence ( $v$ ), as displayed in Eq. 4-5.

$$\Delta = | V - v |. \quad (4-5)$$

In a set of  $k$  elements (different coordination environments) for the metal  $M$  of possible valences  $V$  and having only ligands from the subset  $L$ , the total error  $f(r_0)$  for the use of the BVS model with  $r_0(V, M, L)$  and  $b$  constant is expressed by Eq. 4-6.

$$f(r_0) = \frac{1}{k} \sum_{i=1}^k |V_i - v_i|. \quad (4-6)$$

This formulation provides an average error for the BVS model over all possible valences adopted by the metal  $M$  and represents the objective function of this optimization.

Although a process of optimization based on Eq. 4-6 may appear of easy solution due to the linearity of the terms, it is complicated by the true nature of  $V_i$  as an exponential. For this reason, the objective function is not linear, quadratic or differentiable (due to the presence of the absolute values in the sum) and its optimization requires the use of meta-heuristics methods. Of the various types of meta-heuristics methods, the VNS seems to be the most promising for application to the BVS. This method, described in

detail later, focuses on the search for better solution in a close proximity of solutions already known. Once the interval for each variable has been fully investigated and the method cannot provide any new improved solution, it stops. In this particular case the known solutions are represented by the already known  $r_0$  values from the published literature.

### **The Variable Neighborhood Search**

The VNS method is based on the search for new improved solutions within a variable's interval (*neighborhood*) of adjustable size depending on the new solutions found.<sup>213</sup> In the case of a simple objective function dependent on a single variable  $x$ , the method considers as starting point a known solution  $x_0$ . The  $x_0$  is perturbed by an oscillating function within an interval and a new random solution  $x_1$  is chosen. The new point  $x_1$  becomes the center of a neighborhood of selected extension and a local exhaustive search begins within. When a new solution  $x_0'$  is found so that  $f(x_0') < f(x_0)$  (for a minimization problem),  $x_0$  is replaced by  $x_0'$  and the procedure starts from the beginning. If the new solution  $x_0'$  does not satisfy the condition  $f(x_0') < f(x_0)$ , the size of the interval or neighborhood around  $x_0$  is slightly increased and rechecked for a new solution. As long as there are not new solutions that improve the minimization, the intervals around the original  $x_0$  keep increasing up to reaching the limits imposed by the constraints.

## **Initial Experimental Setup**

### **Selection of the Structural Data**

Initial attempts were directed to the optimization of the BVS parameters for Fe and Mn compounds containing only a combination of N- or O-donor ligands. Two easily available databases belonging to the Christou group (IUMSC, Indiana University

Molecular Structure Center and the CXC, Center for X-ray Crystallography at the University of Florida) were investigated and the relevant *cif* (crystallographic information files) were obtained. Initial difficulties were found for many older structures that required transformation of the file from a different format to the more common *cif* extension. The *cif* files contain various types of information relative to the diffraction experiment and only a portion is relevant to identifying the distances between bonded atoms.

To provide the optimization software with consistent input data, each crystallographic file was manually transformed to a text file containing an entry for each metal ion. Each entry was constituted by five values, which identify metal type, unique metal label, ligand type, unique ligand label, and finally the bond distance. Other type of problems to overcome came from the presence in the *cif* files of non-specific bonding between metal ions and improbable species. For instance, hydrogen atoms in aliphatic chains of a ligand were sometimes reported bonded to a metal ion, or a disordered ligand was reported bound twice in the bond list. These problems were solved by manually screening all the crystallographic structures and applying appropriate corrections to the *cif* files.

Many of the crystallographic files contained metal ions equivalent by symmetry which have the same label and bond distances with the corresponding donors. It has been chosen to use these coordination environments only once as they constitute a single measurement reported multiple times. Although this process lowered the overall number of entries in the input files, it would lead to a more reliable set of data representing each unique topology rather than for the number that was reported in a crystal structure. For example, in the core of complex  $[\text{Mn}_{12}\text{O}_{12}(\text{O}_2\text{CMe})_{16}(\text{H}_2\text{O})_4]$ ,

shown in Fig. 4-3 there are only three different types of Mn ions despite the overall dodecanuclear structure. On the other hand, X-ray determinations of the same species have been each considered in the optimization as representative of a different measurement. The selection process resulted in a collection of 733 combined entries for Fe and Mn.

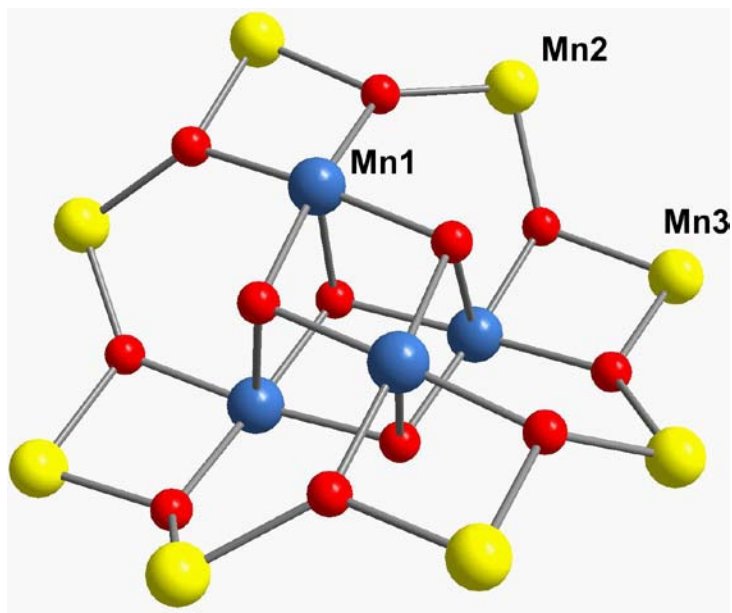


Figure 4-3. Labeled core of  $[\text{Mn}_{12}\text{O}_{12}(\text{O}_2\text{CMe})_{16}(\text{H}_2\text{O})_4]$ . There are only three different types of Mn ions by symmetry.

Table 4-3. BVS parameters for Fe and Mn obtained from the literature<sup>131</sup> and by a preliminary VNS optimization (with  $b$  variable) over a selected database (Å).

Parameters	M-L type	$r_0$ (M <sup>II</sup> )	$r_0$ (M <sup>III</sup> )	$r_0$ (M <sup>IV</sup> )	$b$
Current <sup>a</sup>	Mn-O	1.790	1.760	1.753	0.37
Current <sup>a</sup>	Mn-N	1.849	1.834	1.822	0.37
Optimized	Mn-O	1.7429	1.7202	1.7351	0.4017
Optimized	Mn-N	1.7863	1.7828	1.7961	0.4017
Current <sup>a</sup>	Fe-O	1.734	1.759	-	0.37
Current <sup>a</sup>	Fe-N	1.769	1.815	-	0.37
Optimized	Fe-O	1.7650	1.7397	-	0.3840
Optimized	Fe-N	1.8600	1.7424	-	0.3840

<sup>a</sup> Data reported from ref. <sup>131</sup>

For Fe, only the +2 and +3 oxidation states were analyzed, whereas for Mn the +4 state was included. The computation for the two different metals was executed in

parallel and accounted for the data reported in table 4-3. An important aspect of this optimization is that the parameter  $b$  has been considered variable rather than keeping it constant at 0.37 Å. Such an approach does not require the BVS model to fit as many metals as possible. Although the BVS formula loses in generalization, it can better fit the characteristic behavior of each metal. A plot of the general exponential form contained in the BVS model displays a change in profile that authors like Urusov ascribed to a different degree of softness of the metal ion.<sup>198</sup> According to this interpretation, the  $r_0$  values for the metals have been calculated throughout the transition series assuming early or late metals to possess the same softness or hardness. The variability of  $b$  in this optimization should then provide a means for a greater accuracy of the BVS model based on an improved matching of  $b$  with the polarizability of the electron cloud. As an example of the application of the new parameters to a representative Mn cluster, Fig. 4-3 and Table 4-4 report respectively the core and the BVS calculations for  $[\text{Mn}_{12}\text{O}_{12}(\text{O}_2\text{CMe})_{16}(\text{H}_2\text{O})_4]$ . The BVS data obtained for  $[\text{Mn}_{12}\text{O}_{12}(\text{O}_2\text{CMe})_{16}(\text{H}_2\text{O})_4]$  using the currently available  $r_0$  and  $b$  (0.37 Å), leads to a clear identification of the oxidation states; however, by use of the same formulation, the VNS-optimized  $r_0$  and  $b$  result in better precision with lower errors.

Table 4-4. BVS values for  $[\text{Mn}_{12}\text{O}_{12}(\text{O}_2\text{CMe})_{16}(\text{H}_2\text{O})_4]$  calculated with published literature data<sup>131</sup> and by preliminary VNS optimization of  $r_0$  and  $b$ .

Ion	Parameters	$V_i$ for Mn <sup>II</sup>	$V_i$ for Mn <sup>III</sup>	$V_i$ for Mn <sup>IV</sup>
Mn1	Current	4.519	4.167	4.089 *
Mn1	Optimized	4.109	3.884	4.030 *
Mn2	Current	3.536	3.261 *	3.200
Mn2	Optimized	3.264	3.085 *	3.201
Mn3	Current	3.396	3.131 *	3.073
Mn3	Optimized	3.150	2.997 *	3.089

The numbers with an asterisk represent the only ones being acceptably close to the actual oxidation state.

In the case of an Fe cluster, the cation  $[\text{Fe}_3\text{O}(\text{O}_2\text{CMe})_6(\text{H}_2\text{O})_3]^+$  has been chosen as representative and its labeled structure and BVS data are shown in Fig. 4-4 and Table 4-5. As in the case of Mn, the BVS values obtained from the published data are clear enough to distinguish, without uncertainty, the oxidation state of each Fe ion. Nevertheless, the VNS-optimized parameter leads to smaller errors allowing for a higher precision.

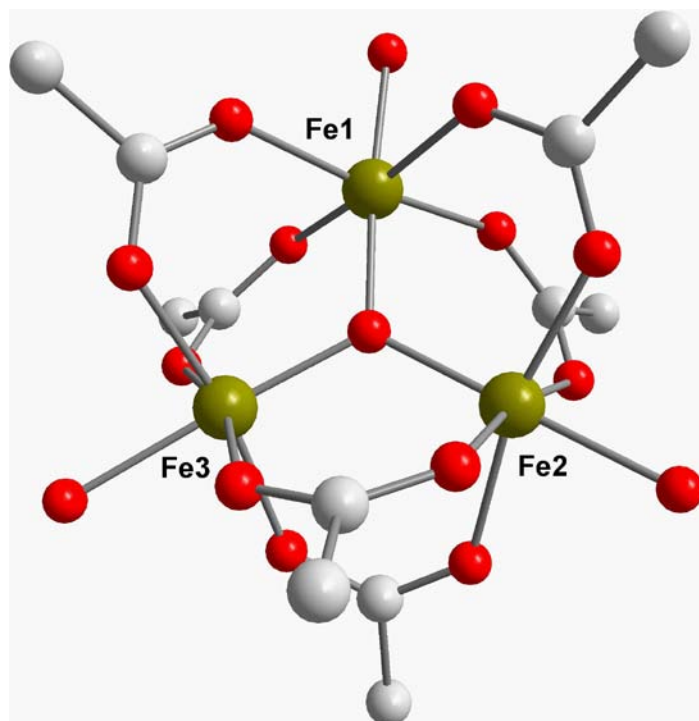


Figure 4-4. Pov-Ray projection of the partially labeled structure of the cation  $[\text{Fe}_3\text{O}(\text{O}_2\text{CMe})_6(\text{H}_2\text{O})_3]^+$ , (CCDC code: cojpum)<sup>8</sup>.

Table 4-5. BVS values for  $[\text{Fe}_3\text{O}(\text{O}_2\text{CMe})_6(\text{H}_2\text{O})_3]^+$  calculated with published literature data<sup>131</sup> and by preliminary VNS optimization of  $r_0$  and  $b$ .

Ion	Parameters	$V_i$ for Fe <sup>II</sup>	$V_i$ for Fe <sup>III</sup>
Fe1	Current	2.962	3.169 *
Fe1	Optimized	3.293	3.083 *
Fe2	Current	2.962	3.169 *
Fe2	Optimized	3.293	3.083 *
Fe3	Current	2.923	3.128 *
Fe3	Optimized	3.252	3.045 *

The numbers with an asterisk represent the only ones being acceptably close to the actual oxidation state.

The two clusters may only be representative of a limited number of structural types; hence, *chopt* has been implemented for the creation of a list reporting the error for each entry based on the currently available BVS parameters and the optimized ones. Figure 4-5 reports the histogram for the errors ( $\Delta$ ) over the entire database.

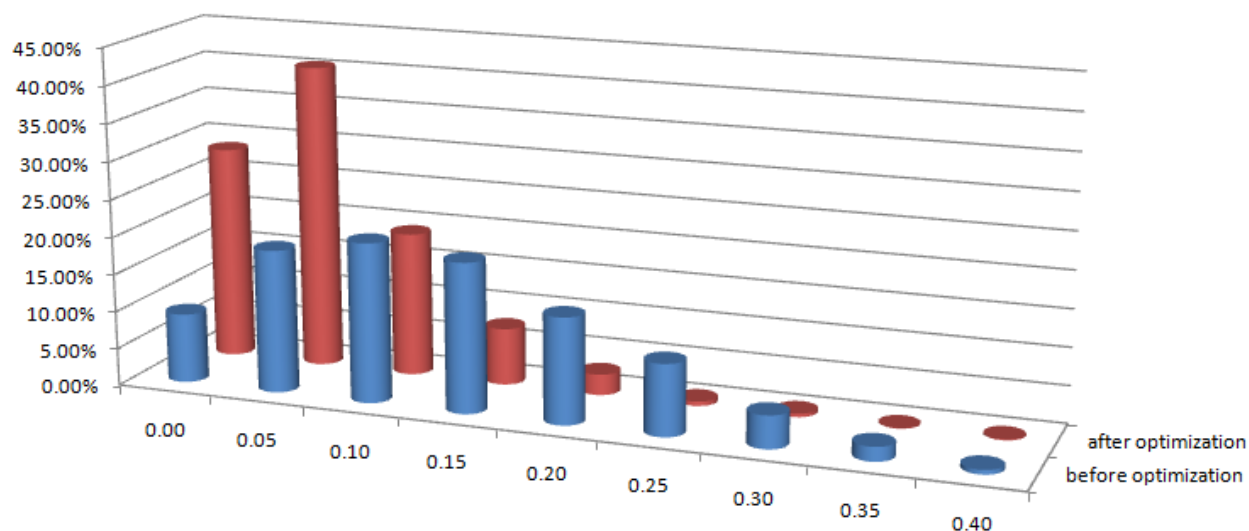


Figure 4-5. Histogram of the errors (absolute values) on the valence estimation by the currently available BVS parameters (blue bars) and the ones derived from optimization (red bars) over an entire selected structural database.

The histogram shows the discrepancies for the BVS model with the non-optimized  $r_0$  parameters to be distributed over a large range than those resulting from application of the model with the optimized  $r_0$  and  $b$ . The histogram for the latter shows a higher proportion of entries with smaller error, and in general is overall more concentrated about zero demonstrating an increased number of structures to statistically provide a smaller error. If for example the error  $\Delta = \pm 0.15$  is considered, only  $\sim 50\%$  of the entries fall within the limits when calculated with the currently published  $r_0$  values (and  $b = 0.37$  Å), whereas  $\sim 90\%$  are found within  $\Delta = \pm 0.15$  application of the newly optimized  $r_0$  and  $b$ . From this point on, any optimized parameter will report the subscript "opt" (for

example,  $r_{0 \text{ opt}}$  or  $b_{\text{opt}}$ ), and any parameter from the literature will be reported without distinctions (for example,  $r_0$  or  $b$ ).

### Proposal for a New BVS Formula

The availability of a selected database of structures and the flexibility of the software adopted for the initial attempt of optimization has encouraged efforts to improve the formulation of the BVS model. According to the current formulation, Eq. 4-1 is applied to every bond to obtain the individual valences ( $s_i$ ) that are then added to gain the bond valence sum, as expressed in Eq. 4-7, where  $r_0$  is function of the metal valence ( $V$ ), metal type ( $M$ ) and the donor ( $L$ ),  $r_i$  is the bond length and  $B$  or  $b$  is a constant set at 0.37.

$$V = \sum_{n=1}^i s_i = \sum_{n=1}^i e^{\frac{r_0(V, M, L) - r_i}{B}} \quad (4-7)$$

In a metal center containing the same donor atom more than once, each bond of the same type will be considered separately despite being correlated to the same  $r_0$  value. A proposed variation would be to approximate the different bond lengths with the same donor type with their average and sum the contribution to the valence for how many times that donor appears in the formula (hence, replace  $r_{A'}$ ,  $r_{A''}$ , and  $r_{A''}$  with  $\overline{r_A}$  and multiply by three its contribution to the valence), see Eq. 4-8. Equation 4-8 describes the BVS formula for a metal ion ( $M$ ) possessing  $n$  different donors, each appearing  $m$  times. It should be noted that the value of  $B$  is now relative to the metal. The new formulation has been implemented in *chopt* and a new optimization iteration was applied to the database using as starting points the  $r_{0 \text{ opt}}$  and  $b_{\text{opt}}$  previously found

and listed in table 4-5. The optimization produced only a slight improvement over  $r_{0 \text{ opt}}$  and  $b_{\text{opt}}$  so that distribution of errors after the optimization is similar to the one before the optimization (with the use of the new BVS formula (Eq. 4-8). Figure 4-6 illustrates the comparison of the error distribution before and after optimization of Eq. 4-8 with the initial  $r_{0 \text{ opt}}$  and  $b_{\text{opt}}$ .

$$V = \sum_{j=1}^n m_n \cdot e \frac{r_0(v, M, L) - \frac{1}{m_n} \sum_{i=1}^m r_i}{B(M)} \quad (4-8)$$

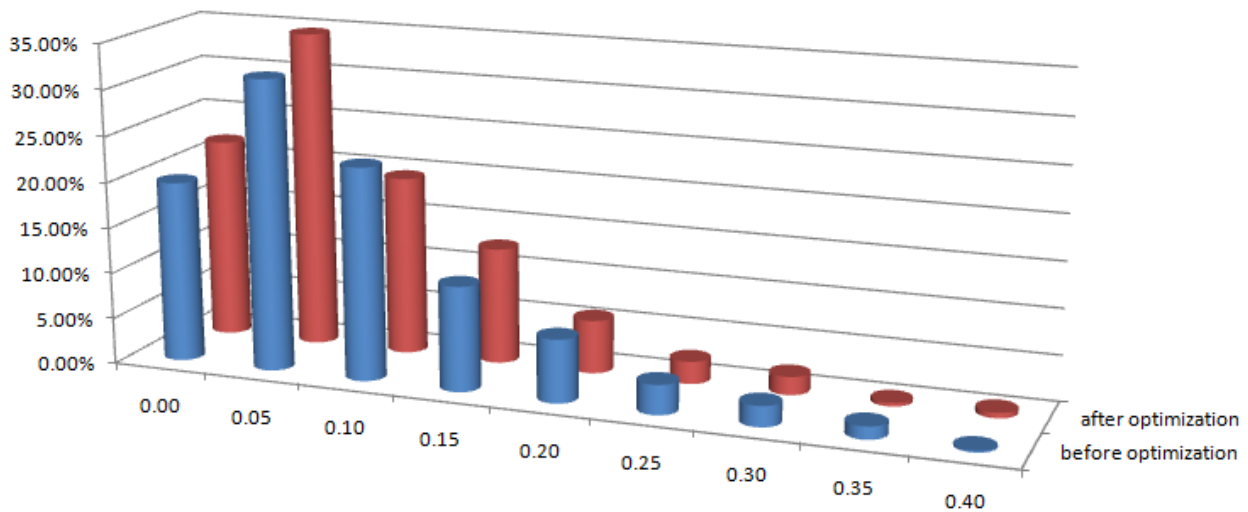


Figure 4-6. Comparison of error distribution for the optimized BVS parameter  $r_0$  and  $b$  with the currently published formula (blue bars) and the optimization of the newly found  $r_{0 \text{ opt}}$  and  $b_{\text{opt}}$  with the new proposed formulation (red bars).

Besides a minor improvement of the errors with the second optimization, the data shows how Eq. 4-8 is not capable of approaching the BVS problem better than Eq. 4-7. The latter could concentrate ~ 90% of the entries within the limit  $\Delta = \pm 0.15$  (from the initial ~ 50% before optimization) whereas the new formulation only reaches ~ 73 %

either with or without optimization. This is proof that averaging the same type of metal-donor bonds is not a convenient approximation to improve the BVS accuracy, hence there is no reason to adopt Eq. 4-8 in place of Eq. 4-7. The VNS approach was useful for a marginal reduction in error by clustering the data for the objective function closer to zero.

## **Application to the CCDC Database**

### **Data Retrieval from the CCDC Database**

The successful application of the VNS optimization technique to the initial database of 733 entries has encouraged the extension of such work to an ample database that could provide a larger set of data for further improvement of the published  $r_0$  and  $b$ . There are multiple advantages for retrieving data from the CCDC database. Besides representing the largest collection to date of single-crystal molecular structures, it also offers dedicated software (*ConQuest* v1.12) for *interrogating* the database and is capable of producing outputs that can be further analyzed or compared through logical functions. Another important advantage is the possibility of extracting the data as cif files possessing roughly the same architecture, hence facilitating the process of locating and copying the bond lengths. For each metal ion belonging to the first transition row a set of approximately 30 queries has been used. The queries located those structures where the metal under scrutiny was bound to the following type of donors: O, N, P, S, F, Cl, Br or I. Cyanide ligands were excluded from this subset due to their particular electronic structure, which may not be representative of N-donors. All those cases where the metal was bound to one of the following: H, B, C, As, Se, Te or another metal were excluded because often associated with non-positive values for the metal oxidation state. The BVS method, does not account for covalency and fails whenever

the system diverge from an electrostatic model. Further considerations on the type of structures have led to the exclusion of those cases that would display obvious bond length distortion, such as macrocyclic chelation. Therefore, all the molecules containing most common macrocyclic ligands with four to six donors N- or O-based have been excluded too. All these queries were applied on the database with a further filter for structures having no disorder, error or powder determinations. This initial type of search produced large outputs with no discrimination over the oxidation state of the metal. Another set of searches was performed on each metal by adding queries that would isolate those structures including only one type of oxidation state. For each metallic species a general set of structures and a series of subsets each relative to a particular oxidation state was obtained. The software, *ConQuest*, showed some pitfalls in locating all structures according to the set of queries, which required additional workup of the output data. For instance, a search for a metal in a particular oxidation state has produced outcome hits that did not appear in the same set of queries without specification of the oxidation state. Due to these mismatches, all the output for each metal was cross-examined to ensure that each structure with known oxidation state would appear also in the more general set for that metal.

### **Data and Software Preparation for the Optimization**

The large volume of data to be analyzed required the coding of a new routine capable of automatically accessing all the cif files and producing the corresponding output text files with entries for each metal ion not reported by symmetry. The algorithm associates errors for anomalous cif files containing an unusual number of donors, unknown donors, or otherwise corrupted data that the *ConQuest* filter failed to exclude.

An entire collection of  $r_0$  is necessary for the final stage of optimization, hence the program was also implemented to calculate  $r_0$  values from each metal subset of known valence (through Eq. 4-2). The last published data on the BVS model report only some of the possible  $r_0$  combinations for the donors O, N, P, S, F, Cl, Br or I for a given metal in common valences. The published collection of  $r_0$  has been used with no modification as starting parameters for the optimization stage.<sup>214</sup> The aforementioned program was compiled to obtain all the missing  $r_0$  data for each M-L combination; however, it failed in some instances that required manual intervention as explained below. Table 4-6 reports, the results of the preliminary  $r_0$  computation in the case of Fe ( $b = 0.37 \text{ \AA}$ ).

Table 4-6.  $R_0$  values obtained by computations on the subset data of known valence for iron ( $b = 0.37 \text{ \AA}$ ).

Donor ( $\downarrow$ ) / Valence ( $\rightarrow$ )	1	2	3	4	5
O	2.29	1.72 *	1.75 *	1.74 *	1.83
N	2.36	1.78 *	1.84 *	1.81 *	1.90 *
P	2.77	2.15 *	2.22 *	2.28 *	2.31
S	2.66	2.10 *	2.14 *	2.10	2.17 *
F	2.06	1.49	1.52	1.51	1.61
Cl	2.63	2.06 *	2.09 *	2.07	2.17
Br	2.78	2.19 *	2.25 *	2.22	2.32
I	2.98	2.40	2.53	2.42	2.45 *

The numbers with an asterisk represent the  $r_0$  ( $\text{\AA}$ ) obtained either from the literature<sup>214</sup> or by software calculation. All the remaining values have been derived from the ones in bold.

The values in Table 4-6 contain the published data and those calculated by the program (both in bold) as well as those that have been otherwise derived. For N-donors all the values for  $r_0$  were found except for the combination  $\text{Fe}^{\text{I}}\text{-N}$ , which was manually calculated as average from homoleptic structures of the type  $\text{Fe}^{\text{I}}\text{-N}$  (i.e.:  $2.36 \text{ \AA}$ ). An analogous approach was used for all the other combinations for which suitable homoleptic structures could be found. It was also noted that there is an almost parallel profile for the correlation between the  $r_0$  values of a donor with the valence. Such

observation has been used for estimating the  $r_0$  data of donors with little or no outcome from the software or in any case where they could not be calculated directly from a structure. In the case of F, for example, it was manually calculated the  $r_0$  for Fe<sup>II</sup>-F (i.e.: 1.49 Å). This datum was then compared with the  $r_0$  value for the Fe<sup>II</sup>-N (taken in this case as reference, i.e.: 1.78 Å) and the difference (0.29 Å) used to create a parallel profile that could represent the other missing data for the Fe-F combinations (Fig. 4-7).

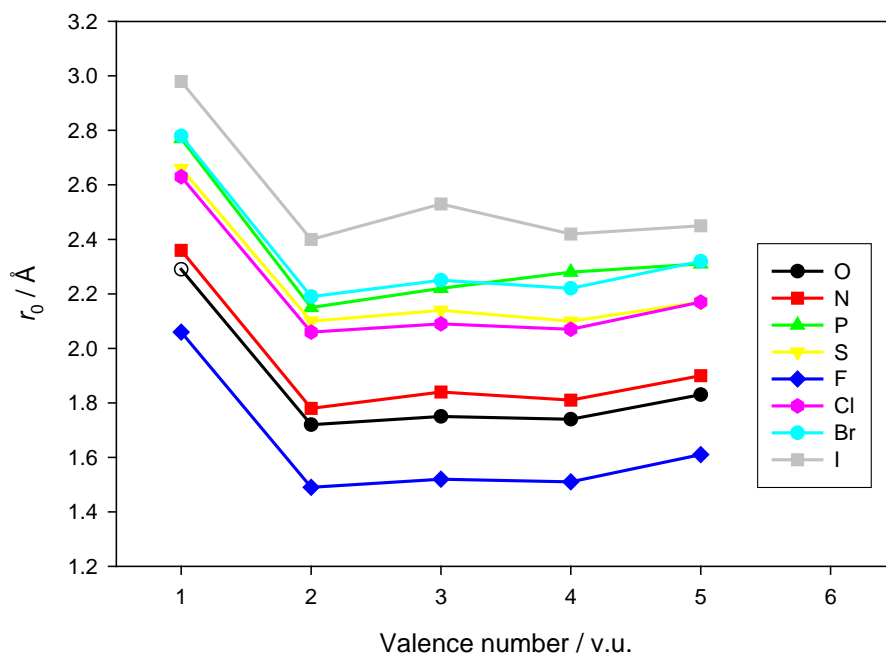


Figure 4-7. Correlation between published<sup>214</sup> or derived  $r_0$  values with the valence for given donors in iron structures.

This approach allowed for the estimation of all possible  $r_0$  for every M-L combination that had sufficient representation in the subset folders of known valence. The full compilation of  $r_0$  provided all the necessary starting points for the VNS optimization performed with an updated version of *chopt*. The optimization was performed on one metal at a time, on the entire set of structures including those with unknown valence. Each entry is read by *chopt* and assigned a tentative valence unless the BVS exceeds a  $\pm 0.30$  limit from the closest integer, in which case it is momentarily

rejected. After an initial cycle of optimization the initial  $r_0$  and  $b$  are replaced with the newly found  $r_{0\text{ opt}}$  and  $b_{\text{opt}}$ , and the previously rejected entries are reanalyzed to include those that now fulfill the  $\pm 0.30$  limit. This procedure is repeated continuously with the aim of extending the optimization over the largest number of entries possible while insuring acceptable BVS estimation through the  $\pm 0.30$  limit. *Chopt* has also an implemented routine that creates a histogram for the error associated with each entry monitoring the overall quality of the optimization. An exemplified flow chart of *chopt* algorithm is reported in Fig. D-1. The large volume of input data (~10000 entries per metal on average, corresponding to ~60000 bond lengths) and the high number of variables to optimize (65 in case of Mn) would required prohibitive computational time on a common calculator. Hence, the data has been moved, along with *chopt*, on the computer cloud *Grid5000* (mainly based in France) with a drastic reduction for the optimization time.

### **Analysis of the Results**

All the newly obtained  $r_{0\text{ opt}}$  and  $b_{\text{opt}}$  have been applied with the Eq. 4-7 to the entire set of data. This approach allows for estimation of error over the population of data rather than a sample of it, providing conclusions that are more reliable. Some combinations are not represented in the database; hence, the optimization could not provide the relative  $r_{0\text{ opt}}$  for them.

### **Titanium**

The most common oxidation state for titanium is +4. The other states of lower valence are air sensitive and its coordination number may range from three to eight.<sup>7</sup> Table D-1 and Fig. D-2 report the list of the new of  $r_{0\text{ opt}}$  and  $b_{\text{opt}}$  and the histogram of

the errors obtained by application of Eq. 4-7, respectively. The optimization is relative to 1746 files corresponding to 2244 entries.

### **Vanadium**

Vanadium compounds have positive oxidation states ranging from +1 to +5, displaying coordination numbers from four to seven. The most widely found oxidation state is +4 due in large part to its stability. Other lower oxidation states are readily oxidized in air. Being a hard metal it prefers oxygen coordination, accounting for the majority of its compounds.<sup>7</sup> The list of  $r_{0\text{ opt}}$  and  $b_{\text{opt}}$  found for this metal are reported in Table D-2 whereas the error distribution over the entire V database is in Fig. D-2. The CCDC database did not report structures for the +1 valence. The optimization was obtained from 2850 cif files corresponding to 5464 entries.

### **Chromium**

Chromium displays in its compounds positive oxidation states ranging from +1 to +6. The most commons are +2, readily oxidized to the more stable and present +3 and the +6, often found in oxides. The coordination numbers vary from three to eight, with a preference for six.<sup>7</sup> Table D-3 reports the new  $r_{0\text{ opt}}$  and  $b_{\text{opt}}$  for chromium while the error over the entire database of entries is in Fig. D-2. In the case of chromium, the optimization was conducted over 1566 cif files corresponding to 2071 entries.

### **Manganese**

Manganese present several oxidation states of which the +2 is the most stable in the range +1 to +7. Permanganate is the most stable high oxidation state followed by manganate. The +5 state is not stable, although it may form as an intermediate. The +3 and +4 states are especially present in hydroxo- or oxo-based clusters. The predominant coordination number is six, although all possibilities between two and eight

have been reported.<sup>7</sup> Table D-4 and Fig. D-2 report the list of new  $r_{0\text{ opt}}$  and  $b_{\text{opt}}$  in the former and the histogram of the errors in the second. The optimization involved 4675 files for 5767 entries.

### **Iron**

Iron can easily assume the oxidation stated +2 or +3. All other states are instable, and the highest reported is the +6, which is rare. The coordination numbers range from three to eight, although the four- and six-coordinations (tetrahedral and octahedral respectively) are preferred. The new  $r_{0\text{ opt}}$  and  $b_{\text{opt}}$  are reported in Table D-5, while the histogram for the error associated to the entire database, Fig. D-2. The optimization on the iron structures was based on 6044 files or 8257 entries.

### **Cobalt**

Cobalt compounds are stable in the +2 and +3 oxidation state. The +4 state is uncommon, while the +1 is more prevalent. The coordination number ranges from three to eight and only the four and six-coordinate are the most representative.<sup>7</sup> The newly obtained  $r_{0\text{ opt}}$  and  $b_{\text{opt}}$  are reported in the Table D-6, while Fig. D-2 reports the histogram of the BVS errors applied to the entire cobalt database. The optimization for cobalt was obtained by analysis of 8897 crystallographic files accounting for 8902 entries.

### **Nickel**

Nickel ions are prevalent in the oxidation state +2, whereas +3 and +4 are respectively uncommon and rare. In the higher oxidation states, it is thought that the ligands may be responsible for the formal assignment by being oxidized. The +1 state is found although also in this case it may not reflect the actual physical configuration of the metal. Nickel coordination is more limited in the number of donors, ranging from three to

six.<sup>7</sup> The data for  $r_{0\text{ opt}}$  and  $b_{\text{opt}}$  are reported in Table D-7, while the histogram of the relative errors is illustrated in Fig. D-2. The optimization was based on 10150 cif files corresponding to 10204 entries.

## Copper

Copper ions have a restricted number of oxidation states allowed, from +1 to +3. The +4 state is only hypothesized, and the +3 is uncommon. Coordination numbers range from two to six with conspicuous presence of pentacoordination.<sup>7</sup> In Table D-8 are listed the new  $r_{0\text{ opt}}$  and  $b_{\text{opt}}$  for the various donors, while Fig. D-2 reports the histogram of the BVS errors counted on the entire copper database. The optimization procedure was carried on 21680 crystallographic files amounting to 22485 entries.

## Conclusions

Current application of the BVS model to molecular systems is known to be feasible despite, in many cases, large discrepancies being found. Attempts to improve the BVS method through its parameters  $r_0$  and  $b$  or even its formulation have led to different sets of data. Each set is tailored to fit only a particular category of compound, for example inorganic polymers rather than inorganic sites of biomolecules. The proposed optimization by meta-heuristic methods was applied for the first time to the BVS model and to largest database of metallic complexes. The unprecedented large set of data allowed for the isolation of parameters that have proven to be a better fit for each transition metal in the first row, as demonstrated by the histograms for the entire population of molecular structures.

The influence exerted by a metal-dependent parameter  $b$  in matching the characteristics of each metal ion rather than using the generalized value of 0.37 Å throughout the series is not negligible. The consequent lack of generalization is

overcome by a significant increase in accuracy on all metal ions considered, especially on early metals. The improvement decreases moving toward later metals up to copper for which the gain in accuracy is minimal. Another important advantage offered by this method consists in the simultaneous analysis on multiple variables, which granted a vast compilation of  $r_{0 \text{ opt}}$  for almost every non-organometallic donor in contrast to previous optimization examples reporting only limited combinations. The preparation of datasets, as well as the complex development of a computer program capable of extrapolating data and automatically proceed to the optimization are limiting factors; however, it may find ease of applicability to several metal ions with consequent potential application of the BVS method in other areas of chemistry.

APPENDIX A  
CODES FOR THE COMPOUNDS LISTED

- [Mn<sub>12</sub>O<sub>12</sub>(O<sub>2</sub>CMe)<sub>16</sub>(H<sub>2</sub>O)<sub>4</sub>] (1)
- [Mn<sub>13</sub>O<sub>8</sub>(OMe)<sub>6</sub>(fdc)<sub>6</sub>] (2)
- [Mn<sub>13</sub>O<sub>8</sub>(OEt)<sub>6</sub>(fdc)<sub>6</sub>] (3)
- [Mn<sub>8</sub>O<sub>4</sub>(fdc)<sub>6</sub>(DMF)<sub>2</sub>(H<sub>2</sub>O)<sub>2</sub>] (4)
- [Mn<sub>8</sub>O<sub>4</sub>(fdc)<sub>6</sub>(DMF)<sub>4</sub>] (5)
- [Fe<sub>7</sub>O<sub>3</sub>(OMe)(fdc)<sub>6</sub>(MeOH)<sub>3</sub>]<sup>3+</sup>[FeCl<sub>4</sub>]<sup>-</sup>·2Cl<sup>-</sup> (6)
- [Fe<sub>6.2</sub>Mn<sub>0.8</sub>O<sub>3</sub>(OMe)(fdc)<sub>6</sub>(H<sub>2</sub>O)<sub>3</sub>]<sup>+</sup>·Cl<sup>-</sup> (7)
- [Fe<sub>x</sub>Co<sub>7-x</sub>O<sub>3</sub>(OMe)(fdc)<sub>6</sub>(MeOH)<sub>3</sub>]<sup>2+</sup>·2Cl<sup>-</sup> (8)
- [Fe<sub>x</sub>Ni<sub>7-x</sub>O<sub>3</sub>(OMe)(fdc)<sub>6</sub>(MeOH)<sub>3</sub>]<sup>+</sup>·Cl<sup>-</sup> (9)
- [Fe<sub>x</sub>Zn<sub>7-x</sub>O<sub>3</sub>(OMe)(fdc)<sub>6</sub>(MeOH)<sub>3</sub>]<sup>+</sup>·½[ZnCl<sub>4</sub>]<sup>2-</sup> (10)

APPENDIX B  
FULL CRYSTALLOGRAPHIC TABLES

Table B-1. Crystal data and structure refinement for **2**·8CH<sub>2</sub>Cl<sub>2</sub>.

Identification code	xm221	
Empirical formula	C <sub>92</sub> H <sub>94</sub> Cl <sub>16</sub> Fe <sub>6</sub> Mn <sub>13</sub> O <sub>38</sub>	
Formula weight	3424.26	
Temperature	173(2) K	
Wavelength	0.71073 Å	
Crystal system	Triclinic	
Space group	P-1	
Unit cell dimensions	a = 14.1308(12) Å	α = 119.4700(10)°.
	b = 15.1738(12) Å	β = 91.4320(10)°.
	c = 15.3656(13) Å	γ = 100.339(2)°.
Volume	2797.0(4) Å <sup>3</sup>	
Z	1	
Density (calculated)	1.969 Mg/m <sup>3</sup>	
Absorption coefficient	2.621 mm <sup>-1</sup>	
F(000)	1643	
Crystal size	0.12 x 0.12 x 0.04 mm <sup>3</sup>	
Theta range for data collection	1.91 to 27.50°.	
Index ranges	-16 ≤ h ≤ 18, -19 ≤ k ≤ 17, -19 ≤ l ≤ 19	
Reflections collected	18432	
Independent reflections	12232 [R(int) = 0.0388]	
Completeness to theta = 27.50°	95.2 %	
Absorption correction	Integration	
Max. and min. transmission	0.8774 and 0.6838	
Refinement method	Full-matrix least-squares on F <sup>2</sup>	
Data / restraints / parameters	12232 / 0 / 615	
Goodness-of-fit on F <sup>2</sup>	1.055	
Final R indices [I > 2σ(I)]	R1 = 0.0479, wR2 = 0.1190 [9167]	
R indices (all data)	R1 = 0.0668, wR2 = 0.1247	
Largest diff. peak and hole	0.951 and -0.573 e.Å <sup>-3</sup>	

$$R1 = \sum(|F_o| - |F_c|) / \sum|F_o|; \quad wR2 = [\sum[w(F_o^2 - F_c^2)^2] / \sum[w(F_o^2)^2]]^{1/2}; \quad S = [\sum[w(F_o^2 - F_c^2)^2] / (n-p)]^{1/2}$$

$$w = 1/[\sigma^2(F_o^2) + (m \cdot p)^2 + n \cdot p], \quad p = [\max(F_o^2, 0) + 2 \cdot F_c^2] / 3, \quad m \text{ \& \ } n \text{ are constants}$$

Table B-2. Crystal data and structure refinement for 4·4DMF·4H<sub>2</sub>O.

Identification code	m89	
Empirical formula	C <sub>90</sub> H <sub>102</sub> Fe <sub>6</sub> Mn <sub>8</sub> N <sub>6</sub> O <sub>40</sub>	
Formula weight	2682.40	
Temperature	173(2) K	
Wavelength	0.71073 Å	
Crystal system	Monoclinic	
Space group	C2/c	
Unit cell dimensions	a = 23.282(3) Å	α = 90°.
	b = 19.331(3) Å	β = 97.885(3)°.
	c = 22.198(3) Å	γ = 90°.
Volume	9896(3) Å <sup>3</sup>	
Z	4	
Density (calculated)	1.660 Mg/m <sup>3</sup>	
Absorption coefficient	1.950 mm <sup>-1</sup>	
F(000)	4980	
Crystal size	0.26 x 0.22 x 0.20 mm <sup>3</sup>	
Theta range for data collection	2.11 to 27.50°.	
Index ranges	-30 ≤ h ≤ 30, -20 ≤ k ≤ 24, -28 ≤ l ≤ 23	
Reflections collected	32126	
Independent reflections	11193 [R(int) = 0.0499]	
Completeness to theta = 27.50°	98.4 %	
Absorption correction	None	
Max. and min. transmission	0.6964 and 0.6310	
Refinement method	Full-matrix least-squares on F <sup>2</sup>	
Data / restraints / parameters	11193 / 0 / 670	
Goodness-of-fit on F <sup>2</sup>	1.010	
Final R indices [I > 2σ(I)]	R1 = 0.0456, wR2 = 0.0927 [7031]	
R indices (all data)	R1 = 0.0934, wR2 = 0.1117	
Largest diff. peak and hole	0.525 and -0.668 e.Å <sup>-3</sup>	

$$R1 = \sum(|F_o| - |F_c|) / \sum|F_o|$$

$$wR2 = [\sum[w(F_o^2 - F_c^2)^2] / \sum[w(F_o^2)^2]]^{1/2}$$

$$S = [\sum[w(F_o^2 - F_c^2)^2] / (n-p)]^{1/2}$$

$$w = 1/[\sigma^2(F_o^2) + (m \cdot p)^2 + n \cdot p], p = [\max(F_o^2, 0) + 2 \cdot F_c^2] / 3, m \text{ \& } n \text{ are constants}$$

Table B-3. Crystal data and structure refinement for 5·3DMF·H<sub>2</sub>O.

Identification code	mas28	
Empirical formula	C <sub>96</sub> H <sub>104</sub> Fe <sub>6</sub> Mn <sub>8</sub> N <sub>8</sub> O <sub>36</sub>	
Formula weight	2720.49	
Temperature	100(2) K	
Wavelength	0.71073 Å	
Crystal system	Monoclinic	
Space group	P2 <sub>1</sub> /c	
Unit cell dimensions	a = 24.015(2) Å	α = 90°.
	b = 14.8647(14) Å	β = 101.088(5)°.
	c = 29.558(3) Å	γ = 90°.
Volume	10354.7(17) Å <sup>3</sup>	
Z	4	
Density (calculated)	1.745 Mg/m <sup>3</sup>	
Absorption coefficient	1.839 mm <sup>-1</sup>	
F(000)	5520	
Crystal size	0.20 x 0.18 x 0.10 mm <sup>3</sup>	
Theta range for data collection	1.54 to 27.50°.	
Index ranges	-31 ≤ h ≤ 31, -19 ≤ k ≤ 19, -38 ≤ l ≤ 38	
Reflections collected	117623	
Independent reflections	23801 [R(int) = 0.0826]	
Completeness to theta = 27.50°	100.0 %	
Absorption correction	Numerical	
Max. and min. transmission	0.8332 and 0.7122	
Refinement method	Full-matrix least-squares on F <sup>2</sup>	
Data / restraints / parameters	23801 / 0 / 1210	
Goodness-of-fit on F <sup>2</sup>	0.928	
Final R indices [I > 2σ(I)]	R1 = 0.0429, wR2 = 0.0947 [15611]	
R indices (all data)	R1 = 0.0703, wR2 = 0.0999	
Largest diff. peak and hole	0.847 and -0.804 e.Å <sup>-3</sup>	

$$R1 = \sum(|F_o| - |F_c|) / \sum|F_o|$$

$$wR2 = [\sum[w(F_o^2 - F_c^2)^2] / \sum[w(F_o^2)^2]]^{1/2}$$

$$S = [\sum[w(F_o^2 - F_c^2)^2] / (n-p)]^{1/2}$$

$$w = 1/[\sigma^2(F_o^2) + (m^*p)^2 + n^*p], p = [\max(F_o^2, 0) + 2^* F_c^2]/3, m \& n \text{ are constants}$$

Table B-4. Crystal data and structure refinement for **6·2MeOH·2H<sub>2</sub>O**.

Identification code	mas05	
Empirical formula	C <sub>86</sub> H <sub>91</sub> Cl <sub>4</sub> Fe <sub>14</sub> O <sub>35</sub>	
Formula weight	2608.29	
Temperature	173(2) K	
Wavelength	0.71073 Å	
Crystal system	Monoclinic	
Space group	P2(1)/c	
Unit cell dimensions	a = 18.4240(12) Å	α = 90°.
	b = 24.6645(15) Å	β = 109.349(1)°.
	c = 24.1746(15) Å	γ = 90°.
Volume	10364.9(11) Å <sup>3</sup>	
Z	4	
Density (calculated)	1.671 Mg/m <sup>3</sup>	
Absorption coefficient	2.075 mm <sup>-1</sup>	
F(000)	5276	
Crystal size	0.25 x 0.14 x 0.08 mm <sup>3</sup>	
Theta range for data collection	1.43 to 27.5°.	
Index ranges	-23 ≤ h ≤ 22, -26 ≤ k ≤ 31, -31 ≤ l ≤ 31	
Reflections collected	70131	
Independent reflections	23599 [R(int) = 0.0675]	
Completeness to theta = 27.50°	99.1 %	
Absorption correction	Integration	
Max. and min. transmission	0.8552 and 0.6558	
Refinement method	Full-matrix least-squares on F <sup>2</sup>	
Data / restraints / parameters	23599 / 15 / 1119	
Goodness-of-fit on F <sup>2</sup>	0.702	
Final R indices [I > 2σ(I)]	R1 = 0.0406, wR2 = 0.0831 [8375]	
R indices (all data)	R1 = 0.0933, wR2 = 0.0859	
Largest diff. peak and hole	1.377 and -1.006 e.Å <sup>-3</sup>	

$$R1 = \sum(|F_o| - |F_c|) / \sum|F_o|$$

$$wR2 = [\sum[w(F_o^2 - F_c^2)^2] / \sum[w(F_o^2)^2]]^{1/2}$$

$$S = [\sum[w(F_o^2 - F_c^2)^2] / (n-p)]^{1/2}$$

$$w = 1/[\sigma^2(F_o^2) + (m \cdot p)^2 + n \cdot p], p = [\max(F_o^2, 0) + 2 \cdot F_c^2] / 3, m \text{ \& n are constants.}$$

Table B-5. Crystal data and structure refinement for 7·3DMF·3H<sub>2</sub>O.

Identification code	xm228	
Empirical formula	C79 H81 Fe6 Mn7 O37	
Formula weight	2342.14	
Temperature	173(2) K	
Wavelength	0.71073 Å	
Crystal system	Rhombohedral	
Space group	R-3	
Unit cell dimensions	a = 15.8534(6) Å	α = 90°.
	b = 15.8534(6) Å	β = 90°.
	c = 64.090(5) Å	γ = 120°.
Volume	13949.7(13) Å <sup>3</sup>	
Z	6	
Density (calculated)	1.611 Mg/m <sup>3</sup>	
Absorption coefficient	1.897 mm <sup>-1</sup>	
F(000)	6798	
Crystal size	0.09 x 0.09 x 0.04 mm <sup>3</sup>	
Theta range for data collection	1.52 to 25.71°.	
Index ranges	-14 ≤ h ≤ 18, -18 ≤ k ≤ 17, -77 ≤ l ≤ 50	
Reflections collected	21258	
Independent reflections	5265 [R(int) = 0.0537]	
Completeness to theta = 25.71°	88.7 %	
Absorption correction	Integration	
Max. and min. transmission	0.9306 and 0.8177	
Refinement method	Full-matrix least-squares on F <sup>2</sup>	
Data / restraints / parameters	5265 / 0 / 352	
Goodness-of-fit on F <sup>2</sup>	0.998	
Final R indices [I > 2σ(I)]	R1 = 0.0359, wR2 = 0.0970 [3756]	
R indices (all data)	R1 = 0.0566, wR2 = 0.1016	
Largest diff. peak and hole	0.682 and -0.570 e.Å <sup>-3</sup>	

$$R1 = \sum(|F_o| - |F_c|) / \sum|F_o|$$

$$wR2 = [\sum[w(F_o^2 - F_c^2)^2] / \sum[w(F_o^2)^2]]^{1/2}$$

$$S = [\sum[w(F_o^2 - F_c^2)^2] / (n-p)]^{1/2}$$

$$w = 1/[\sigma^2(F_o^2) + (m \cdot p)^2 + n \cdot p], p = [\max(F_o^2, 0) + 2 \cdot F_c^2] / 3, m \text{ \& n are constants.}$$

Table B-6. Crystal data and structure refinement for **8**·4MeOH·2H<sub>2</sub>O.

Identification code	mas03	
Empirical formula	C <sub>92</sub> H <sub>131</sub> Fe <sub>6</sub> Co <sub>7</sub> O <sub>49</sub>	
Formula weight	2768.62	
Temperature	173(2) K	
Wavelength	0.71073 Å	
Crystal system	Trigonal	
Space group	P31c	
Unit cell dimensions	a = 16.7433(5) Å	α = 90°.
	b = 16.7433 (5) Å	β = 90°.
	c = 21.0276(12) Å	γ = 120°.
Volume	5105.1(4) Å <sup>3</sup>	
Z	2	
Density (calculated)	1.801 Mg/m <sup>3</sup>	
Absorption coefficient	2.21 mm <sup>-1</sup>	
F(000)	3184	
Crystal size	0.20 x 0.18 x 0.18 mm <sup>3</sup>	
Theta range for data collection	1.85 to 27.51°.	
Index ranges	-20 ≤ h ≤ 18, -15 ≤ k ≤ 20, -26 ≤ l ≤ 26	
Reflections collected	33742	
Independent reflections	7491 [R(int) = 0.0456]	
Completeness to theta = 27.49°	99.9 %	
Absorption correction	Integration	
Max. and min. transmission	0.7234 and 0.6435	
Refinement method	Full-matrix least-squares on F <sup>2</sup>	
Data / restraints / parameters	7491 / 1 / 352	
Goodness-of-fit on F <sup>2</sup>	0.935	
Final R indices [I > 2σ(I)]	R1 = 0.0357, wR2 = 0.0712 [6155]	
R indices (all data)	R1 = 0.0384, wR2 = 0.0672	
Absolute structure parameter	0.477(12)	
Largest diff. peak and hole	0.499 and -0.366 e.Å <sup>-3</sup>	

$$R1 = \frac{\sum(|F_o| - |F_c|)}{\sum|F_o|}$$

$$wR2 = \frac{[\sum[w(F_o^2 - F_c^2)^2]]^{1/2}}{[\sum[w(F_o^2)^2]]^{1/2}}$$

$$S = \frac{[\sum[w(F_o^2 - F_c^2)^2]]^{1/2}}{(n-p)}$$

$$w = 1/[\sigma^2(F_o^2) + (m^*p)^2 + n^*p], \quad p = [\max(F_o^2, 0) + 2^* F_c^2]/3, \quad m \text{ \& \ } n \text{ are constants.}$$

Table B-7. Crystal data and structure refinement for **9**-4MeOH.

Identification code	mas04	
Empirical formula	C <sub>92</sub> H <sub>127</sub> Fe <sub>6</sub> Ni <sub>7</sub> O <sub>47</sub>	
Formula weight	2731.01	
Temperature	173(2) K	
Wavelength	0.71073 Å	
Crystal system	Trigonal	
Space group	P31c	
Unit cell dimensions	a = 16.7578(5) Å	α = 90°.
	b = 16.7578(5) Å	β = 90°.
	c = 20.5954(12) Å	γ = 120°.
Volume	5008.8(4) Å <sup>3</sup>	
Z	2	
Density (calculated)	1.881 Mg/m <sup>3</sup>	
Absorption coefficient	2.22 mm <sup>-1</sup>	
F(000)	2814	
Crystal size	0.23 x 0.19 x 0.19 mm <sup>3</sup>	
Theta range for data collection	1.72 to 27.49°.	
Index ranges	-21 ≤ h ≤ 19, -15 ≤ k ≤ 21, -26 ≤ l ≤ 26	
Reflections collected	32897	
Independent reflections	7427 [R(int) = 0.0416]	
Completeness to theta = 27.49°	99.9 %	
Absorption correction	Integration	
Max. and min. transmission	0.7283 and 0.6445	
Refinement method	Full-matrix least-squares on F <sup>2</sup>	
Data / restraints / parameters	7427 / 1 / 366	
Goodness-of-fit on F <sup>2</sup>	0.951	
Final R indices [I > 2σ(I)]	R1 = 0.0274, wR2 = 0.0650 [6190]	
R indices (all data)	R1 = 0.0343, wR2 = 0.0661	
Absolute structure parameter	0.464(11)	
Largest diff. peak and hole	0.516 and -0.371 e.Å <sup>-3</sup>	

$$R1 = \frac{\sum(|F_o| - |F_c|)}{\sum|F_o|}$$

$$wR2 = \left[ \frac{\sum[w(F_o^2 - F_c^2)^2]}{\sum[w(F_o^2)^2]} \right]^{1/2}$$

$$S = \left[ \frac{\sum[w(F_o^2 - F_c^2)^2]}{(n-p)} \right]^{1/2}$$

$$w = 1/[\sigma^2(F_o^2) + (m^*p)^2 + n^*p], \quad p = [\max(F_o^2, 0) + 2^* F_c^2]/3, \quad m \text{ \& \ } n \text{ are constants.}$$

Table B-8. Crystal data and structure refinement for **10**·6MeOH·2H<sub>2</sub>O.

Identification code	mas11	
Empirical formula	C <sub>94</sub> H <sub>117</sub> Cl <sub>2</sub> Fe <sub>6</sub> O <sub>49</sub> Zn <sub>7.50</sub>	
Formula weight	2927.15	
Temperature	173(2) K	
Wavelength	0.71073 Å	
Crystal system	Trigonal	
Space group	P-3	
Unit cell dimensions	a = 16.7685(8) Å	α = 90°.
	b = 16.7685(8) Å	β = 90°.
	c = 21.507(2) Å	γ = 120°.
Volume	5237.1(6) Å <sup>3</sup>	
Z	2	
Density (calculated)	1.856 Mg/m <sup>3</sup>	
Absorption coefficient	2.635 mm <sup>-1</sup>	
F(000)	2976	
Crystal size	0.26 x 0.12 x 0.02 mm <sup>3</sup>	
Theta range for data collection	1.69 to 27.49°.	
Index ranges	-12 ≤ h ≤ 21, -21 ≤ k ≤ 21, -27 ≤ l ≤ 25	
Reflections collected	35569	
Independent reflections	8028 [R(int) = 0.1275]	
Completeness to theta = 27.49°	100.0 %	
Absorption correction	Integration	
Max. and min. transmission	0.9455 and 0.5903	
Refinement method	Full-matrix least-squares on F <sup>2</sup>	
Data / restraints / parameters	8028 / 8 / 381	
Goodness-of-fit on F <sup>2</sup>	1.105	
Final R indices [I > 2σ(I)]	R1 = 0.0756, wR2 = 0.1985 [4282]	
R indices (all data)	R1 = 0.1208, wR2 = 0.2147	
Largest diff. peak and hole	2.319 and -1.172 e.Å <sup>-3</sup>	

$$R1 = \sum(|F_o| - |F_c|) / \sum|F_o|$$

$$wR2 = [\sum[w(F_o^2 - F_c^2)^2] / \sum[w(F_o^2)^2]]^{1/2}$$

$$S = [\sum[w(F_o^2 - F_c^2)^2] / (n-p)]^{1/2}$$

$$w = 1/[\sigma^2(F_o^2) + (m \cdot p)^2 + n \cdot p], p = [\max(F_o^2, 0) + 2 \cdot F_c^2] / 3, m \text{ \& n are constants.}$$

APPENDIX C  
BOND LENGTHS AND ANGLES

Table C-1. Selected bond lengths [Å] and angles [°] for [Mn<sub>13</sub>O<sub>8</sub>(OMe)<sub>6</sub>(fdc)<sub>6</sub>], **2**.

Mn1-O19#1	1.876(3)	Mn4-O7	2.077(3)
Mn1-O5	1.912(3)	Mn4-O12#1	2.086(3)
Mn1-O2	1.956(3)	Mn4-O15	2.225(3)
Mn1-O17#1	1.999(3)	Mn4-O5	2.226(3)
Mn1-O14#1	2.097(3)	Mn4-O17#1	2.235(3)
Mn1-O16#1	2.299(3)	Mn4-O18	2.465(3)
Mn1-Mn5#1	2.9201(9)	Mn4-Mn3#1	3.2354(9)
Mn1-Mn6#1	2.9215(9)	Mn5-O19	1.868(3)
Mn1-Mn7	3.0349(6)	Mn5-O10	1.909(3)
Mn1-Mn4	3.1757(8)	Mn5-O13	1.959(3)
Mn1-Mn2	3.2294(9)	Mn5-O18	2.022(3)
Mn2-O4	2.059(3)	Mn5-O8	2.106(3)
Mn2-O6	2.074(3)	Mn5-O17	2.321(3)
Mn2-O18	2.195(3)	Mn5-Mn1#1	2.9201(9)
Mn2-O10	2.222(3)	Mn5-Mn6	2.9275(9)
Mn2-O5	2.227(3)	Mn5-Mn7	3.0635(6)
Mn2-O16#1	2.421(3)	Mn6-O19	1.876(3)
Mn2-Mn5	3.1573(9)	Mn6-O15	1.916(3)
Mn2-Mn3	3.1964(9)	Mn6-O9	1.950(3)
Mn2-Mn7	3.1993(7)	Mn6-O16	2.010(3)
Mn2-Mn4	3.2364(9)	Mn6-O1#1	2.108(3)
Mn3-O11	2.062(3)	Mn6-O18	2.304(3)
Mn3-O3	2.092(3)	Mn6-Mn1#1	2.9215(9)
Mn3-O16#1	2.222(3)	Mn6-Mn7	3.0412(6)
Mn3-O15#1	2.223(3)	Mn6-Mn3#1	3.1709(9)
Mn3-O10	2.227(3)	Mn7-O16	1.894(3)
Mn3-O17	2.435(3)	Mn7-O16#1	1.894(3)
Mn3-Mn6#1	3.1709(9)	Mn7-O18#1	1.901(3)
Mn3-Mn7	3.2202(7)	Mn7-O18	1.901(3)
Mn3-Mn4#1	3.2354(9)	Mn7-O17	1.905(3)
Mn3-Mn5	3.2369(9)	Mn7-O17#1	1.905(3)

Mn7-Mn1#1	3.0349(6)	O5-Mn1-O2	92.06(12)
Mn7-Mn6#1	3.0412(6)	O19#1-Mn1-O17#1	89.17(12)
Mn7-Mn5#1	3.0635(6)	O5-Mn1-O17#1	86.68(12)
Fe1-C2	2.035(4)	O2-Mn1-O17#1	167.40(12)
Fe1-C10	2.037(5)	O19#1-Mn1-O14#1	88.22(12)
Fe1-C3	2.041(5)	O5-Mn1-O14#1	100.14(12)
Fe1-C11	2.041(5)	O2-Mn1-O14#1	101.08(12)
Fe1-C12	2.043(5)	O17#1-Mn1-O14#1	91.48(11)
Fe1-C9	2.049(5)	O19#1-Mn1-O16#1	80.61(11)
Fe1-C4	2.050(4)	O5-Mn1-O16#1	90.38(11)
Fe1-C6	2.051(4)	O2-Mn1-O16#1	91.05(11)
Fe1-C5	2.052(5)	O17#1-Mn1-O16#1	76.44(10)
Fe1-C8	2.054(5)	O14#1-Mn1-O16#1	163.56(11)
Fe2-C15	2.031(4)	O19#1-Mn1-Mn5#1	38.65(8)
Fe2-C21	2.043(4)	O5-Mn1-Mn5#1	138.80(9)
Fe2-C22	2.048(4)	O2-Mn1-Mn5#1	128.75(9)
Fe2-C25	2.049(5)	O17#1-Mn1-Mn5#1	52.32(8)
Fe2-C16	2.049(5)	O14#1-Mn1-Mn5#1	79.50(8)
Fe2-C19	2.050(5)	O16#1-Mn1-Mn5#1	84.26(7)
Fe2-C23	2.053(4)	O19#1-Mn1-Mn6#1	38.86(9)
Fe2-C17	2.053(5)	O5-Mn1-Mn6#1	132.74(9)
Fe2-C18	2.057(5)	O2-Mn1-Mn6#1	82.17(9)
Fe2-C24	2.057(4)	O17#1-Mn1-Mn6#1	89.48(8)
Fe3-C34	2.038(4)	O14#1-Mn1-Mn6#1	127.05(9)
Fe3-C29	2.040(4)	O16#1-Mn1-Mn6#1	43.27(7)
Fe3-C38	2.041(5)	Mn5#1-Mn1-Mn6#1	60.15(2)
Fe3-C30	2.043(5)	O19#1-Mn1-Mn7	82.38(8)
Fe3-C35	2.043(5)	O5-Mn1-Mn7	89.29(9)
Fe3-C28	2.044(4)	O2-Mn1-Mn7	129.63(9)
Fe3-C31	2.050(5)	O17#1-Mn1-Mn7	37.88(8)
Fe3-C32	2.051(4)	O14#1-Mn1-Mn7	128.17(8)
Fe3-C37	2.056(4)	O16#1-Mn1-Mn7	38.59(7)
Fe3-C36	2.060(5)	Mn5#1-Mn1-Mn7	61.883(17)
		Mn6#1-Mn1-Mn7	61.370(17)
O19#1-Mn1-O5	170.75(12)	O19#1-Mn1-Mn4	133.36(8)
O19#1-Mn1-O2	90.19(12)	O5-Mn1-Mn4	43.64(8)

O2-Mn1-Mn4	135.71(9)	O5-Mn2-Mn5	128.22(8)
O17#1-Mn1-Mn4	44.30(8)	O16#1-Mn2-Mn5	81.15(7)
O14#1-Mn1-Mn4	89.77(8)	O4-Mn2-Mn3	76.31(9)
O16#1-Mn1-Mn4	89.21(7)	O6-Mn2-Mn3	145.60(9)
Mn5#1-Mn1-Mn4	95.34(2)	O18-Mn2-Mn3	81.23(8)
Mn6#1-Mn1-Mn4	124.34(3)	O10-Mn2-Mn3	44.14(7)
Mn7-Mn1-Mn4	63.022(16)	O5-Mn2-Mn3	123.68(8)
O19#1-Mn1-Mn2	128.87(9)	O16#1-Mn2-Mn3	43.95(7)
O5-Mn1-Mn2	42.36(9)	Mn5-Mn2-Mn3	61.251(19)
O2-Mn1-Mn2	87.45(9)	O4-Mn2-Mn7	126.14(9)
O17#1-Mn1-Mn2	83.18(8)	O6-Mn2-Mn7	126.86(8)
O14#1-Mn1-Mn2	142.20(9)	O18-Mn2-Mn7	35.46(7)
O16#1-Mn1-Mn2	48.42(7)	O10-Mn2-Mn7	80.66(7)
Mn5#1-Mn1-Mn2	123.16(3)	O5-Mn2-Mn7	80.00(7)
Mn6#1-Mn1-Mn2	90.41(2)	O16#1-Mn2-Mn7	36.15(6)
Mn7-Mn1-Mn2	61.329(16)	Mn5-Mn2-Mn7	57.620(16)
Mn4-Mn1-Mn2	60.69(2)	Mn3-Mn2-Mn7	60.463(16)
O4-Mn2-O6	107.00(12)	O4-Mn2-Mn1	94.54(9)
O4-Mn2-O18	157.39(12)	O6-Mn2-Mn1	124.66(9)
O6-Mn2-O18	92.99(11)	O18-Mn2-Mn1	82.15(7)
O4-Mn2-O10	90.22(11)	O10-Mn2-Mn1	129.31(8)
O6-Mn2-O10	101.54(11)	O5-Mn2-Mn1	35.34(7)
O18-Mn2-O10	75.19(10)	O16#1-Mn2-Mn1	45.27(7)
O4-Mn2-O5	101.49(11)	Mn5-Mn2-Mn1	113.91(2)
O6-Mn2-O5	89.81(11)	Mn3-Mn2-Mn1	88.34(2)
O18-Mn2-O5	88.75(10)	Mn7-Mn2-Mn1	56.338(15)
O10-Mn2-O5	160.66(11)	O4-Mn2-Mn4	144.78(9)
O4-Mn2-O16#1	90.39(11)	O6-Mn2-Mn4	76.39(9)
O6-Mn2-O16#1	161.47(11)	O18-Mn2-Mn4	49.57(8)
O18-Mn2-O16#1	71.34(10)	O10-Mn2-Mn4	124.05(7)
O10-Mn2-O16#1	84.34(10)	O5-Mn2-Mn4	43.36(7)
O5-Mn2-O16#1	80.28(10)	O16#1-Mn2-Mn4	85.74(7)
O4-Mn2-Mn5	126.52(9)	Mn5-Mn2-Mn4	87.45(2)
O6-Mn2-Mn5	93.08(9)	Mn3-Mn2-Mn4	121.09(3)
O18-Mn2-Mn5	39.48(7)	Mn7-Mn2-Mn4	60.624(16)
O10-Mn2-Mn5	36.61(7)	Mn1-Mn2-Mn4	58.833(19)

O11-Mn3-O3	106.76(12)	O11-Mn3-Mn4#1	76.21(9)
O11-Mn3-O16#1	156.98(12)	O3-Mn3-Mn4#1	144.46(9)
O3-Mn3-O16#1	92.82(11)	O16#1-Mn3-Mn4#1	80.82(7)
O11-Mn3-O15#1	89.48(11)	O15#1-Mn3-Mn4#1	43.36(7)
O3-Mn3-O15#1	101.18(11)	O10-Mn3-Mn4#1	123.45(7)
O16#1-Mn3-O15#1	74.63(10)	O17-Mn3-Mn4#1	43.65(7)
O11-Mn3-O10	102.25(11)	Mn6#1-Mn3-Mn4#1	60.798(19)
O3-Mn3-O10	91.10(11)	Mn2-Mn3-Mn4#1	120.23(3)
O16#1-Mn3-O10	89.07(10)	Mn7-Mn3-Mn4#1	60.420(16)
O15#1-Mn3-O10	159.91(11)	O11-Mn3-Mn5	95.46(9)
O11-Mn3-O17	91.13(11)	O3-Mn3-Mn5	125.66(9)
O3-Mn3-O17	161.53(11)	O16#1-Mn3-Mn5	82.25(7)
O16#1-Mn3-O17	70.83(10)	O15#1-Mn3-Mn5	128.51(8)
O15#1-Mn3-O17	83.13(10)	O10-Mn3-Mn5	35.11(7)
O10-Mn3-O17	80.41(10)	O17-Mn3-Mn5	45.65(7)
O11-Mn3-Mn6#1	125.79(9)	Mn6#1-Mn3-Mn5	113.44(2)
O3-Mn3-Mn6#1	92.62(9)	Mn2-Mn3-Mn5	58.779(19)
O16#1-Mn3-Mn6#1	38.99(7)	Mn7-Mn3-Mn5	56.644(15)
O15#1-Mn3-Mn6#1	36.56(8)	Mn4#1-Mn3-Mn5	88.34(2)
O10-Mn3-Mn6#1	128.04(8)	O7-Mn4-O12#1	108.77(12)
O17-Mn3-Mn6#1	80.13(7)	O7-Mn4-O15	103.87(11)
O11-Mn3-Mn2	146.20(9)	O12#1-Mn4-O15	90.57(11)
O3-Mn3-Mn2	77.41(9)	O7-Mn4-O5	89.09(11)
O16#1-Mn3-Mn2	49.13(7)	O12#1-Mn4-O5	102.12(11)
O15#1-Mn3-Mn2	123.21(8)	O15-Mn4-O5	158.04(11)
O10-Mn3-Mn2	44.00(7)	O7-Mn4-O17#1	155.76(11)
O17-Mn3-Mn2	85.19(7)	O12#1-Mn4-O17#1	91.98(11)
Mn6#1-Mn3-Mn2	86.69(2)	O15-Mn4-O17#1	87.86(10)
O11-Mn3-Mn7	126.77(9)	O5-Mn4-O17#1	74.01(10)
O3-Mn3-Mn7	126.45(9)	O7-Mn4-O18	90.77(11)
O16#1-Mn3-Mn7	35.03(7)	O12#1-Mn4-O18	159.90(11)
O15#1-Mn3-Mn7	79.81(7)	O15-Mn4-O18	79.88(10)
O10-Mn3-Mn7	80.10(7)	O5-Mn4-O18	82.32(10)
O17-Mn3-Mn7	36.11(6)	O17#1-Mn4-O18	70.19(10)
Mn6#1-Mn3-Mn7	56.823(15)	O7-Mn4-Mn1	125.19(9)
Mn2-Mn3-Mn7	59.813(17)	O12#1-Mn4-Mn1	92.43(9)

O15-Mn4-Mn1	126.49(7)	O13-Mn5-Mn1#1	81.81(9)
O5-Mn4-Mn1	36.36(7)	O18-Mn5-Mn1#1	88.65(8)
O17#1-Mn4-Mn1	38.65(7)	O8-Mn5-Mn1#1	126.96(8)
O18-Mn4-Mn1	79.50(7)	O17-Mn5-Mn1#1	42.96(7)
O7-Mn4-Mn3#1	147.15(9)	O19-Mn5-Mn6	38.66(9)
O12#1-Mn4-Mn3#1	76.35(9)	O10-Mn5-Mn6	137.93(9)
O15-Mn4-Mn3#1	43.31(7)	O13-Mn5-Mn6	129.30(9)
O5-Mn4-Mn3#1	122.27(8)	O18-Mn5-Mn6	51.61(8)
O17#1-Mn4-Mn3#1	48.75(7)	O8-Mn5-Mn6	79.31(8)
O18-Mn4-Mn3#1	84.69(7)	O17-Mn5-Mn6	83.52(7)
Mn1-Mn4-Mn3#1	85.98(2)	Mn1#1-Mn5-Mn6	59.95(2)
O7-Mn4-Mn2	76.06(9)	O19-Mn5-Mn7	81.69(8)
O12#1-Mn4-Mn2	145.51(9)	O10-Mn5-Mn7	89.20(8)
O15-Mn4-Mn2	122.13(8)	O13-Mn5-Mn7	128.62(9)
O5-Mn4-Mn2	43.40(8)	O18-Mn5-Mn7	37.26(8)
O17#1-Mn4-Mn2	79.73(7)	O8-Mn5-Mn7	127.27(8)
O18-Mn4-Mn2	42.67(7)	O17-Mn5-Mn7	38.42(7)
Mn1-Mn4-Mn2	60.474(19)	Mn1#1-Mn5-Mn7	60.900(17)
Mn3#1-Mn4-Mn2	118.68(2)	Mn6-Mn5-Mn7	60.963(16)
O19-Mn5-O10	170.16(12)	O19-Mn5-Mn2	132.04(9)
O19-Mn5-O13	90.67(12)	O10-Mn5-Mn2	43.96(9)
O10-Mn5-O13	92.14(12)	O13-Mn5-Mn2	136.01(9)
O19-Mn5-O18	88.45(12)	O18-Mn5-Mn2	43.65(8)
O10-Mn5-O18	86.51(12)	O8-Mn5-Mn2	90.32(8)
O13-Mn5-O18	165.76(12)	O17-Mn5-Mn2	87.98(7)
O19-Mn5-O8	88.12(12)	Mn1#1-Mn5-Mn2	122.72(3)
O10-Mn5-O8	100.42(12)	Mn6-Mn5-Mn2	94.13(2)
O13-Mn5-O8	102.93(12)	Mn7-Mn5-Mn2	61.878(16)
O18-Mn5-O8	91.24(11)	O19-Mn5-Mn3	128.71(9)
O19-Mn5-O17	80.23(11)	O10-Mn5-Mn3	42.15(8)
O10-Mn5-O17	90.33(11)	O13-Mn5-Mn3	86.81(9)
O13-Mn5-O17	90.20(11)	O18-Mn5-Mn3	82.68(8)
O18-Mn5-O17	75.64(10)	O8-Mn5-Mn3	142.19(8)
O8-Mn5-O17	162.58(11)	O17-Mn5-Mn3	48.60(7)
O19-Mn5-Mn1#1	38.85(8)	Mn1#1-Mn5-Mn3	90.33(2)
O10-Mn5-Mn1#1	132.46(9)	Mn6-Mn5-Mn3	122.33(3)

Mn7-Mn5-Mn3	61.402(17)	Mn1#1-Mn6-Mn7	61.153(16)
Mn2-Mn5-Mn3	59.970(19)	Mn5-Mn6-Mn7	61.727(16)
O19-Mn6-O15	170.77(12)	O19-Mn6-Mn3#1	132.76(9)
O19-Mn6-O9	91.18(12)	O15-Mn6-Mn3#1	43.70(8)
O15-Mn6-O9	91.28(12)	O9-Mn6-Mn3#1	134.92(9)
O19-Mn6-O16	88.79(12)	O16-Mn6-Mn3#1	44.07(8)
O15-Mn6-O16	86.63(12)	O1#1-Mn6-Mn3#1	91.19(8)
O9-Mn6-O16	165.64(12)	O18-Mn6-Mn3#1	88.85(7)
O19-Mn6-O1#1	86.97(12)	Mn1#1-Mn6-Mn3#1	94.51(2)
O15-Mn6-O1#1	101.17(12)	Mn5-Mn6-Mn3#1	124.09(2)
O9-Mn6-O1#1	102.40(12)	Mn7-Mn6-Mn3#1	62.404(17)
O16-Mn6-O1#1	91.94(11)	O16-Mn7-O16#1	180.0(2)
O19-Mn6-O18	80.33(11)	O16-Mn7-O18#1	90.61(12)
O15-Mn6-O18	90.79(11)	O16#1-Mn7-O18#1	89.39(12)
O9-Mn6-O18	89.72(11)	O16-Mn7-O18	89.39(12)
O16-Mn6-O18	76.12(10)	O16#1-Mn7-O18	90.61(12)
O1#1-Mn6-O18	162.65(11)	O18#1-Mn7-O18	180.0(2)
O19-Mn6-Mn1#1	38.87(8)	O16-Mn7-O17	89.26(12)
O15-Mn6-Mn1#1	138.06(9)	O16#1-Mn7-O17	90.74(12)
O9-Mn6-Mn1#1	130.04(9)	O18#1-Mn7-O17	90.76(12)
O16-Mn6-Mn1#1	51.64(8)	O18-Mn7-O17	89.24(12)
O1#1-Mn6-Mn1#1	79.12(8)	O16-Mn7-O17#1	90.74(12)
O18-Mn6-Mn1#1	83.58(7)	O16#1-Mn7-O17#1	89.26(12)
O19-Mn6-Mn5	38.47(8)	O18#1-Mn7-O17#1	89.24(12)
O15-Mn6-Mn5	133.36(9)	O18-Mn7-O17#1	90.76(12)
O9-Mn6-Mn5	81.79(8)	O17-Mn7-O17#1	180.00(17)
O16-Mn6-Mn5	89.32(8)	O16-Mn7-Mn1#1	49.20(9)
O1#1-Mn6-Mn5	125.40(9)	O16#1-Mn7-Mn1#1	130.80(9)
O18-Mn6-Mn5	43.47(7)	O18#1-Mn7-Mn1#1	92.42(8)
Mn1#1-Mn6-Mn5	59.90(2)	O18-Mn7-Mn1#1	87.58(8)
O19-Mn6-Mn7	82.21(8)	O17-Mn7-Mn1#1	40.10(8)
O15-Mn6-Mn7	89.29(8)	O17#1-Mn7-Mn1#1	139.90(8)
O9-Mn6-Mn7	128.37(8)	O16-Mn7-Mn1	130.80(9)
O16-Mn6-Mn7	37.49(8)	O16#1-Mn7-Mn1	49.20(9)
O1#1-Mn6-Mn7	128.04(8)	O18#1-Mn7-Mn1	87.58(8)
O18-Mn6-Mn7	38.65(7)	O18-Mn7-Mn1	92.42(8)

O17-Mn7-Mn1	139.90(8)	O16#1-Mn7-Mn5#1	87.52(8)
O17#1-Mn7-Mn1	40.10(8)	O18#1-Mn7-Mn5#1	40.09(9)
Mn1#1-Mn7-Mn1	180.00(2)	O18-Mn7-Mn5#1	139.91(9)
O16-Mn7-Mn6#1	139.78(8)	O17-Mn7-Mn5#1	130.80(8)
O16#1-Mn7-Mn6#1	40.22(8)	O17#1-Mn7-Mn5#1	49.20(8)
O18#1-Mn7-Mn6#1	49.20(8)	Mn1#1-Mn7-Mn5#1	122.784(16)
O18-Mn7-Mn6#1	130.80(8)	Mn1-Mn7-Mn5#1	57.216(16)
O17-Mn7-Mn6#1	92.26(8)	Mn6#1-Mn7-Mn5#1	57.310(17)
O17#1-Mn7-Mn6#1	87.74(8)	Mn6-Mn7-Mn5#1	122.690(17)
Mn1#1-Mn7-Mn6#1	122.523(16)	O16-Mn7-Mn5	87.52(8)
Mn1-Mn7-Mn6#1	57.477(16)	O16#1-Mn7-Mn5	92.48(8)
O16-Mn7-Mn6	40.22(8)	O18#1-Mn7-Mn5	139.91(9)
O16#1-Mn7-Mn6	139.78(8)	O18-Mn7-Mn5	40.09(9)
O18#1-Mn7-Mn6	130.80(8)	O17-Mn7-Mn5	49.20(8)
O18-Mn7-Mn6	49.20(8)	O17#1-Mn7-Mn5	130.80(8)
O17-Mn7-Mn6	87.74(8)	Mn1#1-Mn7-Mn5	57.216(16)
O17#1-Mn7-Mn6	92.26(8)	Mn1-Mn7-Mn5	122.784(16)
Mn1#1-Mn7-Mn6	57.478(16)	Mn6#1-Mn7-Mn5	122.690(17)
Mn1-Mn7-Mn6	122.522(16)	Mn6-Mn7-Mn5	57.310(17)
Mn6#1-Mn7-Mn6	180.00(3)	Mn5#1-Mn7-Mn5	180.00(3)
O16-Mn7-Mn5#1	92.48(8)		

Table C-2. Selected bond lengths [Å] and angles [°] for  $[\text{Mn}_8\text{O}_4(\text{fdc})_6(\text{DMF})_2(\text{H}_2\text{O})_2]$ , **4**.

Mn1-O15	2.075(3)	Mn2-Mn3	3.0669(8)
Mn1-O11	2.090(3)	Mn2-Mn2#1	3.1150(11)
Mn1-O5	2.099(3)	Mn3-O15	1.930(3)
Mn1-O2	2.122(3)	Mn3-O16	1.979(3)
Mn1-O14	2.168(3)	Mn3-O6	2.003(3)
Mn2-O16#1	1.921(3)	Mn3-O8	2.010(3)
Mn2-O15#1	1.921(2)	Mn3-O9	2.084(3)
Mn2-O3	1.985(3)	Mn3-O16#1	2.138(3)
Mn2-O1	1.987(3)	Mn3-Mn2#1	2.9095(8)
Mn2-O12#1	2.136(3)	Mn3-Mn3#1	3.0926(12)
Mn2-O15	2.219(2)	Fe1-C2#1	2.033(4)
Mn2-Mn3#1	2.9096(8)	Fe1-C2	2.033(4)

Fe1-C3#1	2.038(5)	Fe5-C35	2.040(5)
Fe1-C3	2.038(5)	Fe5-C30	2.047(5)
Fe1-C6	2.046(4)	Fe5-C33	2.048(5)
Fe1-C6#1	2.046(4)	Fe5-C32	2.049(4)
Fe1-C5	2.054(5)	Fe5-C36	2.053(5)
Fe1-C5#1	2.054(5)	Fe5-C29	2.064(5)
Fe1-C4#1	2.054(5)	Fe5-C28	2.064(4)
Fe1-C4	2.054(5)		
Fe2-C14	2.026(4)	O15-Mn1-O11	95.69(10)
Fe2-C9	2.034(4)	O15-Mn1-O5	94.58(10)
Fe2-C18	2.036(4)	O11-Mn1-O5	116.63(11)
Fe2-C8	2.040(4)	O15-Mn1-O2	91.18(10)
Fe2-C12	2.043(4)	O11-Mn1-O2	128.48(11)
Fe2-C15	2.044(4)	O5-Mn1-O2	113.57(11)
Fe2-C17	2.044(4)	O15-Mn1-O14	175.52(12)
Fe2-C10	2.048(4)	O11-Mn1-O14	82.83(13)
Fe2-C11	2.055(5)	O5-Mn1-O14	89.86(13)
Fe2-C16	2.068(5)	O2-Mn1-O14	86.47(12)
Fe3-O10#1	2.058(3)	O16#1-Mn2-O15#1	83.04(11)
Fe3-O16#1	2.065(3)	O16#1-Mn2-O3	95.46(11)
Fe3-O7	2.096(3)	O15#1-Mn2-O3	175.32(11)
Fe3-O4	2.118(3)	O16#1-Mn2-O1	173.53(11)
Fe3-O13	2.173(3)	O15#1-Mn2-O1	92.52(11)
Fe4-C24	2.028(5)	O3-Mn2-O1	88.58(11)
Fe4-C24#1	2.028(5)	O16#1-Mn2-O12#1	94.87(11)
Fe4-C20	2.034(6)	O15#1-Mn2-O12#1	95.43(11)
Fe4-C20#1	2.034(6)	O3-Mn2-O12#1	89.11(11)
Fe4-C21#1	2.043(7)	O1-Mn2-O12#1	90.23(10)
Fe4-C21	2.043(7)	O16#1-Mn2-O15	81.92(10)
Fe4-C23	2.045(6)	O15#1-Mn2-O15	82.37(10)
Fe4-C23#1	2.045(6)	O3-Mn2-O15	93.04(10)
Fe4-C22	2.058(7)	O1-Mn2-O15	92.85(10)
Fe4-C22#1	2.058(7)	O12#1-Mn2-O15	176.29(10)
Fe5-C26	2.021(4)	O16#1-Mn2-Mn3#1	42.52(8)
Fe5-C27	2.034(4)	O15#1-Mn2-Mn3#1	41.04(7)
Fe5-C34	2.039(5)	O3-Mn2-Mn3#1	137.90(8)

O1-Mn2-Mn3#1	133.49(8)	O8-Mn3-O9	87.07(11)
O12#1-Mn2-Mn3#1	91.78(8)	O15-Mn3-O16#1	83.90(10)
O15-Mn2-Mn3#1	84.60(7)	O16-Mn3-O16#1	82.29(11)
O16#1-Mn2-Mn3	43.65(8)	O6-Mn3-O16#1	94.15(10)
O15#1-Mn2-Mn3	85.51(8)	O8-Mn3-O16#1	92.06(10)
O3-Mn2-Mn3	90.35(8)	O9-Mn3-O16#1	177.92(11)
O1-Mn2-Mn3	131.52(7)	O15-Mn3-Mn2#1	40.82(7)
O12#1-Mn2-Mn3	138.22(8)	O16-Mn3-Mn2#1	41.00(8)
O15-Mn2-Mn3	38.82(6)	O6-Mn3-Mn2#1	135.46(8)
Mn3#1-Mn2-Mn3	62.26(2)	O8-Mn3-Mn2#1	134.30(8)
O16#1-Mn2-Mn2#1	83.96(8)	O9-Mn3-Mn2#1	93.39(7)
O15#1-Mn2-Mn2#1	44.97(7)	O16#1-Mn3-Mn2#1	85.85(7)
O3-Mn2-Mn2#1	130.53(8)	O15-Mn3-Mn2	46.13(7)
O1-Mn2-Mn2#1	89.57(7)	O16-Mn3-Mn2	84.39(8)
O12#1-Mn2-Mn2#1	140.34(8)	O6-Mn3-Mn2	90.62(8)
O15-Mn2-Mn2#1	37.72(6)	O8-Mn3-Mn2	130.30(8)
Mn3#1-Mn2-Mn2#1	61.092(18)	O9-Mn3-Mn2	142.61(8)
Mn3-Mn2-Mn2#1	56.147(18)	O16#1-Mn3-Mn2	38.34(7)
O15-Mn3-O16	81.33(10)	Mn2#1-Mn3-Mn2	62.76(2)
O15-Mn3-O6	94.80(11)	O15-Mn3-Mn3#1	84.65(7)
O16-Mn3-O6	174.97(11)	O16-Mn3-Mn3#1	43.28(8)
O15-Mn3-O8	173.76(11)	O6-Mn3-Mn3#1	133.46(8)
O16-Mn3-O8	93.44(11)	O8-Mn3-Mn3#1	89.21(8)
O6-Mn3-O8	90.23(11)	O9-Mn3-Mn3#1	138.65(8)
O15-Mn3-O9	96.80(10)	O16#1-Mn3-Mn3#1	39.40(7)
O16-Mn3-O9	95.86(11)	Mn2#1-Mn3-Mn3#1	61.368(19)
O6-Mn3-O9	87.75(11)	Mn2-Mn3-Mn3#1	56.375(17)

Table C-3. Selected bond lengths [ $\text{\AA}$ ] and angles [ $^\circ$ ] for  $[\text{Mn}_8\text{O}_4(\text{fdc})_6(\text{DMF})_4]$ , **5**.

Mn1-O3	1.8848(19)	Mn1-O1	2.295(2)
Mn1-O2	1.895(2)	Mn1-Mn3	2.8308(7)
Mn1-O5	1.973(2)	Mn1-Mn4	3.1144(7)
Mn1-O24	1.981(2)	Mn1-Mn2	3.2053(7)
Mn1-O16	2.167(2)	Mn2-O4	1.884(2)

Mn2-O1	1.9037(19)	Mn8-O4	2.0941(19)
Mn2-O9	1.961(2)	Mn8-O10	2.108(2)
Mn2-O21	1.983(2)	Mn8-O26	2.117(2)
Mn2-O20	2.145(2)	Mn8-O32	2.176(2)
Mn2-O3	2.340(2)	Fe1-C8	2.031(3)
Mn2-Mn4	2.8327(7)	Fe1-C2	2.035(3)
Mn2-Mn3	3.1279(8)	Fe1-C3	2.043(3)
Mn3-O3	1.872(2)	Fe1-C9	2.046(3)
Mn3-O2	1.903(2)	Fe1-C12	2.054(3)
Mn3-O12	1.938(2)	Fe1-C4	2.058(3)
Mn3-O25	1.980(2)	Fe1-C6	2.062(3)
Mn3-O13	2.149(2)	Fe1-C10	2.064(3)
Mn3-O4	2.310(2)	Fe1-C5	2.074(3)
Mn3-Mn4	3.1490(7)	Fe1-C11	2.078(3)
Mn4-O1	1.885(2)	Fe2-C21	2.031(4)
Mn4-O4	1.8918(19)	Fe2-C20	2.031(3)
Mn4-O8	1.962(2)	Fe2-C14	2.043(3)
Mn4-O28	1.987(2)	Fe2-C18	2.045(3)
Mn4-O17	2.149(2)	Fe2-C22	2.046(4)
Mn4-O2	2.267(2)	Fe2-C15	2.052(4)
Mn5-O3	2.0741(19)	Fe2-C24	2.056(4)
Mn5-O15	2.086(2)	Fe2-C16	2.059(4)
Mn5-O22	2.111(2)	Fe2-C17	2.060(3)
Mn5-O11	2.128(2)	Fe2-C23	2.077(4)
Mn5-O30	2.176(2)	Fe3-C26	2.028(3)
Mn6-O1	2.075(2)	Fe3-C29	2.028(4)
Mn6-O19	2.085(2)	Fe3-C33	2.030(3)
Mn6-O23	2.109(2)	Fe3-C35	2.034(3)
Mn6-O7	2.119(2)	Fe3-C27	2.034(3)
Mn6-O29	2.175(3)	Fe3-C30	2.035(4)
Mn7-O2	2.065(2)	Fe3-C36	2.039(3)
Mn7-O14	2.079(2)	Fe3-C34	2.042(4)
Mn7-O6	2.111(2)	Fe3-C32	2.042(3)
Mn7-O27	2.123(2)	Fe3-C28	2.045(4)
Mn7-O31	2.217(2)	Fe4-C44	2.036(3)
Mn8-O18	2.079(2)	Fe4-C41	2.045(3)

Fe4-C48	2.045(3)	O2-Mn1-O16	95.11(8)
Fe4-C42	2.046(3)	O5-Mn1-O16	89.77(8)
Fe4-C45	2.047(3)	O24-Mn1-O16	88.94(8)
Fe4-C40	2.048(4)	O3-Mn1-O1	81.98(8)
Fe4-C47	2.051(3)	O2-Mn1-O1	82.74(8)
Fe4-C38	2.051(3)	O5-Mn1-O1	91.42(8)
Fe4-C39	2.053(3)	O24-Mn1-O1	93.06(8)
Fe4-C46	2.058(4)	O16-Mn1-O1	177.64(8)
Fe5-C56	2.032(3)	O3-Mn1-Mn3	40.94(6)
Fe5-C51	2.034(3)	O2-Mn1-Mn3	41.92(6)
Fe5-C57	2.037(3)	O5-Mn1-Mn3	137.90(6)
Fe5-C52	2.042(3)	O24-Mn1-Mn3	130.31(6)
Fe5-C50	2.044(3)	O16-Mn1-Mn3	92.51(6)
Fe5-C54	2.048(3)	O1-Mn1-Mn3	85.24(5)
Fe5-C60	2.055(3)	O3-Mn1-Mn4	84.98(6)
Fe5-C53	2.055(3)	O2-Mn1-Mn4	46.31(6)
Fe5-C58	2.058(3)	O5-Mn1-Mn4	89.18(6)
Fe5-C59	2.060(3)	O24-Mn1-Mn4	130.08(6)
Fe6-C68	2.032(3)	O16-Mn1-Mn4	140.98(6)
Fe6-C72	2.036(4)	O1-Mn1-Mn4	37.03(5)
Fe6-C62	2.037(3)	Mn3-Mn1-Mn4	63.757(17)
Fe6-C69	2.041(3)	O3-Mn1-Mn2	46.29(6)
Fe6-C70	2.048(3)	O2-Mn1-Mn2	83.37(6)
Fe6-C66	2.050(3)	O5-Mn1-Mn2	127.18(6)
Fe6-C63	2.051(3)	O24-Mn1-Mn2	88.73(6)
Fe6-C65	2.054(4)	O16-Mn1-Mn2	143.02(6)
Fe6-C64	2.059(4)	O1-Mn1-Mn2	35.90(5)
Fe6-C71	2.062(4)	Mn3-Mn1-Mn2	62.058(17)
		Mn4-Mn1-Mn2	53.238(14)
O3-Mn1-O2	82.28(9)	O4-Mn2-O1	82.28(8)
O3-Mn1-O5	173.33(9)	O4-Mn2-O9	94.04(9)
O2-Mn1-O5	96.01(8)	O1-Mn2-O9	174.06(9)
O3-Mn1-O24	89.56(9)	O4-Mn2-O21	173.25(8)
O2-Mn1-O24	171.26(8)	O1-Mn2-O21	92.85(8)
O5-Mn1-O24	91.74(9)	O9-Mn2-O21	90.42(8)
O3-Mn1-O16	96.80(8)	O4-Mn2-O20	98.63(8)

O1-Mn2-O20	95.68(8)	O2-Mn3-O13	96.17(8)
O9-Mn2-O20	89.47(8)	O12-Mn3-O13	87.35(8)
O21-Mn2-O20	86.46(8)	O25-Mn3-O13	85.53(9)
O4-Mn2-O3	83.16(8)	O3-Mn3-O4	84.26(8)
O1-Mn2-O3	80.37(8)	O2-Mn3-O4	81.97(8)
O9-Mn2-O3	94.60(8)	O12-Mn3-O4	94.73(8)
O21-Mn2-O3	91.44(8)	O25-Mn3-O4	91.19(8)
O20-Mn2-O3	175.44(8)	O13-Mn3-O4	176.16(8)
O4-Mn2-Mn4	41.49(6)	O3-Mn3-Mn1	41.28(6)
O1-Mn2-Mn4	41.37(6)	O2-Mn3-Mn1	41.69(6)
O9-Mn2-Mn4	135.43(7)	O12-Mn3-Mn1	134.59(7)
O21-Mn2-Mn4	134.12(6)	O25-Mn3-Mn1	134.10(6)
O20-Mn2-Mn4	94.08(6)	O13-Mn3-Mn1	94.59(6)
O3-Mn2-Mn4	84.47(5)	O4-Mn3-Mn1	86.27(5)
O4-Mn2-Mn3	47.27(6)	O3-Mn3-Mn2	48.17(6)
O1-Mn2-Mn3	84.19(7)	O2-Mn3-Mn2	85.45(7)
O9-Mn2-Mn3	89.89(7)	O12-Mn3-Mn2	89.63(7)
O21-Mn2-Mn3	127.80(6)	O25-Mn3-Mn2	127.78(6)
O20-Mn2-Mn3	145.73(6)	O13-Mn3-Mn2	146.63(6)
O3-Mn2-Mn3	36.59(5)	O4-Mn3-Mn2	36.80(5)
Mn4-Mn2-Mn3	63.553(16)	Mn1-Mn3-Mn2	64.860(17)
O4-Mn2-Mn1	83.70(6)	O3-Mn3-Mn4	84.18(6)
O1-Mn2-Mn1	44.98(6)	O2-Mn3-Mn4	45.50(6)
O9-Mn2-Mn1	130.17(6)	O12-Mn3-Mn4	131.36(7)
O21-Mn2-Mn1	89.55(6)	O25-Mn3-Mn4	89.49(6)
O20-Mn2-Mn1	140.22(6)	O13-Mn3-Mn4	141.12(6)
O3-Mn2-Mn1	35.60(5)	O4-Mn3-Mn4	36.64(5)
Mn4-Mn2-Mn1	61.736(15)	Mn1-Mn3-Mn4	62.507(17)
Mn3-Mn2-Mn1	53.082(15)	Mn2-Mn3-Mn4	53.652(15)
O3-Mn3-O2	82.38(8)	O1-Mn4-O4	82.56(8)
O3-Mn3-O12	93.53(9)	O1-Mn4-O8	96.64(9)
O2-Mn3-O12	174.96(10)	O4-Mn4-O8	176.70(9)
O3-Mn3-O25	173.61(9)	O1-Mn4-O28	171.61(9)
O2-Mn3-O25	92.56(9)	O4-Mn4-O28	90.86(9)
O12-Mn3-O25	91.31(9)	O8-Mn4-O28	89.64(9)
O3-Mn3-O13	98.86(8)	O1-Mn4-O17	96.64(8)

O4-Mn4-O17	95.62(8)	O3-Mn5-O30	161.02(9)
O8-Mn4-O17	87.65(8)	O15-Mn5-O30	82.72(8)
O28-Mn4-O17	89.15(8)	O22-Mn5-O30	81.36(8)
O1-Mn4-O2	83.72(8)	O11-Mn5-O30	104.47(9)
O4-Mn4-O2	83.39(8)	O1-Mn6-O19	96.80(8)
O8-Mn4-O2	93.34(8)	O1-Mn6-O23	91.59(8)
O28-Mn4-O2	90.39(8)	O19-Mn6-O23	125.88(8)
O17-Mn4-O2	178.90(8)	O1-Mn6-O7	92.96(8)
O1-Mn4-Mn2	41.86(6)	O19-Mn6-O7	114.64(8)
O4-Mn4-Mn2	41.28(6)	O23-Mn6-O7	118.17(8)
O8-Mn4-Mn2	138.28(7)	O1-Mn6-O29	176.49(9)
O28-Mn4-Mn2	132.07(6)	O19-Mn6-O29	85.33(9)
O17-Mn4-Mn2	92.69(5)	O23-Mn6-O29	84.90(9)
O2-Mn4-Mn2	86.87(5)	O7-Mn6-O29	88.66(9)
O1-Mn4-Mn1	47.14(6)	O2-Mn7-O14	100.99(8)
O4-Mn4-Mn1	86.20(6)	O2-Mn7-O6	89.33(8)
O8-Mn4-Mn1	90.90(6)	O14-Mn7-O6	122.85(9)
O28-Mn4-Mn1	127.50(6)	O2-Mn7-O27	92.81(8)
O17-Mn4-Mn1	143.32(6)	O14-Mn7-O27	125.74(9)
O2-Mn4-Mn1	37.19(5)	O6-Mn7-O27	109.37(8)
Mn2-Mn4-Mn1	65.026(15)	O2-Mn7-O31	169.98(9)
O1-Mn4-Mn3	83.86(6)	O14-Mn7-O31	87.49(9)
O4-Mn4-Mn3	46.78(6)	O6-Mn7-O31	81.53(9)
O8-Mn4-Mn3	130.00(6)	O27-Mn7-O31	86.40(8)
O28-Mn4-Mn3	87.84(6)	O18-Mn8-O4	98.65(8)
O17-Mn4-Mn3	142.18(6)	O18-Mn8-O10	114.77(9)
O2-Mn4-Mn3	36.79(5)	O4-Mn8-O10	91.57(8)
Mn2-Mn4-Mn3	62.795(17)	O18-Mn8-O26	138.46(9)
Mn1-Mn4-Mn3	53.736(15)	O4-Mn8-O26	89.82(8)
O3-Mn5-O15	95.65(8)	O10-Mn8-O26	105.48(9)
O3-Mn5-O22	90.63(8)	O18-Mn8-O32	88.88(9)
O15-Mn5-O22	147.99(9)	O4-Mn8-O32	171.09(9)
O3-Mn5-O11	93.76(8)	O10-Mn8-O32	89.57(9)
O15-Mn5-O11	111.49(9)	O26-Mn8-O32	81.36(9)
O22-Mn5-O11	99.32(8)		

Table C-4. Selected bond lengths [Å] and angles [°] for  
 $[\text{Fe}_7\text{O}_3(\text{OMe})(\text{fdc})_6(\text{MeOH})_3]^{3+}[\text{FeCl}_4]^- \cdot 2\text{Cl}^-$ , **6**.

Fe1-O3	1.959(3)	Fe5-C36	2.052(5)
Fe1-O18	1.973(3)	Fe6-O15	1.949(3)
Fe1-O24	2.004(3)	Fe6-O7	1.953(3)
Fe1-O25	2.008(3)	Fe6-O10	1.973(3)
Fe1-O22	2.028(3)	Fe6-O2	2.011(3)
Fe1-O31	2.051(3)	Fe6-O1	2.042(3)
Fe2-O13	1.966(3)	Fe6-O4	2.101(3)
Fe2-O26	1.990(3)	Fe7-O27	1.980(3)
Fe2-O23	2.009(3)	Fe7-O11	1.980(3)
Fe2-O3	2.032(3)	Fe7-O17	1.982(3)
Fe2-O2	2.073(3)	Fe7-O1	2.063(3)
Fe2-O4	2.079(3)	Fe7-O3	2.075(3)
Fe3-O12	1.962(3)	Fe7-O2	2.079(3)
Fe3-O19	1.985(3)	Fe8-C8	2.021(5)
Fe3-O1	1.994(3)	Fe8-C12	2.023(5)
Fe3-O6	2.011(3)	Fe8-C3	2.035(5)
Fe3-O8	2.020(3)	Fe8-C9	2.037(5)
Fe3-O29	2.061(3)	Fe8-C4	2.040(5)
Fe4-O21	1.953(3)	Fe8-C2	2.041(5)
Fe4-O20	1.964(3)	Fe8-C10	2.055(5)
Fe4-O5	1.988(3)	Fe8-C6	2.059(5)
Fe4-O1	2.024(3)	Fe8-C11	2.062(5)
Fe4-O4	2.077(3)	Fe8-C5	2.062(5)
Fe4-O3	2.095(3)	Fe9-C14	2.020(5)
Fe5-C26	2.014(5)	Fe9-C21	2.023(5)
Fe5-C27	2.023(5)	Fe9-C20	2.027(5)
Fe5-C30	2.025(6)	Fe9-C24	2.033(5)
Fe5-C33	2.031(5)	Fe9-C18	2.034(5)
Fe5-C32	2.037(5)	Fe9-C15	2.039(5)
Fe5-C28	2.041(6)	Fe9-C23	2.044(5)
Fe5-C29	2.045(5)	Fe9-C22	2.045(5)
Fe5-C34	2.047(5)	Fe9-C17	2.048(5)
Fe5-C35	2.048(5)	Fe9-C16	2.056(5)

Fe10-O28	1.972(4)	Fe14-Cl3	2.155(3)
Fe10-O2	1.985(3)	Fe14-Cl2	2.159(3)
Fe10-O9	1.995(3)	Fe14-Cl1	2.173(2)
Fe10-O14	2.009(3)	Fe14-Cl4'	2.210(4)
Fe10-O16	2.042(3)	Fe14-Cl2'	2.228(4)
Fe10-O30	2.076(3)	Fe14-Cl3'	2.231(3)
Fe11-C44	2.022(5)	Fe14-Cl4	2.255(3)
Fe11-C39	2.024(5)		
Fe11-C45	2.028(5)	O3-Fe1-O18	92.92(13)
Fe11-C48	2.037(5)	O3-Fe1-O24	98.26(13)
Fe11-C38	2.040(5)	O18-Fe1-O24	168.80(14)
Fe11-C42	2.043(6)	O3-Fe1-O25	94.97(13)
Fe11-C41	2.058(5)	O18-Fe1-O25	95.19(13)
Fe11-C40	2.060(5)	O24-Fe1-O25	83.30(13)
Fe11-C47	2.068(5)	O3-Fe1-O22	95.15(12)
Fe11-C46	2.072(6)	O18-Fe1-O22	95.55(13)
Fe12-C50	2.033(5)	O24-Fe1-O22	84.08(13)
Fe12-C54	2.039(5)	O25-Fe1-O22	164.84(13)
Fe12-C56	2.040(5)	O3-Fe1-O31	175.52(13)
Fe12-C57	2.042(5)	O18-Fe1-O31	82.60(14)
Fe12-C51	2.047(6)	O24-Fe1-O31	86.22(14)
Fe12-C60	2.055(6)	O25-Fe1-O31	85.68(14)
Fe12-C59	2.057(6)	O22-Fe1-O31	85.12(13)
Fe12-C52	2.058(6)	O13-Fe2-O26	92.20(13)
Fe12-C53	2.065(6)	O13-Fe2-O23	85.99(13)
Fe12-C58	2.068(5)	O26-Fe2-O23	96.45(12)
Fe13-C62	2.019(5)	O13-Fe2-O3	174.55(12)
Fe13-C68	2.028(5)	O26-Fe2-O3	92.36(12)
Fe13-C63	2.030(5)	O23-Fe2-O3	96.45(13)
Fe13-C72	2.044(5)	O13-Fe2-O2	93.42(13)
Fe13-C69	2.045(6)	O26-Fe2-O2	96.51(11)
Fe13-C66	2.046(6)	O23-Fe2-O2	167.04(12)
Fe13-C71	2.055(6)	O3-Fe2-O2	83.11(12)
Fe13-C64	2.057(6)	O13-Fe2-O4	94.27(12)
Fe13-C70	2.059(5)	O26-Fe2-O4	172.49(12)
Fe13-C65	2.063(6)	O23-Fe2-O4	87.80(11)

O3-Fe2-O4	80.99(11)	C27-Fe5-C33	108.0(2)
O2-Fe2-O4	79.32(11)	C30-Fe5-C33	165.8(2)
O12-Fe3-O19	94.56(14)	C26-Fe5-C32	109.6(2)
O12-Fe3-O1	92.61(12)	C27-Fe5-C32	120.8(2)
O19-Fe3-O1	95.30(13)	C30-Fe5-C32	127.5(2)
O12-Fe3-O6	170.22(13)	C33-Fe5-C32	40.88(17)
O19-Fe3-O6	85.60(13)	C26-Fe5-C28	68.5(2)
O1-Fe3-O6	97.11(12)	C27-Fe5-C28	40.4(2)
O12-Fe3-O8	94.64(14)	C30-Fe5-C28	69.1(2)
O19-Fe3-O8	164.33(13)	C33-Fe5-C28	118.6(3)
O1-Fe3-O8	96.93(13)	C32-Fe5-C28	154.1(3)
O6-Fe3-O8	83.19(12)	C26-Fe5-C29	67.9(2)
O12-Fe3-O29	84.53(13)	C27-Fe5-C29	67.8(2)
O19-Fe3-O29	83.22(14)	C30-Fe5-C29	40.9(2)
O1-Fe3-O29	176.66(13)	C33-Fe5-C29	152.3(3)
O6-Fe3-O29	85.78(13)	C32-Fe5-C29	165.0(3)
O8-Fe3-O29	85.06(13)	C28-Fe5-C29	40.3(2)
O21-Fe4-O20	90.77(14)	C26-Fe5-C34	164.5(2)
O21-Fe4-O5	88.63(13)	C27-Fe5-C34	125.5(2)
O20-Fe4-O5	98.44(13)	C30-Fe5-C34	152.6(2)
O21-Fe4-O1	173.31(12)	C33-Fe5-C34	40.32(18)
O20-Fe4-O1	93.84(13)	C32-Fe5-C34	68.3(2)
O5-Fe4-O1	95.47(12)	C28-Fe5-C34	106.2(2)
O21-Fe4-O4	93.64(13)	C29-Fe5-C34	118.2(2)
O20-Fe4-O4	174.86(12)	C26-Fe5-C35	154.7(2)
O5-Fe4-O4	84.32(12)	C27-Fe5-C35	162.3(2)
O1-Fe4-O4	81.55(12)	C30-Fe5-C35	119.2(2)
O21-Fe4-O3	91.51(12)	C33-Fe5-C35	67.7(2)
O20-Fe4-O3	97.69(12)	C32-Fe5-C35	68.0(2)
O5-Fe4-O3	163.86(13)	C28-Fe5-C35	125.1(3)
O1-Fe4-O3	83.08(11)	C29-Fe5-C35	107.5(2)
O4-Fe4-O3	79.56(11)	C34-Fe5-C35	40.18(19)
C26-Fe5-C27	41.23(19)	C26-Fe5-C36	121.3(2)
C26-Fe5-C30	40.86(18)	C27-Fe5-C36	156.0(2)
C27-Fe5-C30	69.3(2)	C30-Fe5-C36	108.2(2)
C26-Fe5-C33	128.1(2)	C33-Fe5-C36	68.1(2)

C32-Fe5-C36	40.61(17)	O2-Fe6-O4	80.23(11)
C28-Fe5-C36	162.9(3)	O1-Fe6-O4	80.53(12)
C29-Fe5-C36	126.9(3)	O27-Fe7-O11	88.87(12)
C34-Fe5-C36	67.9(2)	O27-Fe7-O17	90.41(14)
C35-Fe5-C36	40.27(18)	O11-Fe7-O17	89.07(13)
O15-Fe6-O7	86.30(13)	O27-Fe7-O1	170.76(14)
O15-Fe6-O10	97.89(13)	O11-Fe7-O1	88.93(12)
O7-Fe6-O10	89.62(12)	O17-Fe7-O1	98.54(12)
O15-Fe6-O2	96.59(12)	O27-Fe7-O3	99.89(12)
O7-Fe6-O2	176.06(14)	O11-Fe7-O3	171.10(12)
O10-Fe6-O2	92.63(12)	O17-Fe7-O3	89.30(13)
O15-Fe6-O1	165.44(13)	O1-Fe7-O3	82.65(11)
O7-Fe6-O1	92.29(12)	O27-Fe7-O2	89.49(13)
O10-Fe6-O1	96.58(13)	O11-Fe7-O2	99.86(13)
O2-Fe6-O1	84.25(12)	O17-Fe7-O2	171.06(13)
O15-Fe6-O4	85.28(12)	O1-Fe7-O2	82.04(11)
O7-Fe6-O4	97.39(12)	O3-Fe7-O2	81.92(11)
O10-Fe6-O4	172.50(12)		

APPENDIX D  
BVS OPTIMIZATION DATA

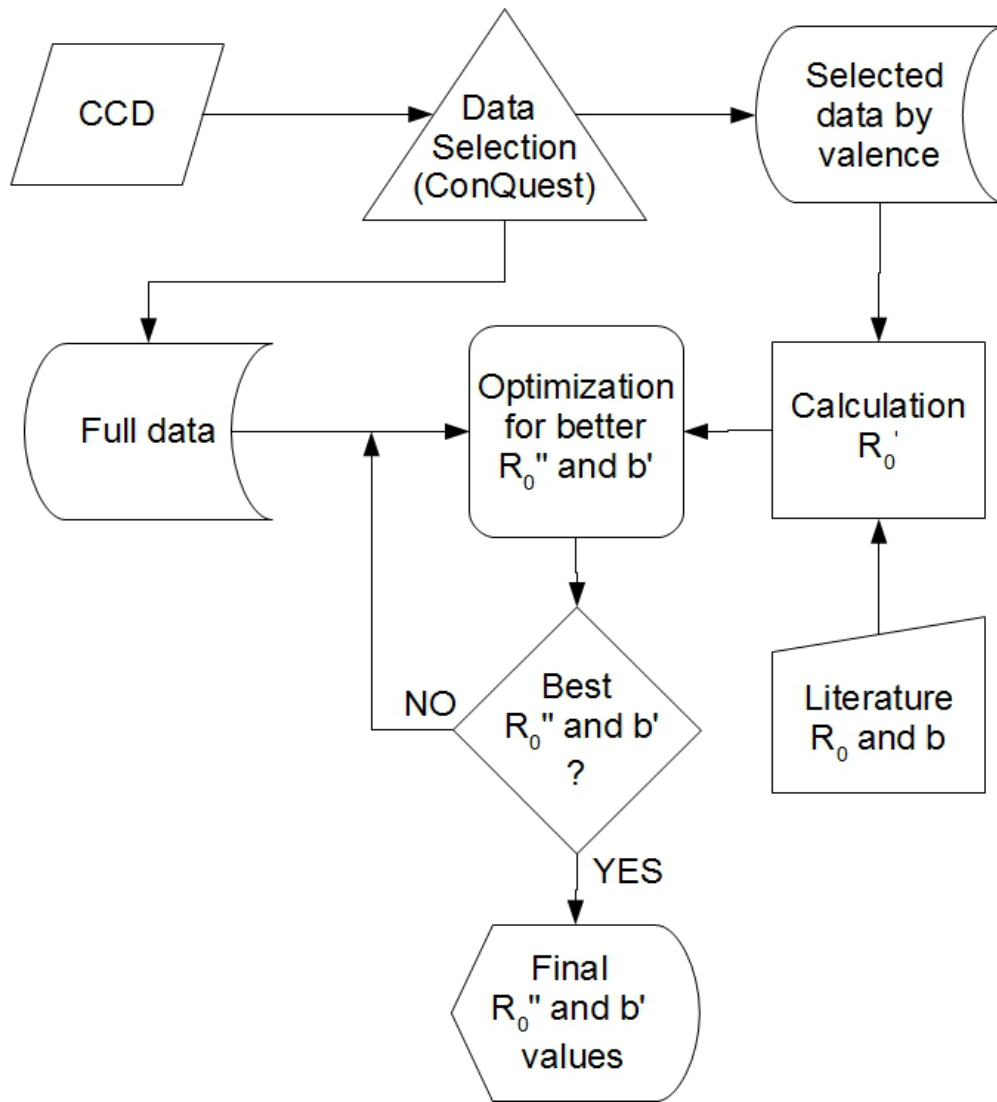


Figure D-1. Exemplified flow chart of *chopt* algorithm.

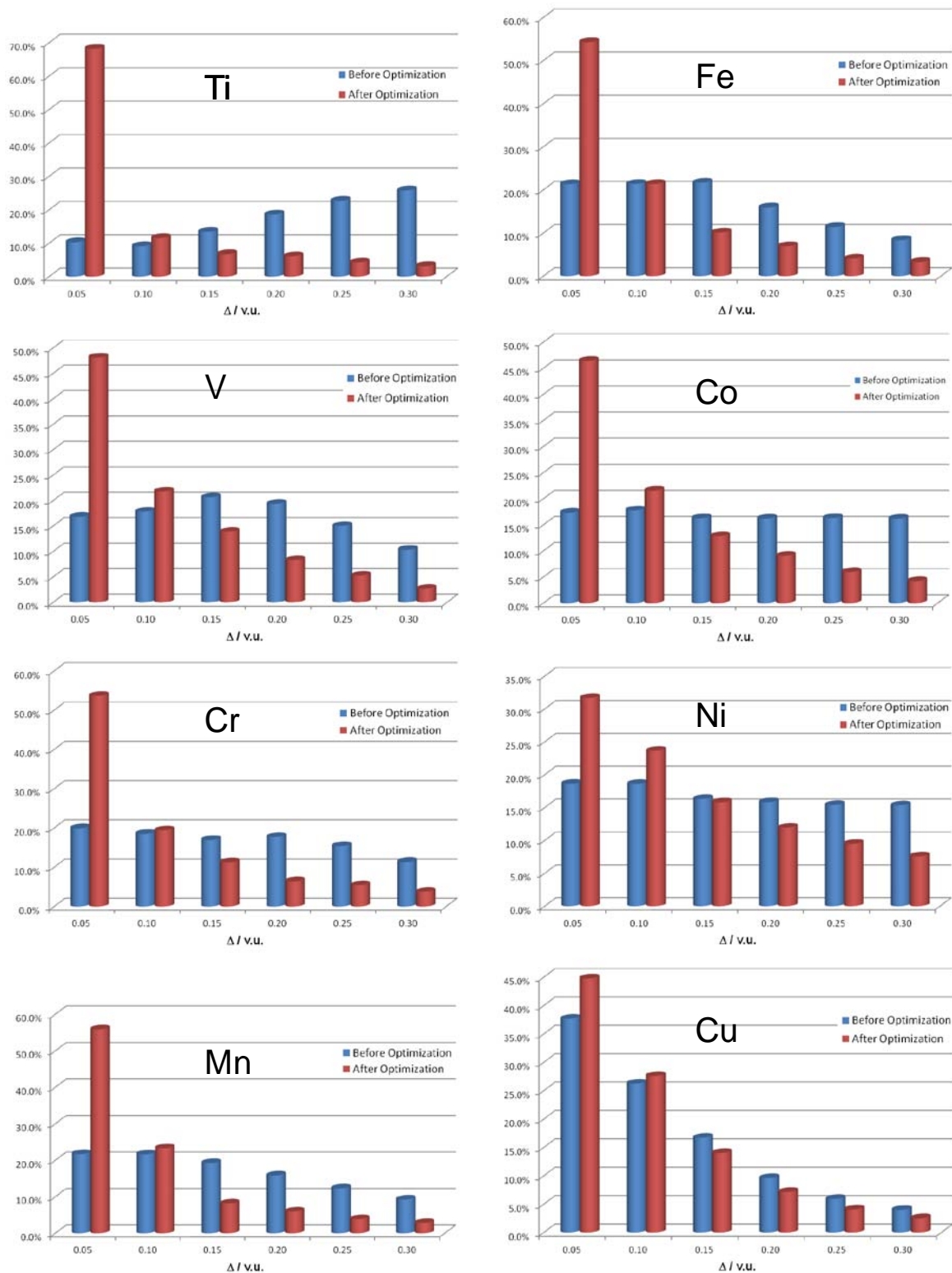


Figure D-2. Histograms for the valence errors ( $\Delta$ ) before and after VNS optimization. Each metal is analyzed independently (blue = before optimization, red = after optimization).

Table D-1.  $R_{0\text{opt}}$  values (Å) obtained for titanium with  $b_{\text{opt}} = 0.447$ .

Donor/Valence	2	3	4
O	1.597	1.841	1.771
N	1.908		1.193
P	1.583	2.318	2.348
S	1.713	1.985	2.180
F	1.245		1.673
Cl	2.002	1.963	2.148
Br	2.194	2.172	2.305
I	2.731		2.686

Table D-2.  $R_{0\text{opt}}$  values (Å) obtained for vanadium with  $b_{\text{opt}} = 0.414$ .

Donor/Valence	2	3	4	5
O	1.615	1.718	1.764	1.800
N	1.630	1.733		1.033
P		1.836		2.161
S	1.434	1.821	1.621	2.076
F		1.612	1.687	1.748
Cl	2.072	1.917	1.762	1.944
Br	2.231	2.301	2.043	
I		2.123		

Table D-3.  $R_{0\text{opt}}$  values (Å) obtained for chromium with  $b_{\text{opt}} = 0.426$ .

Donor/Valence	1	2	3	4	5	6
O	1.207	1.589	1.676	1.683	1.733	1.819
N	1.276	1.657	1.431	1.771	1.830	1.837
P	1.849	2.219	2.166	2.204	2.212	
S	1.646	2.114	2.013	2.142	2.194	2.264
F	1.148	1.217	1.590	1.702		1.818
Cl	1.589	1.573	2.026	1.934	2.009	2.074
Br	1.564	2.255				
I	2.040				2.728	1.193

Table D-4.  $R_{0\text{opt}}$  values (Å) obtained for manganese with  $b_{\text{opt}} = 0.617$ .

Donor/Valence	1	2	3	4	5	6
O	1.198	1.493	1.570	1.648	1.708	
N	1.268	1.571	1.650	1.713	1.791	1.899
P	1.659	1.956		1.522		
S	1.639	1.941	2.066	2.067		
F	1.118	1.460	1.508			
Cl	1.561	1.876	1.975	2.020		
Br	1.728	2.079	2.121			
I	2.016	2.317	2.453			

Table D-5.  $R_{0\text{opt}}$  values (Å) obtained for iron with  $b_{\text{opt}} = 0.630$ .

Donor/Valence	2	3	4	5
O	1.429	1.571	1.638	1.796
N	1.496	1.659	1.657	1.847
P	1.941	2.151	2.296	2.296
S	1.962	1.828	1.930	2.004
F	1.223	1.399		
Cl	1.870	2.001		2.144
Br	1.990	2.152	2.219	2.408
I	2.288	2.480	2.588	2.738

Table D-6.  $R_{0\text{opt}}$  values (Å) obtained for cobalt with  $b_{\text{opt}} = 0.449$ .

Donor/Valence	1	2	3	4
O	1.390	1.599	1.512	
N	1.590	1.664	1.722	1.670
P	1.589	1.593	1.777	
S	1.129	1.485	1.380	
F	1.382	1.572	1.680	
Cl	1.236		1.375	
Br	1.759	2.020	1.712	
I	1.798	1.762	1.628	

Table D-7.  $R_{0\text{opt}}$  values (Å) obtained for cobalt with  $b_{\text{opt}} = 0.376$ .

Donor/Valence	1	2	3	4
O	1.546	1.642	2.059	1.986
N	1.361	1.698	1.532	1.747
P	1.658	1.718	1.712	1.973
S	1.674	2.011	2.097	2.154
F	1.505	1.587		1.637
Cl	1.842	2.008	1.908	2.050
Br	1.959	2.166	2.141	2.306
I	2.183	2.367	2.472	

Table D-8.  $R_{0\text{opt}}$  values (Å) obtained for copper with  $b_{\text{opt}} = 0.433$ .

Donor/Valence	1	2	3
O	1.421	1.603	1.653
N	1.454	1.657	1.678
P	1.685	2.098	
S	1.726	1.921	2.047
F	1.311	1.529	
Cl	1.755	1.955	2.050
Br	1.891	2.089	2.173
I	2.071	2.238	2.379

## LIST OF REFERENCES

- (1) Huheey, J. E. *Inorganic Chemistry. 3rd Ed*; 3rd ed.; Harper and Row: New York, 1983.
- (2) Mingos, D. M. P.; Wales, D. J. *Introduction to cluster chemistry* Prentice Hall: Englewood Cliffs, N.J., 1990.
- (3) Crabtree, R. H. *The Organometallic Chemistry of the Transition Metals*; 5th ed.; John Wiley and Sons, Inc., 2009.
- (4) Mukerjee, S.; Skogerson, K.; DeGala, S.; Caradonna, J. P. *Inorg. Chim. Acta FIELD Full Journal Title:Inorganica Chimica Acta* **2000**, 297, 313.
- (5) Dyson, P. J.; Mcindoe, J. S.; Mcindoe, J. S. *Transition Metal Carbonyl Cluster Chemistry*; Gordon and Breach Science Publishers, 2000.
- (6) Christou, G. *Characterization of Paramagnetic Molecules* Gainesville, 2005.
- (7) Cotton, F. A.; Wilkinson, G. *Advanced Inorganic Chemistry*; 5th ed.; John Wiley & Sons, 1988.
- (8) CCDC, *Cambridge Crystallographic Data Centre*. 2010, <http://www.ccdc.cam.ac.uk/>.
- (9) Ivarsson, G. J. M. *Acta Chemica Scandinavica, Series A: Physical and Inorganic Chemistry* **1979**, A33, 323.
- (10) Charlot, M. F.; Jeannin, S.; Jeannin, Y.; Kahn, O.; Lucrece-Abaul, J.; Martin-Frere, J. *Inorganic Chemistry* **1979**, 18, 1675.
- (11) Chaudhuri, P.; Guttman, M.; Ventur, D.; Wieghardt, K.; Nuber, B.; Weiss, J. *Journal of the Chemical Society, Chemical Communications* **1985**, 1618.
- (12) Zang, Y.; Pan, G.; Que, L., Jr.; Fox, B. G.; Munck, E. *Journal of the American Chemical Society* **1994**, 116, 3653.
- (13) Zheng, H.; Zang, Y.; Dong, Y.; Young, V. G., Jr.; Que, L., Jr. *Journal of the American Chemical Society* **1999**, 121, 2226.
- (14) Honda, Y.; Arii, H.; Okumura, T.; Wada, A.; Funahashi, Y.; Ozawa, T.; Jitsukawa, K.; Masuda, H. *Bulletin of the Chemical Society of Japan* **2007**, 80, 1288.
- (15) Michelsen, K.; Pedersen, E.; Wilson, S. R.; Hodgson, D. J. *Inorganica Chimica Acta* **1982**, 63, 141.

- (16) Dimitrou, E., Indiana University. Avail. Univ. Microfilms Int., DA9539950., 222 pp. From: Diss. Abstr. Int., B **1995**, 56, 3753.
- (17) Cotton, F. A.; Wang, W. *Inorganic Chemistry* **1982**, 21, 2675.
- (18) Beattie, J. K.; Hambley, T. W.; Klepetko, J. A.; Masters, A. F.; Turner, P. *Polyhedron* **1996**, 15, 2141.
- (19) Lippard, S. J.; Berg, J. M. *Principles of Bioinorganic Chemistry* University Science Books, 1994.
- (20) Zouni, A.; Witt, H.-T.; Kern, J.; Fromme, P.; Krauss, N.; Saenger, W.; Orth, P. *Nature (London)* **2001**, 409, 739.
- (21) Kamiya, N.; Shen, J.-R. *Proceedings of the National Academy of Sciences of the United States of America* **2003**, 100, 98.
- (22) Ferreira, K. N.; Iverson, T. M.; Maghlaoui, K.; Barber, J.; Iwata, S. *Science (Washington, DC, United States)* **2004**, 303, 1831.
- (23) Barber, J.; Ferreira, K.; Maghlaoui, K.; Iwata, S. *Physical Chemistry Chemical Physics* **2004**, 6, 4737.
- (24) Hendry, G.; Wydrzynski, T. *Biochemistry* **2003**, 42, 6209.
- (25) Siegbahn, P. E. M. *Current Opinion in Chemical Biology* **2002**, 6, 227.
- (26) Weng, T.-C.; Hsieh, W.-Y.; Uffelman, E. S.; Gordon-Wylie, S. W.; Collins, T. J.; Pecoraro, V. L.; Penner-Hahn, J. E. *Journal of the American Chemical Society* **2004**, 126, 8070.
- (27) Guha, B. C. *Proceedings of the Royal Society of London, Series A: Mathematical, Physical and Engineering Sciences* **1951**, 206, 353.
- (28) Bleaney, B.; Bowers, K. D. *Proceedings of the Royal Society of London, Series A: Mathematical, Physical and Engineering Sciences* **1952**, 214, 451.
- (29) Carlin, R. L. *Magnetochemistry*; Springer, 1986.
- (30) Koegerler, P.; Tsukerblat, B.; Mueller, A. *Dalton Transactions* **2010**, 39, 21.
- (31) Kolks, G.; Lippard, S. J.; Waszczak, J. V.; Lilienthal, H. R. *Journal of the American Chemical Society* **1982**, 104, 717.
- (32) Kambe, K. *Journal of the Physical Society of Japan* **1950**, 5, 48.

- (33) Wilson, A.; Yang, E.-C.; Hendrickson, D. N.; Hill, S. *Polyhedron* **2007**, *26*, 2065.
- (34) Christou, G.; Gatteschi, D.; Hendrickson, D. N.; Sessoli, R. *MRS Bulletin* **2000**, *25*, 66.
- (35) Aubin, S. M. J.; Wemple, M. W.; Adams, D. M.; Tsai, H.-L.; Christou, G.; Hendrickson, D. N. *Journal of the American Chemical Society* **1996**, *118*, 7746.
- (36) Lis, T. *Acta Crystallographica, Section B: Structural Crystallography and Crystal Chemistry* **1980**, *B36*, 2042.
- (37) Caneschi, A.; Gatteschi, D.; Sessoli, R.; Barra, A. L.; Brunel, L. C.; Guillot, M. *Journal of the American Chemical Society* **1991**, *113*, 5873.
- (38) van Wuelen, C. *Journal of Chemical Physics* **2009**, *130*, 194109/1.
- (39) Jaglicic, Z.; Luznik, J.; Pirnat, J.; Trontelj, Z. *Physica B: Condensed Matter (Amsterdam)* **2000**, *284-288*, 1219.
- (40) Evangelisti, M.; Bartolome, J.; Luis, F. *Solid State Communications* **1999**, *112*, 687.
- (41) Barra, A. L.; Debrunner, P.; Gatteschi, D.; Schulz, C. E.; Sessoli, R. *Europhysics Letters* **1996**, *35*, 133.
- (42) Wieghardt, K.; Pohl, K.; Jibril, I.; Huttner, G. *Angewandte Chemie* **1984**, *96*, 66.
- (43) Wang, S.; Tsai, H.-L.; Libby, E.; Folting, K.; Streib, W. E.; Hendrickson, D. N.; Christou, G. *Inorganic Chemistry* **1996**, *35*, 7578.
- (44) Aubin, S. M. J.; Dilley, N. R.; Pardi, L.; Krzystek, J.; Wemple, M. W.; Brunel, L.-C.; Maple, M. B.; Christou, G.; Hendrickson, D. N. *Journal of the American Chemical Society* **1998**, *120*, 4991.
- (45) Yang, E.-C.; Wernsdorfer, W.; Hill, S.; Edwards, R. S.; Nakano, M.; Maccagnano, S.; Zakharov, L. N.; Rheingold, A. L.; Christou, G.; Hendrickson, D. N. *Polyhedron* **2003**, *22*, 1727.
- (46) Gatteschi, D.; Sessoli, R. *Angewandte Chemie (International ed. in English)* **2003**, *42*, 268.
- (47) Ritter, S. K. *Chemical & Engineering News* **2004**, *82*, 29.
- (48) Bogani, L.; Wernsdorfer, W. *Nature Materials* **2008**, *7*, 179.

- (49) Robin, M. B.; Day, P. *Advances in Inorganic Chemistry and Radiochemistry* **1967**, *10*, 247.
- (50) Kealy, T. J.; Pauson, P. L. *Nature (London, United Kingdom)* **1951**, *168*, 1039.
- (51) Wilkinson, G.; Rosenblum, M.; Whiting, M. C.; Woodward, R. B. *Journal of the American Chemical Society* **1952**, *74*, 2125.
- (52) Woodward, R. B.; Rosenblum, M.; Whiting, M. C. *Journal of the American Chemical Society* **1952**, *74*, 3458.
- (53) Jaffe, H. H. *Journal of Chemical Physics* **1953**, *21*, 156.
- (54) Zanello, P. *Inorganic Electrochemistry: Theory, Practice and Application*, 2003.
- (55) Sharp, M.; Petersson, M.; Edstroem, K. *Journal of Electroanalytical Chemistry and Interfacial Electrochemistry* **1980**, *109*, 271.
- (56) Ito, N.; Saji, T.; Aoyagui, S. *Journal of Organometallic Chemistry* **1983**, *247*, 301.
- (57) Gil, M. A.; Maringgele, W.; Dechert, S.; Meyer, F. *Zeitschrift fuer Anorganische und Allgemeine Chemie* **2007**, *633*, 2178.
- (58) Deeth, R. J. *Inorganic Chemistry (Washington, DC, United States)* **2008**, *47*, 6711.
- (59) Rosenblum, M.; Woodward, R. B. *Journal of the American Chemical Society* **1958**, *80*, 5443.
- (60) Laane, J. *Journal of Coordination Chemistry* **1971**, *1*, 75.
- (61) Petter, R. C.; Rao, S. J. *Journal of Organic Chemistry* **1991**, *56*, 2932.
- (62) Pardo, E.; Faus, J.; Julve, M.; Lloret, F.; Munoz, M. C.; Cano, J.; Ottenwaelder, X.; Journaux, Y.; Carrasco, R.; Blay, G.; Fernandez, I.; Ruiz-Garcia, R. *Journal of the American Chemical Society* **2003**, *125*, 10770.
- (63) Catlow, C. R. A.; Editor *Computer Modeling in Inorganic Crystallography*; Academic: San Diego, 1997.
- (64) Pauling, L. *Journal of the American Chemical Society* **1929**, *51*, 1010.
- (65) Bragg, W. L. *Zeitschrift fuer Kristallographie, Kristallgeometrie, Kristallphysik, Kristallchemie* **1930**, *74*, 237.
- (66) Pauling, L. *Journal of the American Chemical Society* **1947**, *69*, 542.

- (67) Donnay, G. *Year Book - Carnegie Institution of Washington* **1970**, 292.
- (68) Donnay, G.; Allmann, R. *American Mineralogist* **1970**, 55, 1003.
- (69) Brown, I. D.; Shannon, R. D. *Acta Crystallographica, Section A: Crystal Physics, Diffraction, Theoretical and General Crystallography* **1973**, 29, 266.
- (70) Brown, I. D.; Wu, K. K. *Acta Crystallographica, Section B: Structural Crystallography and Crystal Chemistry* **1976**, B32, 1957.
- (71) Brown, I. D.; Altermatt, D. *Acta Crystallographica, Section B: Structural Science* **1985**, B41, 244.
- (72) Garcia-Rodriguez, L.; Rute-Perez, A.; Pinero, J. R.; Gonzalez-Silgo, C. *Acta Crystallographica, Section B: Structural Science* **2000**, B56, 565.
- (73) Brown, I. D. *Acta Crystallographica, Section B: Structural Science* **1992**, B48, 553.
- (74) Ardavan, A.; Blundell, S. J. *Journal of Materials Chemistry* **2009**, 19, 1754.
- (75) Price, D. J.; Batten, S. R.; Moubaraki, B.; Murray, K. S. *Polyhedron* **2007**, 26, 305.
- (76) Tasiopoulos, A. J.; Vinslava, A.; Werndorfer, W.; Abboud, K. A.; Christou, G. *Angewandte Chemie, International Edition* **2004**, 43, 2117.
- (77) Aliaga-Alcalde, N.; Edwards, R. S.; Hill, S. O.; Wernsdorfer, W.; Folting, K.; Christou, G. *Journal of the American Chemical Society* **2004**, 126, 12503.
- (78) Schmid, G. *Structure and Bonding (Berlin, Germany)* **1985**, 62, 51.
- (79) Papaefstathiou, G. S.; Perlepes, S. P. *Comments on Inorganic Chemistry* **2002**, 23, 249.
- (80) Boyd, P. D. W.; Li, Q.; Vincent, J. B.; Folting, K.; Chang, H. R.; Streib, W. E.; Huffman, J. C.; Christou, G.; Hendrickson, D. N. *Journal of the American Chemical Society* **1988**, 110, 8537.
- (81) Sessoli, R.; Tsai, H. L.; Schake, A. R.; Wang, S.; Vincent, J. B.; Folting, K.; Gatteschi, D.; Christou, G.; Hendrickson, D. N. *Journal of the American Chemical Society* **1993**, 115, 1804.
- (82) Weast, R. C. *Handbook of Chemistry and Physics*; 52nd ed., 1972.

- (83) Weast, R. C. *Handbook of Chemistry and Physics*; 64th ed., 1983.
- (84) Soler, M.; Artus, P.; Folting, K.; Huffman, J. C.; Hendrickson, D. N.; Christou, G. *Inorganic Chemistry* **2001**, *40*, 4902.
- (85) Artus, P.; Boskovic, C.; Yoo, J.; Streib, W. E.; Brunel, L.-C.; Hendrickson, D. N.; Christou, G. *Inorganic Chemistry* **2001**, *40*, 4199.
- (86) Gerbier, P.; Ruiz-Molina, D.; Domingo, N.; Amabilino, D. B.; Vidal-Gancedo, J.; Tejada, J.; Hendrickson, D. N.; Veciana, J. *Monatshefte fuer Chemie* **2003**, *134*, 265.
- (87) Little, W. F.; Eisenthal, R. *Journal of Organic Chemistry* **1961**, *26*, 3609.
- (88) Meng, X.; Hou, H.; Li, G.; Ye, B.; Ge, T.; Fan, Y.; Zhu, Y.; Sakiyama, H. *Journal of Organometallic Chemistry* **2004**, *689*, 1218.
- (89) Mata, J. A.; Peris, E.; Llusar, R.; Uriel, S.; Cifuentes, M. P.; Humphrey, M. G.; Samoc, M.; Luther-Davies, B. *European Journal of Inorganic Chemistry* **2001**, 2113.
- (90) Loeffler, U.; Goepel, W.; Speiser, B. *Electroanalysis* **1991**, *3*, 917.
- (91) Zhang, X.; Wang, J.; Gao, Y.; Zeng, X. C. *ACS Nano* **2009**, *3*, 537.
- (92) Engtrakul, C.; Sita, L. R. *Nano Letters* **2001**, *1*, 541.
- (93) Rausch, M. D.; Fischer, E. O.; Grubert, H. *Journal of the American Chemical Society* **1960**, *82*, 76.
- (94) Vigato, P. A.; Casellato, U.; Clemente, D. A.; Bandoli, G.; Vidali, M. *Journal of Inorganic and Nuclear Chemistry* **1973**, *35*, 4131.
- (95) Lee, S.-M.; Cheung, K.-K.; Wong, W.-T. *Journal of Organometallic Chemistry* **1996**, *506*, 77.
- (96) Cotton, F. A.; Daniels, L. M.; Lin, C.; Murillo, C. A. *Journal of the American Chemical Society* **1999**, *121*, 4538.
- (97) Cotton, F. A.; Lin, C.; Murillo, C. A. *Inorganic Chemistry* **2001**, *40*, 478.
- (98) Uhl, W.; Spies, T.; Haase, D.; Winter, R.; Kaim, W. *Organometallics* **2000**, *19*, 1128.
- (99) Dong, G.; Li, Y.-t.; Duan, C.-y.; Hong, M.; Meng, Q.-j. *Inorganic Chemistry* **2003**, *42*, 2519.

- (100) Meng, X.; Cheng, W.; Mi, L.; Tang, M.; Hou, H. *Inorganic Chemistry Communications* **2006**, *9*, 662.
- (101) Kondo, M.; Shinagawa, R.; Miyazawa, M.; Kabir, M. K.; Irie, Y.; Horiba, T.; Naito, T.; Maeda, K.; Utsuno, S.; Uchida, F. *Dalton Transactions* **2003**, 515.
- (102) Masello, A.; Murugesu, M.; Abboud, K. A.; Christou, G. *Polyhedron* **2007**, *26*, 2276.
- (103) Das, N.; Arif, A. M.; Stang, P. J.; Sieger, M.; Sarkar, B.; Kaim, W.; Fiedler, J. *Inorganic Chemistry* **2005**, *44*, 5798.
- (104) Guo, D.; Zhang, B.-g.; Duan, C.-y.; Cao, X.; Meng, Q.-j. *Dalton Transactions* **2003**, 282.
- (105) Zheng, G.-L.; Ma, J.-F.; Su, Z.-M.; Yan, L.-K.; Yang, J.; Li, Y.-Y.; Liu, J.-F. *Angewandte Chemie, International Edition* **2004**, *43*, 2409.
- (106) Chandrasekhar, V.; Thirumoorthi, R. *Organometallics* **2007**, *26*, 5415.
- (107) Kim, Y. S.; Kim, J.; Kim, D.; Chae, H. K. *Chemistry Letters* **2007**, *36*, 150.
- (108) Meng, X.; Li, G.; Hou, H.; Han, H.; Fan, Y.; Zhu, Y.; Du, C. *Journal of Organometallic Chemistry* **2003**, 679, 153.
- (109) Mereacre, V.; Prodius, D.; Ako, A. M.; Shova, S.; Turta, C.; Wurst, K.; Jaitner, P.; Powell, A. K. *Polyhedron* **2009**, *28*, 3551.
- (110) Mereacre, V.; Ako, A. M.; Filoti, G.; Bartolome, J.; Anson, C. E.; Powell, A. K. *Polyhedron* **2010**, *29*, 244.
- (111) Wang, L.; Meng, X.; Zhang, E.; Hou, H.; Fan, Y. *Journal of Organometallic Chemistry* **2007**, 692, 4367.
- (112) Bera, J. K.; Clerac, R.; Fanwick, P. E.; Walton, R. A. *Journal of the Chemical Society, Dalton Transactions* **2002**, 2168.
- (113) Maksakov, V. A.; Slovohtova, I. V.; Golovin, A. V.; Babailov, S. P. *Russian Chemical Bulletin (Translation of Izvestiya Akademii Nauk, Seriya Khimicheskaya)* **2001**, *50*, 2451.
- (114) Cowley, A. R.; Hector, A. L.; Hill, A. F.; White, A. J. P.; Williams, D. J.; Wilton-Ely, J. D. E. T. *Organometallics* **2007**, *26*, 6114.

- (115) Kuehnert, J.; Rueffer, T.; Ecorchard, P.; Braeuer, B.; Lan, Y.; Powell, A. K.; Lang, H. *Dalton Transactions* **2009**, 4499.
- (116) Lu, E.-N.; Zhang, J.; Zhu, L.-M.; Xu, Y.; Fan, Y.-T. *Wuji Huaxue Xuebao* **2008**, *24*, 201.
- (117) Wen, L.-L.; Zhang, B.-G.; Peng, Z.-H.; Ren, J.-G.; Cai, P.; Duan, C.-Y. *Wuji Huaxue Xuebao* **2004**, *20*, 1228.
- (118) Yang, Y.-Y.; Wong, W.-T. *Chemical Communications (Cambridge, United Kingdom)* **2002**, 2716.
- (119) Rosenblum, M. *Chemistry of the Iron Group Metallocenes: Ferrocene, Ruthenocene, Osmocene, Part 1 (The Chemistry of Organometallic Compounds)*, 1965.
- (120) Bernstein, T.; Herbstein, F. H. *Acta Crystallographica, Section B: Structural Crystallography and Crystal Chemistry* **1968**, *24*, 1640.
- (121) Nesmeyanov, A. N.; Sazonova, V. A.; Romanenko, V. I. *Doklady Akademii Nauk SSSR* **1963**, *152*, 1358.
- (122) Sorensen, H. S.; Larsen, J.; Rasmussen, B. S.; Laursen, B.; Hansen, S. G.; Skrydstrup, T.; Amatore, C.; Jutand, A. *Organometallics* **2002**, *21*, 5243.
- (123) Yamaji, T.; Saito, T.; Hayamizu, K.; M.Yanagisawa; O.Yamamoto; N.Wasada; K.Someno; S.Kinugasa; K.Tanabe; T.Tamura; K.Tanabe; J.Hiraishi; April, 17 2010 ed. 2010.
- (124) Kubota, N.; Fukuo, T.; Akawa, R. *Journal of the American Society for Mass Spectrometry* **1999**, *10*, 557.
- (125) Nomura, T. *Bulletin of the Chemical Society of Japan* **1983**, *56*, 2937.
- (126) Eppley, H. J.; Tsai, H.-L.; Aubin, S. M.; deVries, N.; Folting, K.; Hendrickson, D. N.; Christou, G. *Book of Abstracts, 210th ACS National Meeting, Chicago, IL, August 20-24* **1995**, INOR.
- (127) Eppley, H. J.; Tsai, H.-L.; de Vries, N.; Folting, K.; Christou, G.; Hendrickson, D. N. *Journal of the American Chemical Society* **1995**, *117*, 301.
- (128) Eppley, H. J.; Christou, G.; Law, N. A.; Pecoraro, V. L. *Inorganic Syntheses* **2002**, *33*, 61.
- (129) Palenik, G. J. *Inorganic Chemistry* **1997**, *36*, 4888.
- (130) Palenik, G. J. *Inorganic Chemistry* **1997**, *36*, 122.

- (131) Brese, N. E.; O'Keeffe, M. *Acta Crystallographica, Section B: Structural Science* **1991**, *B47*, 192.
- (132) Cowan, D. O.; Shu, P.; Hedberg, F. L.; Rossi, M.; Kistenmacher, T. J. *Journal of the American Chemical Society* **1979**, *101*, 1138.
- (133) Bats, J. W.; Scheibitz, M.; Wagner, M. *Acta Crystallographica, Section C: Crystal Structure Communications* **2003**, *C59*, m355.
- (134) McNaught, A. D.; Wilkinson, A. *IUPAC: Compendium of Chemical Terminology*, 2nd. ed. ed., 1997.
- (135) Sun, Z.; Gantzel, P. K.; Hendrickson, D. N. *Inorganic Chemistry* **1996**, *35*, 6640.
- (136) CCDC 2009, *Mercury*, <http://www.ccdc.cam.ac.uk/products/mercury/>
- (137) Berry, R. S. *Journal of Chemical Physics* **1960**, *32*, 933.
- (138) Muetterties, E. L.; Guggenberger, L. J. *J. Amer. Chem. Soc.* **1974**, *96*, 1748.
- (139) Addison, A. W.; Rao, T. N.; Reedijk, J.; Van Rijn, J.; Verschoor, G. C. *Journal of the Chemical Society, Dalton Transactions* **1984**, 1349.
- (140) Davidson, E. R. Bloomington, IN, 1999, *Magnet*.
- (141) Davidson, E. R. Bloomington, IN, 1999, *Grid*.
- (142) Wernsdorfer, W. *Advances in Chemical Physics* **2001**, *118*, 99.
- (143) Crawford, V. H.; Richardson, H. W.; Wasson, J. R.; Hodgson, D. J.; Hatfield, W. E. *Inorganic Chemistry* **1976**, *15*, 2107.
- (144) Atanasov, M. A.; Angelov, S.; Mayer, I. *Solid State Communications* **1985**, *56*, 743.
- (145) Kolks, G.; Lippard, S. J.; Waszczak, J. V.; Lilienthal, H. R. *Journal of the American Chemical Society* **1982**, *104*, 717.
- (146) Connelly, N. G.; Geiger, W. E. *Chemical Reviews (Washington, D. C.)* **1996**, *96*, 877.
- (147) Steckhan, E. *Angewandte Chemie* **1986**, *98*, 681.
- (148) Steckhan, E.; Editor *Topics in Current Chemistry, Vol. 142: Electrochemistry I*, 1987.

- (149) Yueh, W.; Bauld, N. L. *Journal of the American Chemical Society* **1995**, *117*, 5671.
- (150) Kuroda-Sowa, T.; Nakano, M.; Christou, G.; Hendrickson, D. N. *Polyhedron* **2001**, *20*, 1529.
- (151) Dimitrou, K.; Sun, J.-S.; Foltz, K.; Christou, G. *Inorganic Chemistry* **1995**, *34*, 4160.
- (152) Raptis, R. G.; Georgakaki, I. P.; Hockless, D. C. R. *Angewandte Chemie, International Edition* **1999**, *38*, 1632.
- (153) Bruker-AXS Madison, 2000. *Shelxtl6*.
- (154) Van der Sluis, P.; Spek, A. L. *Acta Crystallographica, Section A: Foundations of Crystallography* **1990**, *A46*, 194.
- (155) Spek, A. L. *Journal of Applied Crystallography* **2003**, *36*, 7.
- (156) Andrews, S. C.; Arosio, P.; Bottke, W.; Briat, J. F.; Von Darl, M.; Harrison, P. M.; Lauthere, J. P.; Levi, S.; Lobreaux, S.; Yewdall, S. J. *Journal of Inorganic Biochemistry* **1992**, *47*, 161.
- (157) Ako, A. M.; Hewitt, I. J.; Mereacre, V.; Clerac, R.; Wernsdorfer, W.; Anson, C. E.; Powell, A. K. *Angewandte Chemie, International Edition* **2006**, *45*, 4926.
- (158) Delfs, C.; Gatteschi, D.; Pardi, L.; Sessoli, R.; Wieghardt, K.; Hanke, D. *Inorganic Chemistry* **1993**, *32*, 3099.
- (159) Barra, A. L.; Caneschi, A.; Cornia, A.; de Biani, F. F.; Gatteschi, D.; Sangregorio, C.; Sessoli, R.; Sorace, L. *Journal of the American Chemical Society* **1999**, *121*, 5302.
- (160) Foguet-Albiol, M. D. Dissertation, University of Florida, 2006.
- (161) Gorun, S. M.; Papaefthymiou, G. C.; Frankel, R. B.; Lippard, S. J. *Journal of the American Chemical Society* **1987**, *109*, 4244.
- (162) Goodwin, J. C.; Sessoli, R.; Gatteschi, D.; Wernsdorfer, W.; Powell, A. K.; Heath, S. L. *Dalton* **2000**, 1835.
- (163) Powell, A. K.; Heath, S. L.; Gatteschi, D.; Pardi, L.; Sessoli, R.; Spina, G.; Del Giallo, F.; Pieralli, F. *Journal of the American Chemical Society* **1995**, *117*, 2491.
- (164) Ammala, P.; Cashion, J. D.; Kepert, C. M.; Moubaraki, B.; Murray, K. S.; Spiccia, L.; West, B. O. *Angewandte Chemie, International Edition* **2000**, *39*, 1688.

- (165) Murugesu, M.; Abboud, K. A.; Christou, G. *Polyhedron* **2004**, *23*, 2779.
- (166) Taft, K. L.; Lippard, S. J. *Journal of the American Chemical Society* **1990**, *112*, 9629.
- (167) Ali, L. H.; Cox, A.; Kemp, T. J. *Journal of the Chemical Society, Chemical Communications* **1972**, 265.
- (168) Bozak, R. E. *Advances in Photochemistry* **1971**, *8*, 227.
- (169) Ali, L. H.; Cox, A.; Kemp, T. J. *Journal of the Chemical Society, Dalton Transactions* **1973**, 1468.
- (170) Nesmeyanov, A. N.; Sazonova, V. A.; Romanenko, V. I.; Zol'nikova, G. P. *Izvestiya Akademii Nauk SSSR, Seriya Khimicheskaya* **1965**, 1694.
- (171) Ding, W.; Sanderson, C. T.; Conover, R. C.; Johnson, M. K.; Amster, I. J.; Kotal, C. *Inorganic Chemistry* **2003**, *42*, 1532.
- (172) Yamaguchi, Y.; Ding, W.; Sanderson, C. T.; Borden, M. L.; Morgan, M. J.; Kotal, C. *Coordination Chemistry Reviews* **2007**, *251*, 515.
- (173) Chakraborty, I.; Baran, P.; Sanakis, Y.; Simopoulos, A.; Fachini, E.; Raptis, R. G. *Inorganic Chemistry (Washington, DC, United States)* **2008**, *47*, 11734.
- (174) Gass, I. A.; Milios, C. J.; Whittaker, A. G.; Fabiani, F. P. A.; Parsons, S.; Murrie, M.; Perlepes, S. P.; Brechin, E. K. *Inorganic Chemistry* **2006**, *45*, 5281.
- (175) Hahn, F. E.; Joche, C.; Lugger, T. *Zeitschrift fuer Naturforschung, B: Chemical Sciences* **2004**, *59*, 855.
- (176) Kanowitz, S. M.; Palenik, G. J. *Inorganic Chemistry* **1998**, *37*, 2086.
- (177) Gray, H. B.; Hendrickson, D. N.; Sohn, Y. S. *Inorganic Chemistry* **1971**, *10*, 1559.
- (178) Walters, M. A.; Chaparro, J.; Siddiqui, T.; Williams, F.; Ulku, C.; Rheingold, A. L. *Inorganica Chimica Acta* **2006**, *359*, 3996.
- (179) Duggan, D. M.; Hendrickson, D. N. *Inorganic Chemistry* **1975**, *14*, 955.
- (180) Prins, R. *Molecular Physics* **1970**, *19*, 603.
- (181) Prins, R.; Korswagen, A. R. *J. Organometal. Chem.* **1970**, *25*, C74.
- (182) Greenwood, N. N.; Gibb, T. C. *Mössbauer Spectroscopy*, 1971.

- (183) Morrison, W. H., Jr.; Hendrickson, D. N. *Inorganic Chemistry* **1975**, *14*, 2331.
- (184) Edwards, P. R.; Johnson, C. E. *Journal of Chemical Physics* **1968**, *49*, 211.
- (185) Nemykin, V. N.; Hadt, R. G. *Inorganic Chemistry* **2006**, *45*, 8297.
- (186) Jiao, J.; Long, G. J.; Rebbouh, L.; Grandjean, F.; Beatty, A. M.; Fehlner, T. P. *Journal of the American Chemical Society* **2005**, *127*, 17819.
- (187) Bergamini, P.; Di, M. S.; Maldotti, A.; Sostero, S.; Traverso, O. *Journal of Organometallic Chemistry* **1989**, 365, 341.
- (188) Che, D.-J.; Li, G.; Yao, X. L.; Zou, D. P. *Journal of Organometallic Chemistry* **1998**, *568*, 165.
- (189) Karppinen, M.; Yamauchi, H. *International Journal of Inorganic Materials* **2000**, *2*, 589.
- (190) Bickmore, B. R.; Rosso, K. M.; Tadanier, C. J.; Bylaska, E. J.; Doud, D. *Geochimica et Cosmochimica Acta* **2006**, *70*, 4057.
- (191) Stoilova, D.; Marinova, D.; Georgiev, M. *Vibrational Spectroscopy* **2009**, *50*, 245.
- (192) Adams, S.; Moretzki, O.; Canadell, E. *Solid State Ionics* **2004**, *168*, 281.
- (193) Thorp, H. H. *Inorganic Chemistry* **1992**, *31*, 1585.
- (194) Liu, W.; Thorp, H. H. *Inorganic Chemistry* **1993**, *32*, 4102.
- (195) Brown, I. D. *Acta Crystallographica, Section B: Structural Science* **2009**, *B65*, 684.
- (196) Palenik, G. J.; Hu, S.-Z. *Inorganica Chimica Acta* **2009**, *362*, 4740.
- (197) Sidey, V. *Acta Crystallographica, Section B: Structural Science* **2008**, *B64*, 515.
- (198) Urusov, V. S. *Doklady Physical Chemistry* **2006**, *408*, 152.
- (199) Zocchi, F. *Solid State Sciences* **2000**, *2*, 383.
- (200) Zocchi, F. *Solid State Sciences* **2001**, *3*, 383.
- (201) Naskar, J. P.; Hati, S.; Datta, D. *Acta Crystallographica, Section B: Structural Science* **1997**, *B53*, 885.
- (202) Fletcher, R. *Practical Methods of Optimization*; 2nd Ed. ed. New York, 1987.

- (203) Farach-Colton, M.; Roberts, F. S.; Vingron, M.; Waterman, M. *DIMACS Series indiscrete mathematics and theoretical computer science*; American Mathematical Society: Providence, RI, 1999; Vol. 47.
- (204) Mucherino, A.; Papajorgji, P.; Pardalos, P. M. *Data mining in agriculture*; Springer: New York, 2009.
- (205) Fletcher, R.; Reeves, C. M. *Comput. J.* **1964**, *7*, 149.
- (206) Cafieri, S.; D'Apuzzo, M.; Marino, M.; Mucherino, A.; Toraldo, G. *J. Optim. Theory Appl.* **2006**, *129*, 55.
- (207) Kirkpatrick, S.; Gelatt, C. D.; Vecchi, M. P. *Science* **1983**, *220*, 671.
- (208) Lee, K. S.; Geem, Z. W.; Lee, S.-h.; Bae, K.-w. *Engineering Optimization* **2005**, *37*, 663
- (209) Goldberg, D. E. *Genetic Algorithms in Search, Optimization, and Machine Learning*; 1st. Ed. ed.; Addison-Wesley: New York, 1989.
- (210) Corne, D.; Dorigo, M.; Glover, F. *New ideas in optimization* McGraw-Hill: London, 1999.
- (211) Kennedy, J.; Eberhart, R. In *Proc. IEEE Int'l. Conf. on Neural Networks* Perth, Australia, 1995; Vol. IV, p 1942.
- (212) Mucherino, A.; Seref, O. In *Data Mining, System Analysis and Optimization in Biomedicine* Gainesville, Florida, 2007, p 162.
- (213) Mladenovic, N.; Hansen, P. *Computers & Operations Research* **1997**, *24*, 1097.
- (214) Brown, I. D. *Chemical Reviews* **2009**, *109*, 6858.

## BIOGRAPHICAL SKETCH

Antonio Masello was born in Cagliari, Italy in 1976. He attended the Industrial Technical Institute "M. Giua" earning his diploma in industrial chemistry and biotechnologies. Soon after he enrolled at the "Università degli Studi" of Cagliari where was awarded a master in chemistry in 2002 with the maximum score. During the same year, he became a member of the Italian National Council of Chemists passing the exam with the highest score. In September 2002 he joined the Italian Army as a volunteer and worked for one year in the Italian Joint School for the NBC (Nuclear Biological Chemical) Defense, in the laboratory of Maj. Dr. Giammaria S.

In August 2004, he began his PhD studies at the University of Florida where worked on the synthesis and study of polynuclear clusters containing ferrocene, and performed in collaboration with Dr. Antonio Mucherino a statistical study on the model known as Bond Valence Sum.